

UNIVERSITY OF CALGARY

**New Measurement-While-Drilling Surveying Technique Utilizing Sets of**

**Fiber Optic Rotation Sensors**

by

Aboelmagd Noureldin

A THESIS

SUBMITTED TO THE FACULTY OF GRADUATE STUDIES

IN PARTIAL FULFILLMENT OF THE REQUIREMENTS FOR THE

DEGREE OF DOCTOR OF PHILOSOPHY

DEPARTMENT OF ELECTRICAL AND COMPUTER ENGINEERING

CALGARY, ALBERTA

March, 2002

© Aboelmagd Noureldin 2002

UNIVERSITY OF CALGARY

## ABSTRACT

Horizontal drilling processes in the oil industry utilize directional measurement-while-drilling (MWD) instruments to monitor the position and the orientation of the bottom hole assembly (BHA). The present directional monitoring equipment includes three accelerometers and three magnetometers mounted in three mutually orthogonal directions. At some predetermined surveying stations, the accelerometers measure the Earth gravity components to determine the BHA inclination and tool face angles while the magnetometers measure the Earth's magnetic field to determine the BHA azimuth.

The massive amount of ferrous and steel materials around the drilling rig, the presence of downhole ore deposits, the drill string-induced interference and the geomagnetic influences can all have a deleterious impact on the magnetometer measurements. Therefore, this research proposes the use of fiber optic gyroscopes (FOGs) to replace the magnetometers. A quantitative feasibility study has shown that the FOG has excellent immunity to the severe downhole shock and vibration forces.

This thesis aims at developing new MWD surveying methodologies based on the inertial navigation techniques for integrating the FOG technology with the three-axis accelerometers to provide complete surveying solution downhole.

Inertial navigation systems (INS) determine the position and the orientation of a moving platform using three-axis accelerometers and three-axis gyroscopes forming what is known as inertial measurement unit (IMU). Since the BHA cannot accommodate a complete IMU, this research utilizes some specific conditions related to horizontal drilling operations to minimize the number of gyroscopes so that only one or two high-accuracy FOGs would be sufficient to provide full surveying solution downhole. In addition, some adaptive filtering techniques are utilized to enhance the FOG performance in order to reduce its output uncertainty. Moreover, applied optimal estimation techniques based on Kalman filtering methods are employed to improve the surveying accuracy.

The suggested FOG-based MWD surveying techniques eliminate the costly non-magnetic drill collars in which the presently used magnetometers are installed, survey the borehole continuously without interrupting the drilling process and improve the overall accuracy by utilizing some real-time digital signal processing techniques.

## ACKNOWLEDGEMENT

I would like to express my gratitude to my supervisor, Dr. Martin P. Mintchev, for his professional supervision, critical discussions and immeasurable contributions. To him also belongs the credit for proposing the research project and attracting several sources of funding. I would like also to thank Dr. Dave Irvine-Halliday, my research co-supervisor, for his continuous support, encouragement and guidance throughout my studies. I am very fortunate to have Dr. Klaus-Peter Schwarz as a member of my supervisory committee. I would like to thank him for the time he offered to discuss my research results and for facilitating this research project by providing access to the surveying equipment available at the Inertial Laboratory at the Department of Geomatics Engineering.

I wish to express my gratitude to Mr. Herb Tabler, President of International Downhole Equipment, Ltd., for financially supporting the research project, for his critical discussions on the developed surveying techniques, and for his valuable suggestions. I would like also to express my appreciation to Mr. Winston Smith, Proalta Machine & Mfg. Ltd., for the valuable discussions related to the structure of the bearing assembly. Mr. Ashraf Kinawi is also thanked for doing the three-dimensional drawings of the bearing assembly.

The time and the effort of Mr. Frank Hickli, Mr. Ed Evanik and Mr. Rob Thompson during the implementation of the experimental setup are highly appreciated. I would also like to thank Dr. Alex Bruton, presently with Applanix Corporation, and Mr. Sameh Nasar at the Department of Geomatics Engineering for their help during the experimental part and for processing the reference data using KINGSPAD™. Special thanks should go to Dr. Naser El-Sheimy, Geomatics Engineering, and Dr. Ahmed Mohammed, Alberta Research Council, for their advices and recommendations during the early stages of my research. I would also like to thank my colleagues at the University of Calgary, Dr. Mahmoud Reda, Mr. Ahmed Osman, Mr. Peter Rachev and Mr. Enrique Leon Villeda.

This research was supported in part by International Downhole Equipment, Ltd., Micronet Centers of Excellence, Alberta Energy Research Institute, Province of Alberta Fellowship and Killam Memorial Fund. The scholarship and the research allowance provided by Killam Foundation are gratefully acknowledged.

Finally, I would like to thank my parents, Mahmoud and Khiria, for their continuous and unlimited moral support. They have been a constant source of love, encouragement and inspiration. My brothers, Mohammed and Usama are also thanked for their support. I am also grateful to my wife Mie and my son Abdelrahman for their patience, support and continuous encouragement.

## DEDICATION

*To my mother for her unlimited moral support and continuous encouragement.*

*“You stood by me, supported me and believed in me. Words will never say how grateful I am to you.”*

## TABLE OF CONTENTS

Approval page.....	ii
Abstract.....	iii
Acknowledgement.....	iv
Dedication.....	v
Table of Contents.....	vi
List of Tables.....	xiii
List of Figures.....	xiv
List of Symbols.....	xxiv
List of Abbreviations.....	xxxiii
CHAPTER ONE: INTRODUCTION.....	1
1.1. Background.....	1
1.1.1. Horizontal drilling process.....	1
1.1.2. Borehole surveying.....	3
1.2. Problem statement.....	5
1.3. Research objectives.....	6
1.4. Structure of the thesis.....	7
CHAPTER TWO: PRESENT MWD SURVEYING TECHNOLOGY.....	10
2.1. Principles of MWD magnetic surveying technology.....	12
2.1.1. MWD data processing and telemetry.....	14
2.2. Error analysis of the current MWD magnetic surveying system.....	15
2.2.1. Effect of instrument rotation.....	16
2.2.2. Effect of drill collar deflection.....	16
2.2.3. Effect of geomagnetic influences.....	17
2.2.4. Effect of drill string magnetic interference.....	17
2.3. Recent developments in MWD magnetic surveying systems.....	18
2.4. Present gyroscopic surveying technologies.....	19

2.4.1. Wellbore mapping procedure utilizing gyroscopic surveying systems.....	20
2.4.2. In-hole referencing of magnetic surveys.....	22
2.5. Motivations toward developing a new MWD surveying system.....	23
2.6. Conclusion.....	25
CHAPTER THREE: STUDYING THE FEASIBILITY OF FIBER OPTIC GYROSCOPES (FOG) FOR MWD SURVEYING PROCESSES.....	27
3.1. FOG theory and functionality.....	28
3.1.1. Sagnac effect for two-beam interferometer.....	28
3.1.2. FOG operating principle.....	29
3.2. Computer modeling of FOGs.....	32
3.3. FOG performance characteristics.....	36
3.3.1. Angle random walk (ARW).....	36
3.3.2. Bias drift.....	36
3.3.3. Scale factor.....	38
3.4. Simulation of severe drilling conditions.....	39
3.4.1. Shock effect.....	39
3.4.2. Vibration effects.....	40
3.5. Results.....	45
3.5.1. Simulation of the effect of the ARW.....	45
3.5.2. Simulation of FOG sensitivity and bias drift.....	46
3.5.3. Simulation of the effect of shock forces.....	48
3.5.4. Simulation of the effect of vibration due to the mud pump noise.....	50
3.5.5. Simulation of the effect of bending vibration.....	50
3.7. Conclusion.....	53
CHAPTER FOUR: DE-NOISING THE FOG OUTPUT SIGNAL.....	54
4.1. Available methods for reducing FOG noise level.....	55

4.2. Forward linear prediction (FLP) technique.....	57
4.2.1. FLP filter performance for noise reduction at the FOG output.....	59
4.2.1.1. Impact of step size parameter.....	59
4.2.1.2. Impact of filter order.....	61
4.2.2. Experimental procedure and signal conditioning.....	63
4.2.3. Real-time prediction procedure for the FOG output using the FLP filter.....	63
4.2.4. Results.....	65
4.2.4.1. FLP filter design.....	65
4.2.4.2. Performance characteristics of the FLP filter.....	67
4.2.4.3. Impact of the FLP filter on the FOG noise reduction.....	72
4.2.5. Applications and limitations of FLP noise reduction techniques.....	72
4.3. Noise reduction of FOG output signal using transversal filter designed by known Earth rotation rate component in the reference channel.....	74
4.3.1. Filter design.....	74
4.3.2. Filter performance at the FOG output.....	76
4.3.3. Experimental procedure and signal conditioning.....	76
4.3.4. Results.....	77
4.3.4.1. E-Core-2000 results.....	77
4.3.4.2. LTN90-100 results.....	79
4.4. Comparison between the proposed de-noising techniques.....	83
4.5. Conclusion.....	85
 CHAPTER FIVE: SINGLE-FOG MWD SURVEYING SYSTEM.....	 87
5.1. Overview of inertial navigation systems (INS).....	87
5.1.1. Coordinate frames.....	89
5.1.2. Transformation between coordinate frames.....	91

5.1.3. Modeling motion in the local level frame.....	91
5.2. Single-FOG MWD surveying setup.....	95
5.3. Continuous surveying of near-vertical sections of horizontal wells.....	99
5.3.1. Determination of two synthetic rotation rate components.....	99
5.3.2. Development of the mechanization equations.....	101
5.3.3. Error state model of the MWD surveying parameters.....	104
5.3.4. Quantitative long-term analysis of surveying errors.....	109
5.3.5. Real-time techniques for limiting long-term surveying errors.....	113
5.3.5.1. Continuous aided inertial navigation technique.....	114
5.3.5.2. Zero velocity update (ZUPT) technique.....	117
5.3.5.3. Backward velocity error correction criterion during the ZUPT procedure.....	118
5.3.6. Choice of transitional inclination angle.....	118
5.3.7. Results.....	120
5.3.7.1. Long-term behavior of surveying errors.....	120
5.3.7.2. Limiting the long-term surveying errors with continuous aided inertial navigation.....	123
5.3.7.3. ZUPT technique for limiting surveying errors.....	128
5.3.7.4. Impact of the backward velocity error correction criterion.....	130
5.3.7.5. Analysis of the errors associated with the choice of the transitional inclination angle.....	133
5.3.8. Applications and limitations of the Single-FOG continuous surveying method in MWD.....	135
5.4. Station-based surveying of highly-inclined and horizontal well sections.....	137
5.4.1. Development of surveying equations.....	138
5.4.2. Surveying errors.....	141
5.4.3. Sources of surveying errors.....	142

5.4.3.1. Intrinsic sensor errors.....	142
5.4.3.2. Vibration-induced sensor errors.....	143
5.4.4. Real-time techniques for limiting surveying errors.....	143
5.4.5. Experimental procedure and signal conditioning.....	144
5.4.6. Results.....	145
5.4.6.1. Computation of the inclination and the azimuth angles.....	145
5.4.6.2. Analysis of the inclination and the azimuth errors...	149
5.4.7. Applications and limitations of the single-FOG station-based surveying technique.....	153
 CHAPTER SIX. DUAL-FOG MWD SURVEYING SYSTEM.....	 155
6.1. Dual-FOG MWD surveying setup.....	156
6.2. Continuous surveying of radical sections of horizontal wells.....	156
6.2.1. Establishing the desired azimuth direction.....	156
6.2.2. Surveying the radical section of the well.....	160
6.2.2.1. Determination of the synthetic rotation rate component.....	161
6.2.2.2. Determination of the transformation matrix using the quaternion approach.....	161
6.2.2.3. Computational procedure of the different surveying parameters.....	164
6.2.3. Modeling surveying errors by linear state equations.....	169
6.2.3.1. Attitude errors.....	169
6.2.3.2. Coordinate errors.....	170
6.2.3.3. Velocity errors.....	171
6.2.4. Limiting surveying errors using continuous aided inertial navigation and ZUPT techniques. ....	172
6.2.5. Experimental procedure and signal conditioning.....	172
6.2.6. Results.....	173

6.2.6.1. Comparison between dual-gyro and full IMU solutions.....	173
6.2.6.2. Continuous aided inertial navigation.....	176
6.2.6.3. Impact of the ZUPT procedure.....	178
6.3. Station-based surveying technique.....	180
6.3.1. Motivation for station-based surveying.....	180
6.3.2. Performance improvement by utilizing dual FOG and changing body axes orientation.....	180
6.3.2.1. Station-based surveying of the near-vertical section.....	181
6.3.2.2. Station-based surveying of highly inclined and horizontal well sections.....	183
6.3.3. Real-time techniques for limiting surveying errors.....	185
6.3.4. Comparative performance study between the single and dual gyro systems.....	186
6.3.5. Experimental procedure and signal conditioning.....	188
6.3.6. Results.....	188
6.3.6.1. Computation of the azimuth and the inclination angles.....	188
6.3.6.2. Improvement of azimuth accuracy by the ZUPT procedure.....	195
6.3.6.3. Comparison between the single and the dual gyro systems.....	197
6.4. Conclusion.....	198

CHAPTER SEVEN: CONCLUSION AND RECOMMENDATIONS FOR FUTURE RESEARCH.....	199
7.1. Summary.....	199
7.2. Conclusion.....	200
7.3. Thesis contributions.....	202

7.4. Recommendations for future research.....	204
REFERENCES.....	206
APPENDIX A: DETERMINISTIC ANALYSIS OF FOG PERFORMANCE.....	222
A.1. FOG Operating Principle.....	223
A.2. Deterministic Analysis.....	225
A.3. Feedback FOG with Serrodyne Modulator.....	228
APPENDIX B: DESIGN AND IMPLEMENTATION OF THE EXPERIMENTAL SETUP.....	233
B.1. Design of the experimental setup.....	233
B.2. Implementation of the experimental setup.....	235
B.2.1 Control of rotational motion.....	237
B.2.2. Signal conditioning and data acquisition.....	238
APPENDIX C: STUDYING THE LONG-TERM BEHAVIOR AND THE INTERRELATIONSHIP BETWEEN THE VARIOUS SURVEYING ERRORS.....	245
C.1. The Schuller effect.....	246
C.2. Non-stationary components of surveying errors.....	248
C.3. Solution of the surveying errors state equations.....	249
C.3.1. Surveying errors along the horizontal channels.....	251
C.3.2. Surveying errors along the vertical channel.....	251
C.4. Simulation results	252
APPENDIX D: KALMAN FILTERING ALGORITHM AND THE RELATED DESIGN CONSIDERATIONS.....	256

## LIST OF TABLES

Table 1.1.	The different horizontal drilling categories with the corresponding turning radii and build rates.....	3
Table 5.1.	The azimuth error at different inclination angles for a given known azimuth.....	150
Table C.1.	Sources of velocity errors along any of the horizontal channels.....	250
Table C.2.	Sources of position errors along any of the horizontal channels.....	250
Table C.3.	Sources of attitude errors along any of the horizontal channels.....	250
Table C.4.	Sources of velocity errors along the vertical channel.....	251
Table C.5.	Sources of position errors along the vertical channel.....	251
Table C.6.	Sources of attitude errors along the vertical channel.....	251

## LIST OF FIGURES

Figure 1.1	Horizontal drilling assembly [Rehm et al., 1989].....	2
Figure 2.1	General procedure for designing a surveying program [after Thorogood, 1989 and 1986].....	11
Figure 2.2	Section of the non-magnetic drill collars with the magnetic surveying equipment inside.....	13
Figure 2.3	Schematic diagram of wellbore mapping utilizing gyroscopic equipment [after Noy and Leonard, 1997].....	20
Figure 3.1	Two-beam interferometer using the fiber optic technology [after Lefevre, 1993].....	29
Figure 3.2	Closed loop fiber optic gyroscope (FOG).....	31
Figure 3.3	The FOG as a closed loop first-order system.....	35
Figure 3.4	The step response of the FOG. $L = 1000m$ , $d = 0.1m$ , $n = 1.48$ , $\lambda = 0.85 \mu m$ , $K = 0.5815$ and $G = 10^5$ .....	35
Figure 3.5	Applying the angle random walk (ARW) as a disturbance to the FOG system.....	37
Figure 3.6	The change of the peak wavelength of the optical beam with respect to temperature variation.....	38
Figure 3.7	Representation of impulsive shock forces.....	40
Figure 3.8	Applying angular rate disturbance to the FOG system.....	41
Figure 3.9.a	Initial curvature of the drill collar downhole.....	43
Figure 3.9.b	Cross section of the borehole and the whirling drill collar.....	43
Figure 3.10	Bending moment as a function of time.....	44
Figure 3.11.a	FOG step response with the effect of ARW at $G = 2*10^5$ .....	45
Figure 3.11.b	FOG step response with the effect of ARW at $G = 10^5$ .....	46
Figure 3.11.c	FOG step response with the effect of ARW at $G = 0.5*10^5$ .....	46
Figure 3.12.a	FOG step response for different values of $L$ , $d = 0.1m$ , $n = 1.48$ , $\lambda = 0.85 \mu m$ , $K = 0.5815$ and $G = 10^5$ .....	47
Figure 3.12.b	FOG step response for different values of $G$ , $d = 0.1m$ , $n = 1.48$ , $\lambda = 0.85 \mu m$ , $K = 0.5815$ and $L = 1000m$ .....	48

Figure 3.13.a	Three-dimensional distribution of the percentage error at the output of the FOG with respect to different magnitudes and time duration of the shock forces.....	49
Figure 3.13.b	FOG output signal (containing ARW) with the 1000g shock force acting at the moment $t = 40$ sec for a duration of 0.01 sec.....	49
Figure 3.14.a	FOG output signal (containing no ARW) with the effect of the mud pump noise at $G = 10^5$ .....	51
Figure 3.14.b	FOG output signal (containing no ARW) with the effect of the mud pump noise at $G = 0.5*10^5$ .....	51
Figure 3.14.c	FOG output signal (containing ARW) with the effect of the mud pump noise at $G = 10^5$ .....	51
Figure 3.15.a	FOG output signal (containing no ARW) with the effect of bending vibration at $G = 2*10^5$ .....	52
Figure 3.15.b	FOG output signal (containing no ARW) with the effect of bending vibration at $G = 10^5$ .....	52
Figure 3.15.c	FOG output signal (containing no ARW) with the effect of bending vibration at $G = 0.5*10^5$ .....	52
Figure 4.1	Structure of a tap-delay FIR filter that employs past samples $\{u(n-1), u(n-2), u(n-3), \dots, u(n-M)\}$ to provide an estimate of the current sample value $\hat{u}(n)$ [Haykin, 1996].....	57
Figure 4.2	Adaptive adjustment of the tap weights of the FLP filter using the LMS algorithm.....	59
Figure 4.3	Flow chart describing the adaptive process of determining the tap weights of the FLP filter based on the LMS criterion using changeable step size parameter.....	62
Figure 4.4	Projection of the Earth rotation vector along the vertical direction....	64
Figure 4.5.a	Variation of the Earth rotation rate error with the step size parameter $\mu$ for 300-tap weights FLP filter.....	66
Figure 4.5.b	Variation of the Earth rotation rate error with the step size parameter $\mu$ for 600-tap weights FLP filter.....	66

Figure 4.6	Learning curve for a 300 tap weights FLP filter with $\mu = 0.00005$ and $\mu = 0.001$ .....	67
Figure 4.7	Rate of change of the MSEE for $\mu = 0.001$ in a 300-tap weights FLP filter.....	69
Figure 4.8	Learning curve for 300-tap weights FLP filter with constant step size $\mu = 0.00005$ and with varying step size from $\mu = 0.001$ to $\mu = 1.1 \times 10^{-5}$ .....	69
Figure 4.9	Convergence time versus the filter order for a step size parameter $\mu = 0.0004$ .....	71
Figure 4.10	Frequency response of FLP filters of different order with $\mu = 0.0004$ .....	71
Figure 4.11	FOG output before processing with FLP filters, after processing with a 300-tap weights FLP filter, and after processing with a 600-tap weights FLP filter.....	72
Figure 4.12	Angle random walk ( $^{\circ} / hr / \sqrt{Hz}$ ) versus the filter order.....	73
Figure 4.13	Adaptive adjustment of the tap weights of the transversal filter using the LMS algorithm.....	75
Figure 4.14	The E-Core-2000 output signal before and after filtering with 300 tap weights at an orientation of $10^{\circ}$ pitch, $10^{\circ}$ roll and $20^{\circ}$ azimuth.....	78
Figure 4.15	The E-Core-2000 output signal before and after filtering with 600 tap weights at an orientation of $20^{\circ}$ pitch, $20^{\circ}$ roll and $41^{\circ}$ azimuth.....	78
Figure 4.16	Learning curves of a transversal filter of 100 tap weights at the output of LTN90-100 vertical gyro with respect to different step size parameters $\mu$ .....	79
Figure 4.17	The Gyro output sequence after filtering with 100 tap weights at orientation of $-0.2914^{\circ}$ pitch, $0.8429^{\circ}$ roll and $5.8528^{\circ}$ azimuth.....	80

Figure 4.18	Estimation error of the Earth rotation rate component and the output uncertainty for the first set of data.....	81
Figure 4.19	Estimation error of the Earth rotation rate component and the output uncertainty for the second set of data.....	82
Figure 4.20	Estimation error of the Earth rotation rate component and the output uncertainty for the third set of data.....	82
Figure 5.1	Schematic diagram showing the fundamental concept of INS [after Titterton and Weston, 1997].....	88
Figure 5.2	The $b$ -frame axes for a section inside the drill pipe.....	89
Figure 5.3	The $\ell$ -frame axes for a given point on the Earth's surface.....	90
Figure 5.4	The change of $\ell$ -frame orientation along the Earth's surface.....	93
Figure 5.5	Single-axis FOG-based gyroscopic surveying system mounted inside the bearing assembly.....	97
Figure 5.6	Diagram showing the different sections of a horizontal well.....	98
Figure 5.7	The Single-FOG setup with the $b$ -frame and the $\ell$ -frame represented inside the bearing assembly.....	100
Figure 5.8	Distribution of velocities and Earth rotation rate components along the $\ell$ -frame axes.....	103
Figure 5.9	Block diagram of the Single-FOG technique for MWD continuous surveying process.....	104
Figure 5.10	Block diagram of FOG-based MWD surveying errors.....	109
Figure 5.11	Integration between the system model and the discrete Kalman filter [after Gelb, 1974].....	112
Figure 5.12	The setup while rotating about the three mutually orthogonal axes...	114
Figure 5.13	Block-diagram describing the technique of aided inertial navigation.....	115
Figure 5.14	Mean square estimation error of the velocity error states in $(\text{m/sec})^2$ .....	120
Figure 5.15	Mean square estimation error of the attitude error states in $(\text{deg})^2$ .....	121

Figure 5.16	Mean square estimation error of the latitude in $(deg)^2$ , the longitude in $(deg)^2$ and the altitude in $m^2$ .....	122
Figure 5.17	Velocity errors along the East, the North and the vertical directions in m/sec.....	123
Figure 5.18	The inclination, the roll and the azimuth errors in degrees.....	124
Figure 5.19	The inclination and the azimuth angles in degrees.....	125
Figure 5.20	The azimuth angle after achieving the convergence of the mean square estimation error and performing error correction.....	126
Figure 5.21	Position errors along the North, the East and the vertical directions in meters.....	127
Figure 5.22	Accelerometer measurements (in $m/sec^2$ ) during a stationary experiment.....	128
Figure 5.23	The mean square estimation error of the velocity error states in $(m/sec)^2$ between and during ZUPT procedures.....	129
Figure 5.24	The velocity errors (in m/sec) along the East and the North directions ( $\delta V^e$ and $\delta V^n$ ) between $t = 15$ min and $t = 35$ min .....	131
Figure 5.25	The position errors (in meters) along the East and the North directions ( $\delta P_E$ and $\delta P_N$ ) between $t = 15$ min and $t = 35$ min with the number of each ZUPT station indicated.....	131
Figure 5.26	The velocity errors (in m/sec) along the East and the North directions ( $\delta V^e$ and $\delta V^n$ ) between $t = 15$ min and $t = 35$ min after performing one-step backward error correction.....	132
Figure 5.27	The position errors (in meters) along the East and the North directions ( $\delta P_E$ and $\delta P_N$ ) between $t = 15$ min and $t = 35$ min after performing one-step backward error correction.....	132
Figure 5.28	Analysis of the inclination error associated with different transitional inclination angles considering different accelerometer errors.....	133

Figure 5.29	Errors of the synthetic rotation rate component with respect to different transitional inclination angles at different accelerometer errors.....	134
Figure 5.30	A schematic diagram showing the orientation of the FOG and the accelerometers during the horizontal drilling processes.....	137
Figure 5.31	A model of the bearing assembly with the surveying sensors installed few inches behind the drill bit.....	138
Figure 5.32	Earth gravity components along the BHA b-frame axes.....	139
Figure 5.33	Earth rotation rate components along the BHA moving along the $Y^b$ axis.....	140
Figure 5.34	Accelerometer measurements $f_y$ before and after the filtering procedure.....	146
Figure 5.35	Inclination angle at sections near the horizontal direction.....	146
Figure 5.36	Rotation rate measurement $\omega_y$ before and after filtering.....	147
Figure 5.37	Azimuth angle at surveying station near to the horizontal plane and close to the East direction.....	148
Figure 5.38	Estimated azimuth error and the corresponding uncertainty for different roll angles while the setup near to the horizontal plane and close to the East direction.....	148
Figure 5.39	Inclination error with respect to the inclination angle at different azimuth directions.....	150
Figure 5.40	Azimuth errors with respect to different inclination angles at orientations close to the North direction (worst azimuth accuracy)....	151
Figure 5.41	The azimuth error with respect to the BHA azimuth at two different inclination angles.....	152
Figure 5.42	Earth rotation rate component along the tool spin axis at $90^\circ$ inclination for different azimuth angles.....	153
Figure 6.1	Dual-axis FOG-based gyroscopic surveying system mounted inside the bearing assembly.....	157

Figure 6.2	Determination of the initial azimuth.....	158
Figure 6.3	The initial arrangement of the FOGs and the accelerometers with the body frame axes inside the bearing assembly.....	160
Figure 6.4	A block diagram describing the functionality of the surveying procedure for the radical section of the well.....	168
Figure 6.5	Comparison between the actual rotation rate measurement $\omega_x$ and the corresponding synthetic rotation rate component $\omega_{xs}$ .....	174
Figure 6.6	Differences between the synthetic and the measured rotation rate components along the X-axis.....	174
Figure 6.7	Computation of the attitude components with the dual gyro system and the full IMU system.....	175
Figure 6.8	Computation of the azimuth angle between $t=30 \text{ min}$ and $t=50 \text{ min}$ with the dual-gyro configuration of the full IMU system .....	176
Figure 6.9	Mean square estimation error of the velocity error states in $(\text{m/sec})^2$ .....	177
Figure 6.10	Mean square estimation error of the attitude error states in $(\text{deg.})^2$ ....	177
Figure 6.11	Velocity and position errors along the North direction before applying the backward velocity error correction criterion.....	179
Figure 6.12	Velocity and position errors along the North direction after applying the backward velocity error correction criterion.....	179
Figure 6.13	Surveying the near vertical section of the drilling well.....	181
Figure 6.14.a	Surveying the highly inclined section of the drilling well.....	184
Figure 6.14.b	Surveying the horizontal section of the drilling well.....	184
Figure 6.15	Block diagram showing the surveying methodology with all digital signal processing techniques.....	186
Figure 6.16	Comparison between the reference azimuth and the computed azimuth for inclination angle of $75^\circ$ .....	189
Figure 6.17	The inclination error versus the inclination angle for the near vertical section of the well up to $45^\circ$ inclination.....	189

Figure 6.18	The inclination error versus the inclination angle for the highly inclined section of the well above $45^\circ$ inclination.....	190
Figure 6.19	The inclination error versus the inclination angle in the horizontal section of the well.....	191
Figure 6.20	The inclination error versus the inclination angle in the highly inclined section of the well for different azimuth directions.....	191
Figure 6.21	The azimuth error versus the inclination angle for orientations close to the East direction.....	192
Figure 6.22	The azimuth errors at three different inclination angles for orientations close to the East direction, the North direction and the midway between the East and the North.....	193
Figure 6.23	The inclination angle before and after filtering with a transversal tap delay line filter of 100 tap weights.....	194
Figure 6.24	The value of $\cos(\psi)$ before and after filtering with a transversal tap delay line filter of 100 tap weights.....	195
Figure 6.25	Mean square estimation error of the inclination and the azimuth error states.....	196
Figure 6.26	Variation of the inclination and the azimuth angles during the ZUPT procedure.....	196
Figure 6.27	Comparison of the inclination accuracy between the single and the dual gyro systems.....	198
Figure A.1	Ideal Serrodyne Modulator.....	229
Figure A.2	Frequency function $\eta(t)$ .....	229
Figure B.1	Layout of the experimental setup.....	234
Figure B.2	Closed loop analog position control of DC motor.....	235
Figure B.3	The experimental setup with showing the inertial measurement devices (the FOG and the three accelerometers).....	237
Figure B.4	Connection diagram for the DC motor positioning and speed control.....	239

Figure B.5	The connection diagram for processing the FOG and the accelerometers output signal and interfacing them to the A/D system [Noureldin et al. <sup>b</sup> , 2000].....	240
Figure B.6	Software program for 4-channels data acquisition (courtesy of Karimi and Segal, 1999).....	242
Figure B.7	Changing the range of the vertical axes of the four channels in real-time during the data acquisition process.....	242
Figure B.8	Configuration of the software program for different signal sources (acquiring data through the A/D card or reading data from a file).....	243
Figure B.9	The traditional amplification circuit for differential signals.....	244
Figure B.10	Connection diagram for the amplification of the FOG signal during the alignment process using AD620.....	244
Figure C.1.a	Block diagram showing the Schuller loop describing the coupling between $\delta V^e$ and $\delta\phi$ (i.e. along the East channel).....	247
Figure C.1.b	Block diagram showing the Schuller loop describing the coupling between $\delta V^n$ and $\delta\theta$ (i.e. along the North channel).....	248
Figure C.2	The different factors affecting the velocity error along the horizontal channel and their total effect.....	253
Figure C.3	The different factors affecting the position error along the horizontal channel and their total effect.....	253
Figure C.4	The different factors affecting the pitch or the roll error and their total effect.....	254
Figure C.5	The different factors affecting the vertical velocity error and their total effect.....	254
Figure C.6	The different factors affecting the altitude error and their total effect.....	255
Figure C.7	The different factors affecting the azimuth error and their total effect.....	255
Figure D.1	Block diagram of Kalman filtering sequential recursive algorithm....	257

Figure D.2	Prediction and update procedures of Kalman filtering algorithm.....	257
Figure D.3	Kalman filtering recursive algorithm.....	258

## LIST OF SYMBOLS

$a_s$	Linear acceleration corresponding to the shock force.
$A$	Amplitude of the AC-bias modulator sinusoidal signal.
$A_{\max}$	Maximum amplitude of $p(t)$ .
$b_1:b_M$	FIR filter tap weights.
$b_u$	Accelerometer bias error along the vertical channel.
$b$	Accelerometer bias error along the horizontal channel .
$B$	Bending moment.
$B_x$	Magnetometer measurement along the $x$ -direction.
$B_y$	Magnetometer measurement along the $y$ -direction.
$B_z$	Magnetometer measurement along the $z$ -direction.
$B_N$	Magnetic field component obtained from the published geomagnetic survey data.
$B_V$	Magnetic field component obtained from the published geomagnetic survey data.
$B^T$	Tap weight vector $\{b_1 \ b_2 \ . \ . \ b_M\}$ .
$C_o$	Speed of light in free space.
$d$	Diameter of the fiber optic coil.
$d$	Gyro drift.
$d(n)$	The desired response utilized during the learning process.
$d_u$	Vertical Gyro drift.
$e(n)$	Estimation error.
$E$	Magnitude of the magnetic error vector.
$f$	Vibration frequency due to the mud pump noise.
$f_x$	Accelerometer measurement along the $x$ -direction.
$f_y$	Accelerometer measurement along the $y$ -direction.
$f_z$	Accelerometer measurement along the $z$ -direction.

$f^b$	Accelerometer measurements vector $f^b = (f_x \quad f_y \quad f_z)^T$ .
$f_s$	Schuller frequency.
$F^\ell$	Skew-symmetric matrix corresponding to $f^\ell$ .
$F$	Magnitude of the shock force.
$F_s$	Applied shock force.
$F_{k,k-1}$	Dynamic matrix relating $\chi_{k-1}$ to $\chi_k$ .
$g$	Earth gravity.
$g^\ell$	The Earth gravity vector expressed at the local-level frame.
$G$	Electronic gain.
$G_{k-1}$	Noise coefficient vector.
$h$	Altitude.
$H(s)$	FOG input/output transfer function.
$H_k$	Design matrix of the noiseless relationship between $\chi_k$ and $y_k$ .
$I$	Inclination angle.
$J_1$	1 <sup>st</sup> order polynomial of the Bessel function of 1 <sup>st</sup> kind.
$J(n)$	The expectation of the square value of the estimation error (cost function).
$K$	A constant equal to $S_0 J_1(A)$ .
$K_k$	Kalman gain matrix.
$L$	Length of the fiber optic coil.
$m_b$	Mass corresponding to the total weight on bit.
$m_c$	Mass of the drill collar.
$M$	Filter order.
$M$	Meridian radius of curvature (North-South) in meters.
$n$	Refractive index of the fiber optic coil.
$N$	Number of turns of the fiber optic coil.
$N$	Prime vertical radius of curvature (East-West) in meters.
$p(t)$	Pressure signal produced due to the mud pump noise.
$P_k$	Error covariance matrix.

$P_k(+)$	Error covariance matrix associated with $\hat{\chi}_k(+)$ .
$P_k(-)$	Error covariance matrix associated with $\hat{\chi}_k(-)$ .
$Q$	Covariance matrix of the system noise.
$Q$	Vector of quaternion parameters $Q = (q_1 \quad q_2 \quad q_3 \quad q_4)^T$ .
$r_o$	Outer radius of the drill collar.
$r_i$	Inner radius of the drill collar.
$r^\ell$	Position vector expressed in the local-level frame.
$\bar{r}^\ell$	Computed position vector in the local-level frame.
$R_b^\ell$	Transformation matrix between the body frame and the local-level frame.
$R_\ell^b$	Transformation matrix between the local-level frame and the body frame.
$\dot{R}_b^\ell$	Time rate of change of the transformation matrix between the body frame and the local-level frame.
$R$	Covariance matrix of the observations random noise.
$R_g$	An external resistor connected to the AD620 IC.
$R_o$	Mean radius of the Earth.
$S_0$	Power of the main optical beam.
$t$	Time
$u(n-1):u(n-M)$	Tap inputs of the FLP filter.
$u(n-k)$	Input sequence involving $k$ samples back from the $n^{\text{th}}$ sample.
$u(n)$	The input sample at the current time $n$ .
$\hat{u}(n)$	The estimate of the actual value of the current sample $u(n)$ .
$U(n-1)$	Tap input vector of the FLP filter.
$U(n)$	Vector of the input sequence to the FIR filter.
$v_k$	Observations random noise.
$\tilde{V}$	Output voltage of the FOG open loop configuration.
$V_m$	Linear velocity disturbance due to the mud pump noise.
$V^e$	Velocity component along the East direction in m/sec.

$V^n$	Velocity component along the North direction in m/sec.
$V^u$	Velocity component along the vertical direction in m/sec.
$V^\ell$	Velocity vector expressed in the local-level frame.
$w(t)$	Unity variance white Gaussian noise.
$W_{k-1}$	Unity-variance white Gaussian noise.
$X^\ell$	The East direction of the local-level frame.
$X$	The transverse axis of the body frame.
$y(n)$	FIR filter output.
$y_k$	Observation vector.
$Y$	The forward axis of the body frame.
$Y^\ell$	The North direction of the local-level frame.
$Z$	The vertical axis of the body frame.
$Z^\ell$	The vertical (up) direction of the local level frame.
$\alpha_x$	Reciprocal of the time correlation parameter of the random process associated with the acceleration measurement $f_x$ .
$\alpha_y$	Reciprocal of the time correlation parameter of the random process associated with the acceleration measurement $f_y$ .
$\alpha_z$	Reciprocal of the time correlation parameter of the random process associated with the acceleration measurement $f_z$ .
$\beta$	Reciprocal of the time correlation parameter of the random process associated with the FOG measurement.
$\chi$	Error state vector of both surveying and inertial sensor errors.
$\hat{\chi}_k(-)$	<i>a priori</i> estimate of the error states.
$\hat{\chi}_k(+)$	Updated estimate of the error states.
$\delta\omega_x$	Angular velocity measurement error along the X-direction.
$\delta\omega_y$	Angular velocity measurement error along the Y-direction.
$\delta\omega_z$	Angular velocity measurement error along the Z-direction.
$\delta f_x$	Accelerometer measurement error along the X-direction.

$\delta f_y$	Accelerometer measurement error along the Y-direction.
$\delta f_z$	Accelerometer measurement error along the Z-direction.
$\delta \omega_{xs}$	Synthetic rotation rate component error along the East direction.
$\delta \omega_{ys}$	Synthetic rotation rate component error along the North direction.
$\delta \theta$	Inclination angle error.
$\delta \phi$	Roll angle error.
$\delta \psi$	Azimuth angle error.
$\delta V^e$	Velocity error along the East direction.
$\delta V^n$	Velocity error along the North direction.
$\delta V^u$	Velocity error along the vertical direction.
$\delta \varphi$	Latitude angle error in degrees.
$\delta \lambda$	Longitude angle error in degrees.
$\delta h$	Altitude error in meters.
$\delta P_E$	Position error along the East direction in meters.
$\delta P_N$	Position error along the North direction in meters.
$\delta r^\ell$	Errors in position vector expressed in the local-level frame.
$\delta V^\ell$	Errors in velocity vector expressed in the local-level frame.
$\delta g^\ell$	Gravity computational error.
$\delta V_{Sch}^e$	Schuler component of $\delta V^e$ .
$\delta V_{nst}^e$	Schuler component of $\delta V^e$ .
$\delta V_{Sch}^n$	Schuler component of $\delta V^n$ .
$\delta V_{nst}^n$	Schuler component of $\delta V^n$ .
$\delta \omega_e$	East gyro drift.
$\delta \omega_n$	North gyro drift.
$\delta \omega_u$	Vertical gyro drift.
$\delta f_e$	East accelerometer bias error.

$\delta f_n$	North accelerometer bias error.
$\delta f_u$	Vertical accelerometer bias error.
$\delta P_{E_{nst}}$	Non-stationary position error along the East direction.
$\delta P_{N_{nst}}$	Non-stationary position error along the North direction.
$\delta P$	Position error along the horizontal channels.
$\delta V$	Velocity error along the horizontal channels.
$\delta V_o$	Initial velocity error along the horizontal channels.
$\delta V_{u0}$	Initial velocity errors.
$\delta P_0$	Initial position error.
$\delta h_0$	Initial altitude error.
$\delta \psi_0$	Initial misalignment (i.e. initial azimuth errors).
$\varepsilon_0$	Initial misleveling.
$\varepsilon^\ell$	Vector of attitude angle errors $\varepsilon^\ell = (\delta\theta \ \delta\phi \ \delta\psi)^T$ .
$\phi$	Roll (tool face) angle.
$\phi_s$	Sagnac phase shift.
$\varphi$	The latitude angle.
$\lambda$	Longitude angle.
$\lambda_{\min}$	The minimum eigenvalue of the autocorrelation matrix of the tap input vector.
$\lambda_{\max}$	The maximum eigenvalue of the autocorrelation matrix of the tap input vector.
$\lambda_o$	Free space wavelength of the optical beam.
$\mu$	Step size parameter.
$\theta$	Inclination angle.
$\theta_{ib}^b$	Vector of measured angular increments.
$\theta_{il}^b$	Vector of angular increments corresponding to $\omega_{il}^b$ .

$\sigma_x$	Standard deviation of the random process associated with the acceleration measurement $f_x$ .
$\sigma_y$	Standard deviation of the random process associated with the acceleration measurement $f_y$ .
$\sigma_z$	Standard deviation of the random process associated with the acceleration measurement $f_z$ .
$\sigma_g$	Standard deviation of the random process associated with the FOG measurement.
$\omega^e$	Earth rotation rate around its spin axis ( $15^\circ / hr$ ).
$\omega_Z$	FOG measurements in deg./sec.
$\omega_x$	Angular velocity measurement along the $x$ -axis.
$\omega_y$	Angular velocity measurement along the $y$ -axis.
$\omega_z$	Angular velocity measurement along the $z$ -axis.
$\omega_{xs}$	Synthetic rotation rate component along the East direction in deg./sec.
$\omega_{ys}$	Synthetic rotation rate component along the North direction in deg./sec.
$\omega_{ie}^\ell$	Vector of Earth rotation rate components expressed at the $\ell$ -frame.
$\omega_{e\ell}^\ell$	Angular velocity vector describing the change of orientation of the local-level frame along the Earth's surface.
$\omega_{e\ell}^b$	Vector of angular velocities equivalent to $\omega_{e\ell}^\ell$ after transformation into the body-frame ( $\omega_{e\ell}^b = R_b^\ell \omega_{e\ell}^\ell$ ).
$\omega_{ib}^b$	Vector of angular velocity measurements provided by gyroscopes.
$\omega_{i\ell}^b$	Vector of angular rotations expressed at the body-frame between the local-level frame and the inertial frame.
$\psi$	Azimuth angle.
$\psi_c$	Corrected azimuth angle.
$\psi_{true}$	True azimuth angle.

$\Delta$	Error in the computation in the quaternion parameters.
$\Delta\theta$	Angular increments corresponding to the angular velocity measurements.
$\Delta v$	Velocity increments corresponding to the acceleration measurements.
$\Delta V$	Vector of velocity changes.
$\Delta L$	Path difference between the two counter-propagating beams.
$\Delta t$	Time duration of the shock force.
$\Delta V_s$	Change in the linear velocity corresponding to the shock force.
$\Theta$	Rotation angle about a fixed axis.
$\Omega$	Rotation rate performed by the plane of the fiber optic coil.
$\Omega_s$	Angular velocity disturbance due to the shock force.
$\Omega$	Applied rotation rate.
$\hat{\Omega}$	FOG output.
$\Omega(s)$	Applied rotation rate in $s$ - domain.
$\hat{\Omega}(s)$	FOG output in $s$ - domain.
$\Omega_m$	Angular velocity disturbance due to the mud pump noise.
$\Omega_v$	Angular velocity disturbance due to the bending vibration.
$\Omega_{ie}^{\ell}$	Skew-symmetric matrix corresponding to $\omega_{ie}^{\ell}$ .
$\Omega_{el}^{\ell}$	Skew-symmetric matrix corresponding to $\omega_{el}^{\ell}$ .
$\Omega_{ib}^b$	Skew-symmetric matrix corresponding to $\omega_{ib}^b$ .
$\Omega_{\ell b}^b$	Skew symmetric matrix of the angular rotations expressed at the body-frame between the body-frame and the local-level frame.
$\Omega_{ie}^b$	Skew symmetric matrix of the Earth rotation as observed at the b-frame.
$\Omega_{el}^b$	Skew-symmetric matrix corresponding to $\omega_{el}^b$ .
$\Omega_{il}^b$	Skew symmetric matrix corresponding to $\omega_{il}^b$ ( $\Omega_{il}^b = \Omega_{ie}^b + \Omega_{el}^b$ ).
$\Omega(\omega)$	Skew symmetric matrix of angular rotations.

## LIST OF ABBREVIATIONS

ARW	Angle Random Walk.
BHA	Bottom Hole Assembly.
FIR	Finite Impulse Response.
FLP	Forward Linear Prediction.
FOG	Fiber Optic Gyroscope.
INS	Inertial Navigation System.
IMU	Inertial Measurement Unit.
LMS	Least Mean Square.
MSE	Mean Square Error.
MSEE	Mean Square Estimation Error.
MWD	Measurement While Drilling.
WOB	Weight On Bit.
ZUPT	Zero velocity Update.

## **CHAPTER ONE**

### **INTRODUCTION.**

#### **1.1. Background.**

##### **1.1.1. Horizontal drilling process.**

During the last two decades, horizontal drilling processes have been the subject of intensive research investigations [Conti et al., 1989; Rehm et al., 1989; Joshi et al., 1991; Bell et al., 1994]. A great deal of interest in these technologies has been shown by the oil companies and the drilling contractors [Rehm et al., 1991; Graham, 1994]. It was suggested that by “kicking off” above an oil bearing formation, drilling into it at an angle and then following along within the formation horizontally, productivity and longevity of a producing well could be increased significantly [Fisher et al., 1991; Anon, 1999]. Conti et al. (1989) showed that the horizontal drilling system should include directional measurement-while-drilling (MWD) equipment and a steerable system in addition to the conventional drilling assembly. The drilling assembly for the horizontal drilling process consists of a diamond bit, a high speed motor with a bent housing, a mule-shoe orienting sub with built-in float valve, non-magnetic drill collars which include magnetic surveying tools, and a slick drill pipe [Fig.1.1, Rehm et al., 1989]. The non-magnetic drill collars carry the surveying equipment, and stabilize the movement of the motor. They are usually designed from monel metal to avoid external interference to the magnetic surveying tools [Fisher et al., 1991]. The cost of the non-magnetic drill collars can run up to \$30,000 for single installation, thus directly affecting the overall budget of the horizontal drilling process.

Horizontal well technology involves drilling a vertical hole (usually using conventional rotary drilling) to an appropriate depth. The horizontal drilling equipment is then installed with the bent housing adjusted to an appropriate offset angle (usually less than 3 degrees) [Fisher et al., 1991]. The assembly is installed down the hole and rotated so that the offset points toward the desired azimuth direction. Subsequently, a window is cut through the casing using a special bit, and the “kick off” continues from that point on with the ongoing azimuth angle being monitored using three-axis magnetometers [Russel

and Russel, 1979]. The inclination (the deviation from the vertical direction) and the tool face angle are determined using three-axis accelerometers [Thorogood and Knett, 1989].

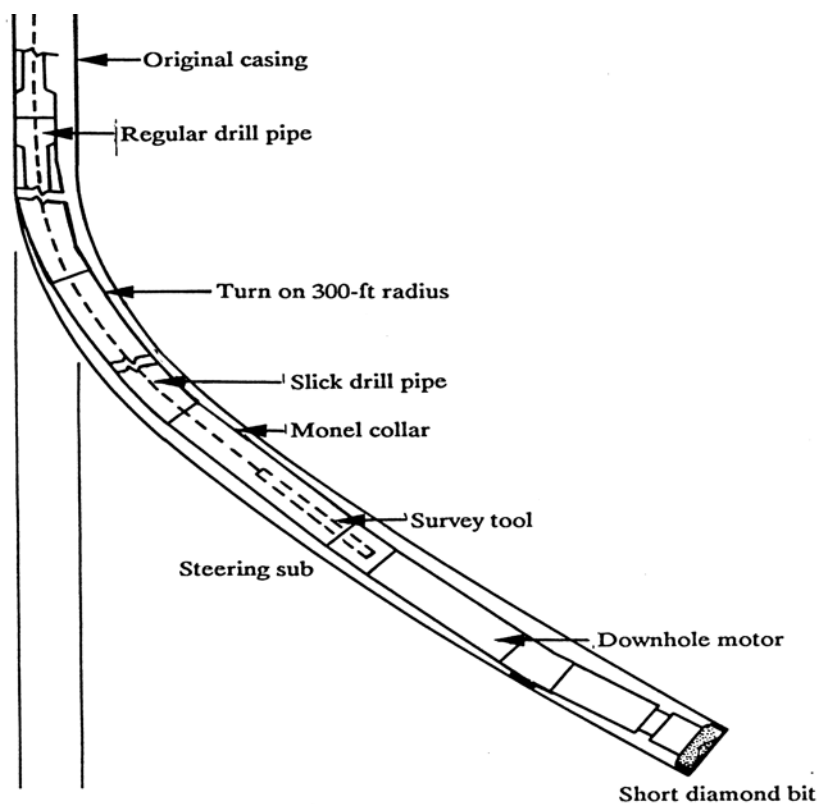


Fig.1.1. Horizontal drilling assembly [Rehm et al., 1989].

The productivity of a horizontal well depends on the well length, which in turn depends on the drilling technique [Joshi et al., 1991]. The horizontal drilling techniques are classified into four different categories based on the turning radius and the angle-building rate [Joshi et al., 1991]. The turning radius is the radius required to turn from the complete vertical to the complete horizontal directions. The angle build rate defines the deviation of the drill pipe from the vertical direction per distance traveled. Since the surveying techniques proposed in this thesis are based on some assumptions related to the penetration rate of the drill pipe through the downhole formation, these four categories are of particular importance for this research. Table 1.1 showed the drilling categories with their turning radii and penetration rates [Joshi et al., 1991]. The category employed in such horizontal drilling process depends on the plans of the drilling contractors, the nature of the downhole formation and the depth of the vertical hole. For the scope of the

present research work, the short, medium and long radii wells are only considered due to their relatively small angle build rate.

**Table 1.1. The different horizontal drilling categories with the corresponding turning radii and build rates.**

<u>Drilling category</u>	<u>Turning radius</u>	<u>Angle build rate</u>
Ultra-short radius	1 – 2 ft.	40°/ft. – 60°/ft.
Short radius	20 – 40 ft.	2°/ft. – 5°/ft.
Medium radius	300 – 800 ft.	6°/100 ft. – 20°/ 100ft.
Long radius	1000 – 3000 ft.	2°/100 ft. – 6°/ 100ft.

In general, horizontal wells have several advantages over the conventional vertical ones. These advantages are well discussed by different researchers [Anon, 1990; Joshi et al., 1991] and are only listed here for reference:

1. Horizontal wells have large contact area with oil or gas reservoirs. Therefore for a fixed delivery rate, the pressure drawdown required in horizontal wells is much smaller when compared to vertical wells.
2. Horizontal wells provide high deliverability if compared to conventional vertical wells. The horizontal well productivity is about 2 to 7 times that of the vertical well.
3. Due to its high deliverability, drilling horizontal wells can reduce the number of wells required and minimize surface disturbance, which is very important in environmentally sensitive areas.

### **1.1.2. Borehole surveying**

When developing a plan for drilling directional and horizontal wells, borehole surveying becomes one of the important prerequisites for the successful completion of the drilling process [Noy and Leonard, 1997]. There are two different aspects of borehole surveying. The first is borehole surveying for the purpose of well-bore mapping of established wells, which is usually done for the purpose of quality assurance. The second is the MWD surveying which is performed in real-time while the drill bit is penetrating

the downhole formation. For the scope of the present research only the MWD surveying will be considered. Unlike the conventional vertical wells, drilling horizontal wells requires the drilling engineer to be all the time aware of the direction of the drill bit. It has been shown that a successful horizontal drilling process needs accurate presentation of well bore trajectory at intervals of less than 30 feet in the radical sections of the well [Clary et al., 1987]. MWD surveying allowed quick evaluation of the effectiveness of the drilling process for the current drilling conditions.

There are many factors that have to be taken into consideration when developing a MWD surveying system [Brindley, 1988; Noureldin et al., 2000]. First of all, the desired accuracy of surveying and the tools that would provide this accuracy should be specified. Moreover, proper operation of these tools should be guaranteed, especially in the severe downhole environment (vibrations, shock and high temperatures). In addition, attention should be paid to eventual budget limitations when choosing the necessary equipment for implementing the system. Reduction of the equipment cost and of the surveying time is an objective as long as the desired accuracy is maintained.

Present MWD surveying systems incorporate three-axis magnetometers and three-axis accelerometers arranged in three mutually orthogonal directions [Russel and Russel, 1979; Thorogood and Knett, 1990; Helm, 1991]. At certain predetermined surveying stations, while the bottom hole assembly (BHA) is completely stationary, the magnetometers and the accelerometers measure three mutually orthogonal components of the Earth magnetic field and the Earth gravity, respectively. In order to avoid external interference on the magnetic surveying tools, the latter are installed inside special nonmagnetic drill collars. The Earth magnetic field components are mathematically processed to calculate the azimuth angle, while the Earth gravity components delivered by the accelerometers are utilized to determine the inclination and the tool face angles. The BHA position is then computed by assuming certain trajectory between the surveying stations [Thorogood and Knett, 1990]. The desired accuracy of most of the present MWD systems is  $\pm 0.1^\circ$  for the inclination and  $\pm 0.5^\circ$  for the azimuth [Phoenix Technology Services, 2002; Computalog Drilling Services, 2002]. However, in some drilling environments, it is usually difficult to achieve this level of accuracy due to several factors that affect the performance of the present magnetic surveying system.

Typically, the satisfactory accuracy when using magnetometer-based surveying system is  $\pm 0.5^\circ$  for the inclination and  $\pm 1^\circ$  for the azimuth [Thorogood, 1989].

## 1.2. Problem statement.

The magnetic surveying system suffers from several inadequacies due to the surrounding environment [Cheatham et al., 1992; Thorogood, 1990]. In fact, the major weaknesses of the present directional sensing instruments stem from the use of magnetometers to monitor the azimuth. Several error sources affect the accuracy of the magnetometers and can be summarized as follows:

1. Magnetic interference of both the downhole ore deposits and the abundance of steel components around the drilling rig disturb the magnetometer measurements of the Earth magnetic field [Thorogood and Knott, 1990]. Although it has been reported that the effect of this magnetic interference could be reduced (mitigated but never entirely eliminated) by utilizing long lengths of non-magnetic drill collars above and below the surveying instruments [Russel and Roesler, 1985; Grindord and Wolf, 1983], this solution could affect the cost benefits of the horizontal drilling technology due to the relatively high cost of these nonmagnetic materials.
2. The installation of the magnetic surveying sensors at 50 feet behind the drill bit due to the additional weight imposed by the nonmagnetic drill collars on the bit [Conti, 1989; Rehm et al., 1989]. Consequently, the MWD surveying sensors might not be capable of monitoring some rotational motions experienced only by the drill bit assembly, thus affecting the overall reliability of the magnetometer-based MWD surveying system.
3. Geomagnetic influences also contribute to the deterioration of the surveying accuracy [Wright, 1988], since variations of the geomagnetic fields over time are quite significant with respect to the performance capabilities of the magnetic surveying tools.

Recent trends in the drilling industry include the establishment of several directional/horizontal wells from the same platform [Njaerheim et al., 1998; Anon, 1999].

This necessitates the utilization of a reliable MWD surveying system that is capable of performing properly within the severe downhole drilling conditions and accurately monitors the BHA position and orientation to avoid collision with adjacent wells. Obviously, MWD magnetic surveying systems have several shortcomings particularly with respect to such drilling operations. Recent developments for improving the magnetic surveying system could not provide a global solution for all reported shortcomings [Dipersio, 1995; Hartmann, 1998; Shiells and Kerridge, 2000]. Therefore, an intensive research effort is required not only to suggest new technology for MWD surveying systems but also to introduce new methodologies that correspond to the present trends in drilling technology.

### **1.3. Research objectives.**

This research aims at introducing a new MWD surveying system that avoids the inadequacies of magnetic surveying techniques and meets more adequately the requirements of modern drilling operations. The new system utilizes surveying technology independent of magnetic-field monitoring and employs different surveying methodologies for the different modes of the drilling process.

The proposed system utilizes the technology of fiber optic gyroscopes (FOGs) for the MWD surveying processes. The FOG is suggested due its small size (less than 2.5'' diameter), low weight (less than 200 grams), high accuracy (drift rate less than  $0.1^\circ/hr$ ), relatively low cost, and high reliability (mean time between failure (MTBF) is approximately 6 years). Inertial navigation techniques will be employed for the integration of the FOGs angular velocity measurements with the linear acceleration measurements provided by three mutually orthogonal accelerometers.

The objectives of this research project are as follows:

1. Quantitative study of the applicability of the FOG technology for MWD surveying processes.
2. Adaptive filtering of the raw measurements obtained from the FOG and the accelerometers to reduce both sensor output noise and external vibration effects existing downhole.

3. Utilization of some specific conditions existing in the directional/horizontal drilling process in order to minimize the number of gyroscopes, so that only one or two high-accuracy FOGs would be sufficient to develop the necessary surveying methodology and to provide a full navigation solution downhole. The first technique is called the Single-FOG technique that is capable of providing continuous surveying of the near-vertical section of the drilling well up to  $20^\circ$  inclination angles, followed by station-based surveying until the end of the drilling process. The second technique is called the Dual-FOG technique, which provides continuous surveying for the whole radical section of the well followed by station-based surveying for the horizontal section.
4. Application of optimal estimation techniques based on the Kalman filter to enhance the performance of the developed surveying methods. These techniques remove the effect of the residual random errors during either continuous or station-based surveying and generate real-time statistical data related to the accuracy of the estimated values.

#### **1.4. Structure of the thesis.**

The thesis is structured in seven chapters and includes a general conclusion, a list of references and four appendices.

The status of present MWD surveying technology is documented in Chapter 2. This chapter reviews the principles of MWD surveying systems, discusses the error sources associated with the present techniques, and provides an overview of the recent developments in this technology. In addition, the limitations of the magnetic surveying systems and the motivations for the development of a new MWD surveying technique are discussed.

Chapter 3 gives an overview of the FOG technology from a theoretical and functional point of view. The development of a FOG computer model is then discussed. This computer model is employed to analyze FOG performance characteristics and to study the effect of shock and vibration forces that may exist downhole during the drilling operation.

Since the FOG is used to monitor the component of the Earth rotation rate along its sensitive axis during station-based surveying processes, de-noising techniques have been developed to reduce the FOG output uncertainties. Two approaches are introduced in Chapter 4 for this purpose. The first approach is based on the forward linear prediction technique, and the second approach includes an adaptive noise reduction of the FOG output signal. Both approaches employ transversal tap delay line filters and utilize the least mean squares (LMS) method to determine the optimal values of the filter tap weights. A changeable step size criterion is also suggested to guarantee fast convergence and minimal mean square error while determining the filter optimal tap weights.

Chapter 5 begins with an overview of inertial navigation systems (INS). The Single-FOG MWD surveying setup is then presented. This chapter introduces two surveying techniques. The first technique is the continuous surveying process, which is developed to survey the near-vertical section of the well. Quantitative long-term analysis of the various surveying errors is presented and continuous aided inertial navigation as well as zero velocity update methods are utilized to limit these surveying errors. In addition, a backward velocity error correction criterion is suggested during the zero velocity update procedure to limit the growth of position errors. Experimental laboratory results are presented to show the performance and the accuracy of the suggested methods. The second technique is the station-based surveying method, which is developed to survey highly-inclined and horizontal well sections. Development of the station-based surveying equations and discussion of the various sources of surveying errors associated with this technique are included. Moreover, the station-based surveying technique is experimentally tested using navigational grade surveying sensors and the results are presented. The applicability and the limitations of both the continuous and the station-based surveying techniques utilizing the Single-FOG system are discussed as well.

Chapter 6 presents the Dual-FOG system, which addresses the limitations of the Single-FOG surveying technique. This chapter discusses the continuous surveying of the whole radial section of the well and the station-based surveying for the horizontal well section. Test results are presented and a comparison with the Single-FOG system and the existing conventional three axes gyroscopic system is made.

Finally, Chapter 7 concludes the research work and provides recommendations for future development of the suggested techniques.

The thesis includes four appendices. Appendix A presents a deterministic analysis of the FOG performance. Appendix B discusses the design and the implementation of the experimental setup used for testing the performance and the accuracy of the developed surveying techniques. Appendix C introduces the relationships between various surveying errors and shows some simulation results of their long-term behavior. Appendix D presents the Kalman filtering algorithm used for limiting the surveying errors during both continuous and station based surveying methods.

## **CHAPTER TWO**

### **PRESENT MWD SURVEYING TECHNOLOGY.**

MWD surveying processes in the oil industry play a major role in optimizing drilling operations and increasing the productivity of drilling processes [Graham, 1994]. Real-time monitoring of the directional/horizontal drilling process utilizes devices installed 50 feet behind the drill bit [Muritala et al., 2000]. The measurements from these devices include MWD directional surveying data, which are collected to provide the BHA position and orientation during the drilling operation [Russel and Russel, 1979; Thorogood and Knott, 1989]. The BHA position is defined by the latitude, the longitude and the altitude (depth). The BHA orientation is determined by the ongoing azimuth direction of the drill bit, the inclination and the tool face angles [Thorogood, 1989]. The azimuth is the deviation from the North direction in the North-East plane. The inclination is the deviation angle of the drill pipe from the vertical direction. The tool face angle corresponds to rotations along the tool spin axis.

Most of the present MWD surveying systems are based on magnetic field monitoring devices for determining the azimuth. The inclination and the tool face angles are calculated after processing gravity field measurements provided by three-axis accelerometers [Thorogood, 1989].

The MWD surveying process is usually discussed in terms of distinct topics such as type of surveying instruments, surveying procedure and desired accuracy. In fact, it is essential to study the performance and the accuracy of a given surveying system in relation to surveying time, latitude, inclination, azimuth and other relevant aspects of surveying environment [Thorogood, 1990]. Part of the MWD surveying problem stems from the fact that the behavior of the surveying instruments is strongly influenced by the environment in which these instruments operate. Consequently, surveying programs may differ depending on the end user requirements and the surrounding environment [Thorogood, 1986]. To consistently and effectively manage a surveying program, the drilling engineer must have a well-defined approach to the drilling operation. In addition,

a clear idea of the end user accuracy requirement should be present. Furthermore, the drilling engineer should compare the surveying environment against the performance capabilities of available instruments. An overview of an MWD surveying process designed to achieve this purpose is illustrated on Fig.2.1 [Thorogood, 1986].

This chapter aims at introducing the principles of present surveying systems as well as giving an overview of recent industrial developments in the MWD surveying technology. In addition, the limitations and the inadequacies of these systems are discussed in order to define the motivations toward developing a novel MWD surveying system.

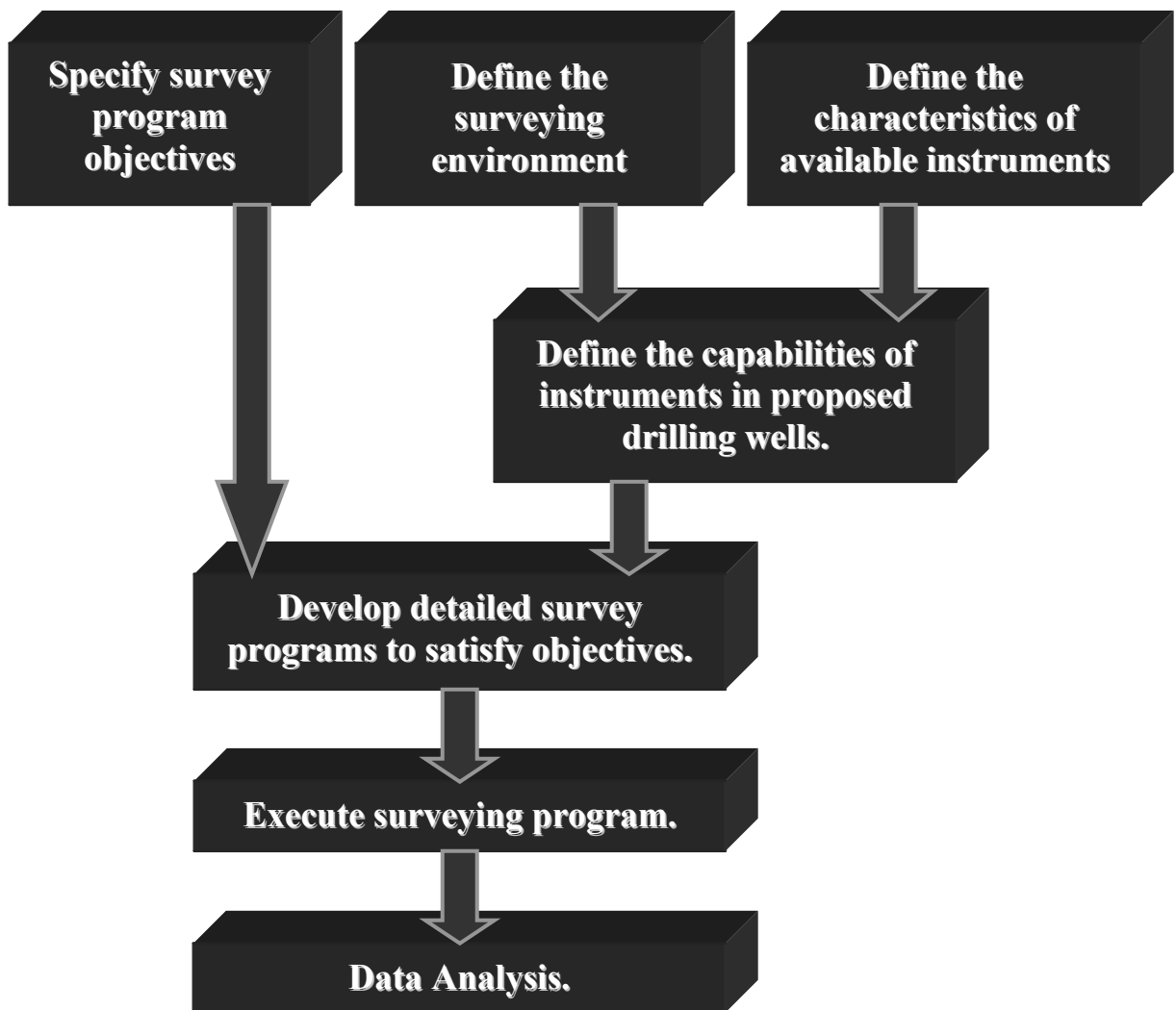


Fig. 2.1. General procedure for designing a surveying program [after Thorogood, 1989 and 1986].

### 2.1. Principles of MWD magnetic surveying technology.

MWD surveying was performed originally using pivoted compass devices to monitor the azimuth [Walstrom et al., 1969; Wolf and de Wardt, 1981]. Although simple, this system suffered from the inherent imperfection of the compass and the magnetization of the drill string that caused errors in the readings taken by the compass. In addition, it was reported that the errors due to the drill string magnetization increased significantly at high inclination angles [Russel and Russel, 1979]. Moreover, the algorithm used to provide the azimuth requires the knowledge of the magnetic moment of the compass magnet. This knowledge is largely empirical in nature [Wolf and de Wardt, 1981].

Russel and Russel (1979) introduced a new instrument responsive to the Earth's magnetic field. This instrument included three mutually orthogonal magnetometers to monitor the Earth's magnetic field in three mutually orthogonal directions. The azimuth angle is then determined by incorporating these measurements with the values of both the inclination and the tool face angles determined by three mutually orthogonal accelerometers. The algorithm provided by Russel and Russel (1979) determines the BHA orientation at certain surveying stations with the assumption that the error vector that modifies the Earth's magnetic field vector in the instrument is in the direction of the borehole. This assumption was justified by installing these magnetometers inside a non-magnetic housing. This system necessitates the use of non-magnetic drill collars around the surveying equipment at a cost approaching \$30,000 per single installation. Based on the installation of the three-axis magnetometers ( $B_x, B_y$  and  $B_z$ ) and the three-axis accelerometers ( $f_x, f_y$  and  $f_z$ ) as shown on Fig. 2.2, Russel and Russel (1979) showed that the inclination  $\theta$ , the tool face  $\phi$  and the azimuth  $\psi$  can be determined as follows:

$$\theta = \arctan \left( \sqrt{\frac{f_x^2 + f_y^2}{f_z^2}} \right) \quad (2.1)$$

$$\phi = \arctan \left( -\frac{f_y}{f_x} \right) \quad (2.2)$$

$$\psi = \arctan \left( \frac{-(B_x \sin \phi + B_y \cos \phi)}{B_z \sin \theta + \cos \theta (B_x \cos \phi - B_y \sin \phi)} \right) \quad (2.3)$$

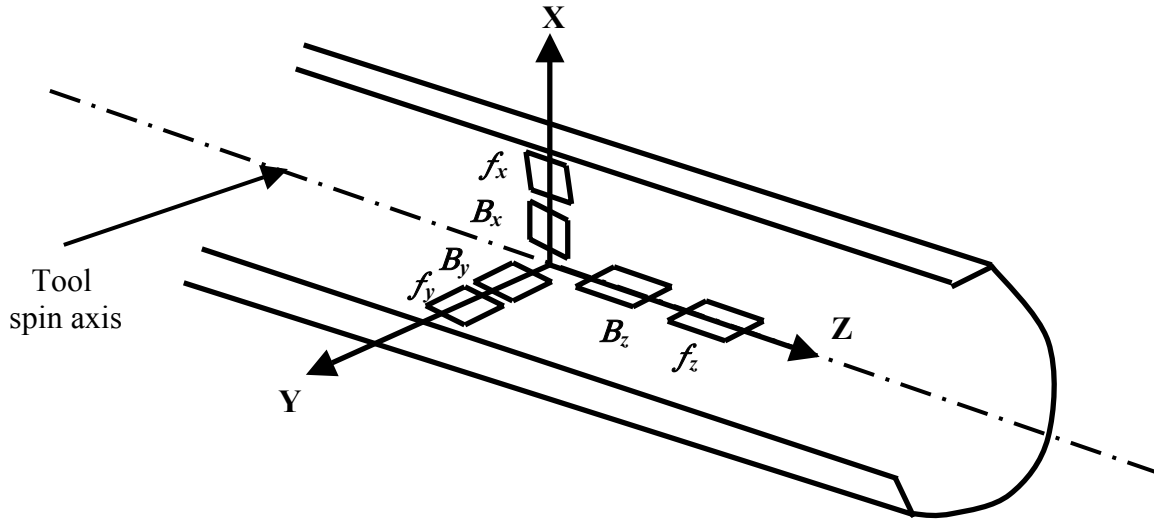


Fig.2.2. Section of the non-magnetic drill collars with the magnetic surveying equipment inside.

Practically, the local Earth's magnetic field vector at the location of the surveying tool is modified by the effect of the drill string magnetization above and below the non-magnetic drill collars. Russel and Russel (1979) assumed that the modification to the local Earth's magnetic field vector is approximately an error vector in the direction of the drill string. Thus, it can be concluded that the direction of this error vector is defined by the azimuth and the inclination angles. This error vector was used, according to the assumptions made by Russel and Russel (1979), to obtain a correction azimuth angle  $\psi_c$  such that the true azimuth angle is given as

$$\psi_{true} = \psi + \psi_c \quad (2.4)$$

where  $\psi_c$  was presented as

$$\psi_c = \arctan \left( \frac{E \sin \theta \sin \psi}{E \sin \theta \cos \psi + B_N} \right) \quad (2.5)$$

Here  $E$  is the magnitude of the error vector and is given as

$$E = B_Z - B_N \cos \psi \sin \theta + B_V \cos \theta \quad (2.6)$$

where  $B_N$  and  $B_V$  can be obtained from the published geomagnetic survey data.

Although the MWD surveying system suggested by Russel and Russel (1979) provided complete algorithm for determining the drill bit orientation at certain surveying stations, it did not take into consideration the presence of downhole ore deposits which can highly affect the measurements taken by the magnetometers. In addition, Thorogood (1990) showed that the magnetic surveying tools installed inside the non-magnetic drill collar are still subject to the influence of the other steel components in the drill string. It has been shown that drill string-induced surveying errors increase with the inclination and become particularly significant when inclination exceeds 30 degrees. In addition, the geomagnetic influences contribute to the deterioration of the accuracy of magnetic surveying. Variations of the geomagnetic fields are quite significant in relation to the performance capabilities of the magnetic surveying tools [Thorogood, 1990].

#### **2.1.1. MWD data processing and telemetry.**

The raw measurements are acquired at the magnetometers and the accelerometers outputs at each surveying station. These signals are filtered, digitized and processed by the downhole microprocessor system to determine the three attitude angles (the inclination, the tool face and the azimuth). These attitude angles are then sent to the surface via an appropriate telemetry technique. The BHA position can then be determined by assuming certain trajectory between surveying stations [Russel and Russel, 1979].

During the last two decades different telemetry techniques have been developed and modified to achieve efficient communication of the surveying data to the surface. Telemetry processes originally utilized the hardwired electromagnetic (EM) technique. It was suggested that a single conductor logging cable run out of the drill string through a special side entry located above the MWD tools could be utilized to telemeter the MWD data to the surface [Anderton, 1975]. Although this system was relatively cheap and provided high data rates, it was not reliable enough with the existing severe drilling conditions and imposed many restrictions on the rotation of the drill string.

Presently, most of the drilling operations employ mud pulse telemetry techniques, which utilize low frequency pressure pulses to telemeter the MWD data to the surface [Tubel et al., 1992]. A valve installed inside the drill string disturbs the circulation of

mud, thus sending pressure waves to the surface [Holmes et al., 1995]. The major disadvantages of the present mud pulse telemetry system are the low data rate and the noise created by the mud pump noise. Some digital signal processing methods have been developed to limit the effect of mud pump noise [Gardner and Merchant, 1996; Girard and Mintchev, 1998; Brandon et al., 1999].

In order to relatively increase data rate of telemetry systems, EM methods have been modified to suit the drilling operation. Two approaches are presently employed. The first approach is based on telemetering the MWD data by sending low frequency EM signal directly through the Earth to the surface [Xia and Chen, 1993]. The second approach considers the drill string as a one conducting path and the Earth is the other [Trofimenkoff et al., 2000]. The first approach is limited by the reflections and the interferences of the EM signal with the drill pipe and the other materials existing downhole. On the other hand, the effectiveness of the second approach depends on the frequency of the EM wave, the Earth depth through which the signal travels and the conductivity of the surrounding environment. The improvement of data rates can be accomplished by utilizing repeaters along the drill string. This increases the cost and decreases the overall system reliability. However, this EM approach has some advantages over the mud pulse telemetry technique. In addition to providing higher data rates, the EM telemetry system is independent of mud circulation, thus it becomes unaffected by the absence of drilling mud through the drill pipe.

## **2.2. Error analysis of the current MWD magnetic surveying system**

MWD surveying errors can be categorized as inherent sensor errors and external error sources. The inherent sensor errors include bias calibration error, cross axis sensitivity, bias temperature drift and output noise. Holmes (1987) assumed that the inherent errors in either the accelerometers or the magnetometers are normally distributed and gave simple expressions for the errors in the inclination, the tool face, and the azimuth angles. However, this analysis assumes that each accelerometer or magnetometer has similar error characteristics to the other two in its triad. Moreover, the above analysis assumes constant geomagnetic field. Thorogood and Knott (1989, 1990) provided more

comprehensive error analysis model that includes all the magnetic influences and other external error sources. The external effects include the axial misalignment, bottom hole assembly deflection, geomagnetic influences, and drill string-induced interference. It was found that the latter two effects dominated the ultimate performance of the magnetometers as well as any other magnetic field-based measurements.

### **2.2.1. Effect of instrument rotation.**

Post analysis of the results made by Thorogood and Knott (1990) showed that, at any particular surveying station, the inclination and the azimuth as well as the absolute values of the measured gravity and magnetic field strength varied with the axial rotation of the tool. Two factors were considered responsible for that. The first factor is the existence of residual biases in the individual sensor output, which cause deviation in the measurements taken by the accelerometers and the magnetometers. Pre-survey and post-survey calibration data were used to eliminate these bias terms, which resulted in partial smoothing of the gravity and magnetic field data. However, this research suggests that the residual errors are random in nature and should be modeled using stochastic processes. The variation in the inclination and the azimuth readings was found to be due to the second factor, which is known as misalignment. When the z-axis of the surveying tool is not coincidental with the axis of the borehole assembly (i.e. the tool spin axis, see Fig. 2.2), misalignment error exists. Thorogood and Knott (1989) provided a model to compensate for these error sources. This model depends on receiving at least three well-conditioned sets of measurements in which the inclination and the azimuth are known.

### **2.2.2. Effect of drill collar deflection.**

It was suggested that the static deflection of the bottom hole assembly (BHA) being imposed upon the surveying instrument package affects the readings taken by the surveying sensors. It was shown also that significant deflections occur at the instrument sensor location [Thorogood, 1986]. These deflections are large and, without compensation, will obviously have a significant impact on system accuracy especially at high inclinations. Thorogood and Knott (1989) compensated for the effect of the BHA

deflection by using a mathematical model of the two-dimensional BHA simulator provided by Walker (1973).

### **2.2.3. Effect of geomagnetic influences.**

The geomagnetic influences are defined by the variation of the dip angle, declination and total magnetic field strength with respect to time. The dip angle is the angle between the Earth's magnetic field and the horizontal plane. The declination is the angle between the magnetic north and the true north. It was recorded that during any given day at a random location the standard deviation of the variation of the dip angle, declination and magnetic field strength were  $0.3^\circ$ ,  $0.9^\circ$  and  $0.3\mu$ -Tesla respectively [Parkinson, 1983]. The variation in the geomagnetic field is quite significant in relation to the performance capabilities of the magnetic surveying tools currently used [Wolf and de Wardt, 1981; Thorogood and Knott, 1989]. Therefore, geomagnetic effects must be taken into account when considering absolute surveying accuracy and will impose definite limitations on the levels of accuracy that can ultimately be achieved.

### **2.2.4. Effect of drill string magnetic interference.**

Magnetic surveying tools run in non-magnetic drill collars are subject to the influence of the other steel components in the drill string. Thorogood and Knott (1989) showed that drill string-induced surveying errors increase with inclination and with the borehole direction approaching the East-West direction. The drill string magnetic interference is particularly noticeable when inclination exceeds  $30^\circ$ . Grindord and Wolf (1983) showed that the effect of the drill string magnetic interference could be reduced (mitigated, but never entirely eliminated) by running long lengths of non-magnetic materials above and below the surveying instruments. However, a solution like this could affect the entire cost benefits of the horizontal drilling technology. The effect of drill string magnetic interference as well as the presence of downhole ore deposits can neither be quantified, nor compensated.

### **2.3. Recent developments in MWD magnetic surveying system.**

Several investigations have reported improvement in magnetic surveying accuracy. Shiells and Kerridge (2000) introduced the interpolated in-field referencing method in which absolute local geomagnetic field data is determined from spot measurements of the Earth's magnetic field. These measurements are taken at local site which is sufficiently close to the drilling site so that the measurement data is indicative of the Earth's magnetic field at the drilling site but is sufficiently remote from it so that the measurement data is unaffected by magnetic interference from the site. This technique compensates for the geomagnetic influences but the measurements taken by the magnetometers still suffer from the drill string magnetic interference. In addition, measurements of the geomagnetic field at a local site might not be applicable in an area that has many drilling rigs. Moreover, such technique adds more complexity that may give rise to additional cost.

Hartmann (1998) introduced a method to improve the accuracy of surveying boreholes. This method is based on determining the uncertainty in the magnetic field measurements by comparing the measured magnetic field with a corresponding known value at specific location. However, this method does not take into account two phenomena. The first phenomenon is the increase of the drill string magnetic interference at high inclinations. The second phenomenon is the presence of ore deposits that can be found randomly downhole. These two phenomena add additional errors that are not taken into consideration when referencing the theoretical value of the magnetic field to the measured value at the known location.

Dipersio (1995) introduced a new method for compensating geomagnetic influences. This method is based on matching both the calculated magnetic field strength and the calculated dip angle to their corresponding nominal values at a particular geomagnetic location. This results in determining an error-free value of the axial component of the magnetic field, which is directly used to determine the azimuth. However, at high inclinations, the drill string magnetic interference generates additional errors in cross-axial directions.

Several other techniques have been introduced to improve MWD magnetic surveying systems [Trowsdale, 1982; van Dongen et al., 1987; Helm, 1991; Engebretson, 1992; Nicholson, 1995]. However, none of these techniques is free of inadequacies or capable of providing a global solution of the present MWD magnetic surveying problems.

Each of the above techniques tried to provide a particular solution for the MWD magnetic surveying system under specific drilling conditions, which cannot be generalized. In addition, all these approaches introduced some referencing methods for magnetic fields, while employing the same magnetic surveying equipment instead of aiming at exploring new MWD surveying methods and utilizing surveying equipment insensitive to magnetic fields.

#### **2.4. Present gyroscopic surveying technologies.**

Although some efforts have been directed towards improving MWD magnetic surveying technology, many error sources exist that are difficult to model consistently, and therefore cannot be eliminated. These include variations of the Earth's magnetic field strength and dip angle, abnormalities in nonmagnetic drill collars, geomagnetic influences and drill string magnetic interference [Noy and Leonard, 1997].

Alternatively, gyroscopic instruments are not subject to the adverse effects of magnetic fields [Uttecht and deWardt, 1983]. In addition, they offer means of quantifying several error sources, thus giving relatively high levels of accuracy [Merhav, 1993]. These instruments incorporate one, two or three mutually orthogonal gyroscopes with three-axis accelerometers. The type of gyroscopes utilized in this technology are either mechanical or ring laser gyroscopes [Gibbons and Hense, 1987; Stephenson and Wilson, 1992; Noy and Leonard, 1997]. However, due to the complex procedure of drilling directional/horizontal wells and the severe downhole vibration and shock forces, gyroscopic instruments could not be employed for MWD surveying operations for the entire drilling process. Thus, their utilization has been limited to two applications. The first application is the wellbore mapping procedure, which is performed after the establishment of the drilling well. The second application is related to providing

reference for MWD magnetic surveying systems within open hole sections of the drilling well. Although wellbore mapping procedures are not the subject of this research, an overview of the techniques associated with this technology is offered in this section, in order to comparatively evaluate their utilization and limitations with respect to MWD surveying processes.

#### 2.4.1. Wellbore mapping procedure utilizing gyroscopic surveying systems.

During the wellbore mapping procedure, a special probe carrying the surveying sensors run through the borehole. Fig.2.3 illustrates a gyroscopic surveying system configured for wellbore mapping [Noy and Leonard, 1997].

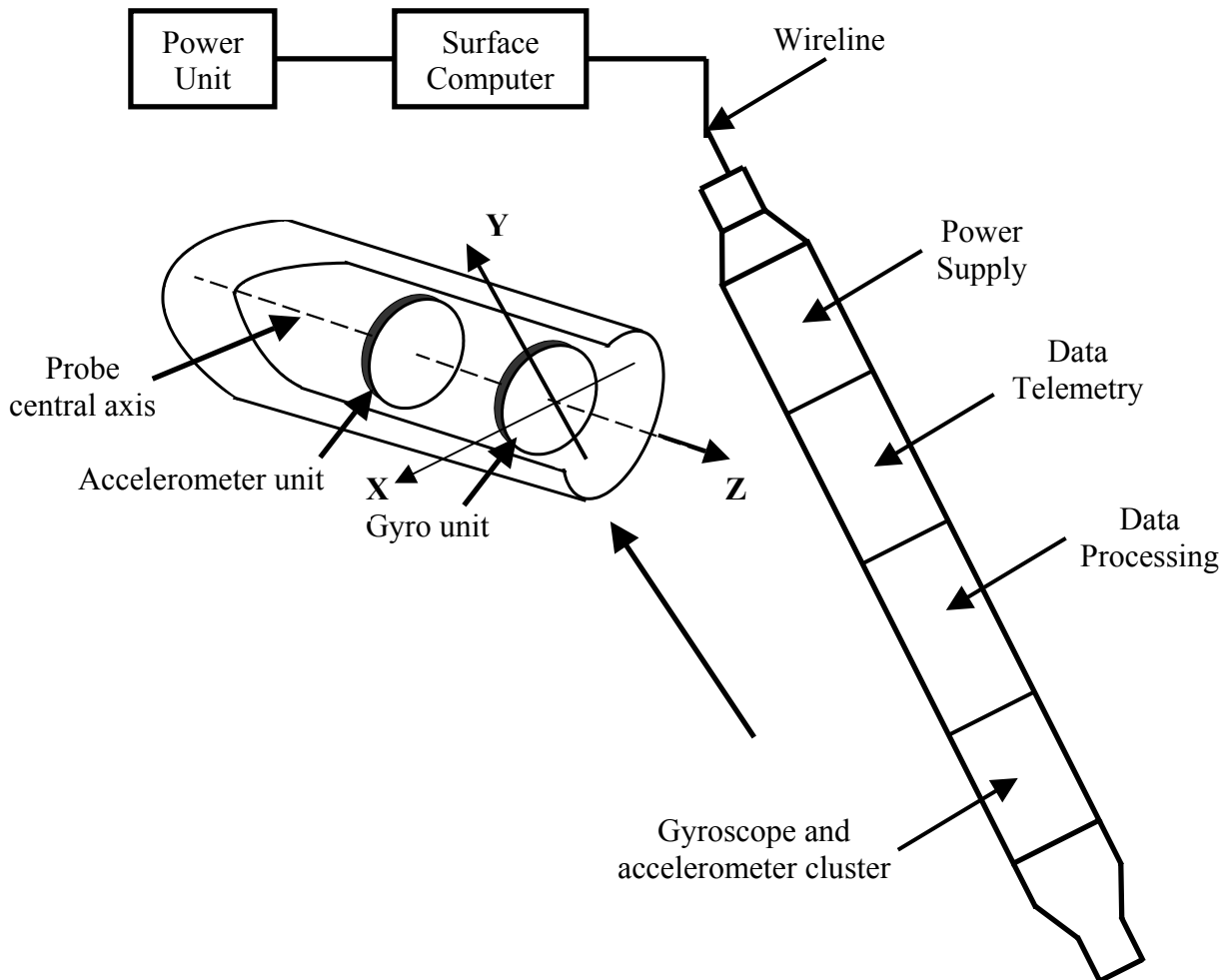


Fig. 2.3. Schematic diagram of wellbore mapping utilizing gyroscopic equipment [after Noy and Leonard, 1997].

The objective of the wellbore mapping procedure is different from MWD surveying. While MWD processes are concerned with real-time monitoring of the BHA orientation (particularly the inclination and the azimuth) and position, the wellbore mapping is utilized to determine the wellbore direction as a function of depth. Two measurement techniques are employed for this purpose.

The first technique is based on the gyrocompassing procedure, which is employed to survey near vertical wellbore sections at some predetermined surveying points. During this procedure, the probe is lowered into the wellbore on an electric conductor wireline to measure the Earth's gravity field and the Earth's rotation rate while the instrument is held stationary at predetermined depths [Noy and Leonard, 1997]. The gyroscopic system used for this process is single or dual axes North-seeking mechanical gyroscopes with drift rates of  $0.1^{\circ}/hr$  [Kelsey, 1983; Dubrule and Nelson, 1987; Thorp, 1987; deLange et al., 1988; Noy and Leonard, 1997]. In fact, the current high accuracy gyroscopic tools are capable of determining wellbore position and true vertical depth (TVD) to an accuracy that satisfies the requirements of the majority of wells being drilled today (errors less than  $1m$  for the TVD and less than  $100m$  in the lateral directions [Noy and Leonard, 1997]). However, the performance of such gyrocompassing procedure may degrade in high inclinations and along East-West directions at high latitudes [Thorogood, 1986; Noy and Leonard, 1997]. This imposes a lot of restrictions on the utilization of such technology for MWD surveying of horizontal wells. In addition, one of the main problems with gyrocompassing surveying system is that their use interrupts the drilling process. Since the full cost of a gyroscopic surveying system includes rig time, an economic incentive often exists to acquire the necessary information as a byproduct of the drilling process. This excites the motivation towards developing continuous MWD surveying procedure.

The second wellbore surveying technique is based on measuring relative instrument rotations while the system is continuously traversing through the wellbore. After taking stationary reference measurements in the gyrocompassing mode, some modeling procedures determine the probe azimuth and inclination [Noy and Leonard, 1997]. In order to calculate the actual wellbore trajectory, the changes of both the azimuth and the inclination angles are incorporated with the depth measurement (derived

by the wireline). This continuous mode of wellbore surveying is currently implemented by either two mechanical gyros in a gimbaled structure that maintain stationary platform for the accelerometers [Morgan and Scott, 1979; Wright, 1983; Uttecht and deWardt, 1983; Noy and Leonard, 1997] or by three-axis mechanical or ring laser gyros in a strapdown inertial navigation system [Gibbons and Hense, 1987; Hulsing, 1989; Stephenson and Wilson, 1992]. However, the available continuous wellbore surveying methods cannot be applied for MWD processes.

In fact, several aspects should be taken into consideration while designing an MWD gyroscopic surveying system. The impact of the various shock and vibration forces should be analyzed and taken into account. The present technology of both mechanical and ring laser gyroscopes cannot provide rotation rate sensors that can perform properly within the severe downhole environment especially with their internal moving parts. Furthermore, due to the limited space available downhole, these types of gyroscopic instruments (especially the ring laser gyros) cannot be accommodated downhole inside the drill pipe. In addition, different surveying methodologies should be considered for the different operation modes of the drilling process (rotary or steering modes). The MWD surveying system should also be capable of adapting itself to the change of orientation of the drill pipe from complete vertical to complete horizontal directions during horizontal drilling operations. Moreover, the proper installations of the gyroscopic tools inside the drill pipe below or above the mud motor should be determined in relation to the surveying requirements and the environmental effects.

#### **2.4.2. In-hole referencing of magnetic surveying.**

Thorogood and Knott (1990) have reported that it is possible to reduce the declination and magnetic interference errors by referencing the MWD magnetic surveying to a baseline derived from a gyroscopic surveying. This was achieved by running the gyroscopic surveying tool down the casing and out into an open hole to establish a reference section of between 500 and 700 feet in length. Subsequent magnetic surveys were taken in such a way that between 10 and 15 stations overlap with the gyroscopic in-hole reference section. The systematic biases resulting from magnetic

interferences, geomagnetic variations and drill collar bending can be estimated by observing the differences between the two surveying methods. These differences can then be used to correct the surveying parameters for the rest of the surveying process. The above procedure takes place at the near-vertical section of the drilling well. The in-hole referencing technique enhanced the MWD surveying accuracy and was capable of reducing the lateral position uncertainty from 200 feet to about 80 feet for a well of 10,000 feet TVD [Thorogood and Knott, 1990]. However, this technique caused a considerable delay for the drilling process. In addition, since the in-hole referencing system was applied only for the near-vertical section of the drilling well, the effect of drill string magnetic interference (which increases at high inclination angles) may create more bias errors for the highly inclined sections of the well. Furthermore, the presence of downhole ore deposit may jeopardize the overall surveying accuracy since they are located randomly downhole.

## **2.5. Motivations toward developing a new MWD surveying system.**

Directional/horizontal drilling processes in the oil industry require reliable and efficient MWD surveying system in order to achieve the objectives of the drilling plan. This necessitates keeping the drilling assembly within the desired path towards the oil reservoir. We have determined that the following requirements are necessary for successful drilling operation:

1. *Determination of the initial azimuth at the vertical section of the well.* After the establishment of the vertical section of the well to an appropriate depth, the MWD surveying systems should be capable of determining the BHA initial azimuth and accurately monitor the azimuth changes while rotating the whole drill pipe around its central axis towards the desired azimuth direction. The present MWD magnetic surveying system suffers from the deviation of the Earth's magnetic field due to the steel casing of the vertical whole. Therefore, insensitivity of the monitoring devices to magnetic fields is imperative to ensure accurate initial azimuth.

2. *Collision avoidance with nearby wells at sections of multi-well structure.* In some drilling sites, especially for offshore drilling operations, all wells are clustered together due to the limited area of the platform. Therefore, the azimuth direction is critical to avoid collision with nearby wells and it should be precisely estimated. The MWD magnetic surveying system suffers from the deviation of the measured Earth's magnetic field in this multi-well structure due to the casing of the adjacent wells. Thus, MWD monitoring devices independent of magnetic fields are essential for successful drilling operations.
3. *MWD near-bit surveying.* A new trend in drilling industry is near-bit surveying that guarantees accurate computation of the surveying parameters. The present MWD surveying system is currently located 50 feet behind the drill bit, thus it is not affected by the rotations performed by the bearing assembly located right behind the drill bit. It has been reported that mounting the MWD surveying equipment closer to the drill bit would be highly beneficial in providing reliable MWD surveying data, especially in sections of multi-well structure [Noureldin et al.<sup>c</sup>, 2000; Noureldin et al.<sup>a</sup>, 2001]. The recent near-bit MWD surveying was only introduced to provide accurate computation of the BHA inclination angle and TVD [Muritala et al., 2000; Berger and Sele, 2000; Skillingstad, 2000] by mounting the accelerometers inside the bearing assembly behind the drill bit. However, it is highly desirable to provide near-bit azimuth computation as well in order to keep the BHA within its desired path.
4. *Accurate surveying of the highly-inclined and the horizontal well sections.* As the BHA approaches the oil reservoir at high inclination angles, it is highly crucial to have accurate surveying data. Clary et al. (1987) reported that an error of  $0.5^\circ$  while estimating the inclination angle near  $90^\circ$  inclination could move the intersection of the target several hundred feet. Unfortunately, the present MWD surveying systems suffer from the increase of inclination errors

at high inclination angles. Therefore, some methods should be developed to keep these errors as minimal as possible.

5. *Continuous MWD surveying.* As explained earlier, the present MWD surveying system interrupts the drilling process at some predetermined surveying stations to provide the inclination and the azimuth angles. This increases the total rig time and consequently the overall cost of the drilling process. Continuous surveying is therefore highly desirable to reduce the cost associated with increasing the time of drilling operation and to provide the exact BHA trajectory for the entire drilling process.

## **2.6. Conclusion.**

Apparently, the major weaknesses of the present MWD surveying instruments stem from the use of magnetometers to monitor the azimuth and from the hostile environment in which these devices must operate. The problem encountered with the use of magnetometers is the presence of massive amount of steel around the drilling rig. The abundance of ferromagnetic material necessitates the separation of the magnetometers by non-magnetic drill collars. The cost of non-magnetic drill collars can run higher than \$30,000 for a single installation. Aside from the cost of utilizing non-magnetic drill collars, their use introduces a second problem. Since the non-magnetic drill collars impose an additional weight on the drill bit, the surveying tools are separated from the bearing assembly and the drill bit by about 50 feet [Conti, 1989; Rehm et al., 1989]. Elimination of the non-magnetic drill collars could reduce the distance between the instrument package and the drill bit and facilitate the trend of near-bit surveying. The third problem associated with the use of magnetometers is their lack of reliability when used underground due to the deviation of the Earth's magnetic field from ore deposits.

In the search for a replacement for the magnetometers it seems that some of the technological devices used for inertial navigation and guidance systems can be utilized for the azimuth monitoring in horizontal drilling applications [Merhav, 1993]. Such devices must have a long-term accuracy, long mean time between failures (MTBF), and should be able to withstand high temperatures as well as substantial vibration and shock

forces, which are considered the most hostile phenomena in the downhole environment. In addition, these devices should not require any frequent calibration or maintenance.

The present commercially available navigation devices such as mechanical gyroscopes and ring laser gyroscopes cannot be adopted for the downhole drilling application. Mechanical gyroscopes contain moving parts, which cannot perform properly in the harsh environment existing downhole. In addition, they are of relatively small MTBF (*9000 hrs*) with high drift rates and need frequent calibration and maintenance [Merhav, 1993]. Although the ring laser gyroscopes are of high accuracy, their size is larger than the minimum instrument size allowed for downhole applications.

In this research we investigate whether the fiber optic gyroscope (FOG) could be suitable for downhole drilling applications. This type of gyroscope is superior to its mechanical counterpart since it contains no moving parts, thus allowing for high reliability (high MTBF) with no need for frequent calibration or maintenance [Lefevre, 1993; Kim, 1994; Perlmutter, 1997]. In addition, the FOGs exhibit low environmental sensitivity since they can withstand relatively high temperatures, shocks and vibrations [Noureldin et al., 1999; Noureldin et al., 2000]. Moreover, currently available FOGs are of small size (*1.6''* diameter) with a drift rate less than  $0.1^{\circ}/hr$ , angle random walk less than  $0.005^{\circ}/\sqrt{hr}$ , long MTBF (*60000 hrs*), no gravitational effects and excellent immunity to vibration and shock forces [Fibersense Technology Corporation, 2001].

In addition, new methodologies have to be developed to integrate the FOG technology with the three-axis accelerometers and to provide MWD surveying solution satisfying the requirements discussed in the previous section. The technology of inertial navigation systems (INS) will be utilized for the development of these methodologies. The utilization of the FOG technology in the MWD surveying application and the design of the surveying methods are the subjects of the following chapters.

### **CHAPTER THREE**

#### **STUDYING THE FEASIBILITY OF FIBER OPTIC GYROSCOPES (FOGs) FOR MWD SURVEYING PROCESSES.**

A gyroscope is an instrument predominantly utilized for monitoring angular velocities and has been used in many applications [Merhav, 1993]. If a set of gyroscopes is combined with accelerometers, they can determine the position and the orientation of a moving platform [Burns, 1994]. Therefore, gyroscopes have been incorporated in many positioning and navigation systems including ones for aircrafts, missiles, vehicles, submarines, etc [Bielas and Taylor, 1993; Bennett et al., 1997].

Two main categories of gyroscopes are presently used: the mechanical and the optical gyroscopes. Mechanical gyroscopes have been utilized in different navigation applications during 1970s and 1980s. Their principle of operation is based on the rotation of a spinning wheel about the axis of rotation of the platform [Merhav, 1993]. The internal moving parts of mechanical gyroscopes limit their reliability in applications involving high shock and vibration forces [Nuttall, 1987]. In addition, mechanical gyroscopes suffer from the increase of their drift at relatively high angular velocities and high temperatures. This might jeopardize the overall system performance, particularly when the mechanical gyroscopes are utilized in strapdown inertial navigation systems [Nuttall, 1987]. Therefore, since late 1980s, optical gyroscopes started replacing the mechanical gyroscopes in a variety of navigation and positioning applications [Kim, 1994]. Optical gyroscopes are two types, the ring laser gyroscope (RLG) and the fiber optic gyroscope (FOG). Although of high accuracy, the size and the cost of RLGs limit their utilization in some applications where dimensions are important [Burns, 1994]. In addition, the operation of RLGs requires the circulation of a laser beam between a set of mirrors precisely positioned inside the internal cavity of the gyro. Thus, the RLG cannot perform properly within the severe downhole vibration and shock forces if utilized for MWD surveying processes. If compared to mechanical gyroscopes and RLGs, FOGs have the following technical advantages [Burns, 1994]:

1. They support high rotation rates;
2. They can operate adequately in high shocks and vibrations environment;
3. They can operate at relatively high temperatures (up to 85°C);
4. They give high reliability (6 years MTBF) with low cost and small size;
5. They provide high performance in terms of scale factor stability, output uncertainty and drift characteristics. In addition, they have the advantage of high accuracy and high sensitivity to very small rotation rates.

### **3.1. FOG theory and functionality.**

The FOG is a single axis rotation sensor and its principle of operation is based on the Sagnac effect. In 1913, Sagnac showed that two counter-propagating light waves traversing a loop interferometer have a phase difference when the loop is rotating about its axis [Lefevre, 1993]. Sagnac's loop interferometer was constructed firstly with bulk optics in a free space medium [Arditty and Lefevre, 1981]. The advent of low-loss optical fibers had stimulated the development of several new methods of implementing the Sagnac effect for rotational measurement [Nuttall, 1987]. It was discovered that the sensitivity of the Sagnac interferometer could be improved using a multiple-turn optical fiber coil, which is presently known as a FOG [Burns, 1994]. Subsequently, FOGs have been utilized in many applications providing cheaper, lighter, smaller in size and more rugged solution [Chin et al., 1990; Bielas and Taylor, 1993].

#### **3.1.1. Sagnac effect for two-beam interferometer.**

According to Sagnac effect, two light beams propagating along two opposite directions in a rotating frame experience an optical path length difference, and consequently, a phase difference with respect to each other. Both the optical path and the phase differences are proportional to the rotation rate [Lefevre, 1993].

The principle of operation of FOGs is based on the two-beam interferometer shown on Fig.3.1 [Lefevre, 1993]. A special fiber optic coupler splits an incident optical beam of intensity  $I_{in}$  into two counter-propagating beams of equal intensities  $I_1$  and  $I_2$ , which propagate through  $N$ -turn fiber optic coil. Upon completing one cycle around the

fiber optic coil, the two beams interfere together at the coupler, giving an output intensity of  $I_o$ . If there is no rotation of the plane of the fiber optic coil, the two beams interfere giving maximum intensity at the output.

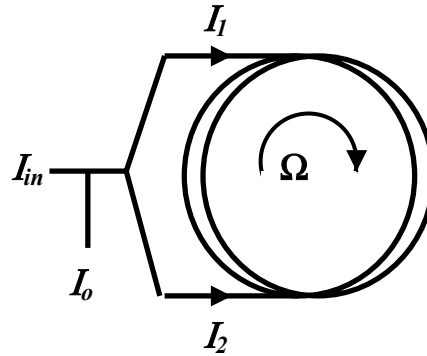


Fig.3.1. Two-beam interferometer using the fiber optic technology [after Lefevre, 1993].

Upon rotation, the path difference  $\Delta L$  between the two counter-propagating beams is related to the rotation rate  $\Omega$  and is expressed as follows [Lefevre, 1993; Burns, 1994]:

$$\Delta L = \left( \frac{\pi d^2}{C_o} N \right) \Omega \quad (3.1)$$

where  $d$  is the diameter of the fiber optic coil,  $N$  is the number of turns and  $C_o$  is the speed of light in free space. For a fiber optic coil of length  $L = \pi d N$ , the optical path difference  $\Delta L$  can be rewritten as [Aein, 1995]:

$$\Delta L = \left( \frac{L d}{C_o} \right) \Omega \quad (3.2)$$

It can be noticed that by increasing the number of turns of the fiber optic coil (i.e. increasing the length of the fiber optic cable), the sensitivity of the two-beam Sagnac interferometer can be enhanced. However, the attenuation of the light beam along the fiber optic coil will impose restrictions on the increase of its length [Senior, 1993].

### 3.1.2. FOG operating principle.

The block diagram of a closed-loop FOG is shown on Fig.3.2. A single-mode polarization-maintaining fiber optic coil of length  $L$  and diameter  $d$  is used [Aein, 1995]. A superluminescent diode, with its relatively narrow spectral width and high emitting

power, is usually utilized. An optical directional coupler is used to divide and inject the optical source beam into the opposite ends of the fiber coil. The coupler also adds the two returning counter-propagating beams together. A photodetector analyzes the resulting interference beam and provides a voltage signal that is proportional to the intensity of this beam. An *AC*-bias modulator activates the phase shifter to phase-modulate the counter-propagating light beams. This phase modulation improves the sensitivity of the FOG and produces a direction sensitive output [Aein, 1995; Noureldin et al., 1999]. Serrodyne phase modulator is used to filter the Sagnac signal and to drive a voltage controlled optical phase shifter, which cancels out the Sagnac phase shift. The rotation rate can be extracted from the input to the voltage controlled optical shifter [Aein, 1995]. Appendix (A) gives a detailed discussion of the FOG operating principle and a deterministic analysis of its performance.

The FOG, like any other type of gyroscope, measures the angular velocity along its sensitive axis. If the FOG is installed in the horizontal plane of a moving platform, the mathematical integration of its output angular velocity will directly give the azimuth angle [Noureldin et al.<sup>a</sup>, 2000]. This requires the value of the initial azimuth to be known. The initial value of the azimuth can be established using the well-known alignment procedures, which determine the initial orientation of the platform [Britting, 1971; Titterton and Weston, 1997; Salychev, 1998]. Since the FOG might not be positioned entirely on the horizontal plane during directional/horizontal drilling processes, the mathematical integration of the FOG output does not directly deliver the azimuth. Some special mathematical transformation techniques are needed to take into account the inclination of the drill pipe inside the borehole [Schwarz and Wei, 1990; 1999]. These procedures are performed in real-time to provide continuous monitoring of the azimuth angle. A FOG-based surveying system that continuously monitors the azimuth with high accuracy can deliver substantial savings of time and effort needed to return the bottom hole assembly (BHA) to the desired azimuth direction after detecting its deviation at each survey station, which is the common practice in magnetometer-based MWD surveying [Thorogood J.L. and Knott, 1990].

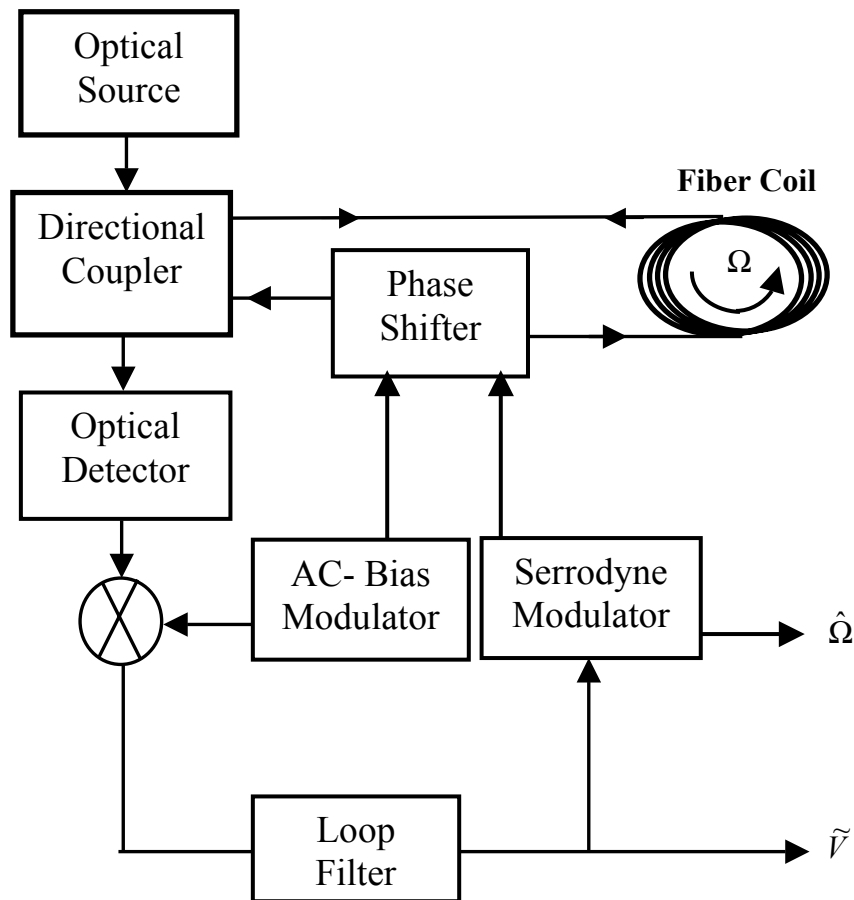


Fig.3.2. Closed loop fiber optic gyroscope (FOG).

The aim of this chapter is to study quantitatively the feasibility of using the FOG to monitor the azimuth in horizontal drilling applications. The effects of all internal parameters of the FOG on its performance, as well as the impact of the severe downhole environmental factors are analyzed. Special attention is given to the effects of downhole vibrations and shocks, since these can be considered the most severe environmental factors that the FOG would encounter downhole. The analysis in this study is performed using a specially-designed computer model of the FOG [Noureldin et al., 1999]. All environmental effects are formulated and applied to this computer model. The impact of these effects on the output signal of the FOG is studied, and the accuracy of the FOG model working in the simulated severe downhole environment is investigated [Noureldin et al.<sup>c</sup>, 2000].

### 3.2. Computer modeling of FOGs.

Computer simulation of FOGs has not been well elucidated in existing studies. In this research, a comprehensive method for FOG modeling is introduced. The FOG was modeled and analyzed as a closed loop system with a rotation rate input and an output signal depending on this rotation rate [Noureldin et al., 1999]. The modeling was implemented using MATLAB/SIMULINK computer-aided design software (Mathworks, Natick, MA) on an IBM-PC P400 system. Unlike other FOG systems described previously [Lin et al., 1994; Tanaka et al., 1994] this system depends on all FOG parameters. Thus all factors affecting the overall performance could be investigated.

When the FOG sensing coil rotates, a phase difference between the two counter-propagating beams is produced due to the Sagnac effect. This phase difference is related to the optical path difference given in Eq.3.2 as follows:

$$\phi_s = \frac{2\pi}{\lambda_o} \Delta L = \left( \frac{2\pi L d}{\lambda_o C_o} \right) \Omega \quad (3.3)$$

where  $\phi_s$  is the phase difference and is known as the Sagnac phase shift,  $\lambda_o$  is the peak wave length of the optical beam in free space,  $C_o$  is the speed of light in free space and  $\Omega$  is the applied rotation rate. It should be noted that the refractive index of the fiber cable does not appear in Eq.3.3. Although the free space definitions of both the wavelength and the speed of light participate in Eq.3.3, this relationship is independent of the refractive index. This is because the two counter-propagating light beams are traveling through an angularly accelerating medium (i.e. the fiber core) and therefore the laws of relativity are applied to derive the phase shift  $\phi_s$  between the two beams. The derivation of this relationship results in a complex formula, which is simplified in Eq.3.3 using first order approximation [Burns, 1994].

Considering the rotation rate  $\Omega$  as an input to the FOG system, a gain block can describe the relation between  $\Omega$  and the output Sagnac phase shift  $\phi_s$ . This gain block is related to the different optical parameters of the FOG. The phase shift produced by the AC-bias modulator causes the output signal  $\tilde{V}$  from Fig.3.2 to be of the form [Aein, 1995],

$$\tilde{V} = S_0 J_1(A) \sin \phi_s \quad (3.4)$$

where  $S_0$  is the power of the main optical beam,  $A$  is the amplitude of the sinusoidal signal produced by the AC-bias modulator activating the phase shifter, and  $J_1(A)$  is a 1<sup>st</sup> order polynomial of the Bessel function of  $I^{st}$  kind. This polynomial can be maximized by choosing specific values for  $A$  [Aein, 1995], thus, the sinusoidal AC-bias modulator produces a direction-sensitive output.

For low values of the rotation rate and respectively low values of the Sagnac phase shift,  $\sin \phi_s$  can be expressed as  $\phi_s$ . The output voltage in this case is directly proportional to the Sagnac phase shift and consequently to the rotation rate,

$$\tilde{V} = K \phi_s \quad (3.5)$$

where  $K$  is a constant equal to  $S_0 J_1(A)$ .

Unfortunately this simple open loop structure fails if the produced Sagnac phase shift becomes large with high input rotation rates. In addition, the open loop system suffers from the non-linearity of the sinusoidal function at high rotation rates. The serrodyne modulator was proposed as a solution to this problem [Aein, 1995]. The serrodyne modulator generates a sawtooth signal that has a maximum phase value of  $2\pi$  while the frequency and the slope of the individual sawtooth waves are controlled by the output signal  $\tilde{V}$ . The modulator cancels out the Sagnac phase shift,  $\phi_s$ , produced by the rotation rate  $\Omega$ . The output signal from the open loop configuration,  $\tilde{V}$ , is fed back to the serrodyne modulator (Fig.3.2) where it is integrated and fed to a voltage controlled oscillator (VCO). The signal used to drive the VCO is found to be directly proportional to the input rotation rate  $\Omega$  [Aein, 1995]. Thus, the FOG output signal  $\hat{\Omega}$  is taken from the input to the VCO and it can be written as,

$$\hat{\Omega} = \left( \frac{d}{\lambda_0 n} \right) \Omega \quad (3.6)$$

where  $n$  is the refractive index of the fiber optic coil.

Since the serrodyne modulator forces the phase shift between the counter propagating beams to be of a very low value, the AC-bias phase shifter can be modeled as

a gain block in the forward path of the system. The serrodyne modulator is modeled as an integrator block, which integrates the output of the AC-bias phase shifter and delivers the output of the FOG system. This output is fed back through a gain block to deliver an estimate of the Sagnac phase shift  $\hat{\phi}_s$ , which is used to cancel the actual Sagnac phase shift  $\phi_s$  produced by the input rotation rate so that the loop is kept locked.

The overall system block diagram describing the FOG as a closed-loop system utilizing the serrodyne modulator is shown on Fig.3.3. The FOG is therefore able to measure the azimuth of the drill bit if mounted in the horizontal plane inside the BHA. The output rotation rate signal from the FOG should be integrated to give the corresponding azimuth angle. As the analysis in the present study is performed using the rotation rate signal, which is physically affected by vibration, shock and other environmental factors, then the rotation rate signal should be processed to compensate for all these factors before it is integrated to deliver the azimuth angle.

The input/output transfer function of the FOG described in the s-domain can be given as [Noureldin et al., 1999; Noureldin et al.<sup>c</sup>, 2000],

$$\frac{\hat{\Omega}(s)}{\Omega(s)} = H(s) = \frac{KG \left( 2\pi \frac{Ld}{\lambda_o C_o} \right)}{s + 2\pi KG \left( \frac{Ln}{C_o} \right)} \quad (3.7)$$

An abrupt change in the input rotation rate was considered to correspond to a unity step input and the resulting step response analyzed. In the step-response analysis it was assumed that the FOG had the following configuration:  $L = 1000m$ ,  $d = 0.1m$ ,  $\lambda_o = 0.85 \mu m$ ,  $n = 1.48$ ,  $K = 0.5815$  and  $G$  (electronic gain) =  $10^5$ .

The step response of this FOG model is shown on Fig.3.4. The system is stable since it has only one pole located on the negative part of the real axis in the s-plane close to the origin.

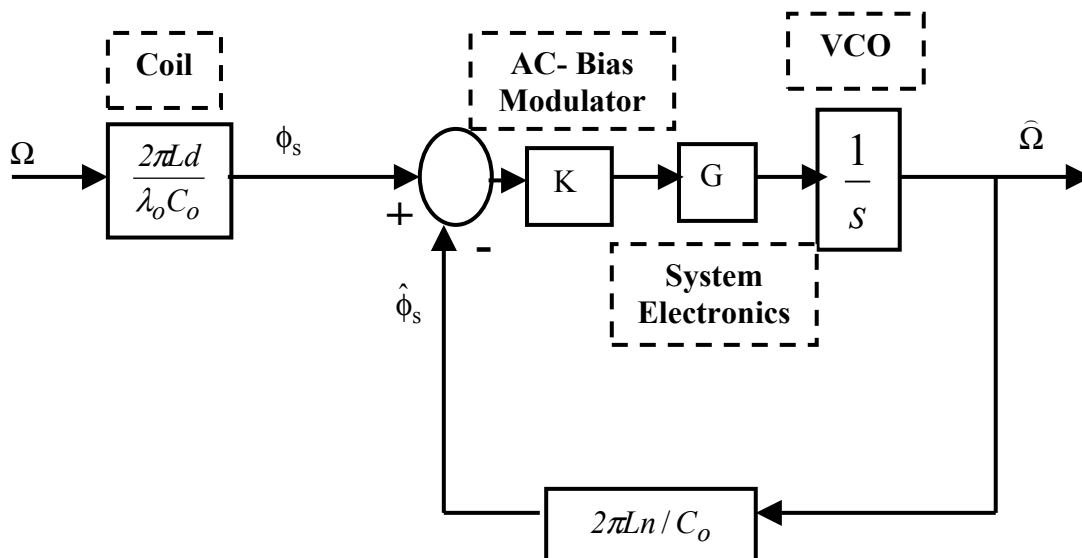


Fig. 3.3. The FOG as a closed loop first-order system.

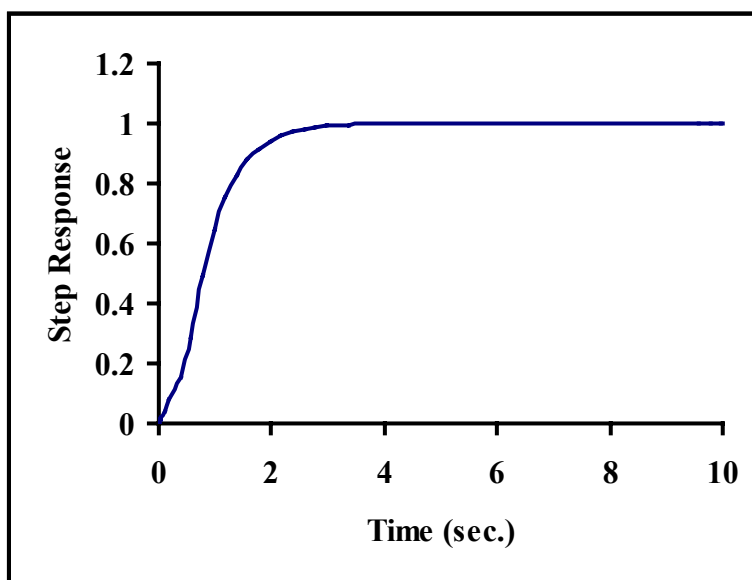


Fig. 3.4. The step response of the FOG.  $L = 1000\text{m}$ ,  $d = 0.1\text{m}$ ,  $n = 1.48$ ,  $\lambda_o = 0.85\ \mu\text{m}$ ,  $K = 0.5815$  and  $G = 10^5$ .

### **3.3. FOG performance characteristics.**

The performance of the FOG is determined by three major variables: (1) the angle random walk, (2) the bias drift and (3) the scale factor.

#### **3.3.1. Angle random walk (ARW).**

The output of the FOG contains a broadband random noise component, which results both from the shot noise and the thermal noise in the photodetector [Senior, 1993]. The shot noise is generated due to the dark current at the photodetector, which is a small reverse leakage current that flows from the photodetector terminals when there is no optical power incident on it. This dark current contributes to the total system noise and gives random fluctuations about the average particle flow of the photocurrent. Therefore it manifests itself as shot noise on the photocurrent [Senior, 1993]. On the other hand, the thermal noise is the spontaneous fluctuation due to the thermal interaction between the free electrons and the vibrating ions in a conducting medium [Senior, 1993]. Within the FOG output bandwidth the noise spectral density is very broad. This noise is known as the angle random walk (ARW) [Lefevre, 1993; Burns, 1994] and is modeled as a white noise input to a separate system (Fig.3.5). The transfer function of this system has the same denominator as the original system [Franklin et al., 1990]. However, the numerator of this transfer function is a constant gain obtained after the multiplication of the two gain blocks  $K$  and  $G$  in the forward path of the original system. This is related to the fact that the  $AC$ -bias demodulation and the electronic gain affect the output of the detector before delivering the output of the FOG (see Fig. 3.3).

#### **3.3.2. Bias Drift.**

The bias drift is defined as the deviation in the measured rotation rate at constant temperature [Burns, 1994]. This drift occurs due to internal imperfections of the FOG as a sensor and it is one of the major parameters that determine the FOG accuracy. Measurement of the bias drift is done at room temperature with a long time series of data because for short-duration data the bias drift is masked by the ARW [Bennet et al., 1998]. The bias drift is strongly affected by the electronic gain  $G$  and the length of the fiber coil

L. Increasing either L or G increases the degree of stability of the system, reduces the rise time, increases the sensitivity and reduces the bias drift. In general, the gain of the electronic system is usually kept large enough to ensure small rise time and a tight loop closure (i.e. fast convergence to the applied rotation rate) [Noureldin et al., 1999]. However, the length of the fiber coil cannot be increased beyond  $1000m$  since the attenuation and dispersion problems related to the optical beam become evident. Typical fiber coil lengths in practical FOG applications range from  $160m$  to  $1000m$  [KVH Industries Inc.; Fibersense Technology Corporation].

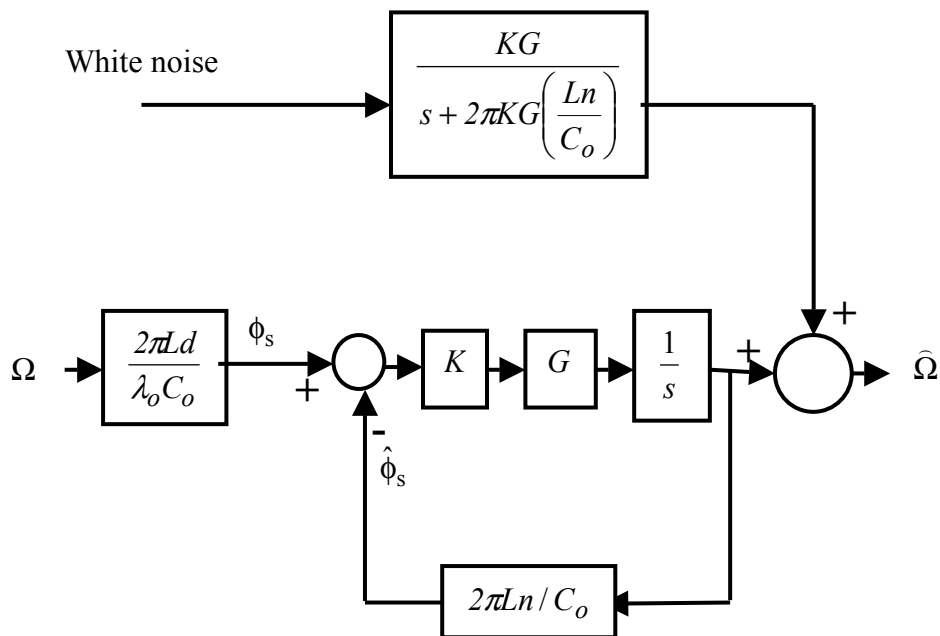


Fig.3.5. Applying the angle random walk (ARW) as a disturbance to the FOG system.

### 3.3.3. Scale factor.

The scale factor is the constant of proportionality between the actual rotation rate and the FOG output signal as given in Eq.3.6. The instability of the scale factor  $\left(\frac{d}{\lambda_0 n}\right)$  is due to the temperature variation, which changes the value of the peak wavelength  $\lambda$  (Fig.3.6). In general, most of the commercially available FOG products can perform properly up to temperatures of 90°C and in most of the drilling sites in the USA and Canada the downhole temperature does not exceed this limit [Noureldin et al.<sup>c</sup>, 2000]. For higher temperature environments a mathematical model can be provided to compensate for the instability of the scale factor [Jones, 1987]. Practically, various temperature-shielding methods can be provided to maintain the temperature within the above limit, therefore, no further attention was devoted to the scale factor in the present study.

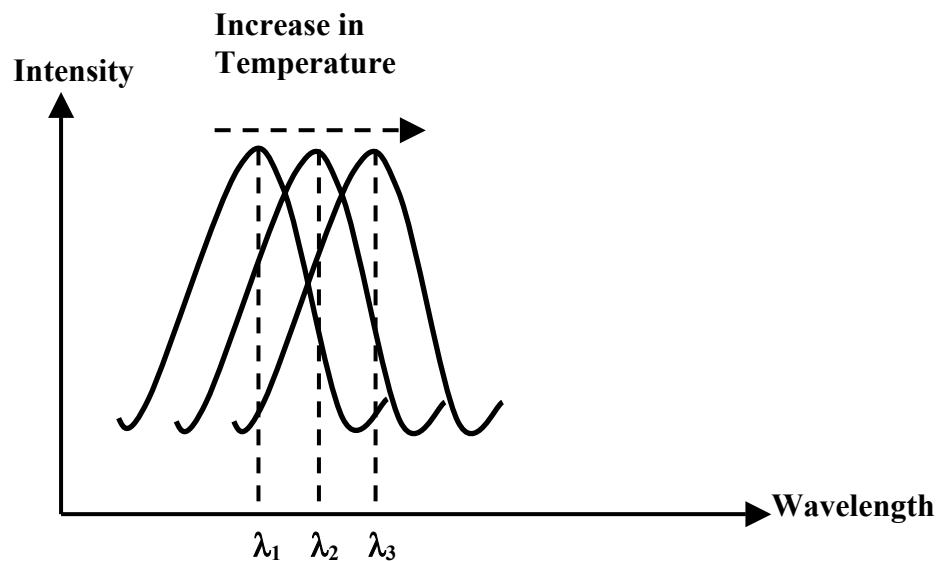


Fig.3.6. The change of the peak wavelength of the optical beam with respect to temperature variation.

### 3.4. Simulation of Severe Drilling Conditions.

#### 3.4.1. Shock effect.

The effect of shock is always observed while penetrating hard rocks [Skaugen, 1987]. Although these shock forces produce different kinds of vibrations along the drill collars, they also have an instantaneous effect on the measurements taken by the FOG. The vibrations produced by the shock forces along the drill string will be analyzed in the following section while the instantaneous effect of a shock force on the FOG measurement is considered in this section. While drilling through hard rocks the drill bit may encounter forces of a very large magnitude and which act for a very short duration. Such forces are called impulsive forces [Thomson, 1965]. Fig.3.7 shows an impulsive force of magnitude  $F_s$  with time duration of  $\Delta t$ . This instantaneous force is simulated as an impulse input to the FOG model. As the FOG measures angular rates, the corresponding rotation rate  $\Omega_s$  produced in response to the applied shock force should be determined. Let  $F_s$  denote the instantaneous shock force. According to Newton's second law, it can be expressed as,

$$F_s = m_b a_s \quad (3.8)$$

where  $m_b$  is the mass corresponding to the total weight on bit (WOB) and  $a_s$  is the linear acceleration produced due to the shock forces. The acceleration  $a_s$  is expressed as  $\frac{\Delta V_s}{\Delta t}$ , where  $\Delta V_s$  is the corresponding change of the linear velocity. The corresponding angular velocity  $\Omega_s$  affecting the FOG can be obtained from  $\Delta V_s$  and is expressed as,

$$\Omega_s = \Delta V_s / r_o = \frac{F_s \Delta t}{m_b r_o} \quad (3.9)$$

where  $r_o$  is the outer radius of the drill pipe.

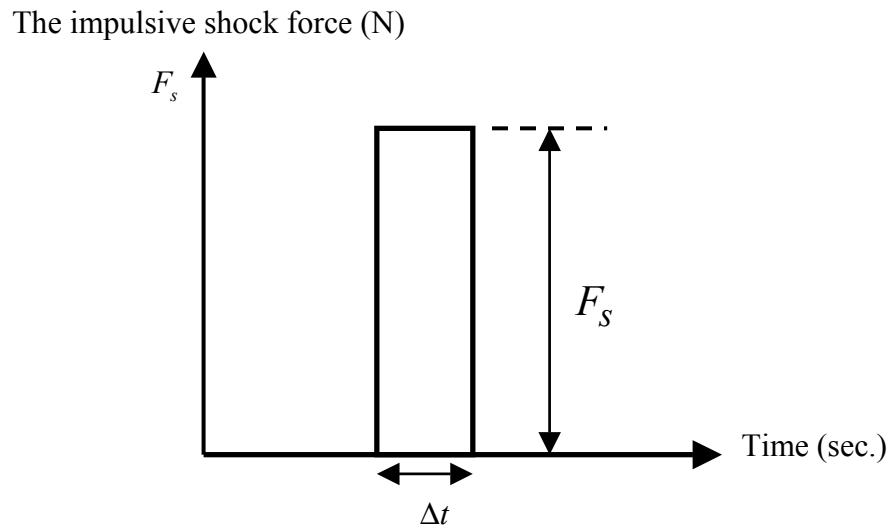


Fig.3.7. Representation of impulsive shock forces.

The rotation rate  $\Omega_s$  is considered as a disturbance to the original system and is incorporated into the FOG model in the same manner to the angle random walk, except that the gain in the numerator of the parallel system now includes the gain block  $\frac{2\pi Ld}{\lambda_o C_o}$  which describes the linear relationship between the Sagnac phase shift and the applied rotation rate (Fig.3.8). This is related to the fact that the fiber optic coil senses the rotation rate corresponding to the shock force before being processed by the AC-bias modulator and the electronic system.

### 3.4.2. Vibration effects.

During the drilling process the FOG is affected by two sources of vibration. The first is due to the circulation of the mud through the drill string and the second is the BHA vibration due to the interaction between the drill bit and the formation.

The vibration due to the circulation of mud is mainly due to the mud pump noise. The mud pump noise was considered a sinusoidal signal with a frequency of  $1.7Hz$  and maximum amplitude of  $200\text{ psi}$  [Brandon et al., 1999]. This pressure signal is expressed as follows:

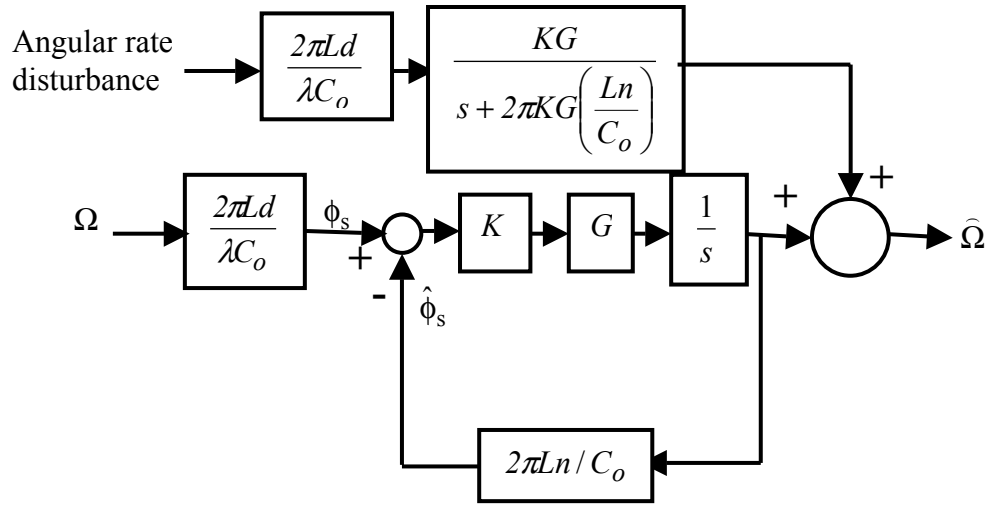


Fig.3.8. Applying angular rate disturbance to the FOG system.

$$p(t) = A_{\max} \sin(2\pi ft) \quad (3.10)$$

where  $A_{\max}$  is the maximum amplitude of the pressure signal and  $f$  is the vibration frequency due to mud pump noise. The corresponding force acting on the FOG due to this pressure signal is simply given as,

$$F = m_c \frac{dV_m}{dt} = p(t)\pi r_i^2 \quad (3.11)$$

where  $r_i$  is the internal radius of the drill collar,  $V_m$  is the corresponding linear velocity and  $m_c$  is the mass of the drill collar. Substituting the pressure signal  $p(t)$  with its corresponding sinusoidal expression (see Eq.3.10), the linear velocity  $V_m$  can be obtained. Dividing the linear velocity  $V_m$  by the internal radius of the drill collar, the corresponding angular velocity  $\Omega_m$  affecting the FOG can be obtained as,

$$\Omega_m = \frac{A_{\max} r_i}{2 f m_c} \cos 2\pi ft \quad (3.12)$$

The angular velocity  $\Omega_m$  due to the mud pump noise is considered a disturbance input to the FOG model and is processed similarly to the disturbance caused by shock forces (Fig.3.8).

The second source of vibrations affecting the FOG accuracy is the BHA vibration and a considerable effort has been invested in explaining and understanding this phenomenon [Vandiver et al., 1989]. It was found that the BHA can vibrate in longitudinal, torsional and lateral mode when the drill bit penetrates through hard rocks [Skaugen, 1987]. In borehole surveying during the horizontal drilling process, the FOG might be mounted in the horizontal plane with its sensitive axis normal to the axis of the drill collar so that it could determine the azimuth after incorporating its output with the output from the three accelerometers. Thus, this FOG, as a single axis rotation sensor, would not be affected by the longitudinal mode of vibration, which acts along the axis of the drill collar. In addition, the torsional mode of vibration would have minor effects especially when brought under control by shock absorbers [Skaugen, 1987]. The major source of vibration that will affect the FOG accuracy is the bending vibration. There are two sources of BHA bending vibration [Vandiver et al., 1989]. The first is the linear coupling of the longitudinal and transverse vibration due to the initial curvature of the BHA. The second is the drill collar whirling. Linear coupling between the axial forces on the bit and transverse vibration occur frequently in real drilling assemblies and the source of the linear coupling is the initial curvature of the BHA, which is shown on Fig.3.9.a. Drill collar whirling is simply the centrifugally-induced bowing of the drill collar resulting from rotation. It occurs when the center of gravity of the drill collar is not initially located precisely on the hole center line (Fig. 3.9.b). In a situation when the collar rotates a centrifugal force acts at the center of gravity, which causes the collar to bend.

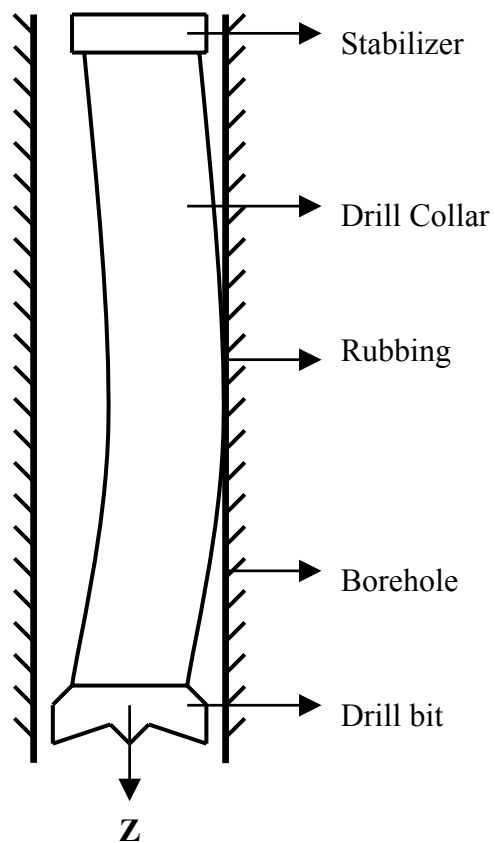


Fig.3.9.a. Initial curvature of the drill collar downhole.

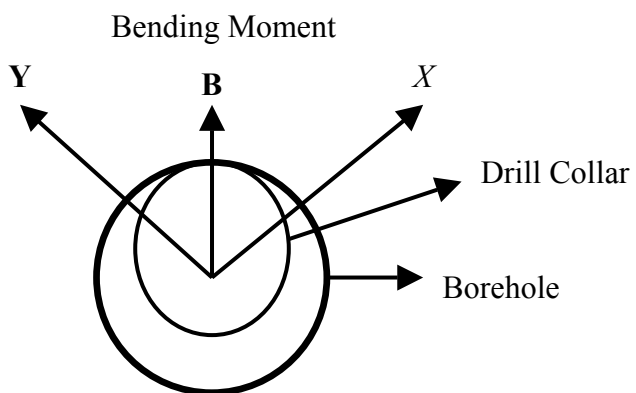


Fig.3.9.b. Cross section of the borehole and the whirling drill collar.

Several case studies were made to analyze the above two phenomena and the bending moment produced was measured by special mechanical devices [Vandiver et al., 1989]. The pattern of this bending moment was found to be completely random in nature (Fig.3.10). This random distribution is applied to the FOG model using a random number generation module, which is adapted to simulate the highest possible bending moment. The corresponding angular velocity to this bending force can be expressed as,

$$\Omega_V = \frac{F\Delta t}{m_c r_o} = \frac{B\Delta t}{m_c r_o^2} \quad (3.13)$$

where  $F$  is the bending force,  $B$  is the corresponding bending moment ( $B = Fr_o$ ) and  $m_c$  is the mass of the drill collar. This angular velocity is considered a disturbance to the FOG model and is processed similarly to the shock force and vibration due to the mud pump noise.

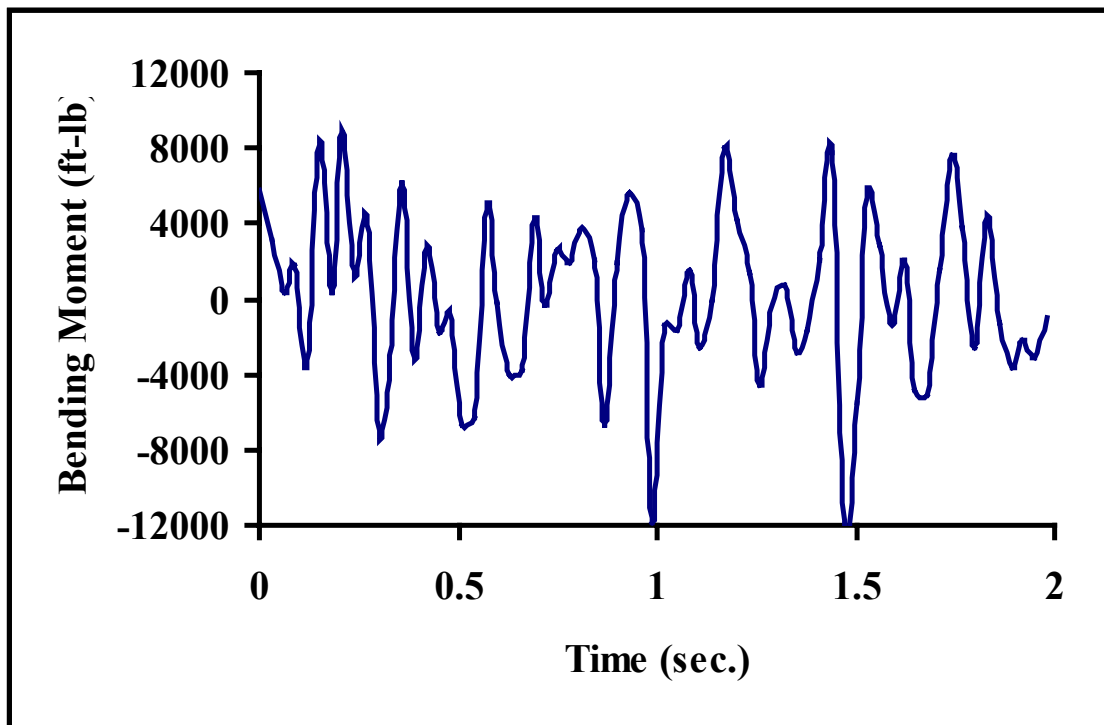


Fig.3.10. Bending moment as a function of time.

In reality, downhole vibration recorders have provided clear insight into the vibration events existing downhole. However, since many different vibration phenomena occur simultaneously, it becomes difficult to evaluate any of them separately. For example, torsional and bending vibrations are intimately coupled [Vandiver et al., 1989]. In addition, bit bounce, stick-slip and drill collar whirl are all existing at the same time and cannot be separated. The measurement of the severest vibration conditions as reported by Vandiver et al. (1989) is used in this study and is applied to the FOG model as an angular disturbance.

### 3.5. Results.

#### 3.5.1. Simulation of the effect of the ARW.

The electronic gain  $G$  had a major effect on the ARW. The other FOG parameters (e.g. coil length, diameter, refractive index and wavelength) did not affect the ARW. Figs.3.11.a, 3.11.b and 3.11.c show, respectively, the outputs of the FOG with different values of the electronic gain  $G$  of  $2*10^5$ ,  $10^5$  and  $0.5*10^5$ . It is clear that the FOG output shown on Fig.3.11.a is noisier than the FOG outputs shown on Fig.3.11.b and Fig.3.11.c. The maximum deviations from the steady state value were found to be about 13% for  $G=2*10^5$ , 7% for  $G=10^5$ , and 4% for  $G=0.5*10^5$ . Reducing the electronic gain reduced the noise level at the FOG output but increased the rise time and the bias drift. Some signal processing techniques can be developed to reduce the effect of the ARW on the FOG output signal.

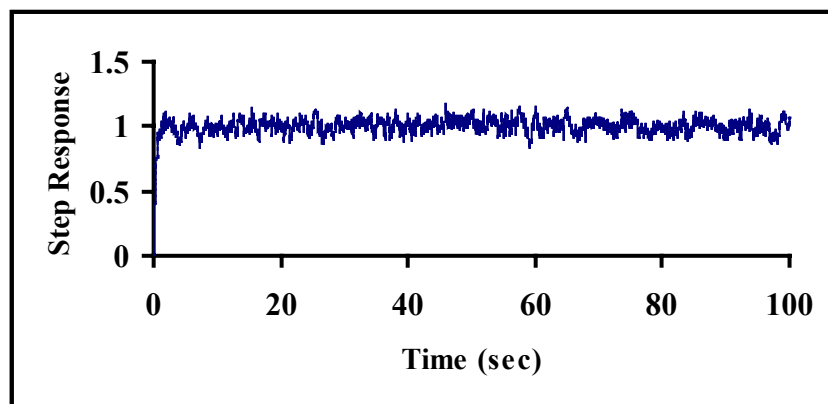


Fig. 3.11.a. FOG step response with the effect of ARW at  $G = 2*10^5$ .

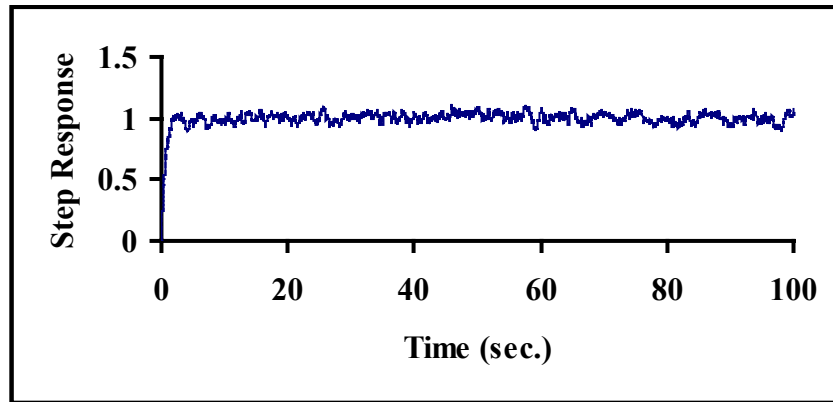


Fig. 3.11.b. FOG step response with the effect of ARW at  $G = 10^5$ .

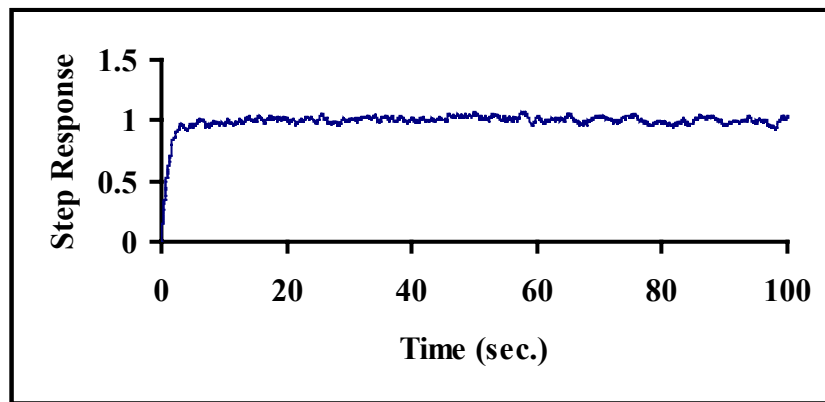


Fig. 3.11.c. FOG step response with the effect of ARW at  $G = 0.5 \cdot 10^5$ .

### 3.5.2. Simulation of FOG sensitivity and bias drift.

The sensitivity of the designed FOG to changes in the input rotation rate was analyzed with respect to the length of the fiber optic coil  $L$  and the electronic gain. Fig.3.12.a shows the FOG step response for different values of the fiber optic coil length while keeping  $G = 10^5$ . It is clear that increasing the coil length reduces the FOG system rise time. This makes the FOG more sensitive to changes in the input rotation rate and consequently reduces the bias drift. The rise time decreased by one-half when the length of the fiber optic coil was doubled. The rise time was found to be equal to 1.5, 3, and 6 seconds for fiber optic coil length of 1000m, 500m and 250m respectively.

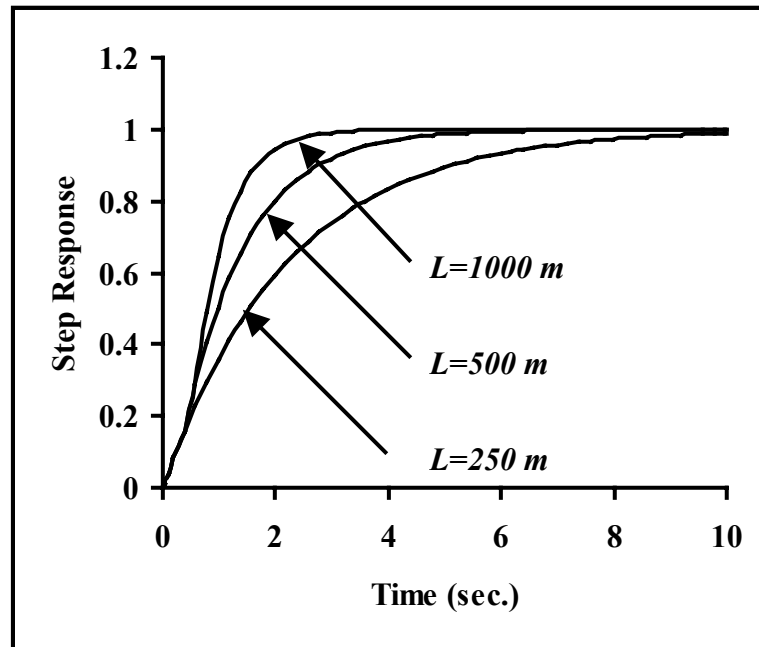


Fig.3.12.a. FOG step response for different values of  $L$ .  
 $d = 0.1\text{m}$ ,  $n = 1.48$ ,  $\lambda_o = 0.85\ \mu\text{m}$ ,  $K = 0.5815$  and  $G = 10^5$ .

The electronic gain  $G$  had exactly the same effect on the FOG system. It is shown (Fig.3.12.b) that increasing  $G$  increases the FOG sensitivity and reduces both the rise time and the bias drift. The coil length was kept at  $1000\text{m}$  while analyzing the effect of the electronic gain. Rise times of  $1.5$ ,  $3$  and  $6$  seconds were recorded for electronic gain values of  $10^5$ ,  $0.5 \cdot 10^5$ , and  $0.25 \cdot 10^5$ , respectively. Increasing either  $L$  or  $G$  is limited by their side effects. Any further increase of  $L$  above  $1000\text{m}$  would increase the attenuation of the optical signal along the coil and the FOG overall performance would deteriorate. The increase of  $G$  increases the impact of the angle random walk (ARW) on the FOG output signal and makes the FOG more sensitive to vibration effects.

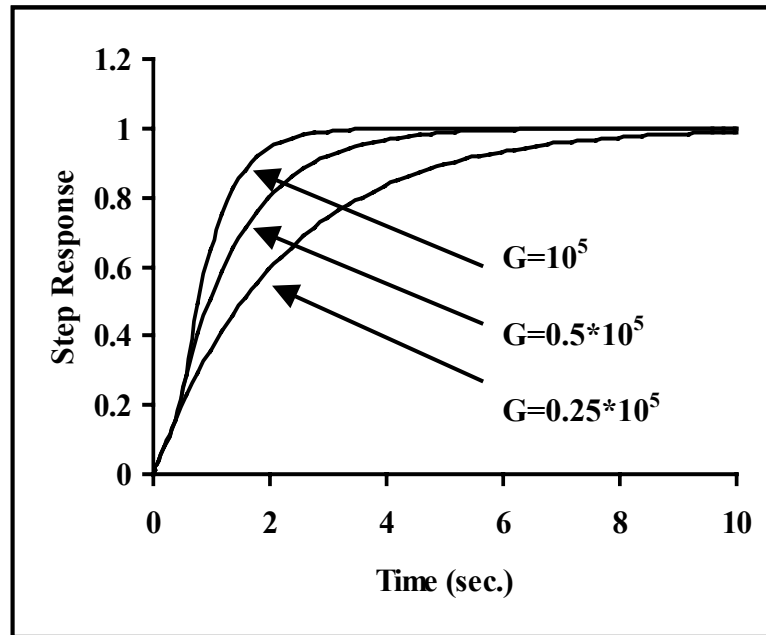


Fig. 3.12.b. FOG step response for different values of  $G$ .  
 $d = 0.1\text{m}$ ,  $n = 1.48$ ,  $\lambda_o = 0.85 \mu\text{m}$ ,  $K = 0.5815$  and  $L = 1000\text{m}$ .

### 3.5.3. Simulation of the effect of shock forces.

The impulsive shock forces produced an instantaneous effect on the FOG output signal. The corresponding angular rates to these shock forces were applied to the FOG model as discussed earlier. A drill collar of 4.75'' outer diameter was considered together with a total WOB of 34,000 kg. Different impulsive shock forces from 100g [N] to 1000g [N] were applied, where  $g$  is the gravitational acceleration ( $9.81 \text{ m/sec}^2$ ). The effect of these forces was studied in conjunction with varying their time duration from 0.001 sec to 0.01 sec. The three-dimensional distribution describing the variation of the percentage error at the FOG output with respect to the magnitude of the shock force and its duration is shown on Fig.3.13.a. From this distribution a maximum error of about 8.5% can be observed in the FOG reading corresponding to shock force magnitude of 1000g and duration of 0.01 sec. The FOG output with such shock force is shown on Fig.3.13.b. Clearly, the FOG can perform properly with a reasonable accuracy (percentage error less than 8.5%) under the effect of short-duration shock forces up to 1000g [N].

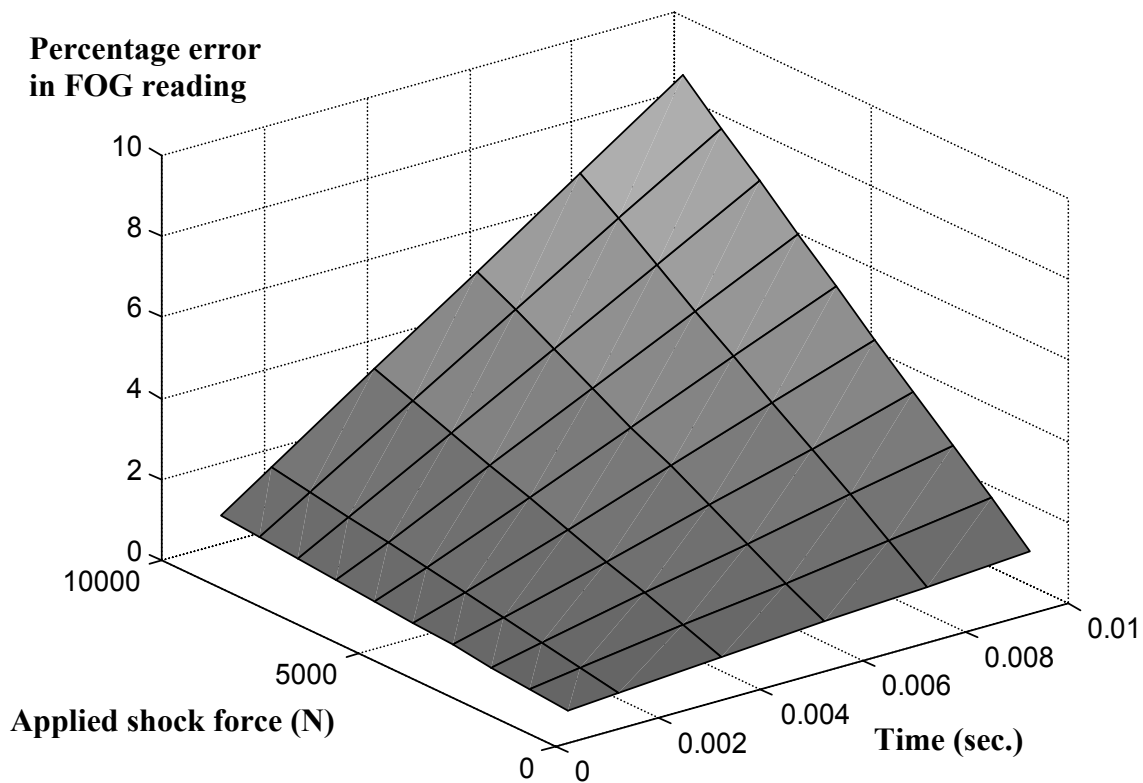


Fig. 3.13.a. Three-dimensional distribution of the percentage error at the output of the FOG with respect to different magnitudes and time duration of the shock forces.

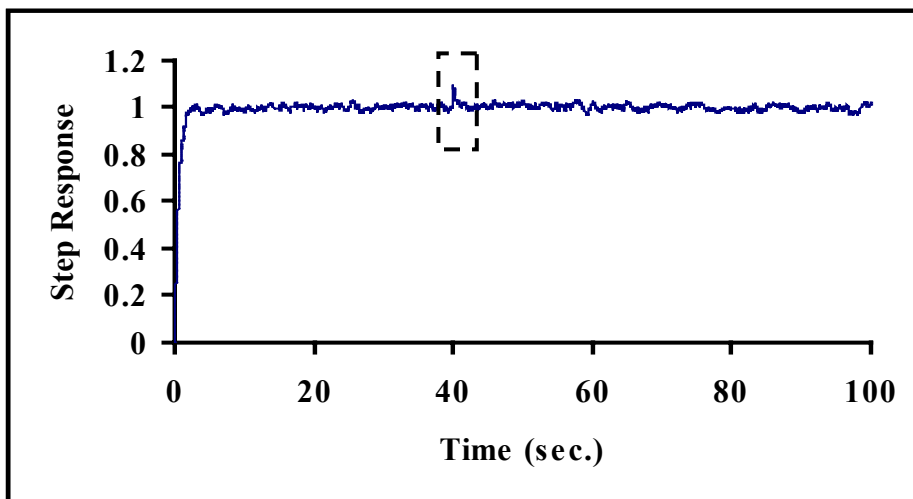


Fig. 3.13.b. FOG output signal (containing ARW) with the 1000g shock force acting at the moment  $t = 40$  sec for a duration of 0.01 sec.

#### 3.5.4. Simulation of the effect of vibration due to the mud pump noise.

For the purpose of this analysis, a drill collar of 4.75'' outer diameter, length of 30 feet and weight of 45 lb./ft was considered. The effect of the mud pump noise can be seen on Fig.3.14.a and Fig.3.14.b for  $G = 10^5$  and  $0.5*10^5$  respectively. It is clear that high electronic gain increases the FOG sensitivity to this vibration effect. In both curves (Fig. 3.14.a & Fig. 3.14.b), it can be seen that the FOG signal (containing no ARW) manifests itself as an envelope to the mud pump noise. This indicates that the FOG signal can be extracted from the mud pump noise using some signal processing techniques. Fig.3.14.c shows the FOG signal with the effect of the ARW as an envelope to the mud pump noise which is obtained with  $G = 10^5$ . In this case, a percentage error of 18.5% was recorded. This error is the highest percentage error obtained in the present study. However, the vibration due to the mud pump noise is deterministic in nature and depends on the constant physical parameters of the drilling process. Thus, some signal processing techniques can be designed to extract the FOG signal and minimize the effect of the mud pump noise.

#### 3.5.5. Simulation of the effect of bending vibration.

The highest bending moment recorded in previous case studies [Vandiver et al., 1989] had a magnitude about  $\pm 10,000$  ft-lb. The angular rate corresponding to this bending moment was applied to the FOG model as a disturbance in order to study its effect on the FOG performance. A drill collar of 6.25'' diameter was considered [Vandiver et al., 1989]. Figs.3.15.a, 3.15.b and 3.15.c show, respectively, the FOG output signal corrupted by the bending moment for electronic gain  $G$  of  $2*10^5$ ,  $10^5$  and  $0.5*10^5$ . It is clear that higher values of  $G$  make the FOG more sensitive to this vibration effect. The maximum percentage error recorded in FOG reading was found to be 18%, 10% and 7% for  $G=2*10^5$ ,  $10^5$  and  $0.5*10^5$  respectively. It seems that the bending vibration has the most serious effect on the FOG accuracy since it is completely random in nature. Decreasing the electronic gain to make the FOG less sensitive to this vibration effect appears, for the moment, to be the only way to compensate for its impact.

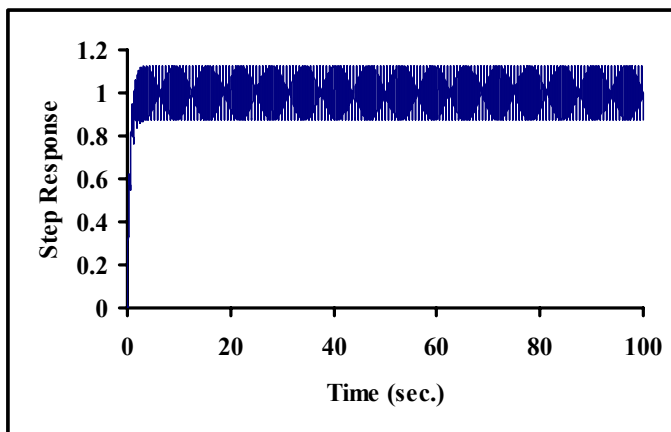


Fig.3.14.a. FOG output signal (containing no ARW) with the effect of the mud pump noise at  $G = 10^5$ .

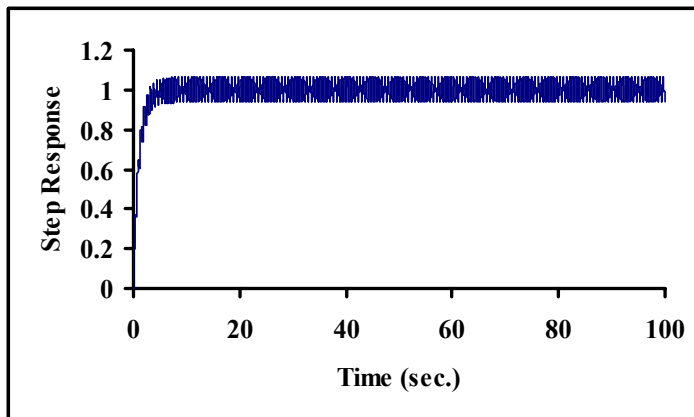


Fig.3.14.b. FOG output signal (containing no ARW) with the effect of the mud pump noise at  $G = 0.5 \cdot 10^5$ .

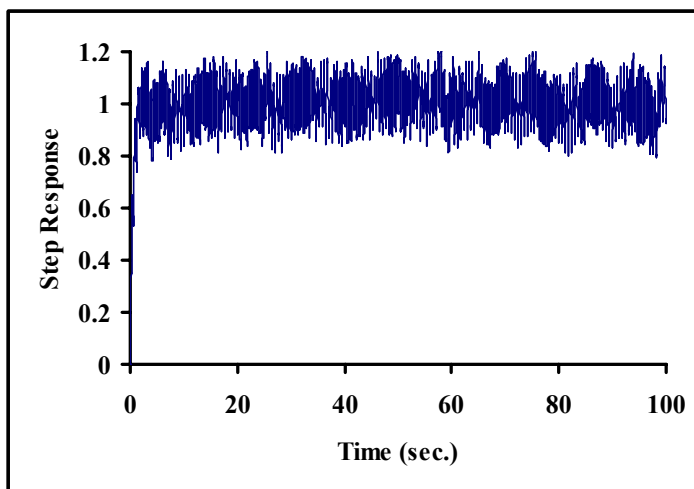


Fig.3.14.c. FOG output signal (containing ARW) with the effect of the mud pump noise at  $G = 10^5$ .

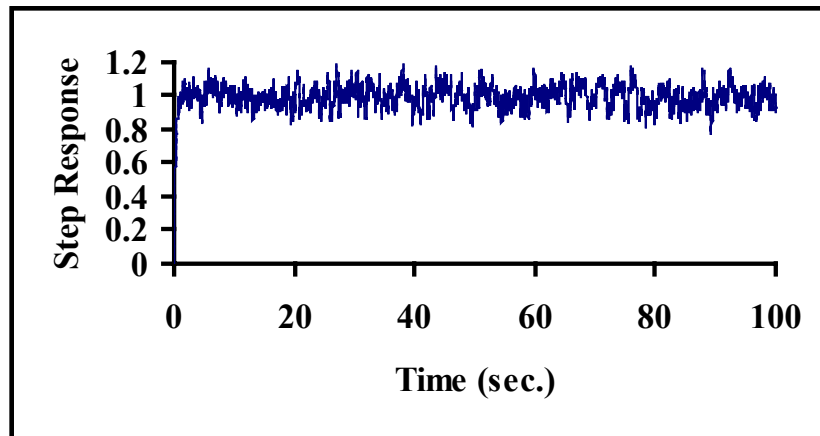


Fig.3.15.a. FOG output signal (containing no ARW) with the effect of bending vibration at  $G = 2*10^5$ .

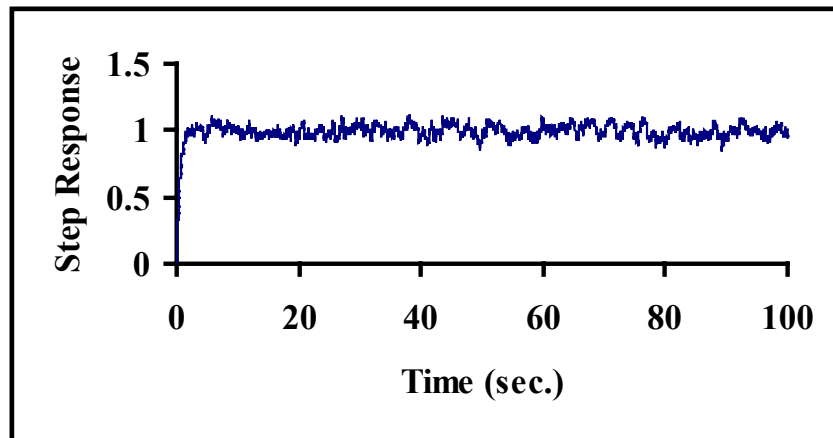


Fig.3.15.b. FOG output signal (containing no ARW) with the effect of bending vibration at  $G = 10^5$ .

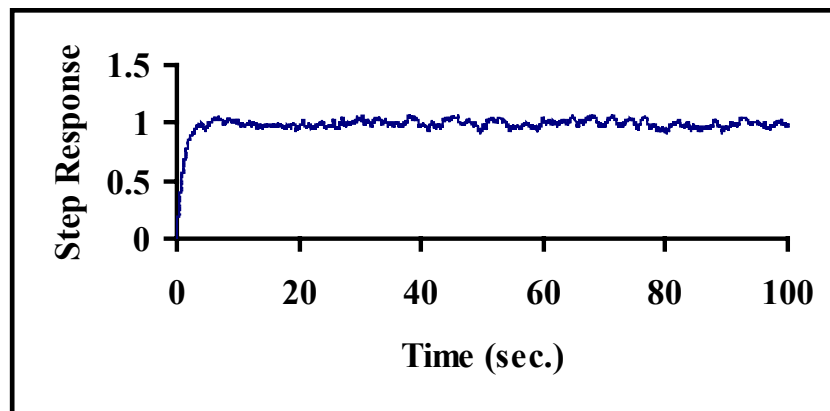


Fig. 3.15.c. FOG output signal (containing no ARW) with the effect of bending vibration at  $G = 0.5*10^5$ .

### 3.6. Conclusion.

In this chapter, the applicability of microelectronic fiber optic gyroscope (FOG) in horizontal drilling has been investigated. Particular attention was paid to the impact of hostile downhole conditions on the FOG performance. In order to study this impact a quantitative system model of the FOG was developed and tested against the manufacturer specifications [Noureldin et al., 1999]. In addition, the impact of various FOG parameters on its performance was quantitatively studied, thus providing a reference for future design improvements from the perspective of the downhole horizontal drilling application [Noureldin et al.<sup>c</sup>, 2000]. The results from this study showed that the desired accuracy could be achieved by controlling either the length of the fiber optic cable or the gain of the electronic system. The increase in the length of the fiber optic cable or the electronic gain improved the FOG sensitivity and reduced the bias drift. Unfortunately, the overall performance of the FOG deteriorates for cable lengths above  $1000m$  due to the increase in the attenuation of the optical signal. In addition, very high values for the electronic gain increase the ARW and make the FOG more sensitive to vibration and shock forces.

In general, FOGs can be a reliable and inexpensive replacement of magnetometers in MWD borehole surveying. In the hostile downhole environment the FOG can perform with a reasonable accuracy under the impact of short duration shock forces of up to  $1000g$  [N]. Although the vibration due to the mud pump noise produces relatively high percentage errors at the FOG output, some signal processing techniques can be applied to extract the FOG signal and to reduce this vibration effect [Girard and Mintchev, 1998]. On the other hand, the effect of bending vibration is random in nature and cannot be completely removed from the FOG output. It is observed that the severest condition of bending vibration produces a percentage error of about  $10\%$  with an electronic gain of  $10^5$ . If further improvement of the FOG sensitivity requires setting the electronic gain to  $2*10^5$ , the percentage error due to bending vibration increases to  $18\%$ . However, if the vibration and shock forces are brought under control using shock absorbers and stabilizers, significant improvement of the FOG performance can be achieved.

## CHAPTER FOUR

### DE-NOISING THE FOG OUTPUT SIGNAL

As discussed in the previous chapter, FOG performance characteristics are limited by the bias drift and the angle random walk (ARW). Bias drift affects the long-term performance of the FOGs and some procedures have been reported to compensate for it [Perlmutter, 1994; Bowser et al., 1996; Perlmutter et al., 1997]. On the other hand, ARW affects the short-term (15-minute or less) performance and is defined as the broadband noise component at the FOG output [Lefevre, 1993]. It has been shown that, for data portions of short duration, it is usually not possible to determine the FOG bias drift since it is masked by the ARW, which becomes the major source of error in the FOG output signal [Bennet et al., 1998]. The shot noise and the thermal noise introduced by the photodetector, the back-scattering of the optical beam inside the fiber optic coil, and the light source intensity noise are all noise components which combine together to form the ARW [Senior, 1993; Aein, 1995]. Analysis of low cost tactical grade FOGs showed that the output uncertainty is relatively high ( $40\text{-}50^\circ/\text{hr}$ ) and it is usually considered as white noise component at the FOG output [Bennet et al., 1998]. On the other hand, statistical analysis of the random noise at the output of navigational grade FOGs shows that it is different from white noise and can be represented as a random walk or 1<sup>st</sup> order Gauss-Markov process [Gelb, 1974; Brown and Hwang, 1992; Schwarz and Wei, 1999].

During stationary surveying processes of inertial navigation systems (INS), FOGs are employed to monitor the components of the Earth rotation rate along their sensitive axes in order to determine the attitude of the moving platform [Titterton and Weston, 1997]. The absolute value of the Earth's rotation rate component, which is to be measured by a FOG is below  $15.04^\circ/\text{hr}$  depending on the orientation of the platform on which the FOG is installed. In some orientations, especially while approaching the East direction, the value of the Earth rotation rate component can become as low as  $1^\circ/\text{hr}$  [Britting, 1971; Titterton and Weston, 1997]. Theoretically, this value becomes  $0^\circ/\text{hr}$  when the platform is on the horizontal plane, while the FOG sensitive axis is along the

East direction. This necessitates the ARW to be as small as possible in order to reduce the uncertainty in measuring the Earth's rotation rate and to eliminate the dependency of the measurement percentage error on the platform orientation.

In situations where a minimum number of FOGs is needed (e.g. in MWD surveying processes for the oil industry), reduction of the ARW before processing the FOG measurements is necessary [Noureldin et al.<sup>c,d</sup>, 2001]. Current commercially available FOGs have an ARW that varies from  $5^{\circ} / hr / \sqrt{Hz}$  for low cost gyros [KVH Industries Inc., Rhode Island, N.Y.] to  $0.1^{\circ} / hr / \sqrt{Hz}$  for high cost gyros [Fibersense Technology Corp., Canton, MA]. With a standard FOG bandwidth of  $100 Hz$ , a low cost gyro would produce a measurement uncertainty of  $50^{\circ} / hr$ , while for a high cost gyro this uncertainty would be  $1^{\circ} / hr$ . These levels of uncertainty deteriorate the computational accuracy of the stationary surveying process and prevent the use of single gyroscope for reliably determining the Earth's rotation rate. Therefore, a reduction of ARW prior to the measurement itself is imperative in order to adequately utilize FOGs in INS and to minimize the number of gyroscopes needed to implement this task.

#### **4.1. Available methods for reducing the FOG noise level.**

Several techniques have been reported for the reduction of ARW at the FOG output. These techniques can be classified in two different categories: (1) hardware techniques; and (2) real-time digital signal processing techniques.

The first category is related to modifications of the internal optical design of the FOG. It has been reported that up to  $50\%$  reduction of the random intensity noise component of the ARW can be achieved by utilizing a polarized light signal within the internal FOG design [Huang et al., 1999]. In addition, two parallel photodetectors with a polarization-maintaining coupler have been suggested to reduce the light source intensity noise [Killian, 1994]. Moreover, the noise induced by the backscattering and the closed loop operation of the FOG has been reduced with a resonator FOG structure [Hotate and Hayashi, 1994].

While hardware improvements can provide significant reduction of the ARW (up to  $0.012^\circ / hr / \sqrt{Hz}$  [Killian, 1994]), the second category of techniques for ARW reduction can be regarded as complementary. Real-time signal processing techniques have proven to be invaluable in improving the quality and the reliability of FOG measurements regardless of the advances in hardware design [Brown and Hwang, 1994]. Most of the signal processing methodologies currently employed utilize Kalman filtering techniques to reduce the effect of ARW and to improve the estimation accuracy [Algrain and Ehlers, 1995; Salychev, 1998]. Unfortunately, the convergence of these methods (the time to remove the effect of the ARW and to provide an accurate performance) during the alignment processes can take up to 15 minutes. In addition to their time-consuming algorithms, these techniques are complex to design and require a considerable effort to achieve real-time processing. Alternatively, neural network techniques have been introduced to reduce the noise level at the FOG output [Rong et al., 2000]. Although some promising simulation results have been presented, real-time implementation with an actual FOG system has not been reported.

The existing adaptive signal processing techniques [Haykin, 1996] have been used successfully to reduce the noise level in a variety of applications predominantly related to channel equalization of communication channels [Gesbert and Duhamel, 2000], speech recognition [Mantha et al., 1999] and video sequence restoration [Doo and Kang, 1999]. However, this exciting new technology has not been applied in FOG-based INS for the purpose of ARW reduction.

This chapter aims at employing adaptive signal processing techniques to reduce the noise component at the FOG output of INS so that the Earth's rotation rate can be reliably monitored with a single FOG. A transversal tap delay line filter is designed for this purpose using a least-mean square (LMS) adaptive technique with variable step size parameter to ensure fast convergence of the adaptive algorithm. Two different criteria are utilized. The first criterion is based on forward linear prediction (FLP) while the second criterion utilizes known Earth rotation rate component at the reference channel.

## 4.2. Forward linear prediction (FLP) method.

FLP methods employ a set of past samples from a stationary process to predict future sample values [Haykin, 1996]. The algorithm that performs this process is known as a predictor and can be designed to predict values that are one sample time unit or multiple sample time units in the future. The most common and practical is the single time-unit predictor (one-step predictor) [Haykin, 1996]. Such a predictor employs a tap-delay line filter of a predetermined order to deliver an estimation of the current sample value. Since simple parametric multipliers without any feedback are used for the tap weights, the predictor is of finite impulse response (FIR), which guarantees its stability. The structure of such FIR tap-delay line filter of order  $M$  is shown on Fig.4.1.

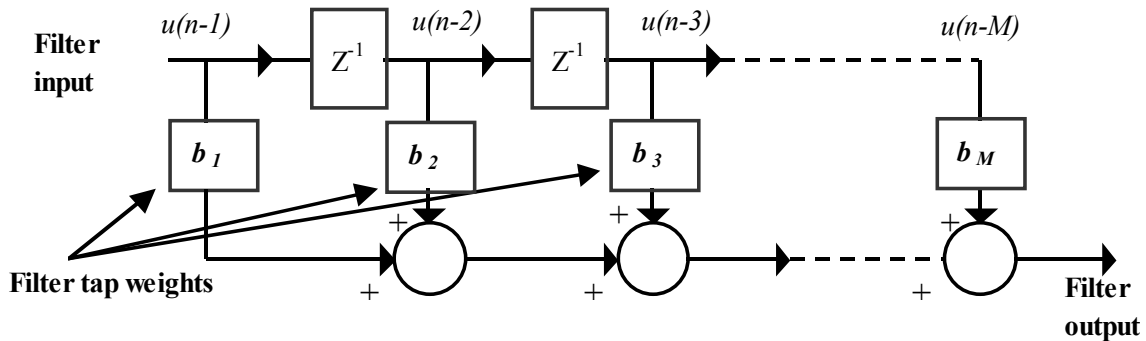


Fig.4.1. Structure of a tap-delay FIR filter that employs past samples  $\{u(n-1), u(n-2), u(n-3), \dots, u(n-M)\}$  to provide an estimate of the current sample value  $\hat{u}(n)$  [Haykin, 1996].

The output  $\hat{u}(n)$  is an estimate of the actual value of the current sample  $u(n)$  and is given as,

$$\hat{u}(n) = \sum_{k=1}^M b_k u(n-k) = B^T U(n-1) \quad (4.1)$$

where  $b_k$  are the tap weights, or the coefficients of the FIR filter;  $u(n-k)$  is the input sequence involving  $k$  samples back from the  $n^{\text{th}}$  sample;  $B^T = \{b_1 \ b_2 \ \dots \ b_M\}$  is the tap weight vector, and  $U(n-1) = \{u(n-1) \ u(n-2) \ \dots \ u(n-M)\}^T$  is the tap input vector. The statistical criterion used for optimization employs the minimization of

the mean-square value of the estimation error (also known as the forward prediction error [Haykin, 1996]) between  $u(n)$  and  $\hat{u}(n)$  [Widrow and Stearns, 1985]:

$$e(n) = u(n) - \hat{u}(n) \quad (4.2.a)$$

$$J(n) = E[e^2(n)] \quad (4.2.b)$$

where  $e(n)$  is the forward prediction error and  $J(n)$  is the expectation of its square value, known as the mean-square estimation error (MSEE) or the cost function [Widrow and Stearns, 1985]. The prediction problem is related to selecting the filter tap weights vector  $B = (b_1 \ b_2 \ b_3 \ \dots \ b_M)^T$  that minimizes the forward prediction errors in the mean square sense. It has been shown that Eq.4.2.b describes a quadratic surface with a minimum at  $B = B_o$ , where  $B_o$  is the column vector containing the optimum values of the tap weights [Solo and Xuan, 1995]. Since this surface has a unique minimum, the optimal solution  $B_o$  is also unique. The LMS technique is used to design the FLP filter and determine adaptively the optimal values of the tap weights. According to the LMS criterion, the tap weights are iteratively adjusted towards their optimum values using the following update equation [Haykin, 1996; Sesay, 1999]:

$$B(n+1) = B(n) + \mu E[e(n) U(n-1)] \quad (4.3)$$

where  $\mu$  is a small positive constant that controls the step size of the iterative changes in the tap weights which is known as the step size parameter. In real-time applications, since it is not appropriate to perform averaging, the expectation  $E[e(n) U(n-1)]$  is replaced by direct multiplication of the forward prediction error  $e(n)$  and the tap input vector  $U(n-1)$  [Solo and Xuan, 1995; Sesay, 1999]. The update equation is therefore modified as follows:

$$B(n+1) = B(n) + \mu e(n) U(n-1) \quad (4.4)$$

Because of neglecting the calculation of expectation in the update equation (compare Eq.4.3 to Eq.4.4), the values of the tap weights change at each iteration based on imperfect estimates. Therefore, one can expect the adaptive process to be noisy (i.e. it would not follow the true line of the steepest descent on the standard performance curve [Solo and Xuan, 1995]).

In the present study, the design of the FLP filter (Fig.4.2) was tested using MATLAB computer-aided design software (Mathworks, Natick, MA) on an IBM-PC P400 system.

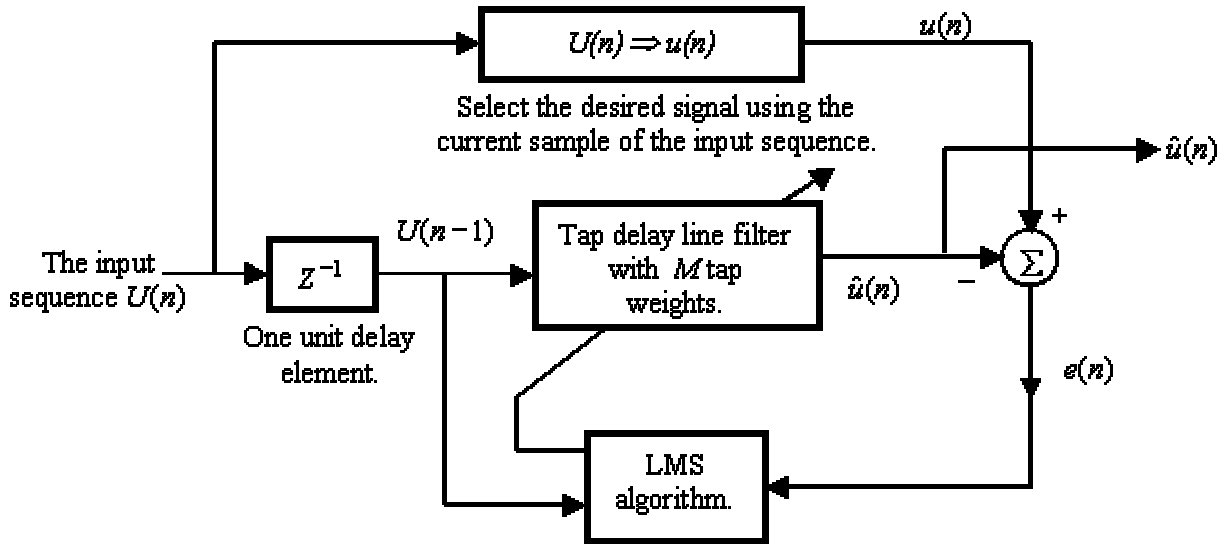


Fig. 4.2. Adaptive adjustment of the tap weights of the FLP filter using the LMS algorithm.

#### 4.2.1. FLP filter performance for noise reduction at the FOG output.

Two parameters control the filter performance, the step size parameter and the filter order. The step size parameter  $\mu$  plays an important role during the design phase of the filter in controlling the convergence and the misadjustment. The convergence is the time required for the cost function to reach its minimal value, which corresponds to the steady state value of the MSEE [Solo and Xuan, 1995]. The misadjustment manifests itself as a deviation from the minimal MSEE.

##### 4.2.1.1. Impact of step size parameter.

The update equation of the filter tap weights (Eq.4.4) implies that large values of the step size parameter  $\mu$  provide fast convergence to the corresponding optimal values. However, this increases the MSEE, and consequently the misadjustment.

Several techniques have been reported to provide variation of the step size parameter while updating the tap weights in order to achieve both fast convergence and

minimal misadjustment [Pazaitis and Constantinides, 1999; Hsu et al., 2000; Dooley and Nandi; 2000]. These techniques employed an MSEE estimator to provide update equation of the step size parameter  $\mu$ . The optimal step size sequence is obtained after minimizing the MSEE with respect to the step size on an iterative basis. Furthermore, in order to guarantee filter stability, it has been shown that the minimum and maximum limits of the step size parameter should be identified and introduced as a constraints to the step size update equation [Dooley and Nandi; 2000]. Unfortunately, these techniques impose additional complexity on the LMS adaptive algorithm if utilized for real-time design of the adaptive FLP filter, because additional calculations are required to determine the optimal step size.

Alternatively, this problem is approached in this research in a more practical way that can be implemented in real-time without affecting the functionality of the LMS adaptive algorithm [Noureldin et al.<sup>f</sup>, 2001]. It has been hypothesized that if a large step size is used during the transient process (i.e. during the first few iterations of the adaptive algorithm) and small step size is used during the convergence period, the LMS adaptive algorithm can provide small MSEE with very fast convergence. Therefore, it is proposed starting the LMS adaptive algorithm with the highest possible value of  $\mu$  to guarantee fast convergence and once the time rate of change of the MSEE becomes extremely small (close to zero),  $\mu$  is changed to its lowest possible value to guarantee the minimal possible MSEE [Noureldin et al.<sup>f</sup>, 2001].

The upper limit of  $\mu$  is particularly critical in order to guarantee the stability of the adaptive algorithm and is theoretically defined as [Solo and Xuan, 1995]:

$$\mu_{\max} = 1/(\lambda_{\max} + \lambda_{\min}) \quad (4.5)$$

where  $\lambda_{\min}$  and  $\lambda_{\max}$  are the minimum and the maximum eigenvalues of the autocorrelation matrix of the tap input vector,  $U(n-1)$ . On the other hand, the lower limit is a very small value larger than zero.

In this study, the FOG output was examined to determine the upper and the lower limits of the step size parameter. The upper limit was determined by the step size value after which the LMS adaptive algorithm diverged and consequently became unstable. The lower limit was chosen as the minimal step size that could track the variation of the

MSEE [Noureldin et al.<sup>f</sup>, 2001]. The upper limit of the step size parameter is constant since it depends on the minimum and maximum eigenvalues of the autocorrelation matrix of the tap input vector which does not depend on either the FOG orientation or the filter order. On the other hand, since the filter order determines the variation of the MSEE during the adaptation process, the lower limit of  $\mu$  has a different value for each filter order. It has been determined that the change of  $\mu$  from its higher to lower limits should take place when the time rate of change of the MSEE became an extremely small value close to zero, which corresponds to approaching the steady state region of the MSEE. In the present study, this condition is equivalent to a reduction of the estimation error  $e(n)$  to one-tenth of its original value [Noureldin et al.<sup>f</sup>, 2001]. Consequently, no additional calculations were required for  $\mu$  and the LMS adaptive algorithm was kept simple, while providing fast convergence and minimal MSEE. A flowchart of the program used to design the optimal tap weights of the FLP filter including the change of  $\mu$  during the adaptation process can be reviewed on Fig.4.3. It should be noted that the step size parameter  $\mu$  does not affect the ARW. It controls only the values of the tap weights and the convergence of the algorithm.

#### **4.2.1.2. Impact of filter order.**

The minimization of ARW depends on the number of delay elements required to store the given set of samples used to perform the prediction process (i.e. the filter order). The increase of the FLP filter order means that the prediction process is performed based on more information about the past samples of the FOG input sequence. Thus, the uncertainty at the FOG output is reduced, and consequently the ARW is minimized. However, the increase in the filter order results in a longer convergence time of the LMS adaptive algorithm. Moreover, the real-time realization of the FLP filter with its tap delay structure necessitates collecting a number of samples of the input sequence equal to the number of tap weights (i.e. filter order) before delivering the output. Therefore, the FLP filter results in a time delay at the FOG output, which increases with the filter order.

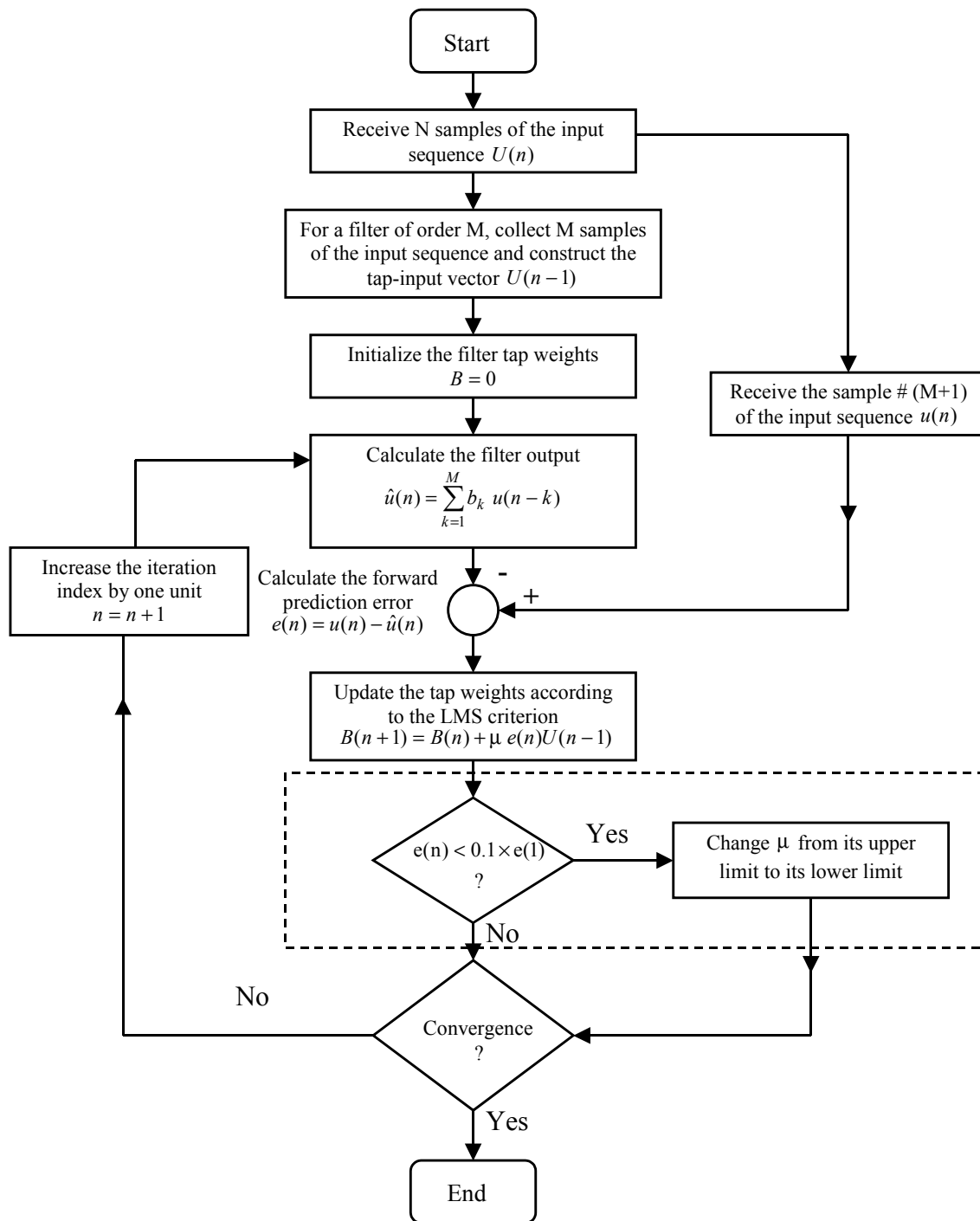


Fig.4.3. Flow chart describing the adaptive process of determining the tap weights of the FLP filter based on the LMS criterion using changeable step size parameter.

#### 4.2.2. Experimental procedure and signal conditioning.

The FLP technique proposed in this chapter was tested using E-Core-2000 FOG (KVH, Orland Park, IL), a low-cost gyroscope with  $7.2^\circ / hr$  drift rate,  $5^\circ / hr / \sqrt{Hz}$  ARW and bandwidth of 100 Hz. The FOG was mounted inside a custom-designed setup capable of providing changes in the FOG orientation in three mutually orthogonal directions [Noureldin et al.<sup>b</sup>, 2000]. The measurements were collected from the FOG while it was oriented entirely in the horizontal plane and its sensitive axis was pointing towards the vertical direction. The FOG measurements were acquired at a sampling rate of 128 Hz using 12-bit analog-to-digital converter (DAQCard-1200, National Instruments, Austin, TX), which was connected to a laptop IBM computer (Compac-433 MHz AMD Processor, Houston, TX) mounted inside the same setup. The design and the implementation of this experimental setup are discussed in Appendix B.

#### 4.2.3. Real-time prediction procedure for the FOG output using the FLP filter

The FLP filter was implemented using a software program to process the FOG output in real-time and reduce the ARW. Since the setup was completely stationary, the FOG was able to monitor the vertical component of the Earth rotation rate given as:

$$\omega_z = \omega^e \sin \varphi \quad (4.6)$$

where  $\omega^e$  is the value of the Earth rotation rate around its spin axis ( $15^\circ / hr$ ) and  $\varphi$  is the latitude angle (Fig.4.4). Since the experiment was performed at a latitude  $\varphi = 51.08^\circ$ , the vertical component of Earth rotation rate was  $11.67^\circ / hr$ . Unfortunately, the ARW at the FOG output ( $5^\circ / hr / \sqrt{Hz}$ ) produced an uncertainty about four times larger than the vertical component of the Earth rotation rate. Therefore, this value of the ARW had to be reduced to at least  $0.1^\circ / hr / \sqrt{Hz}$  in order to achieve an uncertainty of  $1^\circ / hr$  at the FOG output. If the FLP filter were designed to reduce the uncertainty at the FOG output directly with the FOG measurements acquired at 128 Hz, this would have resulted in a very large number of tap weights, which would have corresponded to a very high filter order, thus jeopardizing the real time operation. To avoid this difficulty in both the design

and the implementation of large number of tap delay elements, it has been proposed to average the FOG output within certain time interval before submitting it to the FLP filter [Noureldin et al.<sup>f</sup>, 2001]. This averaging process helps in two aspects. First, it removes some of the high frequency noise components and reduces the uncertainty so that a better FLP filter performance can be achieved. Second, the number of tap weights (i.e. the filter order) required to achieve a certain level of minimization of the ARW at the FOG output becomes significantly less than that when the averaging process is not performed. It has been determined that a 1-second averaging interval is the best compromise for this application [Noureldin et al.<sup>f</sup>, 2001]. With a longer averaging interval, a better FLP filter performance can be achieved but a longer time delay would be produced by the FLP filter at the FOG output. On the other hand, shorter averaging intervals could not reduce the uncertainty at the FOG output to a level that could facilitate the FLP filter in providing the optimal ARW reduction with a reasonable filter order. After performing the averaging process at 1-second data intervals, the output of the filter was determined according to Eq.4.1. As mentioned earlier, the first sample of the reduced ARW sequence at the filter output was determined after collecting a number of the averaged FOG samples equal to the filter order. However, once the first sample was delivered, the filter continued to provide output at the same data rate as the averaged FOG sequence, which in the present case was 1 second.

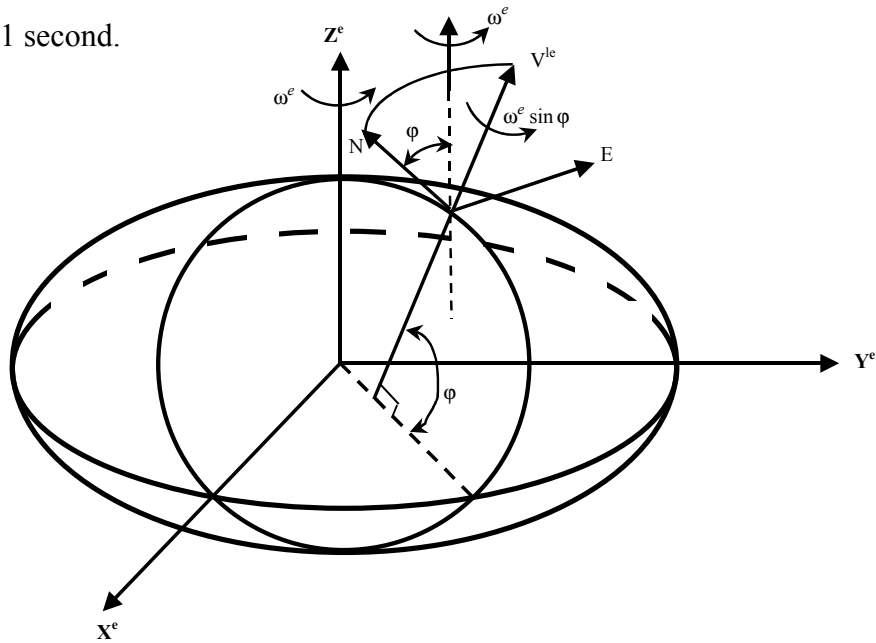


Fig.4.4. Projection of the Earth rotation vector along the vertical direction.

#### 4.2.4. Results.

##### 4.2.4.1. FLP filter design.

The LMS technique discussed earlier (see Fig.4.2 and Fig.4.3) was employed to determine the optimal values of the FLP filter tap weights. The tap weights were initially chosen equal to zero, then were updated according to Eq.4.4. The ARW was calculated as  $4.66^\circ / hr / \sqrt{Hz}$  which produced an uncertainty of  $46.6^\circ / hr$  at the FOG output in the 100-Hz bandwidth. The averaging process over 1-second intervals was able to reduce the noise level at the output to  $4.49^\circ / hr$ , which facilitated the design of the FLP filter. It was determined that a reduction in the FOG measurement uncertainty down to  $1^\circ / hr$  could be achieved with 200 tap weights, if the FOG output signal were averaged at a 1-second interval before submitting it to the FLP filter [Noureldin et al.<sup>f</sup>, 2001]. This number of tap weights was 30 times less than that required when the averaging process was not performed.

The analysis started with 300 tap weights since this number of tap weights delivered a significant reduction of the ARW at the FOG output within reasonable time (5 minutes for 1-Hz data rate). As discussed in section 4.2.1, the upper limit of  $\mu$  is independent of the filter order and it was calculated as  $\mu_{\max} = 0.001$  using Eq.4.5. This value was used for all filter orders. For values of  $\mu > 0.001$ , the LMS algorithm became unstable and consequently could not converge. As a result, the MSEE (i.e. the cost function) continued increasing and the optimal solution could not be reached. The upper limit of the step size parameter was used to ensure fast convergence during the beginning of the adaptation process. The lower limit of  $\mu$  had to be determined separately for each filter order. To do that, the variation of the error in the Earth rotation rate component monitored by the FOG with respect to  $\mu$  is studied and can be depicted on Fig.4.5.a for 300 tap weights and on Fig.4.5.b for 600 tap weights. The lower limit of  $\mu$  (which corresponds to the minimum value of error) was determined as  $1.1 \times 10^{-5}$  for the 300 tap weights and  $2.8 \times 10^{-4}$  for the 600 tap weights, which corresponded to errors in the monitored Earth rotation rate of  $0.0427^\circ / hr$  and  $0.0122^\circ / hr$ , respectively.

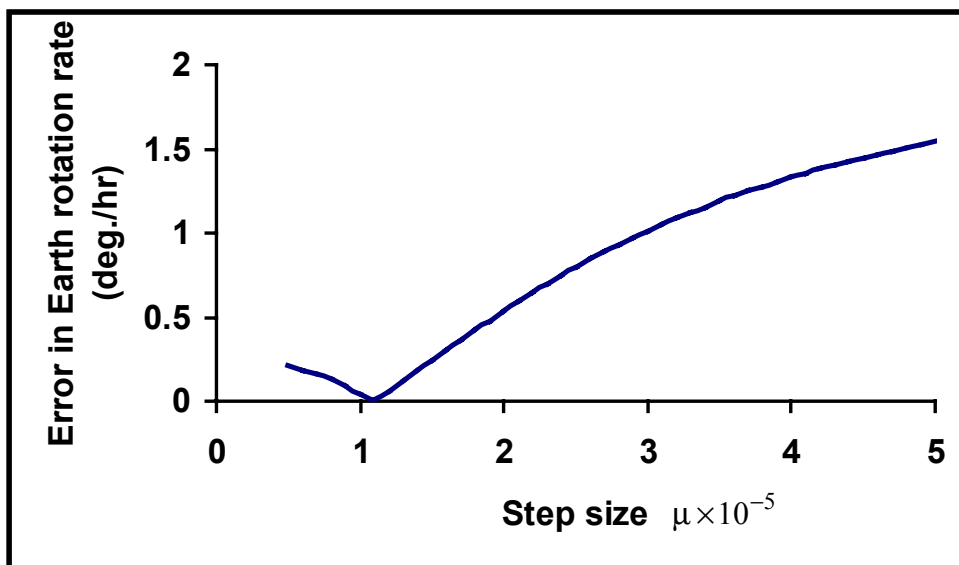


Fig.4.5.a. Variation of the Earth rotation rate error with the step size parameter  $\mu$  for 300-tap weights FLP filter.

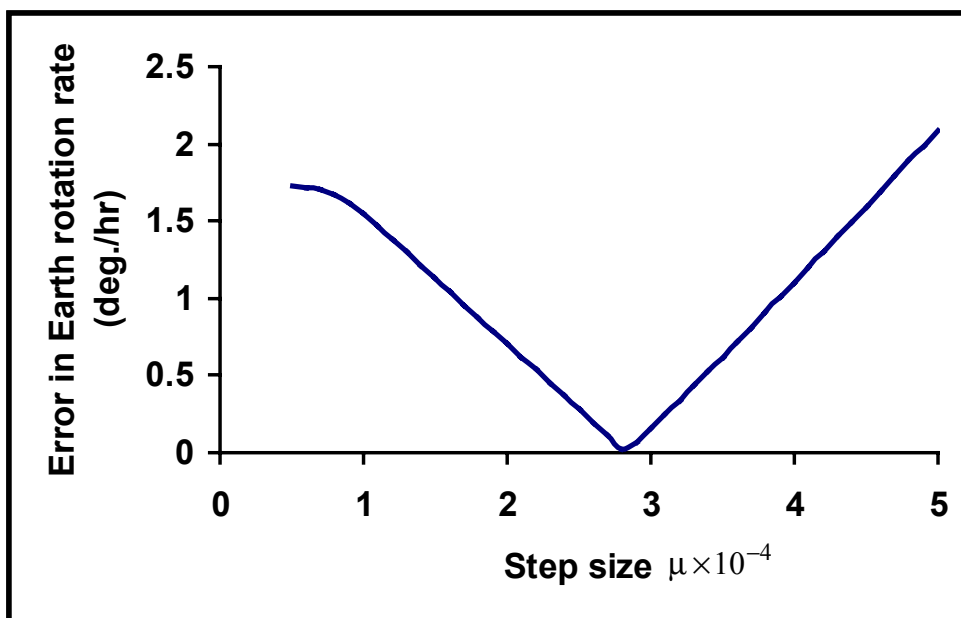


Fig.4.5.b. Variation of the Earth rotation rate error with the step size parameter  $\mu$  for 600-tap weights FLP filter.

#### 4.2.4.2. Performance characteristics of the FLP filter.

The learning curve of an adaptive filter describes the continuous change of the MSEE with time while updating the filter tap weights to establish their optimal values [Widrow and Stearns, 1985]. The learning curves of a FLP filter of 300 tap weights are shown on Fig.4.6 for two values of the step size parameter,  $\mu = 0.00005$  and  $\mu = 0.001$ . For each curve, the step size was kept constant and no changes were performed during the adaptation process. It is evident that the MSEE decreased progressively until reaching a steady state value. Once the learning curve converged to its steady state, the values of the tap weights could no longer change and the learning process was stopped, since no further improvement to the values of the tap weights could be expected after the MSEE reached its steady state value [Widrow et al., 1975; Widrow and Stearns, 1985; Solo and Xuan, 1995].

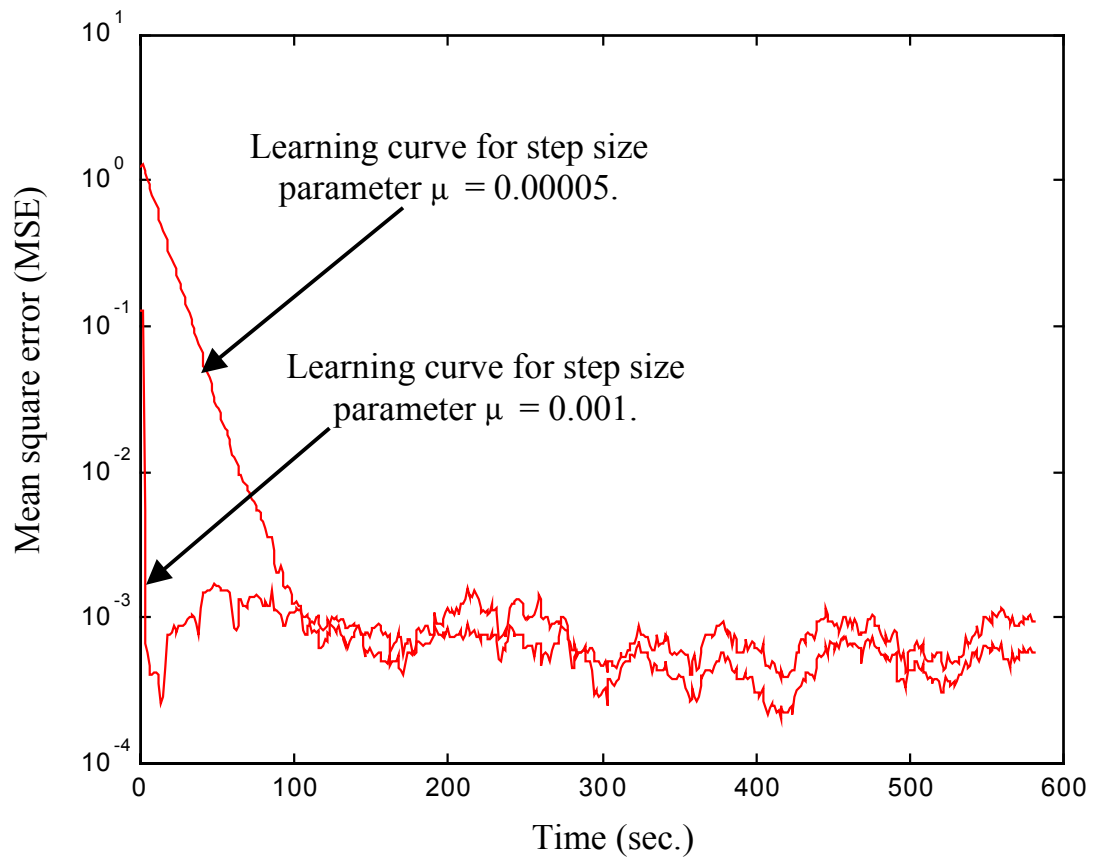


Fig.4.6. Learning curve for a 300 tap weights FLP filter with  $\mu = 0.00005$  and  $\mu = 0.001$ .

The learning curve during the adaptive process was noisy due to the imperfect estimates used to update the filter tap weights (compare Eq.4.3 to Eq.4.4). As shown on Fig.4.6, the learning curve for  $\mu = 0.001$  converged in 6 seconds while that for  $\mu = 0.00005$  converged in about 150 seconds. Although it gave faster convergence, the value of  $\mu = 0.001$  increased the misadjustment between the steady state MSEE and the absolute MMSEE. The steady state values of MSEE were calculated as  $8.5 \times 10^{-4}$  and  $5.7 \times 10^{-4}$  for  $\mu = 0.001$  and  $\mu = 0.00005$ , respectively. This tradeoff was overcome by introducing the change of  $\mu$  from 0.001 (the upper limit of  $\mu$ ) to  $1.1 \times 10^{-5}$  (the lower limit of  $\mu$ ) when the time rate of change of the MSEE became an extremely small value.

Fig.4.7 shows that the MSEE time rate of change approaches zero after 4 seconds of the adaptive process designed with  $\mu = 0.001$ . Since it was determined that this was equivalent to a change of the estimation error  $e(n)$  to one-tenth of its original value (see methods),  $e(n)$  was continuously compared to one-tenth of the original value of the estimation error  $e(1)$  within each iteration of the adaptive algorithm to perform the step size change. This condition was imposed after 6 iterations of the adaptive algorithm for 300-tap weights FLP filter.

Fig.4.8 shows a comparison between the learning curves for the case of constant step size ( $\mu = 0.00005$ ) and for the case of step size change. It is clear that the step size change within the LMS algorithm was capable of providing fast convergence with minimal MSEE ( $4.7 \times 10^{-4}$ ). Furthermore, the error in the computation of the Earth rotation rate component was reduced from  $1.54^\circ / hr$  for constant step size ( $\mu = 0.00005$ ) to  $0.043^\circ / hr$ .

In addition to its dependence on the step size parameter  $\mu$ , the convergence time is also related to the filter order. This relationship was studied while keeping a constant step size during the whole adaptive process and thus explore the effect of the filter order separately, since the lower limit of  $\mu$  depends on the filter order.

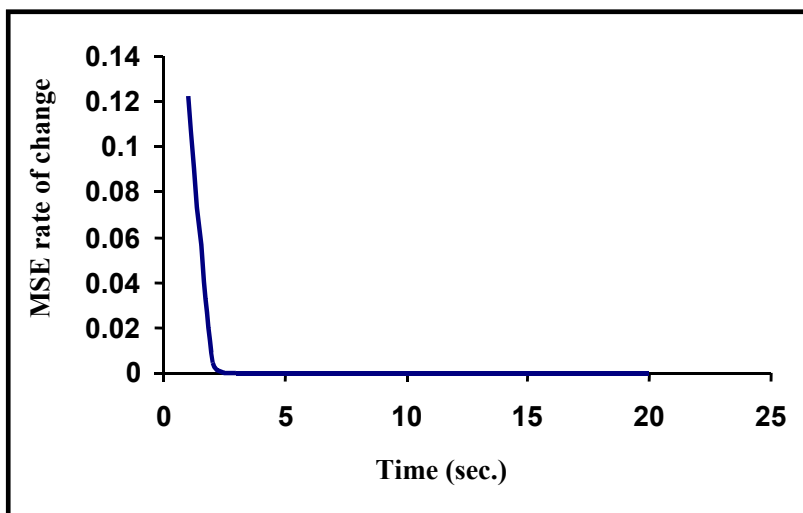


Fig.4.7. Rate of change of the MSE for  $\mu = 0.001$  in a 300-tap weights FLP filter.

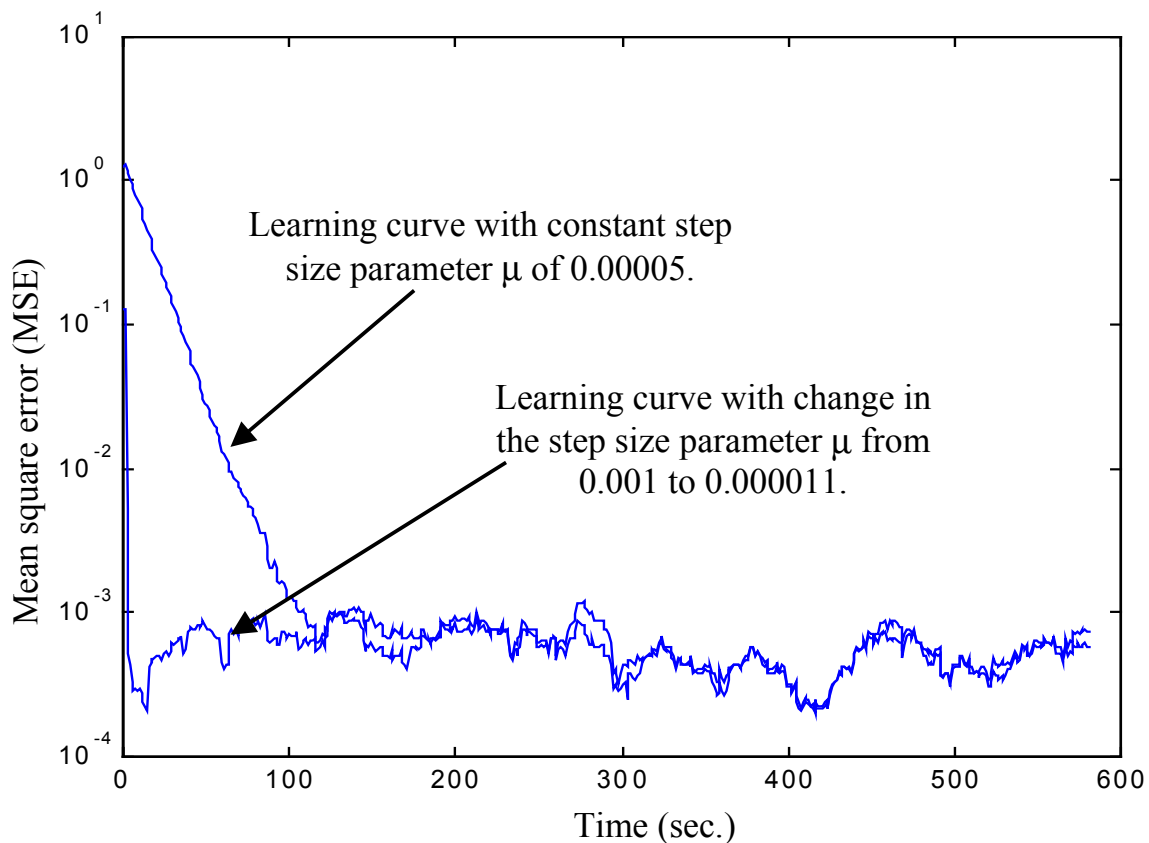


Fig.4.8. Learning curve for 300-tap weights FLP filter with constant step size  $\mu = 0.00005$  and with varying step size from  $\mu = 0.001$  to  $\mu = 1.1 \times 10^{-5}$ .

Fig.4.9 shows the variation of the convergence time with respect to the filter order while keeping constant step size  $\mu = 0.0004$ . It is clear that the adaptive algorithm converges faster for filters of lower orders. However, it should be noted that, due to the design of the FLP filter with the tap delay line structure, the adaptive algorithm cannot start before collecting a number of data samples at least equal to the filter order to construct the input sequence  $U(n-1)$ . For example, with FLP filter of 600 tap weights and data interval of 1 second, the algorithm converged in 7 seconds after collecting 600 seconds of the FOG data. On the other hand, for FLP filter of 300 tap weights, the same algorithm took about 25 seconds to converge after collecting 300 seconds of FOG data. This means that although the higher order filters are more effective in achieving the optimal solution, the adaptive algorithm takes longer time to establish the inputs to the filter tap weights, thus jeopardizing the real-time requirements (see Fig.4.1).

The amplitude spectrum of the FLP filter is shown on Fig.4.10 for different filter orders. The four different cases shown on Fig.4.10 were obtained while changing the step size from  $\mu = 0.001$  to  $\mu = 1.1 \times 10^{-5}$ . The 300-tap weights filter provided a cut-off frequency of 0.0012 Hz while the 50-tap weights filter provided a cut-off frequency of 0.009 Hz. Although this FLP filter with its infra-low cut-off frequency cannot be used for kinematic positioning, it is highly beneficial for alignment processes when the whole setup is completely stationary.

The 600-tap weights filter had a cut-off frequency of 0.000384 Hz. When compared to the 300-tap weights filter, it provided better performance with lower noise level. However, the output of the whole system (the FOG and the FLP filter) was delivered after 600 seconds for the case of 600 tap weights while for the 300-tap weights FLP filter, it took only 300 seconds. Therefore, the designer of the whole system should compromise between the performance and the delay provided by the FLP filter.

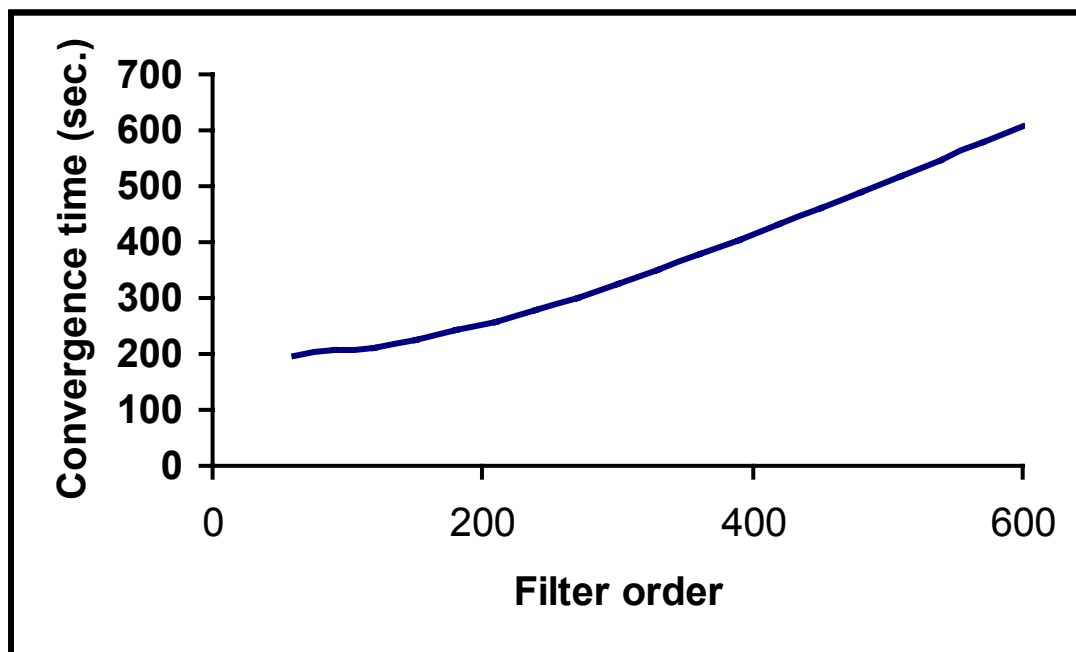


Fig.4.9. Convergence time versus the filter order for a step size parameter  $\mu = 0.0004$ .

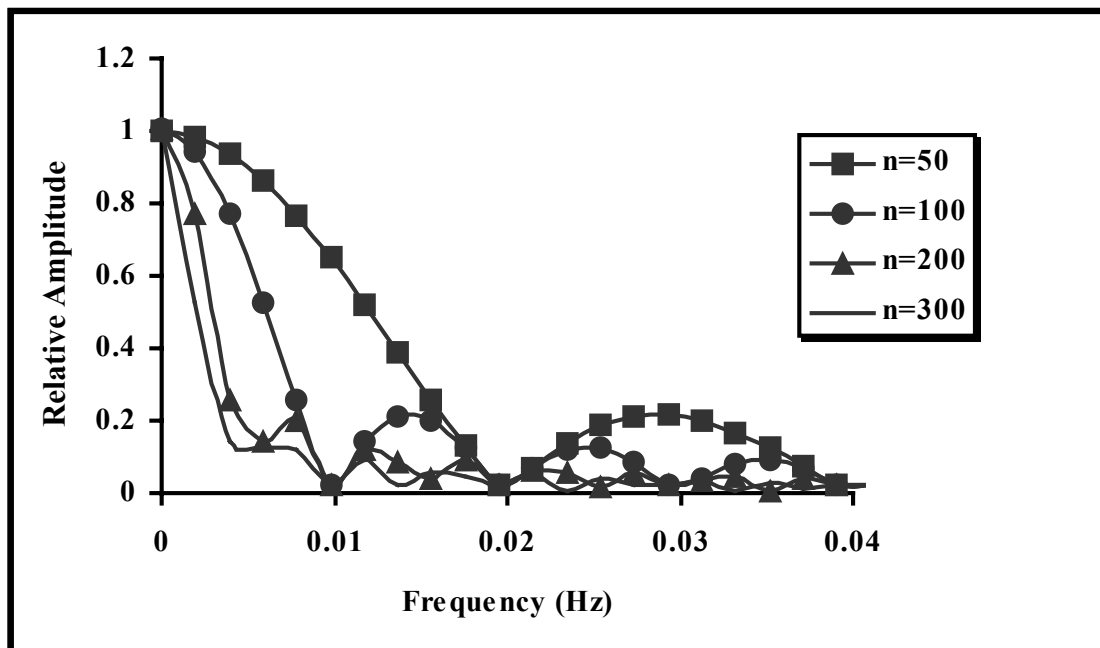


Fig.4.10. Frequency response of FLP filters of different order with  $\mu = 0.0004$ .

#### 4.2.4.3. Impact of the FLP filter on the FOG noise reduction.

After the design phase was completed, the FLP filter was used to reduce the ARW at the FOG output signal and various FLP filters of different orders were tested. Fig.4.11 shows the FOG output after averaging at 1-second intervals, and after processing with FLP filters of 300 and 600 tap weights. The noise level was significantly reduced after processing the FOG output signal by the FLP filter. The 300-tap weights filter reduced the uncertainty at the FOG output to  $0.694^{\circ}/hr$  (i.e. the ARW was brought down to  $0.0694^{\circ}/hr/\sqrt{Hz}$ ) while the 600-tap weights filter reduced the uncertainty to  $0.152^{\circ}/hr$  (i.e. the ARW was brought down to  $0.0152^{\circ}/hr/\sqrt{Hz}$ ). In addition, the ARW values for different orders of the FLP filter were determined (Fig.4.12). There was no variation of the ARW value at the FOG output while changing the step size parameter and the filter order was the only parameter capable of controlling the ARW. The changeable step size parameter, however, significantly reduces the convergence time of the FLP filter tap weights to their optimal values and reduces the error in the monitored Earth rotation rate, thus providing an accurate and efficient stationary surveying procedure with minimum number of FOGs.

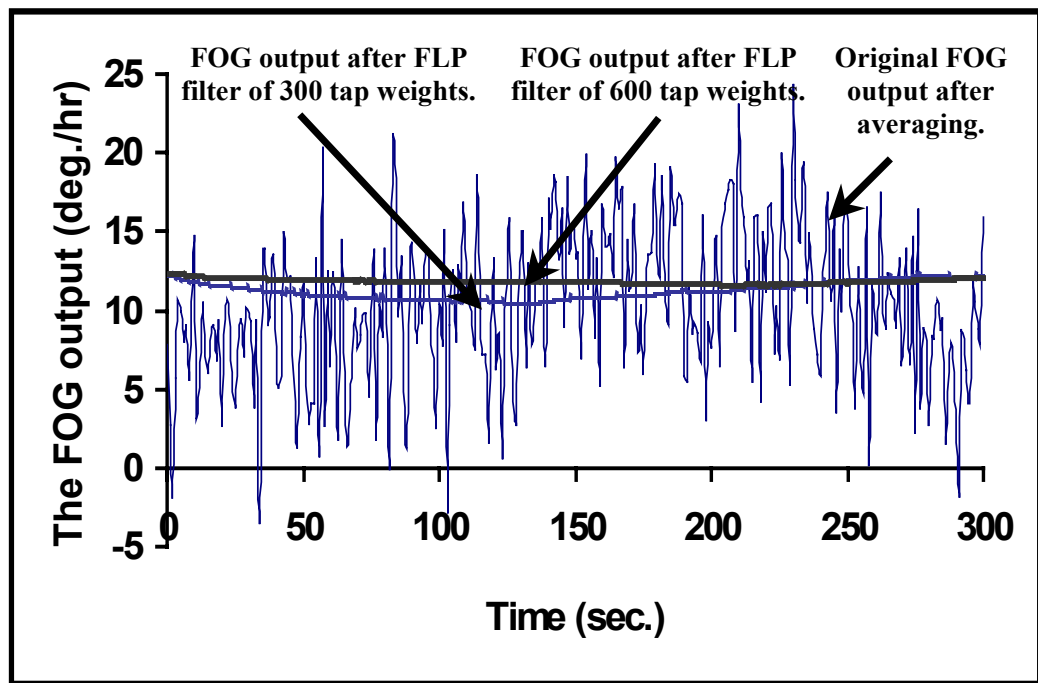


Fig.4.11. FOG output before processing with FLP filters, after processing with a 300-tap weights FLP filter, and after processing with a 600-tap weights FLP filter.

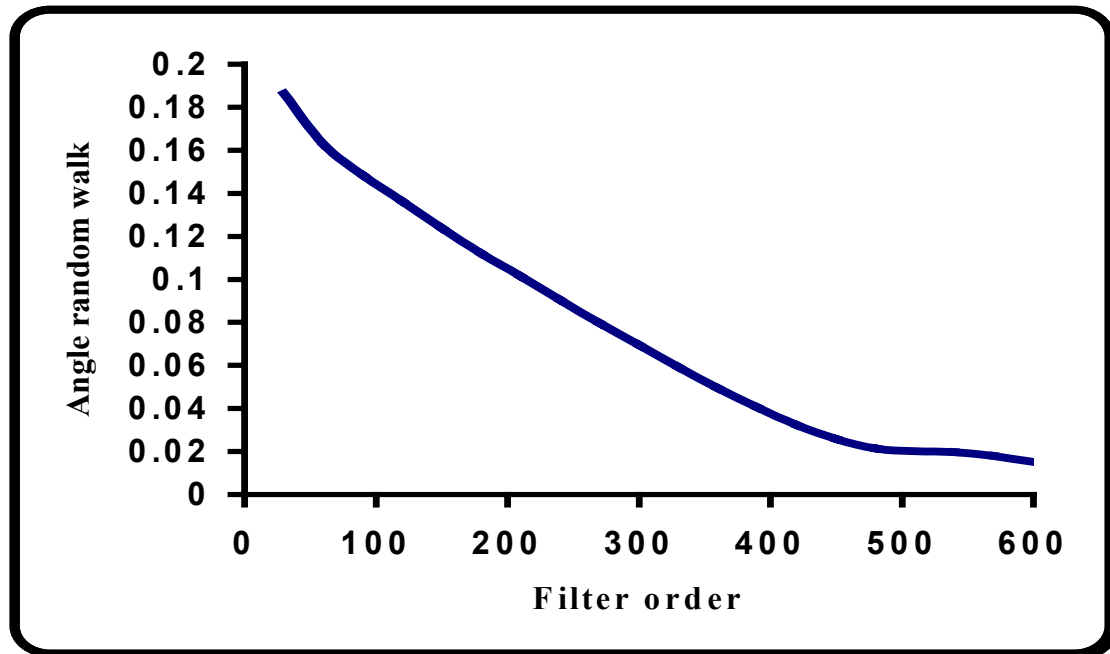


Fig.4.12. Angle random walk ( $^{\circ} / hr / \sqrt{Hz}$ ) versus the filter order.

#### 4.2.5. Applications and limitations of FLP noise reduction techniques.

Section 4.2 introduces a new technique for limiting the FOG output uncertainty based on the FLP technology. The technique utilizes the LMS adaptive algorithm for designing a FLP tap delay line filter, but suggests a changeable step size parameter during the adaptation process to ensure fast convergence of the algorithm while providing minimal error of the monitored Earth rotation rate. This technique can be beneficial in INS applications that employ reduced number of FOGs to determine the attitude angles at predetermined surveying stations. In addition, the same procedure can be applied to the conventional three-axis FOG structure. Since it provides fast convergence and significant ARW reduction, the proposed method can successfully replace the other existing filtering techniques. Moreover, this method is complementary to the hardware efforts that have been introduced to limit the uncertainties at the FOG output.

Since the FLP technique is utilized to predict the Earth rotation rate component at the FOG output signal, the noise component would be completely unpredictable [Haykin, 1996]. Consequently, the statistical properties of the noise component at the FOG output

should follow that of white noise. This implies that the autocorrelation function of the FOG noise sequence can be approximated by an impulse function [Brown and Hwang, 1992]. Therefore, if the noise component at the FOG output is correlated over time, the FLP technique would fail to accurately predict the Earth rotation rate component since part of the correlated noise component would be predicted at the output as well. As discussed earlier in this chapter, tactical grade low cost FOGs have relatively high output uncertainties with the output noise usually characterized as a white sequence. However, the noise component at the output of navigational grade FOGs is time-correlated and its autocorrelation function follows random walk or 1<sup>st</sup> or 2<sup>nd</sup> order Gauss-Markov processes. The FLP technique cannot be applied for these types of FOGs and some other technique not involving prediction should be utilized. Such technique is discussed in the following section.

### **4.3. Noise reduction of FOG output signal using transversal filter designed by known Earth rotation rate component in the reference channel.**

#### **4.3.1. Filter design.**

In order to reduce FOG measurement uncertainties, a transversal tap-delay filter of the same structure as discussed in the previous section (see Fig.4.1) was utilized at the FOG output. The optimal values of the filter tap weights were chosen to minimize the mean-square value of the estimation error  $e(n)$  between the filter output  $y(n)$  and a certain desired response  $d(n)$  using the least-mean squares (LMS) technique (Fig.4.13) [Widrow and Stearns, 1985]. The desired response  $d(n)$  is the Earth rotation rate component along the vertical direction, which is known at any given latitude angle. Therefore, during the design (learning) process of the filter, while the LMS criterion is applied to determine the optimal values of the tap weights, the FOG is mounted on the horizontal plane with its sensitive axis along the vertical direction. The error  $e(n)$  between the filter output  $y(n)$  and the desired response  $d(n)$  is processed by the LMS algorithm to update the values of the filter tap weights toward their optimal values.

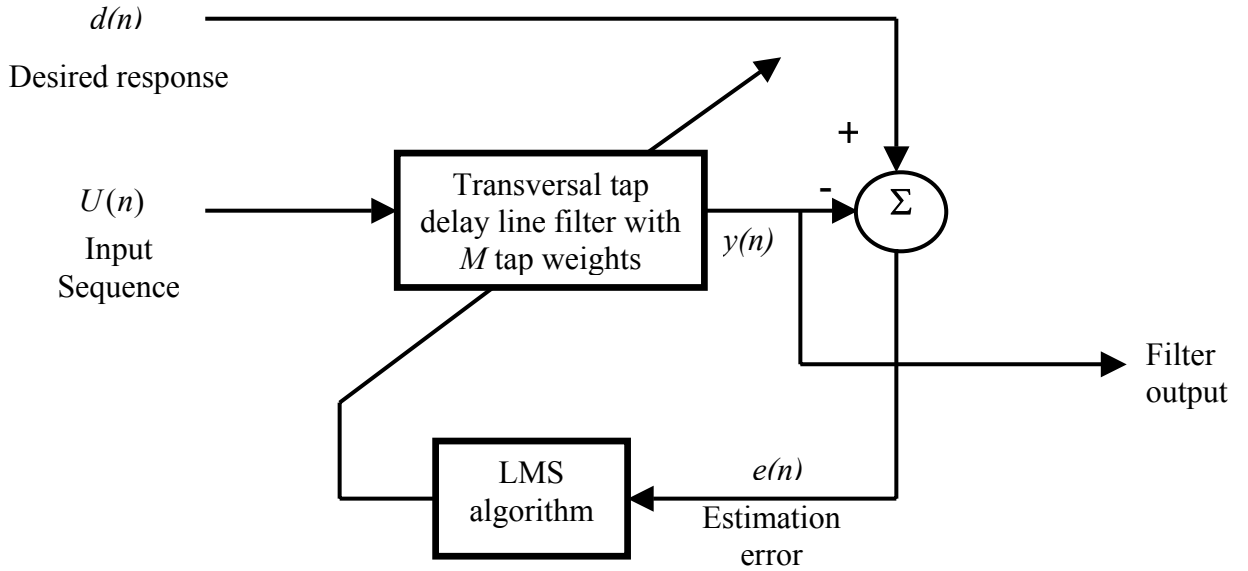


Fig.4.13. Adaptive adjustment of the tap weights of the transversal filter using the LMS algorithm.

The update equation of the filter tap weights is given as follows:

$$B(n+1) = B(n) + \mu e(n)U(n) \quad (4.7)$$

where  $B(n)$  and  $B(n+1)$  are the vectors of the filter tap weights at time  $n$  and time  $n+1$ , respectively, and  $U(n)$  is the vector of the input sequence of the filter defined as:

$$U(n) = (u(n) \quad u(n-1) \quad \dots \quad u(n-M+1))^T \quad (4.8)$$

where  $M$  is the filter order. It can be noticed that this update equation is slightly different from the one employed for the design of the FLP filter (compare Eq.4.4 to Eq.4.7). While the FLP technique utilizes past samples of the FOG output signal to predict the present sample, the technique presented in this section includes the present sample of the FOG output into the input sequence  $U(n)$ , in order to give the appropriate estimate at the filter output [Noureldin et al.<sup>c</sup>, 2001].

The first sample of the filter output  $y(n)$  was obtained after collecting a number of input samples equal to the number of tap weights. The filter output was then compared with the desired response  $d(n)$ , and the error between them was applied to the tap weights update equation until the MSEE reached its steady-state value, and the filter tap weights reached their optimal values. The changeable step size criterion introduced for the FLP

filter design is utilized during the learning process of the transversal filter shown on Fig.4.13 as well.

#### **4.3.2. Filter performance at the FOG output**

During station-based surveying processes, the optimal tap weights determined during the learning process are utilized to reduce the FOG output uncertainty. Unlike the FLP filter, the values of these tap weights are kept the same for different surveying locations. This implies that these values will not change with respect to the dynamics existing at such surveying location. However, they have the advantage of filtering out either color or white noise components at the FOG output.

The minimization of FOG output uncertainties depends on the order of the filter used. Higher filter orders provide lower cutoff frequencies, thus reducing the uncertainty at the FOG output. However, the real-time implementation of the filter, with its tap delay structure, necessitates collecting a number of samples from the input sequence equal to the number of tap weights (i.e. the filter order) before delivering the output. Therefore, this transversal filter results in a time delay at the FOG output, which increases with the filter order. Although the same time delay exists while utilizing the FLP filter, no further time delay is required for determining the optimal tap weights of the transversal filter, which is pre-designed with known Earth rotation rate at the reference channel during the learning process. This time delay is necessary for the FLP filters to determine their optimal tap weights during the prediction process.

#### **4.3.3. Experimental procedure and signal conditioning.**

The technique of designing a transversal filter with known Earth rotation rate at the reference channel was applied to two different types of optical gyroscopes. The first type was a tactical grade FOG (E-Core-2000, KVH, Orland Park, IL) which was employed to test the FLP filter performance. The second type was a navigational grade optical gyroscope (LTN90-100, Litton, Woodland Hills, CA). The LTN90-100 is an inertial measurement unit, which incorporates three-axis accelerometers and three-axis optical gyroscopes mounted in three mutually orthogonal directions. Although the optical

gyroscopes utilized in this unit are of ring laser type, they have the same performance characteristics as FOGs [Merhav, 1993; Lefevre, 1993]. These gyros differ from the FOGs in the way the laser beam is propagating inside, while the drift and the noise behaviors are exactly the same [Lefevre, 1993].

In these experiments, the signal conditioning procedure discussed in section 4.2.2 was applied for both the E-Core-2000 and one of the gyros of the LTN90-100. The filter was designed with the gyros mounted on the horizontal plane. The same number and values of the tap weights were used to filter out the FOG output noise at several other orientations, thus testing the performance of the proposed filtering technique at various FOG positions.

#### **4.3.4. Results.**

##### **4.3.4.1. E-Core-2000 results.**

The filter designed during the learning process with known Earth rotation rate at the reference channel was utilized to reduce the FOG output uncertainty. The characteristics of this filter were quite similar to the one designed using the FLP method including the cutoff frequencies ( $0.0012\text{ Hz}$  using 300 tap weights and  $0.000384\text{ Hz}$  using 600 tap weights) and the reduction of the levels of uncertainties ( $0.694^\circ/\text{hr}$  with 300 tap weights and  $0.152^\circ/\text{hr}$  with 600 tap weights).

At an orientation corresponding to  $9.629^\circ/\text{hr}$  Earth rotation rate component along the FOG sensitive axis (pitch, roll and azimuth angles of about  $10^\circ$ ,  $10^\circ$  and  $20^\circ$ , respectively), a filter with 300 tap weights was capable of reducing the FOG output uncertainty from  $4.5871^\circ/\text{hr}$  to  $0.4424^\circ/\text{hr}$  as shown on Fig.4.14. In addition, the drift of the FOG output signal over time from  $8.8435^\circ/\text{hr}$  to  $10.307^\circ/\text{hr}$  could be observed. This indicated that the maximum estimation error of this Earth rotation rate component is  $0.7855^\circ/\text{hr}$ .

A 600 tap-weight filter was utilized at the FOG output while monitoring the Earth rotation rate at an orientation of  $20^\circ$  pitch,  $20^\circ$  roll and  $41^\circ$  azimuth (corresponding to Earth rotation rate component of  $5.92^\circ/\text{hr}$ ). Fig. 4.15 shows the FOG output before and after processing with the 600 tap weights. This filter was able to limit the FOG output

uncertainty from  $4.5871^{\circ}/hr$  to  $0.2034^{\circ}/hr$ , thus monitoring the Earth rotation rate component along the FOG sensitive axis with errors of less than  $0.6^{\circ}/hr$ .

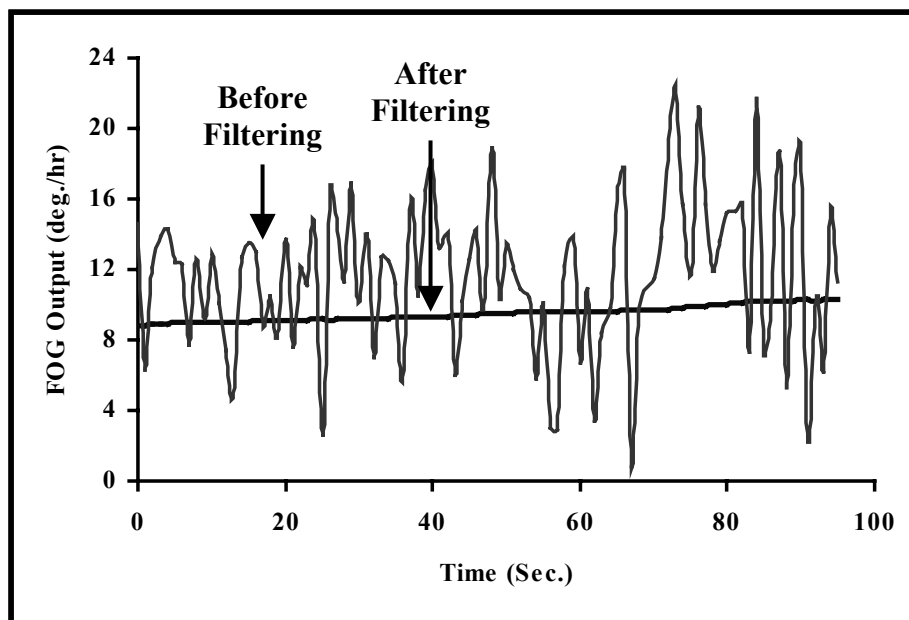


Fig.4.14. The E-Core-2000 output signal before and after filtering with 300 tap weights at an orientation of  $10^{\circ}$  pitch,  $10^{\circ}$  roll and  $20^{\circ}$  azimuth.

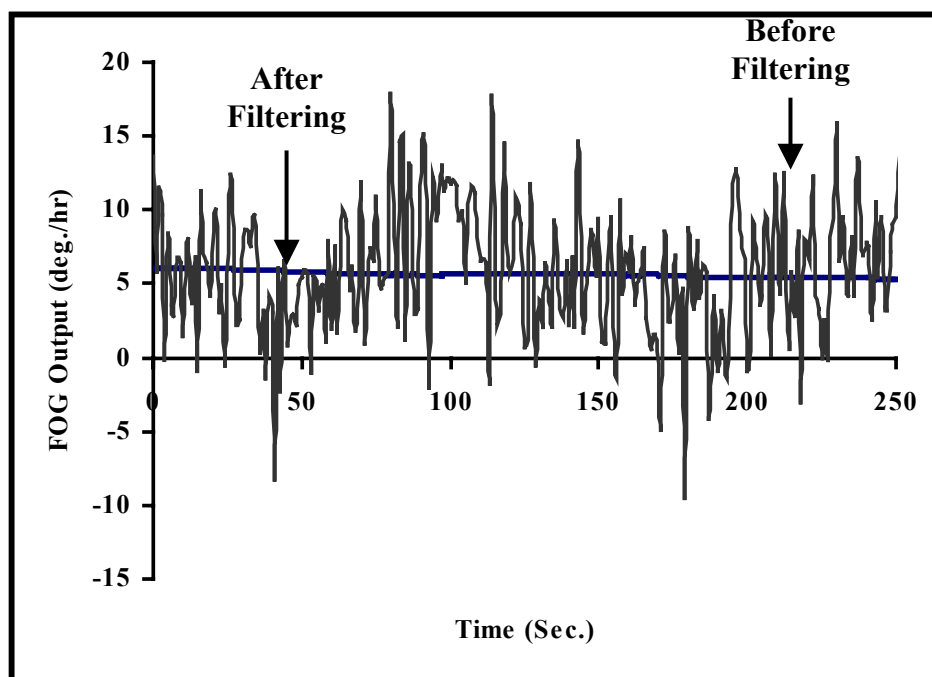


Fig.4.15. The E-Core-2000 output signal before and after filtering with 600 tap weights at an orientation of  $20^{\circ}$  pitch,  $20^{\circ}$  roll and  $41^{\circ}$  azimuth.

#### 4.3.4.2. LTN90-100 results.

Since the LTN90-100 is a navigational grade unit, the output uncertainties are smaller than these of the E-Core-2000. Thus, it was estimated that a transversal filter with 100 tap weights would be enough to achieve proper reduction of the output uncertainty. The learning process of the filter was performed while the LTN90-100 was mounted at  $-0.5248^\circ$  pitch,  $0.4716^\circ$  roll and  $95.1698^\circ$  azimuth, which corresponds to Earth rotation component of  $11.6152^\circ/hr$  along the sensitive axis of the vertical gyro. Fig.4.16 shows the learning curve for different values of the step size parameter  $\mu$ . The changeable step size criterion (implemented during the learning process) determined that  $\mu = 2 \times 10^{-5}$  was the optimal step size that corresponded to the minimal MSE (see Fig.4.16). It should be noted that this optimal step size ( $\mu = 2 \times 10^{-5}$ ) was only suitable for the 100 tap-weight filter and the LTN90-100 gyro output sequence.

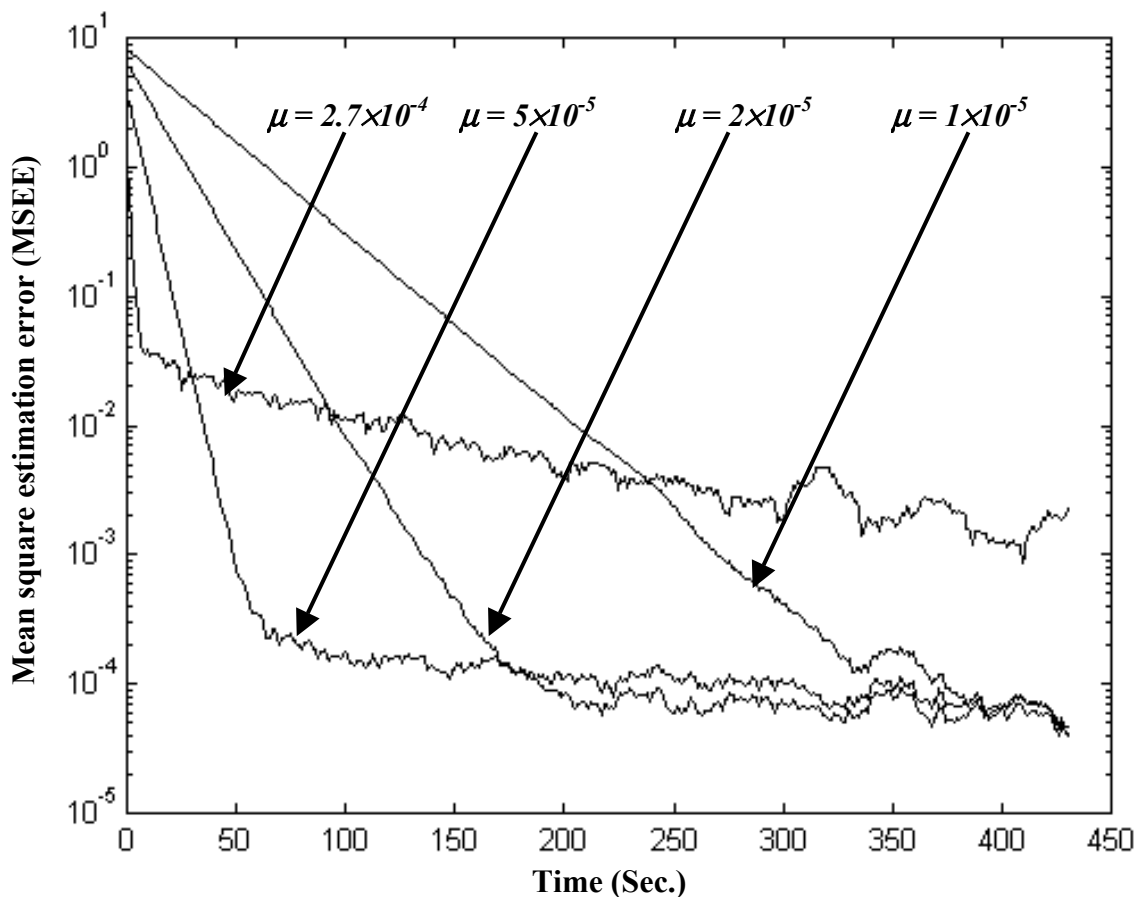


Fig.4.16. Learning curves of a transversal filter of 100 tap weights at the output of LTN90-100 vertical gyro with respect to different step size parameters  $\mu$ .

The 100 tap-weights filter was employed to process the gyro measurements at different orientations in order to reduce the measurement uncertainties and to facilitate monitoring of the Earth rotation component at certain orientation using a single gyro. The Earth rotation rate estimated at each orientation was compared to the corresponding reference value obtained after processing the same measurements by KINGSPAD™ software (University of Calgary, Department of Geomatics Engineering). Fig.4.17 shows the filtered output sequence and the reference value for the measurements obtained at  $-0.2914^\circ$  pitch,  $0.8429^\circ$  roll and  $5.8528^\circ$  azimuth. It was determined that after the averaging over 200-second period shown on Fig.4.17, the Earth rotation rate would be estimated with an error of about  $0.045^\circ/hr$  when compared to the reference value. In addition, the filtered output sequence had an uncertainty of  $0.0558^\circ/hr$ .

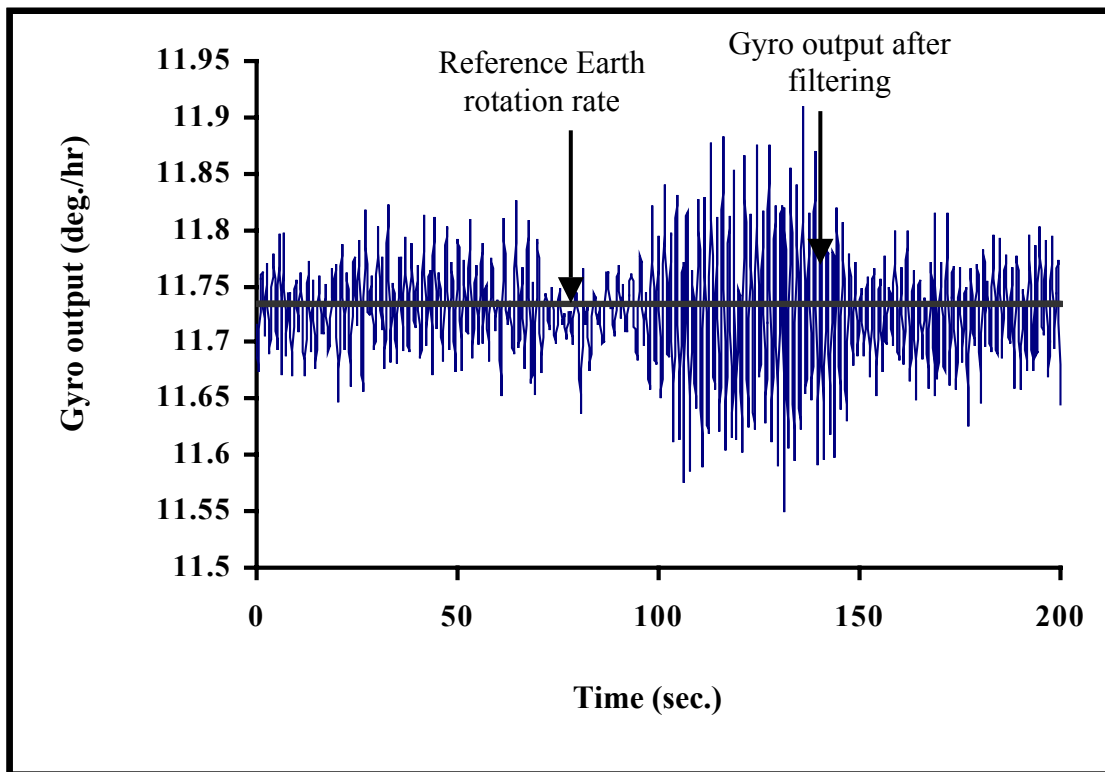


Fig.4.17. The Gyro output sequence after filtering with 100 tap weights at orientation of  $-0.2914^\circ$  pitch,  $0.8429^\circ$  roll and  $5.8528^\circ$  azimuth.

The same number and values of the tap weights were used at 3 different sets of experiments. Each experiment involved collecting stationary data at certain orientation for 5 minutes. During each set of experiments the LTN90-100 was kept pointing towards certain azimuth direction while rotating the setup to give different pitch and/or roll angles. The LTN90-100 was pointing close to the East direction (about  $95^\circ$  azimuth) during the first set of experiments, close to the North direction (about  $6^\circ$  azimuth) during the second set and at the mid way between the East and the North directions (about  $55^\circ$  azimuth) during the third set. The gyro sequence after filtering was compared in each experiment with the reference value provided by KINGSPAD<sup>TM</sup> to determine the estimation error. The results of each set of experiments are presented on Figs.4.18, 4.19 and 4.20, which show the estimation error and the output uncertainty. It can be concluded that although the output uncertainty varies slightly from one experiment to another, the estimation error of the Earth rotation rate component increases considerably over time for each set of experiments.

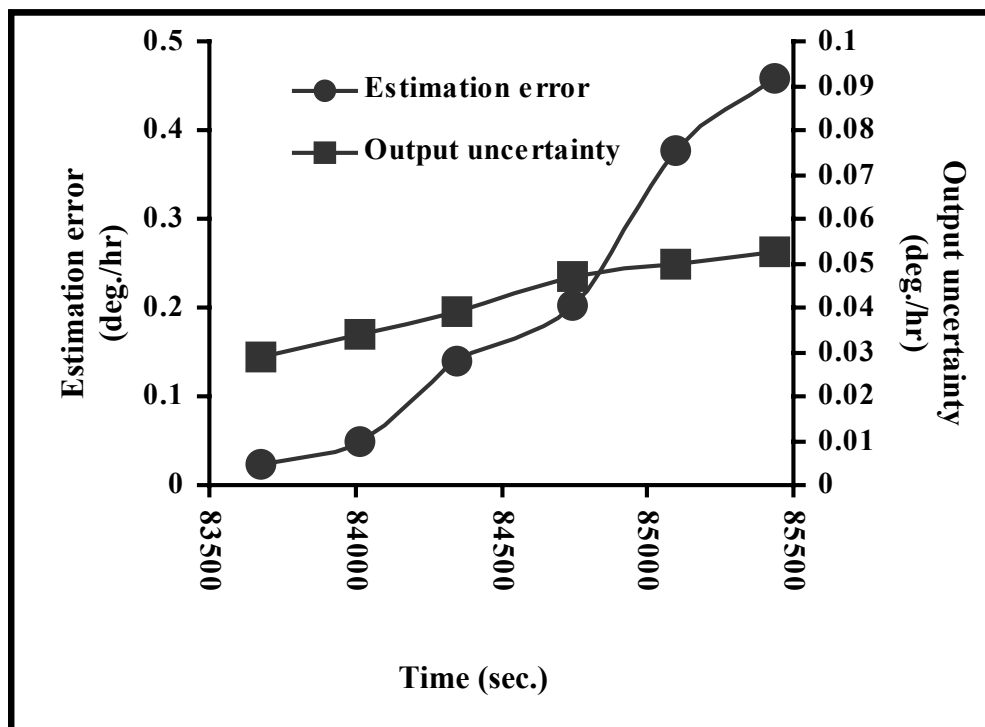


Fig.4.18. Estimation error of the Earth rotation rate component and the output uncertainty for the first set of data.

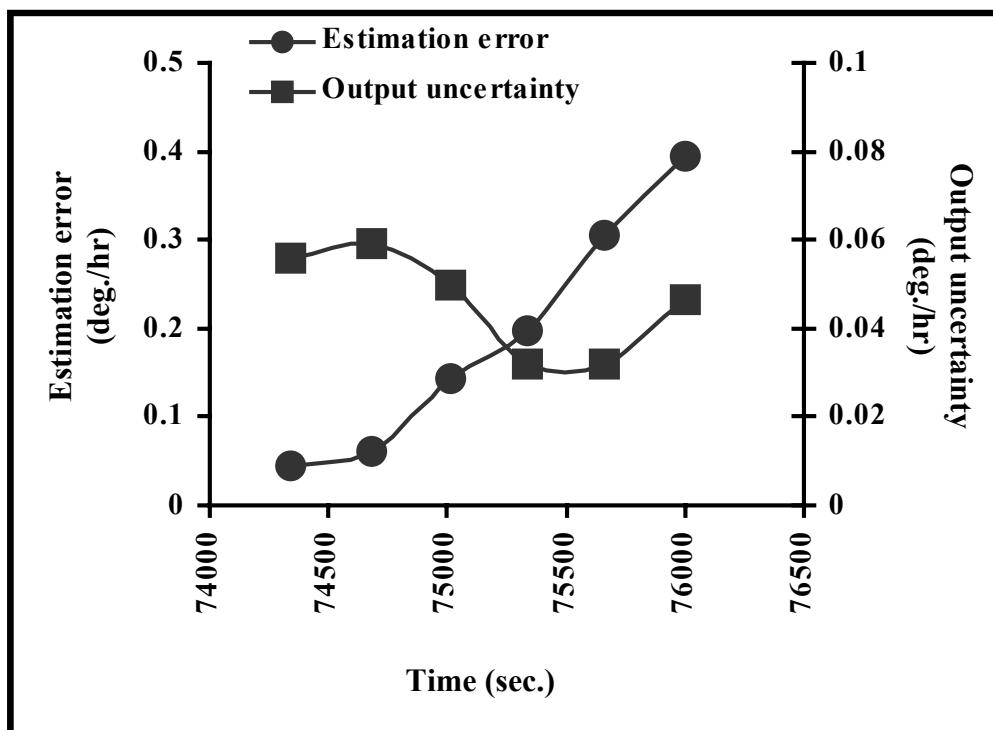


Fig.4.19. Estimation error of the Earth rotation rate component and the output uncertainty for the second set of data.

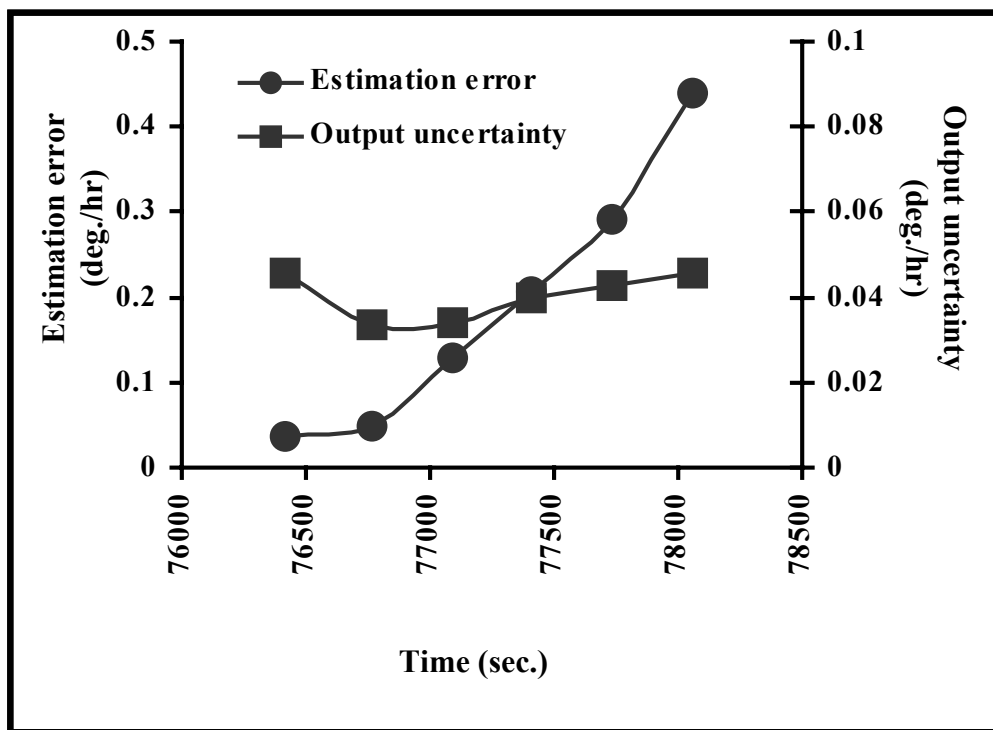


Fig.4.20. Estimation error of the Earth rotation rate component and the output uncertainty for the third set of data.

The estimation error calculated in each experiment had two components. The first component was due to the MSEE of the LMS algorithm, which might not achieve the absolute theoretical minimal value. The second component was the gyro bias error, which included the run-to-run bias and the bias drift over time, which affected the long-term performance of the overall surveying system. This presents a powerful case for the utilization of navigational grade inertial sensors. However, despite the utilization of LTN90-100, Figures 4.18, 4.19 and 4.20 show that the estimation error changed from about  $0.04^\circ/hr$  to about  $0.4^\circ/hr$  within less than 40 minutes. In fact, another factor is responsible for this error growth. The LTN90-100 was not designed to perform at high inclinations similar to the ones in this experimental procedure. Consequently some other error sources most likely participated in the estimation error.

On the other hand, the output uncertainty is controlled by the filter order. Filters of 100 tap weights introduce a time delay of 100 seconds before delivering the filtered output. Since the desirable time of station-based surveying process at any orientation is 300 seconds (i.e. 5 minutes), the remaining 200 seconds were used for precise computation of the attitude angles based on some applied optimal estimation techniques to compensate for the effect of the drift of the inertial sensors.

#### **4.4. Comparison between the proposed de-noising techniques.**

The two de-noising techniques presented in this chapter employ transversal tap delay line filter to limit the uncertainty at the FOG output. In addition, they are similar in utilizing the LMS technique for determining the optimal values of the filter tap weights. The changeable step size criterion was also applied successfully for the two techniques. However, these two techniques differ both in the design and the application of the transversal filter:

1. Filter design: The design of the FLP filter is repeated at each surveying station and the filter tap weights might have different values at each station. In addition, the number of the tap weights might be changed from one station to another depending on the desirable level of uncertainty reduction and the time allowed for the station-based surveying process. Alternatively, the other filter

is designed with a known Earth rotation rate component in the reference channel. Consequently, the number of tap-weights and their values would remain the same in all surveying stations. Although this saves the time required by the learning process to achieve the optimal tap weights at each surveying station, the different dynamics existing at different surveying stations might not be accounted for.

2. Application: The filter designed with a known Earth rotation rate in the reference channel has the advantage of being applicable for both navigational and tactical grade inertial sensors. The application of the FLP filter is only limited to tactical grade (low cost) inertial sensors with their output uncertainty characterized as white noise. However, the FLP filter has the advantage of flexible changes in the number of tap weights between different surveying stations, thus giving the opportunity of controlling the level of uncertainty reduction.

#### **4.5. Conclusion.**

During the last decade, FOGs have been employed in various INS applications [Bowser et al., 1996]. Due to their compactness, reliability and high environmental insensitivity, they have also been suggested for MWD applications in oil-well drilling [Noureldin et al.<sup>c</sup>, 2000]. However, the ARW limits the FOG accuracy in the computation of the initial attitude angles during INS alignment processes. In addition, some applications require monitoring of the attitude angles at predetermined surveying points while the whole system is stationary [Noureldin et al.<sup>d,e</sup>, 2001]. The existing systems incorporate three-axis FOGs and three-axis accelerometers mounted in three mutually orthogonal directions to determine the attitude angles [Titterton and Weston, 1997, Merhav, 1993]. In these cases, the uncertainties in the values of the attitude angles due to the ARW of the FOG are removed with Kalman filtering techniques [Salychev, 1998]. In some applications, due to the limited space available for inertial sensors, one or two mutually orthogonal FOGs can be incorporated with three-axis accelerometers inside the INS instead of the conventional three-axis structure [Noureldin et al.<sup>d,e</sup>, 2001]. In such

situations, it is usually not possible to calculate the attitude angles before removing the measurement uncertainties [Noureldin et al.<sup>b</sup>, 2000]. Thus, the ARW should be as small as possible in order to reduce the uncertainty in the FOG measurements, since these uncertainties can jeopardize the computation of the attitude angles during the alignment processes.

This chapter introduced two techniques for ARW minimization based on the adaptive filtering technology. Both techniques used the LMS adaptive algorithm for designing a tap delay line filter, but suggested the utilization of a changeable step size parameter during the adaptation process to ensure fast convergence of the algorithm while providing minimal error of the monitored Earth rotation rate.

The proposed technique significantly reduced FOG measurement uncertainty while monitoring the Earth rotation rate. Thus, a single FOG installed along the forward direction of an INS could precisely monitor the component of the Earth rotation rate along its sensitive axis. Consequently, the deviation from the North direction (i.e. the azimuth angle) could be determined accurately [Noureldin et al.<sup>d,e</sup>, 2001]. The other two attitude angles (the pitch and the roll) were determined by monitoring the gravity components along three mutually orthogonal directions employing three-axis accelerometers. Since the noise behavior of the accelerometers is quite similar to that of the FOG, the same filtering approaches could be employed to provide precise monitoring of both the pitch and the roll angles. Thus, a single FOG system can determine the platform orientation at predetermined surveying points in applications that cannot accommodate a complete INS with its three-axis structure because of the limited space (e.g. downhole drilling applications for the oil industry).

The techniques introduced in this chapter provide several advantages over the existing methods that are based predominantly on Kalman filtering. First, the tap delay line structure of the filter is simple for design and implementation in real-time processes. Second, unlike Kalman-filter based techniques, the noise is removed from the measurements before calculating the attitude angles, which is necessary to avoid computational instability in single FOG systems. Third, the proposed technique does not

impose any restrictions on the statistical properties of the random noise component associated with the FOG output.

Although the de-noising techniques presented in this chapter are beneficial in INS applications that employ a reduced number of FOGs to determine the attitude angles at predetermined surveying points, the same procedure could be applied to the conventional three-axis FOG structure. Since they provide fast convergence and significant ARW reduction, the proposed methods can successfully replace the other existing filtering techniques. Moreover, these methods are complementary to the hardware efforts that have been introduced to limit the uncertainties at the FOG output [Killing, 1994; Huang et al., 1999].

## **CHAPTER FIVE SINGLE-FOG MWD SURVEYING SYSTEM**

With the utilization of FOGs in MWD surveying processes, the technology of inertial navigation is suggested as a replacement of the present magnetic surveying systems [Noureldin et al.<sup>a</sup>, 2000]. Inertial navigation systems (INS) determine the position, the velocity and the orientation of a moving body in three-dimensional space by integrating the measured components of the acceleration (provided by accelerometers) and the angular velocity (provided by gyroscopes) [Schwarz and Wei, 1990; Titterton and Weston, 1997]. Conventional INS incorporates three-axis gyroscopes and three-axis accelerometers arranged in three mutually orthogonal directions. Due to the limited space available downhole, this chapter proposes a novel INS-based surveying technique based on a single FOG and three-axis accelerometers.

The aim of this chapter is to give an overview of inertial navigation techniques and to discuss the development of single-FOG surveying methodologies.

### **5.1. Overview of inertial navigation systems (INS).**

The operation of an INS is based on processing the inertial sensor measurements received as inputs and delivering a set of navigation parameters (position, velocity and attitude) of the moving platform as outputs [Titterton and Weston, 1997]. In general, these navigation parameters are determined with respect to a certain reference frame. The accelerometers are attached to the moving platform to monitor its acceleration, including the effect of gravity, in three mutually orthogonal directions. The time integral of each acceleration component gives a continuous estimate of the corresponding velocity component of the platform, provided that the initial velocities are known. A second integration yields the position with respect to a known starting point. Since platforms are not necessarily moving in a straight line, it is necessary to detect the rotational motion in addition to the translational motion. The gyroscope measurements are utilized for this purpose. The angular orientation (attitude) of the platform is determined by integrating the gyroscope measurements, provided that the initial attitude angles (the pitch, the roll and the azimuth) are known [Titterton and Weston, 1997]. Obviously, inertial navigation

is fundamentally dependant on an accurate knowledge of the initial position, velocity and attitude of the platform prior to the start of navigation.

In most applications the axis set defined by the sensitive axes of the inertial sensors is made coincident with the axes of the moving platform in which the sensors are mounted [Titterton and Weston, 1997]. These axes are usually known as the body frame. The gyroscope measurements are used to determine the platform attitude with respect to the reference frame within which it is required to navigate. The attitude angles are then used to transform the accelerometer measurements from the body frame into the reference frame [Titterton and Weston, 1997]. The resolved accelerations can then be integrated twice to give the platform velocity and position in the reference frame.

It should be noted that the accelerometers cannot separate the total platform acceleration from the one caused by the presence of gravity. In fact, accelerometers provide the sum of platform acceleration in space and the acceleration due to gravitational attraction [Titterton and Weston, 1997]. Hence, the accelerometer measurements must be combined with the knowledge of the gravitational field of the moving platform in order to determine the acceleration of the vehicle with respect to a specific reference frame. A schematic diagram of such an INS is given on Fig.5.1 [Titterton and Weston, 1997].

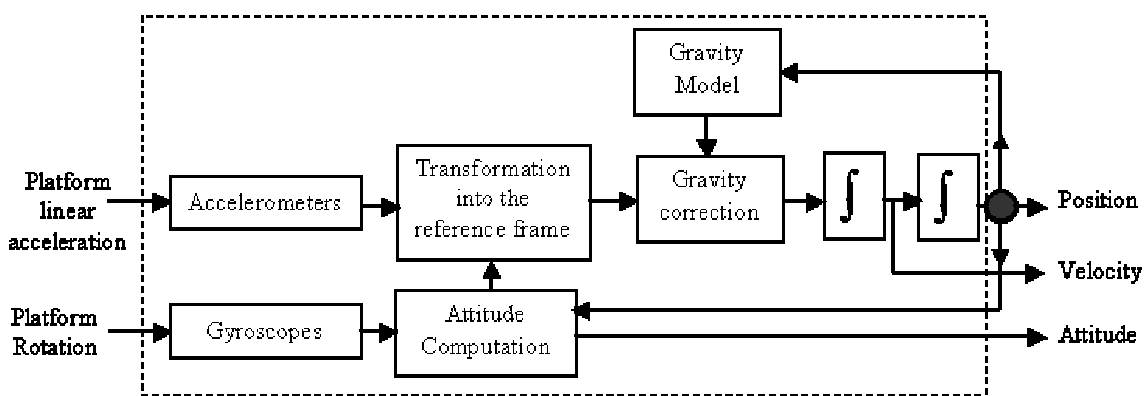


Fig.5.1. Schematic diagram showing the fundamental concept of INS [after Titterton and Weston, 1997].

### 5.1.1. Coordinate frames.

When the inertial sensors (gyroscopes and accelerometers) are installed inside a moving platform, their sensitive axes are pointing towards three mutually orthogonal directions known as sensor axes [Schwarz and Wei, 1999]. The coordinate frame that represents the sensor axes is called the body frame (*b*-frame). The *b*-frame is an orthogonal frame with its axes pointing toward the forward (Y), the transverse (X) and the upward (Z) directions. Fig.5.2 shows the *b*-frame axes for a section inside the drill pipe.

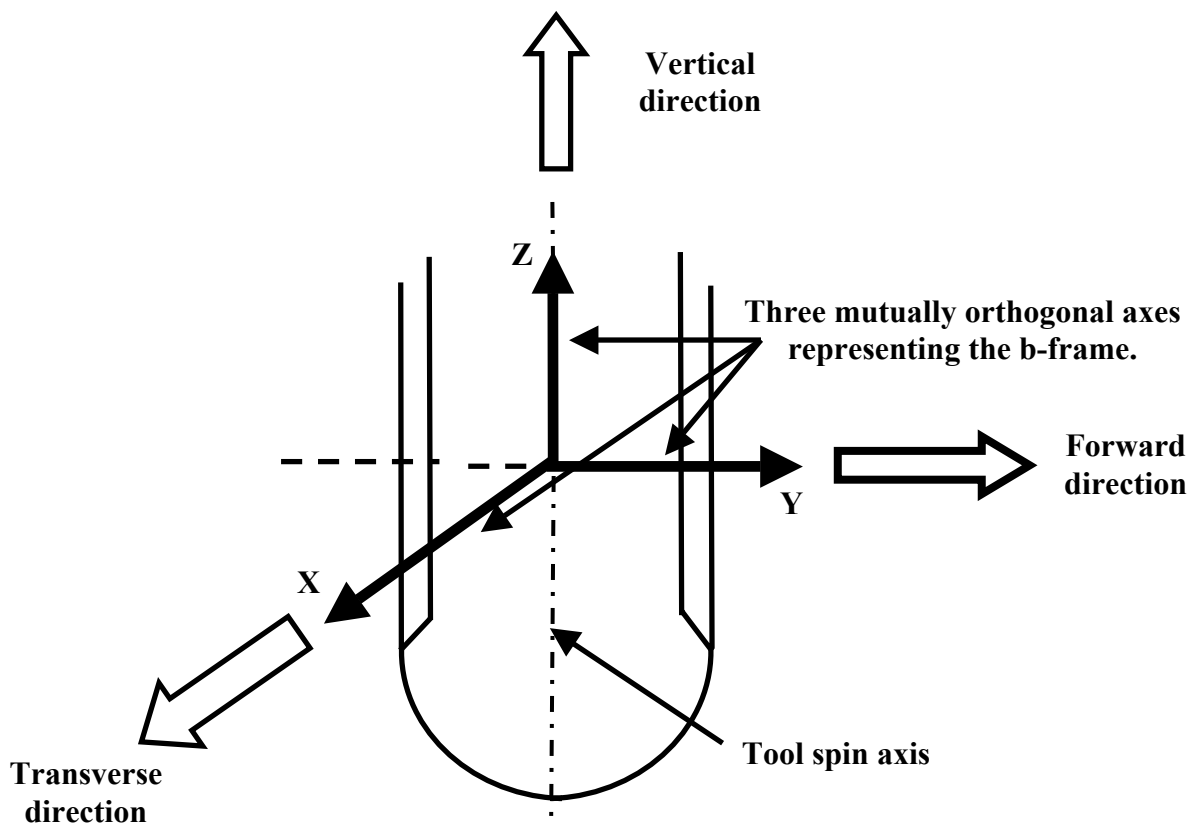


Fig.5.2. The *b*-frame axes for a section inside the drill pipe.

The measurements of linear acceleration and angular velocities are taken in the *b*-frame. These measurements should be transformed into specific reference frame within which they are processed to provide the position, velocity and attitude components of the moving platform. The reference frames most frequently used in inertial navigation are the

inertial frame, the Earth-fixed terrestrial frame and the local level frame ( $\ell$ -frame) [Salychev, 1998; Schwarz and Wei, 1999]. In Chapters 5 and 6, the  $\ell$ -frame is utilized as the reference frame. It has the same origin as the  $b$ -frame with its  $Z^\ell$ -axis orthogonal to the reference ellipsoid of the Earth and pointing upward,  $Y^\ell$ -axis pointing toward the geodetic North and  $X^\ell$ -axis pointing towards the East direction and completing a right handed orthogonal frame (see Fig.5.3). The advantage of utilizing the  $\ell$ -frame is that its axes are aligned to the local East, North and vertical directions. Thus, the inclination, the tool face and the azimuth angles describing the BHA attitude can be obtained directly at the output of the mechanization equations solved in the  $\ell$ -frame. In addition, the computational errors in the navigation parameters on the horizontal plane (the North-East plane) are bound due to the Schuler's effect [Titterton and Weston, 1997; Schwarz and Wei, 1999; Mohammed, 1999]. This effect stipulates that the inertial system errors of the horizontal plane components are coupled together, producing what is called a Schuler loop. Consequently, these errors oscillate with a frequency called the Schuler frequency (1/5000 Hz). [Appendix C presents a brief description of the Schuler effect]

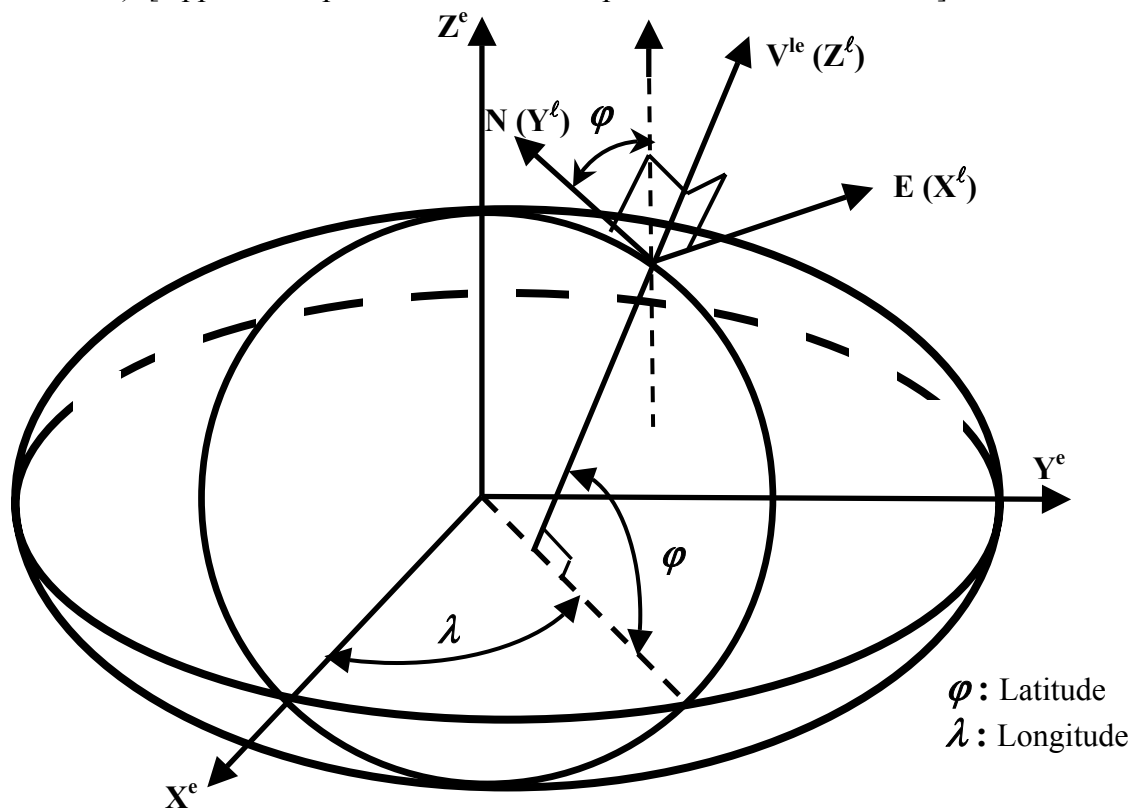


Fig.5.3. The  $\ell$ -frame axes for a given point on the Earth's surface.

### 5.1.2. Transformation between coordinate frames.

The transformation from the  $b$ -frame to the  $\ell$ -frame is performed using the transformation matrix  $R_b^\ell$ , which is expressed as a function of the attitude components (azimuth  $\psi$ , tool face (roll)  $\phi$  and inclination (pitch)  $\theta$ ) as follows [Schwarz and Wei, 1999]:

$$R_b^\ell = \begin{pmatrix} \cos \psi \cos \phi + \sin \psi \sin \theta \sin \phi & \sin \psi \cos \theta & \cos \psi \sin \phi - \sin \psi \sin \theta \cos \phi \\ -\sin \psi \cos \phi + \cos \psi \sin \theta \sin \phi & \cos \psi \cos \theta & -\sin \psi \sin \phi - \cos \psi \sin \theta \cos \phi \\ -\cos \theta \sin \phi & \sin \theta & \cos \theta \cos \phi \end{pmatrix} \quad (5.1)$$

The inverse of the transformation matrix  $R_b^\ell$  describes a transformation from the  $\ell$ -frame to the  $b$ -frame and is denoted by:

$$R_\ell^b = \left( R_b^\ell \right)^{-1} \quad (5.2)$$

Since both the  $b$ -frame and the  $\ell$ -frame are orthogonal coordinate frames,  $R_b^\ell$  and  $R_\ell^b$  are also orthogonal [Titterton and Weston, 1997]. Consequently,  $R_\ell^b$  becomes equal to the transpose of  $R_b^\ell$  and can be expressed as follows:

$$R_\ell^b = \left( R_b^\ell \right)^T = \begin{pmatrix} \cos \psi \cos \phi + \sin \psi \sin \theta \sin \phi & -\sin \psi \cos \phi + \cos \psi \sin \theta \sin \phi & -\cos \theta \sin \phi \\ \sin \psi \cos \theta & \cos \psi \cos \theta & \sin \theta \\ \cos \psi \sin \phi - \sin \psi \sin \theta \cos \phi & -\sin \psi \sin \phi - \cos \psi \sin \theta \cos \phi & \cos \theta \cos \phi \end{pmatrix} \quad (5.3)$$

### 5.1.3. Modeling motion in the local level frame.

The position of the moving platform as described in the  $\ell$ -frame is expressed in terms of the curvilinear coordinates (latitude  $\varphi$ , longitude  $\lambda$  and altitude  $h$ ):

$$r^\ell = \begin{pmatrix} \varphi \\ \lambda \\ h \end{pmatrix} \quad (5.4)$$

The velocity is alternatively expressed by three components along the East direction ( $V^e$ ), North direction ( $V^n$ ) and vertical direction ( $V^u$ ):

$$V^\ell = \begin{pmatrix} V^e \\ V^n \\ V^u \end{pmatrix} \quad (5.5)$$

Therefore, the time rate of change of the position components is related to the velocity components as follows [Schwarz and Wei, 1990]:

$$\dot{r}^\ell = \begin{pmatrix} \dot{\phi} \\ \dot{\lambda} \\ \dot{h} \end{pmatrix} = \begin{pmatrix} 0 & \frac{1}{M+h} & 0 \\ \frac{1}{(N+h)\cos\varphi} & 0 & 0 \\ 0 & 0 & 1 \end{pmatrix} \begin{pmatrix} V^e \\ V^n \\ V^u \end{pmatrix} = D^{-1}V^\ell \quad (5.6)$$

where  $N$  is the prime vertical radius of curvature of the best fitting Earth ellipsoid (East-West),  $M$  is the corresponding meridian radius of curvature (North-South) and  $D^{-1}$  is a 3-by-3 matrix defined as:

$$D^{-1} = \begin{pmatrix} 0 & \frac{1}{M+h} & 0 \\ \frac{1}{(N+h)\cos\varphi} & 0 & 0 \\ 0 & 0 & 1 \end{pmatrix} \quad (5.7)$$

The acceleration of the bearing assembly is measured in three mutually orthogonal directions in the  $b$ -frame  $f^b = (f_x \ f_y \ f_z)^T$ . These measurements are transformed into the  $\ell$ -frame using the rotation matrix  $R_b^\ell$  ( $f^\ell = R_b^\ell f^b$ ). However, the acceleration components expressed in the  $\ell$ -frame,  $f^\ell$ , cannot directly give the velocity components of the moving platform due to three reasons. The first is the rotation rate of the Earth about its spin axis ( $\omega^e = 15.04^\circ/\text{hr}$ ), which is expressed in the  $\ell$ -frame as  $\omega_{ie}^\ell = (0 \ \omega^e \cos\varphi \ \omega^e \sin\varphi)^T$ . The second is the change of orientation of the  $\ell$ -frame with respect to the Earth. This change of orientation is shown along one of the meridians

in Fig.5.4. The change is due to the definition of the local North and vertical directions.

The North direction (N) is tangent to the meridian all the time while the vertical direction ( $V^{le}$ ) is normal to the Earth's surface. This effect is interpreted as rotation rate vector

expressed as  $\omega_{e\ell}^{\ell} = (-\dot{\varphi} \quad \dot{\lambda} \cos \varphi \quad \dot{\lambda} \sin \varphi)^T$ , which can also be written as

$$\omega_{e\ell}^{\ell} = \begin{pmatrix} -V^n & V^e & V^e \tan \varphi \\ M+h & N+h & N+h \end{pmatrix}^T \quad (\text{see Eq.5.6}).$$

The third reason is the gravity field of the Earth, which is given as  $g^{\ell} = (0 \quad 0 \quad -g)^T$ , where  $g$  is obtained from the well-known normal gravity model given as follows [Schwarz and Wei, 1999]:

$$g = a_1(1 + a_2 \sin^2 \varphi + a_3 \sin^4 \varphi) + (a_4 + a_5 \sin^2 \varphi)h + a_6 h^2 \quad (5.8)$$

where,  $a_1 = 9.7803267715 \text{ m/sec}^2$        $a_4 = -0.000003087691089 \text{ 1/sec}^2$   
 $a_2 = 0.0052790414$                        $a_5 = 0.000000004397731 \text{ 1/sec}^2$   
 $a_3 = 0.0000232718$                        $a_6 = 0.000000000000721 \text{ 1/(m sec}^2)$

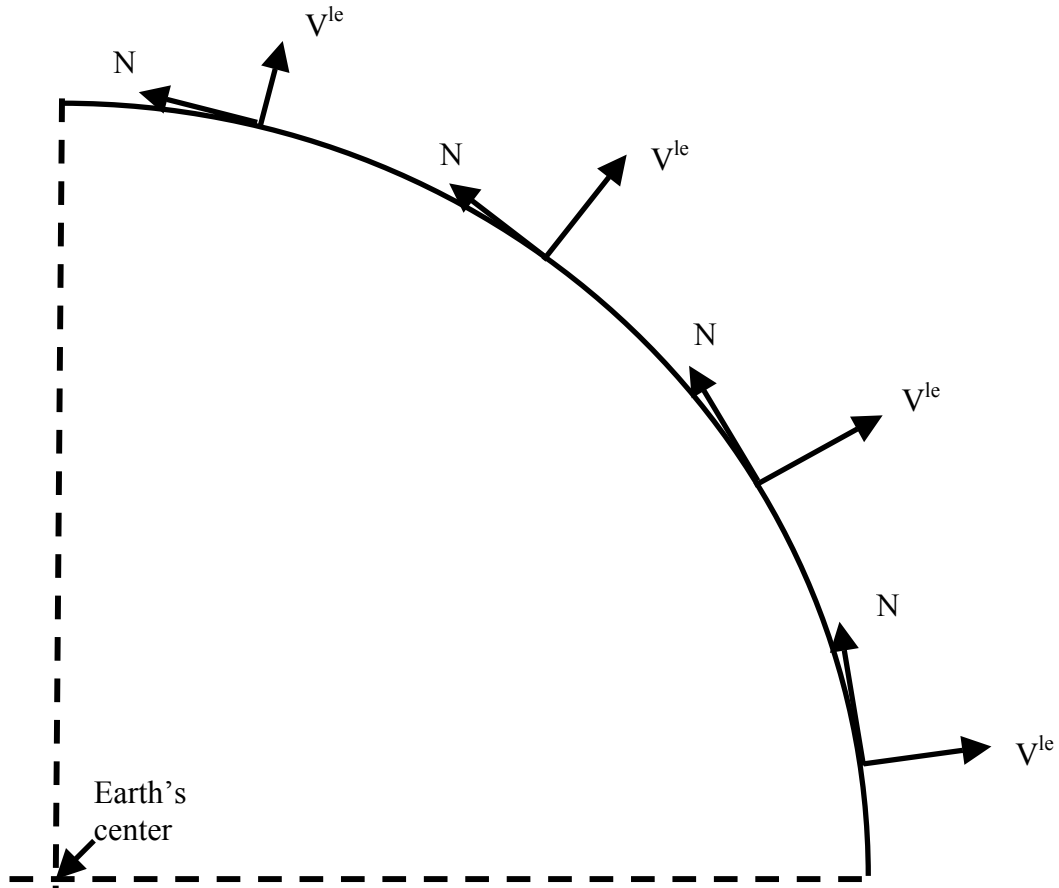


Fig.5.4. The change of  $\ell$ -frame orientation along the Earth's surface.

Therefore, the time rate of change of the velocity components  $V^\ell$  of the moving platform can be expressed as follows [Schwarz and Wei, 1999]:

$$\dot{V}^\ell = R_b^\ell f^b - (2\Omega_{ie}^\ell + \Omega_{el}^\ell)V^\ell + g^\ell \quad (5.9)$$

where  $\Omega_{ie}^\ell$  and  $\Omega_{el}^\ell$  are the skew-symmetric matrices corresponding to  $\omega_{ie}^\ell$  and  $\omega_{el}^\ell$  respectively and they are expressed as follows:

$$\Omega_{ie}^\ell = \begin{pmatrix} 0 & -\omega^e \sin \varphi & \omega^e \cos \varphi \\ \omega^e \sin \varphi & 0 & 0 \\ -\omega^e \cos \varphi & 0 & 0 \end{pmatrix} \quad (5.10)$$

$$\Omega_{el}^\ell = \begin{pmatrix} 0 & \frac{-V^e \tan \varphi}{N+h} & \frac{V^e}{N+h} \\ \frac{V^e \tan \varphi}{N+h} & 0 & \frac{V^n}{M+h} \\ \frac{-V^e}{N+h} & \frac{-V^n}{M+h} & 0 \end{pmatrix} \quad (5.11)$$

The rotation matrix  $R_b^\ell$  can be obtained by solving the following differential equations [Schwarz and Wei, 1999]:

$$\dot{R}_b^\ell = R_b^\ell \Omega_{\ell b}^b = R_b^\ell (\Omega_{ib}^b - \Omega_{il}^b) \quad (5.12)$$

where  $\Omega_{ib}^b$  is the skew-symmetric matrix of the measurements of angular velocities provided by the gyroscopes.  $\Omega_{ib}^b$  corresponds to the angular velocity vector

$\omega_{ib}^b = (\omega_x \quad \omega_y \quad \omega_z)^T$  and is given as:

$$\Omega_{ib}^b = \begin{pmatrix} 0 & -\omega_z & \omega_y \\ \omega_z & 0 & -\omega_x \\ -\omega_y & \omega_x & 0 \end{pmatrix} \quad (5.13)$$

Since the gyroscopes measure both the Earth rotation and the change in orientation of the  $\ell$ -frame in addition to the angular velocities of the bearing assembly, the term  $\Omega_{il}^b$  in Eq.5.12 is subtracted from  $\Omega_{ib}^b$  to remove these two effects. The term

$\Omega_{i\ell}^b$  consists of two parts. The first part is  $\Omega_{ie}^b$  which accounts for the Earth rotation rate and the second part is  $\Omega_{e\ell}^b$  which accounts for the orientation change of the  $\ell$ -frame.

Therefore,  $\Omega_{i\ell}^b$  can be written as follows:

$$\Omega_{i\ell}^b = \Omega_{ie}^b + \Omega_{e\ell}^b \quad (5.14)$$

Since  $\omega_{ie}^b = R_\ell^b \omega_{ie}^\ell$  and  $\omega_{e\ell}^b = R_\ell^b \omega_{e\ell}^\ell$ , then  $\omega_{i\ell}^b = R_\ell^b (\omega_{ie}^\ell + \omega_{e\ell}^\ell)$  and in component form as follows:

$$\omega_{i\ell}^b = R_\ell^b \left[ \begin{array}{c} 0 \\ \omega^e \cos \varphi \\ \omega^e \sin \varphi \end{array} \right] + \left[ \begin{array}{c} \frac{-V^n}{M+h} \\ \frac{V^e}{N+h} \\ \frac{V^e \tan \varphi}{N+h} \end{array} \right] = R_\ell^b \left[ \begin{array}{c} \frac{-V^n}{M+h} \\ \frac{V^e}{N+h} + \omega^e \cos \varphi \\ \frac{V^e \tan \varphi}{N+h} + \omega^e \sin \varphi \end{array} \right] \quad (5.15)$$

Consequently, the corresponding skew-symmetric matrix  $\Omega_{i\ell}^b$  can be determined.

When Eqs 5.6, 5.9 and 5.12 are combined together, they form what is known as the mechanization equations in the  $\ell$ -frame and they are usually given together as follows [Schwarz and Wei, 1990; 1999]:

$$\begin{pmatrix} \dot{r}^\ell \\ \dot{V}^\ell \\ \dot{R}_b^\ell \end{pmatrix} = \begin{pmatrix} D^{-1}V^\ell \\ R_b^\ell f^b - (2\Omega_{ie}^\ell + \Omega_{e\ell}^\ell)V^\ell + g^\ell \\ R_b^\ell (\Omega_{ib}^b - \Omega_{i\ell}^b) \end{pmatrix} \quad (5.16)$$

The inputs to these mechanization equations are the gyroscope and accelerometer measurements,  $f^b$  and  $\Omega_{ib}^b$ , while the outputs are the curvilinear coordinates, three velocity components and three attitude components.

## 5.2. Single-FOG MWD surveying setup.

As discussed earlier, an INS incorporates three-axis accelerometers and three-axis gyroscopes (known as inertial measurement unit (IMU)) mounted in three mutually orthogonal directions to monitor both the linear and rotational motions and to provide both the BHA position and orientation. Therefore, in the quest for replacing the

magnetometers, a FOG-based inertial measurement unit can be mounted inside the drill pipe and the proposed technique can be employed for a complete navigation solution downhole. Unfortunately, present inertial sensor technology cannot provide a FOG-based IMU of small size so that it fits in the limited space available downhole and high accuracy so that it can deliver reliable surveying data. However, future technological advances in the miniaturization of inertial measurement units may lead to three-axis gyroscopes that have the necessary minimal dimensions and high accuracy to be mounted inside the BHA.

At present, the FOG size determines the overall size of the inertial measurement unit. As mentioned earlier, the present technological level of FOG-based inertial measurement units do not permit direct installation of 3 FOGs inside the BHA. Therefore, a novel structure for the inertial measurement unit is introduced with one or two specially designed FOGs in order to accommodate space and precision requirements. The single FOG system is presented in this chapter while the dual FOG system is discussed in Chapter 6.

The FOG monitors the rotations rate signal along the tool spin axis of the drill pipe. The other two rotation rate signals will be generated using the time rate of change of the inclination and the roll angles calculated with the three-axis accelerometer measurements. The FOG and the three-axis accelerometers can be mounted in several locations inside the drill pipe and the technique provided in the following sections will process their measurements to determine the surveying data. However, it is highly desirable to install the surveying sensors close to the drill bit in order to achieve near-bit surveying system. Therefore, a novel structure of the MWD inertial surveying sensors that fit inside the bearing assembly close to the drill bit is suggested.

The proposed MWD surveying setup introduced herewith is installed inside the bearing assembly 17'' behind the drill bit (Fig.5.5). This setup consists of the following:

1. A single fiber optic gyroscope (FOG): This FOG is installed with its sensitive axis along the tool spin axis. It is designed like a torus to allow the flow of mud through the drill pipe (Fig.5.5). This FOG has an internal diameter of 2.75'' and an external diameter of 3.75'' and is labeled the Torus FOG. It is

desirable for this FOG to have drift rate less than  $0.1^\circ/hr$  and angle random walk of less than  $0.01^\circ/hr/\sqrt{Hz}$  in the  $100\text{ Hz}$  bandwidth.

2. A three-axis accelerometers arranged in three mutually orthogonal directions with one of them having its sensitive axis parallel to the tool spin axis.
3. Standard wireless communication between the new setup inside the bearing assembly and the MWD tools behind [Orban and Richardson, 1995; Skillingstad, 2000]. With this new setup, the non-magnetic drill collars can be removed and the MWD processing tools can be installed within only 20 feet behind the bearing assembly.
4. A battery package providing the necessary power supply to the FOG, the accelerometers package and the wireless communication system.

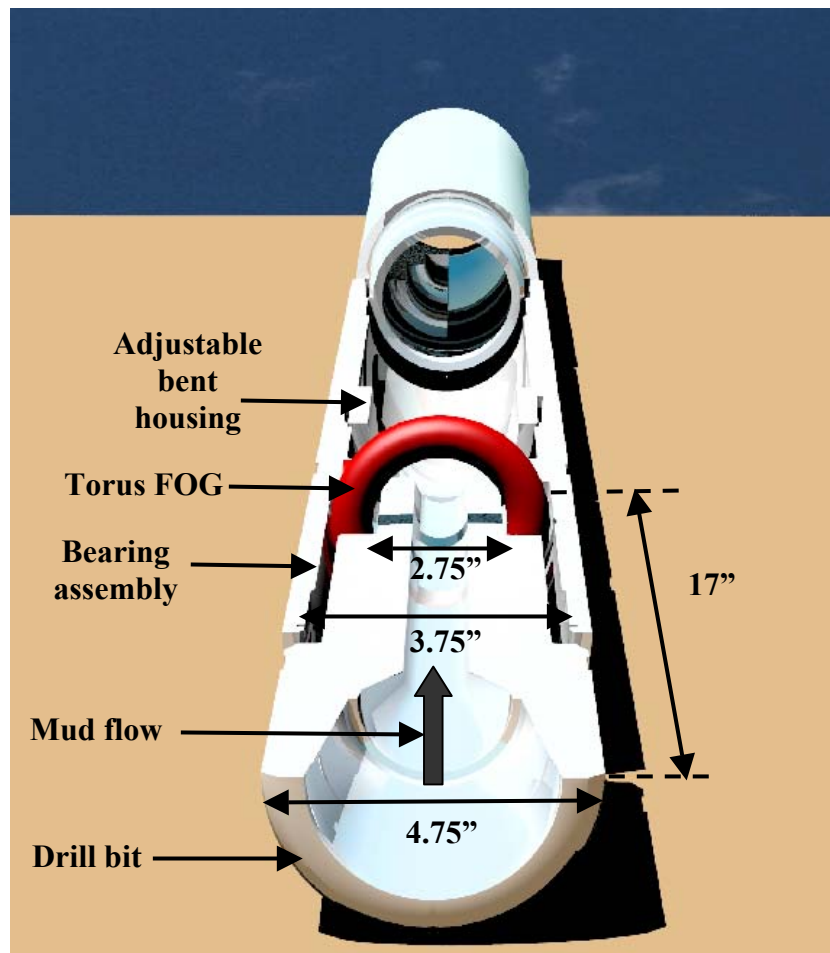


Fig.5.5. Single-axis FOG-based gyroscopic surveying system mounted inside the bearing assembly.

The directional drilling process involves three main stages (Fig.5.6). A vertical hole is established to a certain depth using conventional drilling operations. The directional drilling equipment (including MWD surveying tools) is then installed and the drill pipe is rotated about its spin axis towards a certain azimuth direction. The surveying tools are employed to determine the desired azimuth direction while rotating the drill pipe. A radical section is then built using the steering drilling mode. During this process, the BHA azimuth, inclination and position should be monitored in order to properly approach the oil reservoir. The horizontal section is established using rotary drilling mode during which the MWD surveying tools monitor the BHA azimuth and inclination.

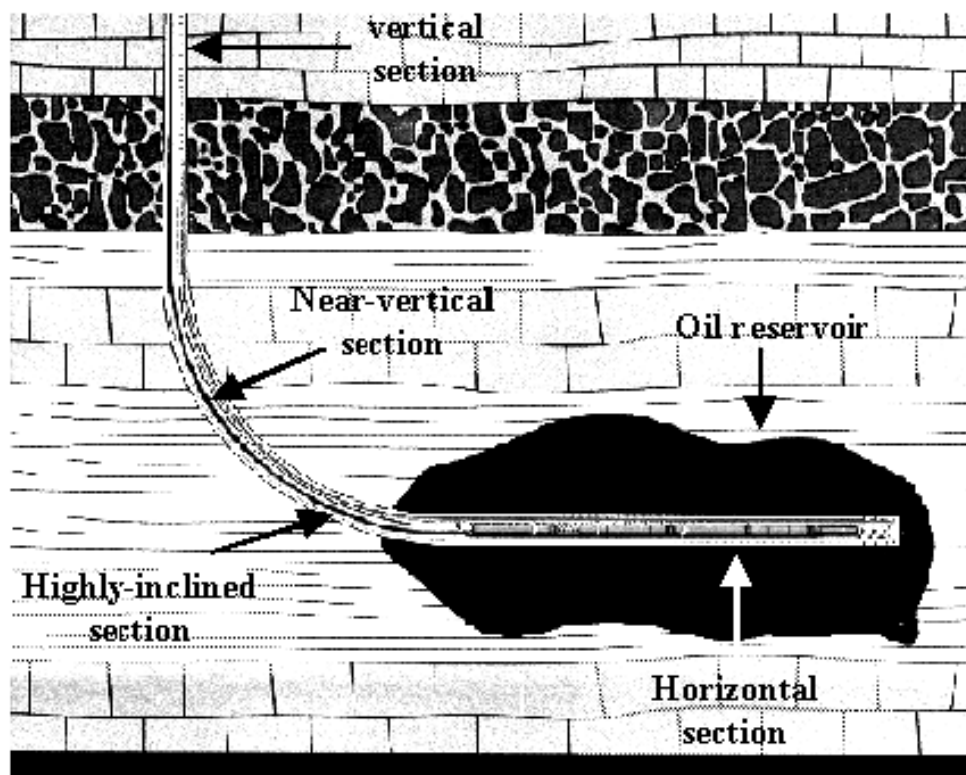


Fig.5.6. Diagram showing the different sections of a horizontal well.

The single FOG system can continuously survey the near-vertical section of the well (up to  $20^\circ$  inclination) [Noureldin et al.<sup>a,b</sup>, 2001]. Unfortunately, the continuous surveying process cannot be applied for the entire drilling process. For highly inclined

and horizontal well sections, the Single-FOG system can no longer resolve the changes on the azimuth by monitoring the rotation rate along the tool spin axis. Therefore, station-based surveying is suggested for the highly inclined and horizontal well sections.

The following sections present both the continuous surveying process for the near-vertical section of the well and the station-based surveying procedure for highly-inclined and horizontal well sections. In addition, quantitative long-term error analysis of the Single-FOG system is discussed. Furthermore, Digital signal processing methods for both surveying techniques are suggested to limit the long-term growth of surveying errors.

### **5.3. Continuous surveying of near-vertical sections of horizontal wells.**

The  $b$ -frame axes ( $X^b$ ,  $Y^b$ ,  $Z^b$ ) are chosen as shown on Fig.5.7. The accelerometers deliver specific force measurements  $f_x$ ,  $f_y$  and  $f_z$  (m/sec<sup>2</sup>) along the  $b$ -frame axes. The FOG with its sensitive axis along the  $Z^b$  direction provides measurement  $\omega_z$  of the rotation rate imposed along the tool spin axis. Since the Single-FOG system utilizes only one FOG, the three-axis accelerometers are used to generate two synthetic rotation rate components  $\omega_{xs}$  and  $\omega_{ys}$ .

#### **5.3.1. Determination of two synthetic rotation rate components.**

Due to the small BHA penetration rate through the downhole formation, it can be assumed that the accelerometers are affected only by the Earth's gravity components. This assumption is justified by the fact that the angle-building rate in most directional drilling operation is reported as about  $10^\circ / 100ft$  [Joshi et al., 1991], which indicates how small the BHA velocity components are. However, the above assumption is not valid in some special applications when the angle-building rate of the drilling operation becomes as high as  $40^\circ / ft$  [Joshi et al., 1991]. In these situations, the technique described in this chapter may not be applicable. The MWD surveying process starts with receiving the accelerometer measurements, which are affected predominantly by the

Earth's gravity according to the above assumption. The gravity vector of the Earth expressed in the  $\ell$ -frame is given as follows [Schwarz and Wei, 1999]:

$$\mathbf{g}^{\ell} = (0 \quad 0 \quad -g)^T \quad (5.17)$$

where  $g$  is determined using the normal gravity model given in Eq.5.8.

The accelerometer measurement vector  $f^b$  in stationary mode is related to the gravity vector  $\mathbf{g}^{\ell}$  as follows:

$$\mathbf{f}^b = \begin{pmatrix} f_x \\ f_y \\ f_z \end{pmatrix} = R_{\ell}^b \mathbf{g}^{\ell} = R_{\ell}^b \begin{pmatrix} 0 \\ 0 \\ -g \end{pmatrix} \quad (5.18)$$

where  $R_{\ell}^b$  transforms the gravity vector defined in the  $\ell$ -frame into the  $b$ -frame( Eq.5.3).

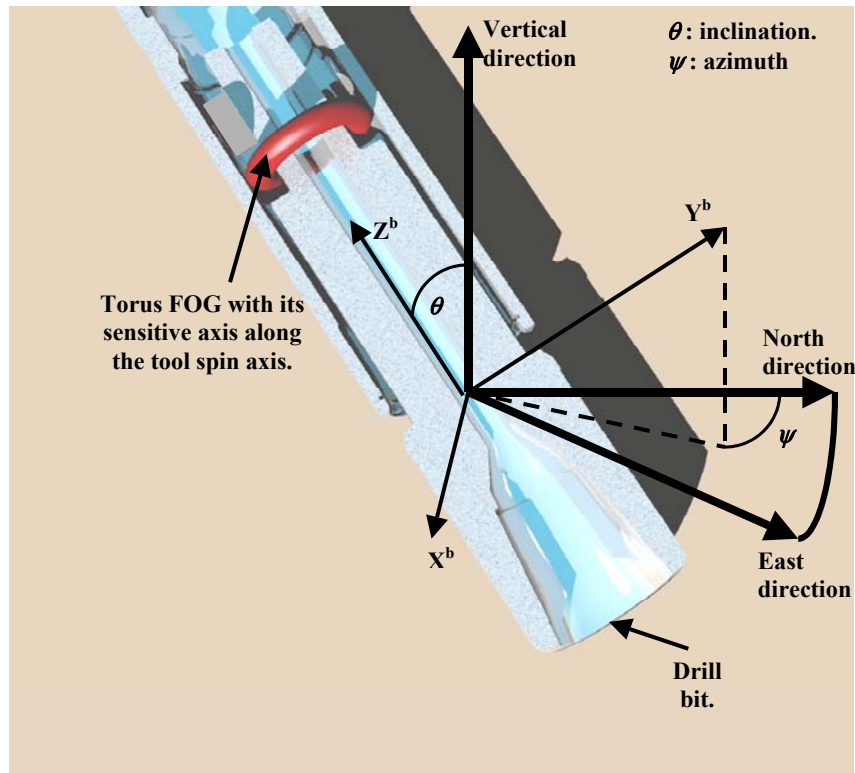


Fig.5.7. The Single-FOG setup with the  $b$ -frame and the  $\ell$ -frame represented inside the bearing assembly.

The three-axis accelerometer measurements can be written as a function of normal gravity:

$$f_x = g \cos \theta \sin \phi \quad (5.19)$$

$$f_y = -g \sin \theta \quad (5.20)$$

$$f_z = -g \cos \theta \cos \phi \quad (5.21)$$

These three equations can be used to determine the inclination and the roll respectively:

$$\sin \theta = \frac{-f_y}{g} \quad (5.22)$$

$$\tan \phi = \frac{-f_x}{f_z} \quad (5.23)$$

Consequently, the two synthetic rotation rate components corresponding to the ones along the  $X^b$  and  $Y^b$  directions can respectively be given as:

$$\omega_{xs}(t_k) = \frac{\theta(t_k) - \theta(t_{k-1})}{t_k - t_{k-1}} \quad (5.24)$$

$$\omega_{ys}(t_k) = \frac{\phi(t_k) - \phi(t_{k-1})}{t_k - t_{k-1}} \quad (5.25)$$

It should be emphasized that the two synthetic rotation rate components  $\omega_{xs}$  and  $\omega_{ys}$  represent the BHA rotation rates after being transformed into the  $\ell$ -frame.

### 5.3.2. Development of the mechanization equations.

The Single-FOG MWD surveying system describes the BHA position by the latitude  $\varphi$ , the longitude  $\lambda$  and the altitude  $h$ . The position vector  $r^\ell = (\varphi \ \lambda \ h)^T$  is given in terms of the velocity vector  $V^\ell = (V^e \ V^n \ V^u)^T$  as described in Eq.5.6.

The BHA velocity components  $V^e$ ,  $V^n$  and  $V^u$  are defined along the East, North and vertical directions, respectively. These velocities can be determined from the accelerometer measurements using Eq.5.9 after removing the effect of gravity  $g^\ell$  and

the Coriolis acceleration  $(2\Omega_{ie}^\ell + \Omega_{e\ell}^\ell)$ . For the Single-Fog system, the Coriolis effect was neglected and has not been taken into consideration while determining  $V^e$ ,  $V^n$  and  $V^u$ . The Coriolis effect accounts for the effect of the Earth's rotation and the change of the  $\ell$ -frame orientation while moving along the Earth's surface. This effect results in some terms of the Earth rotation rate being multiplied by the velocity components. Due to the low BHA penetration rate and the small value of the Earth rotation rate ( $\omega_e = 15^\circ / hr$ ), the multiplication of  $\omega_e$  by any of the velocity components gives a very small value, which can be neglected. Thus, the BHA velocities are determined as follows:

$$\dot{V}^\ell = R_b^\ell f^b + g^\ell \quad (5.26)$$

The Single-FOG MWD surveying system defines the BHA orientation by the inclination, the roll and the azimuth angles. The two synthetic rotation rate components  $\omega_{xs}$  and  $\omega_{ys}$  are the dominant factors that control the time rate of change of both the inclination angle,  $\dot{\theta}$ , and the roll angle,  $\dot{\phi}$ , respectively. However, the Earth rotation rate  $\omega^e$  and the effect of the velocity components along the East and the North directions should be taken into account. It can be inferred from Fig.5.8 that the time rate of change of the inclination angle,  $\dot{\theta}$ , should include the effect of the velocity component along the North direction  $V^n$ , which gives an angular rotation of  $V^n/(M+h)$  along the East direction [Schwarz and Wei, 1990; 1999; Titterton and Weston, 1997]. Therefore, the time rate of change of the inclination angle  $\dot{\theta}$  is given as follows:

$$\dot{\theta} = \frac{V^n}{M+h} + \omega_{xs} \quad (5.27)$$

Similarly, the velocity component along the East direction contributes to the time rate of change of the roll by a rotation rate of  $V^e/(N+h)$  [Titterton and Weston, 1997]. In addition, the component of the Earth rotation rate along the North direction is considered. Then, the expression of the time rate of change of the roll angle is written as:

$$\dot{\phi} = -\frac{V^e}{N+h} - \omega_e \cos \varphi + \omega_{ys} \quad (5.28)$$

The azimuth expression is different from that of the inclination and the roll because the rotation rate provided by the FOG is given along the  $Z^b$  axis of the  $b$ -frame. This rotation rate signal ( $\omega_z$ ) should be transformed into its corresponding  $\ell$ -frame component. Since the change in the azimuth angle is due to the rotation along the vertical axis of the  $\ell$ -frame, the angular velocity along the tool spin axis  $\omega_z$  contributes by  $\omega_z \cos \theta \cos \phi$  (see Fig.5.8). The Earth rotation component along the vertical direction  $\omega^e \sin \phi$  is removed while continuously monitoring the azimuth angle. Moreover, the East velocity  $V^e$  produces a  $V^e \tan \phi / (N+h)$  rotation rate along the vertical direction of the  $\ell$ -frame [Titterton and Weston, 1997]. Taking all these factors into consideration, the time rate of change of the azimuth angle is written as:

$$\dot{\psi} = \omega_z \cos \theta \cos \phi - \omega^e \sin \phi - \frac{V^e \tan \phi}{N+h} \quad (5.29)$$

The MWD surveying method depends on Eq.5.6 to provide three coordinate components describing the BHA position, on Eq.5.26 to give three velocity components and on Eqs.5.27-5.29 to determine the BHA orientation. These first order differential equations are solved in real-time using Euler numerical method with a first order approximation [Yakowitz and Szidarovszky, 1989; Noureldin et al.<sup>a</sup>, 2001]. A block diagram of the Single-FOG MWD surveying system is given on Fig.5.9.

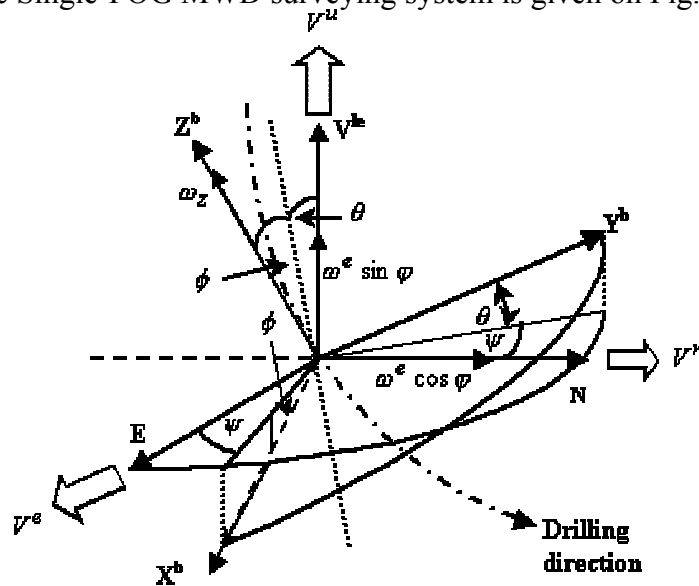


Fig.5.8. Distribution of velocities and Earth rotation rate components along the  $\ell$ -frame axes.

### 5.3.7. Results.

#### 5.3.7.1. Long-term behavior of surveying errors.

The averaging process of the inertial sensor measurements over 1-second interval was capable of reducing the FOG output uncertainty from  $50^{\circ}/hr$  to  $4.7^{\circ}/hr$ . Similarly, the accelerometer measurement uncertainties were reduced from about  $0.006g$  [ $m/sec^2$ ] to  $0.0006g$  [ $m/sec^2$ ].

Since velocity updates were continuously performed, the velocity errors were observable states and optimal estimates of these errors were provided by the Kalman filter. Fig.5.14 shows the MSEE of the velocity error states. It can be observed that these error states were optimally estimated by the Kalman filter with minimum MSEEs of  $2.13 \times 10^{-5} (m/sec)^2$ ,  $0.8 \times 10^{-5} (m/sec)^2$  and  $4.9 \times 10^{-5} (m/sec)^2$  for  $\delta V^e$ ,  $\delta V^n$  and  $\delta V^u$ , respectively. Since they were strongly observable, the MSEEs of the velocity error states converged to the steady-state values of the minimum MSEE within a short transition period of a few seconds (see Fig.5.14). The Kalman filter continued then to provide the estimates with constant accuracy, which could not be improved with time.

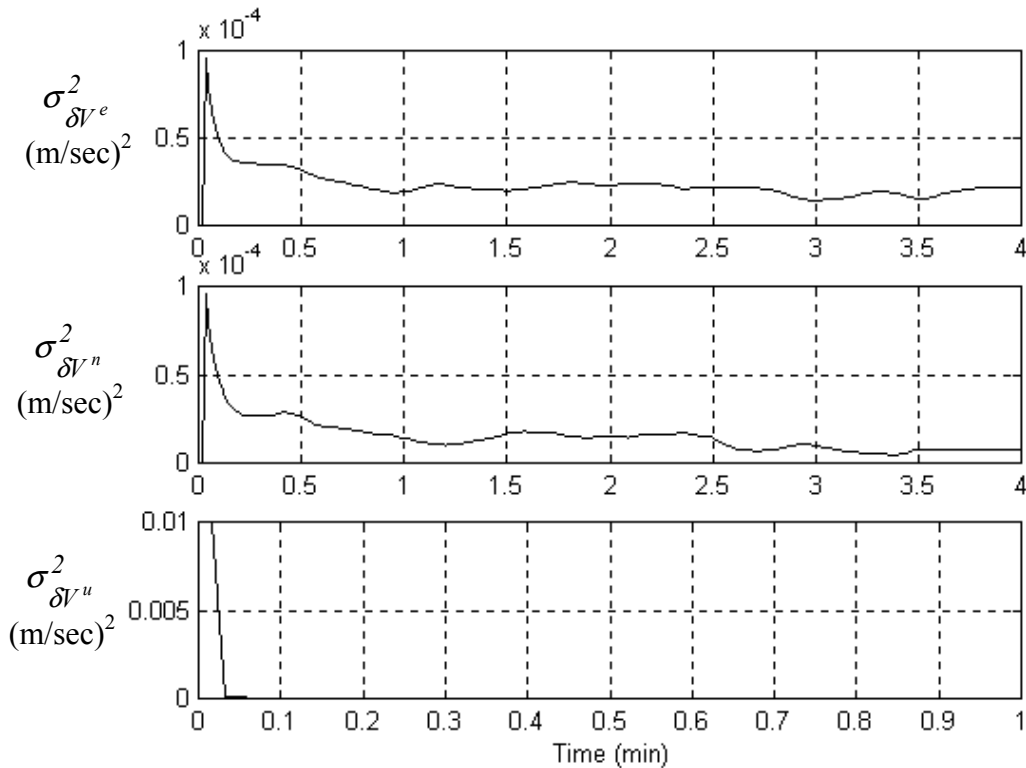


Fig.5.14. Mean square estimation error of the velocity error states in  $(m/sec)^2$ .

Fig.5.15 shows the MSEEs of the attitude error states. It is evident that both the inclination and the roll errors were strongly observable by the Kalman filter with their MSEEs converging in 10 seconds to the steady-state minimal value. Although the azimuth error state was theoretically observable, its MSEE exhibited slow convergence towards the minimal value (convergence after 100 minutes) (see Fig.5.15). Furthermore, due to their strong observability, the inclination and the roll errors were estimated with MSEEs of  $4.4 \times 10^{-5} \text{ (deg.)}^2$  and  $8.5 \times 10^{-5} \text{ (deg.)}^2$ , respectively, which were much less than the MSEE of the azimuth error state ( $0.011 \text{ deg.}^2$ ) achieved after 100 minutes after the start of the experiment. Since no optimal estimates of the azimuth error state were provided during the first 100 minutes of the experiment, the azimuth accuracy became limited by the performance of the FOG utilized. Therefore, navigational grade gyros (drift rates less than  $0.1^\circ / \text{hr}$ ) should be employed to guarantee satisfactory performance until convergence of the MSEE of the azimuth error state is achieved. Fortunately, the current FOG technology provides navigational grade performance within small size, which can be mounted downhole with the configuration discussed earlier in this chapter.

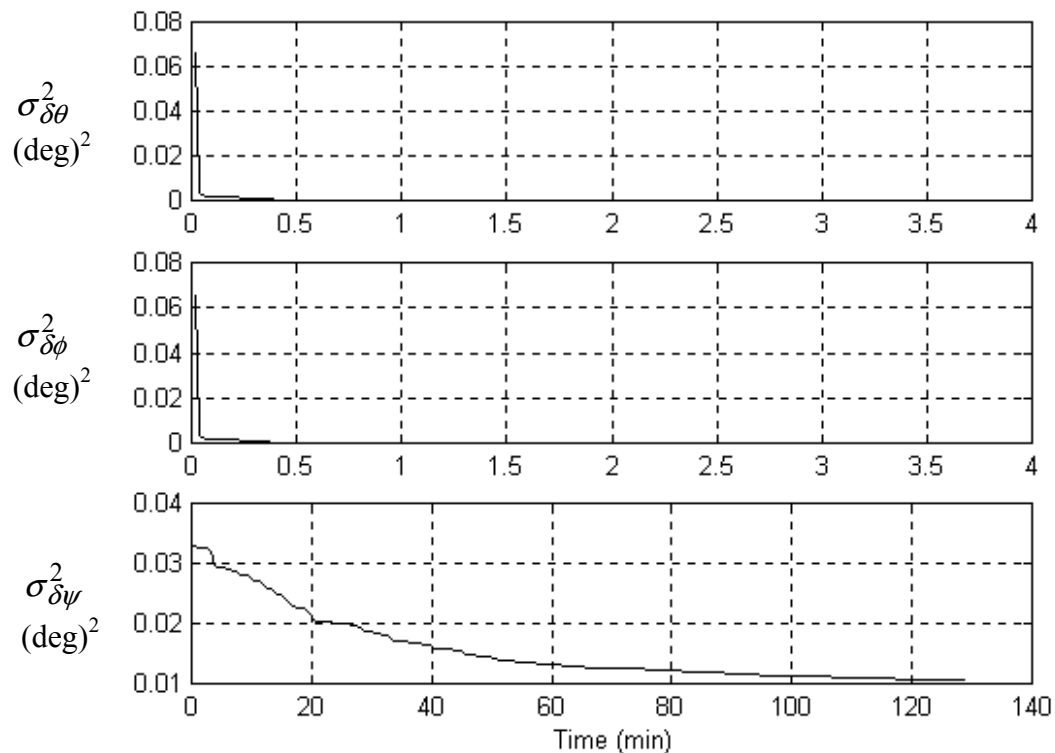


Fig.5.15. Mean square estimation error of the attitude error states in  $(\text{deg})^2$ .

On the other hand, the MSEEs of both the latitude and the longitude error states ( $\delta\varphi$  and  $\delta\lambda$ ) suffered from divergence. Fig.5.16 shows that the MSEEs of these two error states had unlimited increase with time. Consequently, no optimal estimates could be provided for  $\delta\varphi$  and  $\delta\lambda$  in real-time and they became unobservable error states by the Kalman filter. However, due to the altitude update provided to the Kalman filter, the MSEE of the altitude error  $\delta h$  converged to a minimum steady-state value of  $0.0009 m^2$  after a short transition process of 5 seconds (see Fig.5.16). The divergence of the MSEEs of both  $\delta\varphi$  and  $\delta\lambda$  is one of the limitations of the single FOG-based MWD surveying system, since the Kalman filter cannot limit the long-term latitude and longitude errors. Thus, the accuracies of both the latitude and the longitude were limited by the accuracy of the inertial sensors employed.

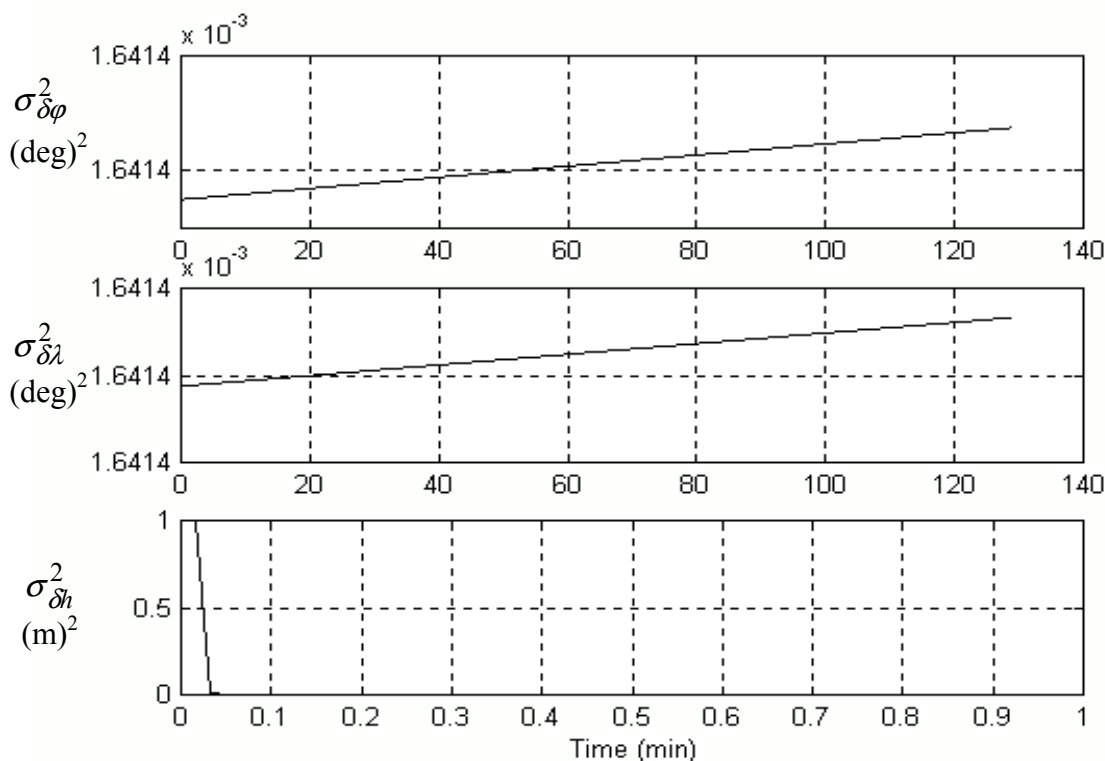


Fig.5.16. Mean square estimation error of the latitude in  $(deg)^2$ , the longitude in  $(deg)^2$  and the altitude in  $m^2$ .

### 5.3.7.2. Limiting the long-term surveying errors with continuous aided inertial navigation.

The long-term analysis of various surveying errors and their observability by the Kalman filter excludes the latitude and the longitude error states ( $\delta\varphi$  and  $\delta\lambda$ ) from the closed loop criterion of the aided inertial navigation technique in order to avoid affecting the other observable error states.

As shown on Fig.5.17, the velocity errors were optimally estimated by the Kalman filter and were limited to  $0.05 \text{ m/sec}$ . These errors did not drift with time even in the presence of system disturbance. For example, the velocity error along the North direction ( $\delta V^n$ ) experienced some disturbances, which started 18 minutes after the beginning of the experiment (see Fig.5.17), however, the error was kept limited during the course of this disturbance, which lasted 12 minutes.

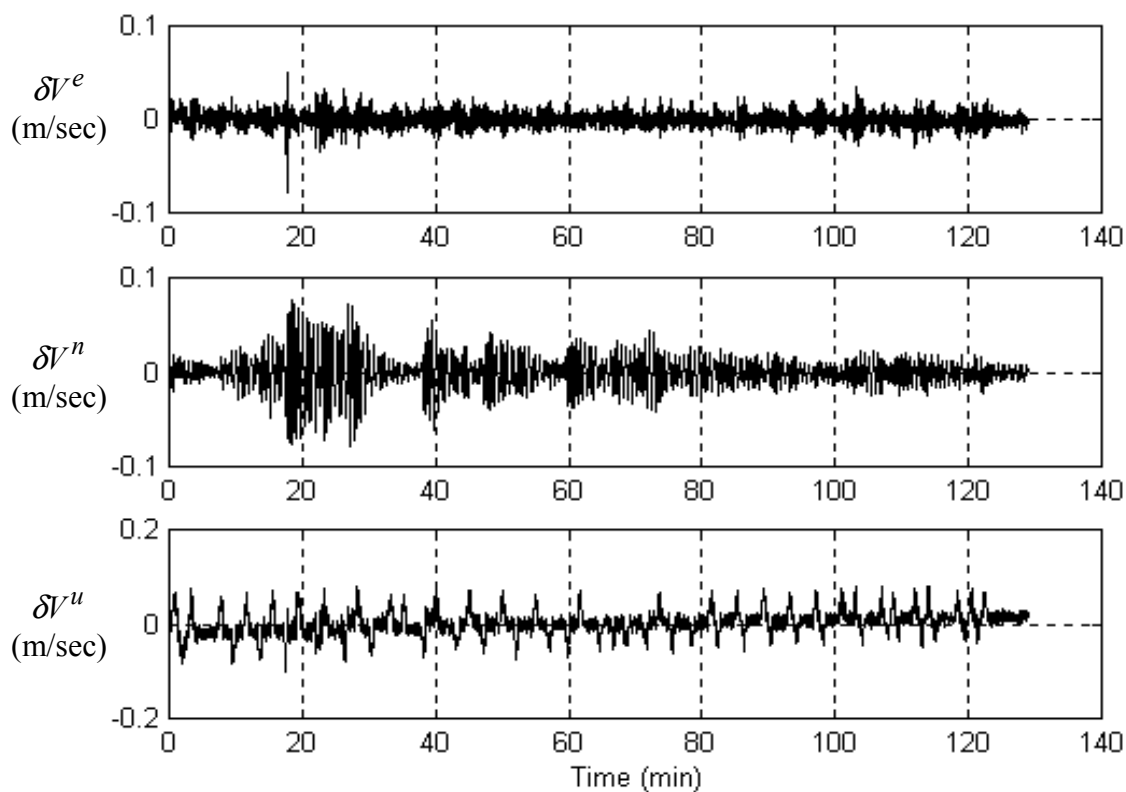


Fig.5.17. Velocity errors along the East, the North and the vertical directions in m/sec.

The errors in the attitude angles (inclination, roll and azimuth) as estimated by the Kalman filter are shown on Fig.5.18. Both the inclination and the roll errors (being strongly observable by the Kalman filter) were limited over time while the azimuth error continued to increase until 100 minutes (the time for convergence), after which the azimuth error became constant, corresponding to a certain FOG bias error. During the time of MSE convergence of the azimuth error state,  $\delta\psi$  was excluded from the closed loop criterion for error correction.

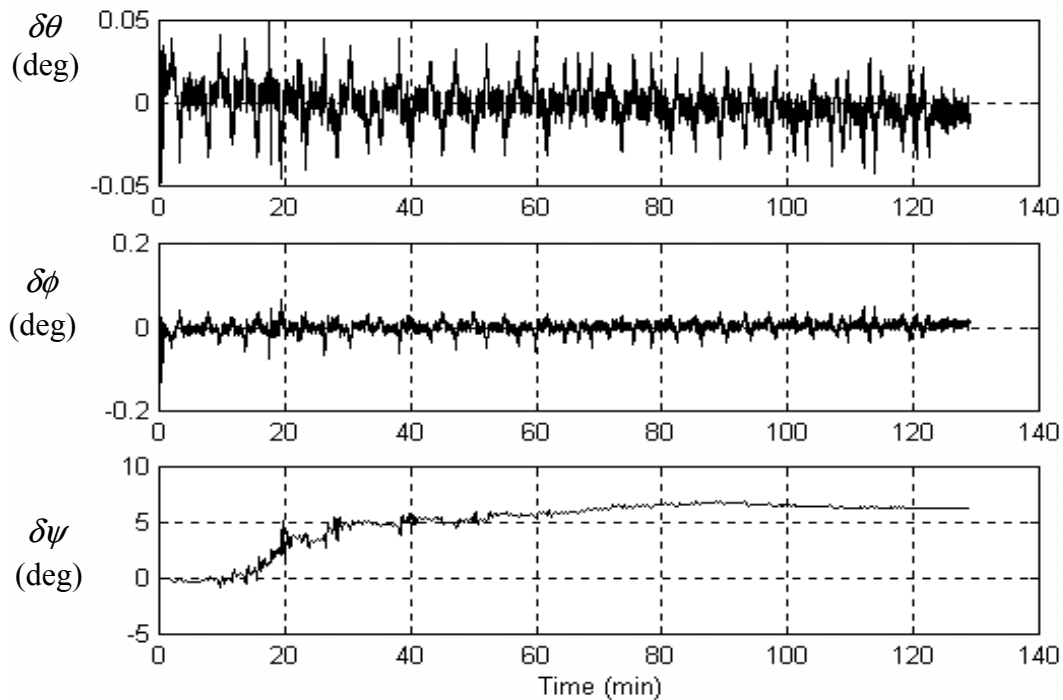


Fig.5.18. The inclination, the roll and the azimuth errors in degrees.

Fig.5.19 shows the dynamics of the inclination and the azimuth angles over more than 2 hours experiment. The accuracy of the FOG-based MWD surveying system was checked by comparing the inclination and the azimuth angles with the corresponding external reference values ( $\theta_{ref} = 0^\circ$ ,  $\psi_{ref} = 156.2^\circ$ ). The reference lines for both the inclination and the azimuth are shown on Fig.5.19 and they can only be used for comparison with the output of the FOG-based MWD surveying system when stopping the surveying process at  $0^\circ$  inclination (i.e. at the horizontal plane). The maximum error determined for the inclination was found to be less than  $0.4^\circ$  while that of the azimuth

was  $6.7^\circ$  at the end of the experiment. However, since the azimuth error started to be optimally estimated after 100 minutes, it has been determined that if the azimuth error was included in the closed loop error correction criterion of the aided inertial navigation technique for the rest of the experiment (after the initial 100 minutes), significant improvement of the azimuth accuracy (errors of less than  $1^\circ$ ) could be obtained [Noureldin et al.<sup>b</sup>, 2001]. This effect is shown on Fig.5.20, where it can be observed that the azimuth angle continued to drift with time until  $t=100 \text{ min}$ , after which the azimuth error started to decrease to as low as  $0.3^\circ$ . Therefore, the azimuth accuracy, although depending on the FOG drift characteristics, improved in the long-term depending on how fast the MSEE could converge and how strongly the azimuth error state was coupled to the velocity error states.

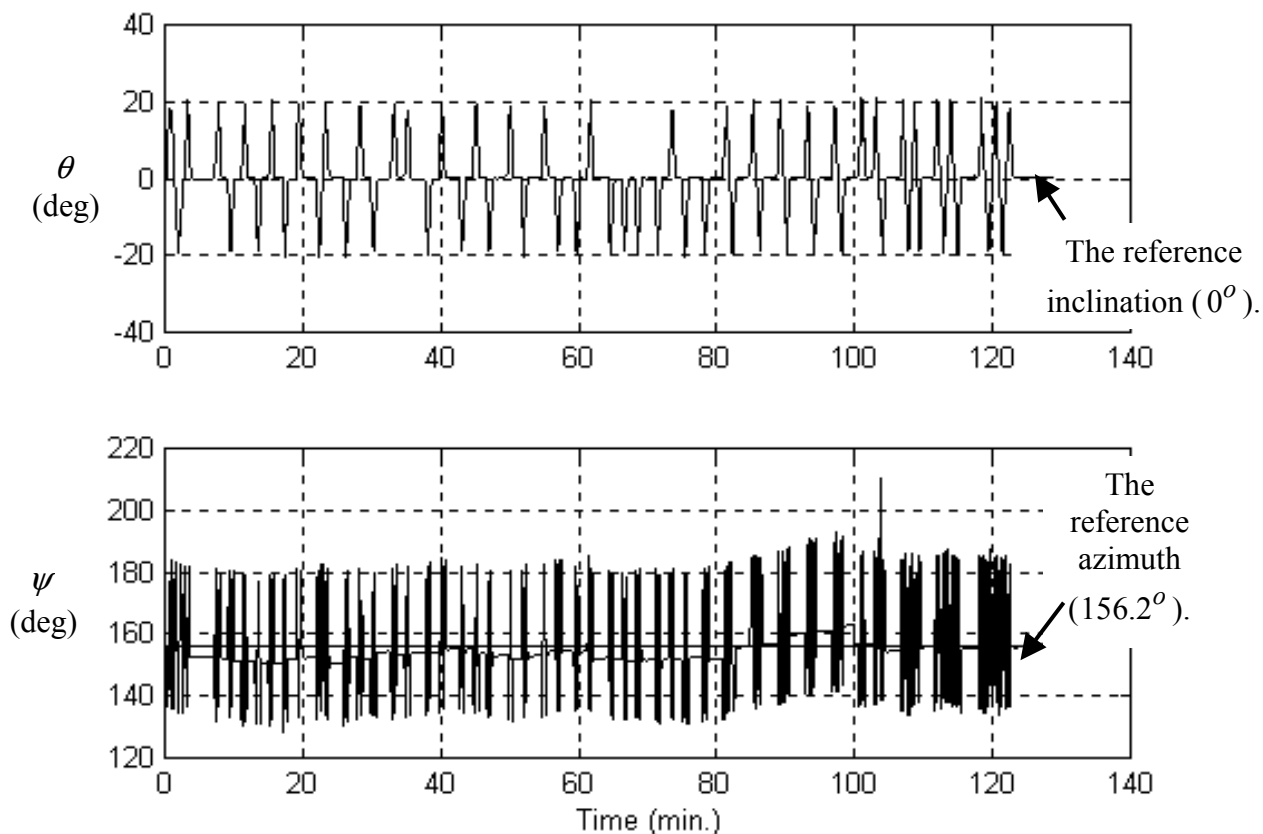


Fig.5.19. The inclination and the azimuth angles in degrees.

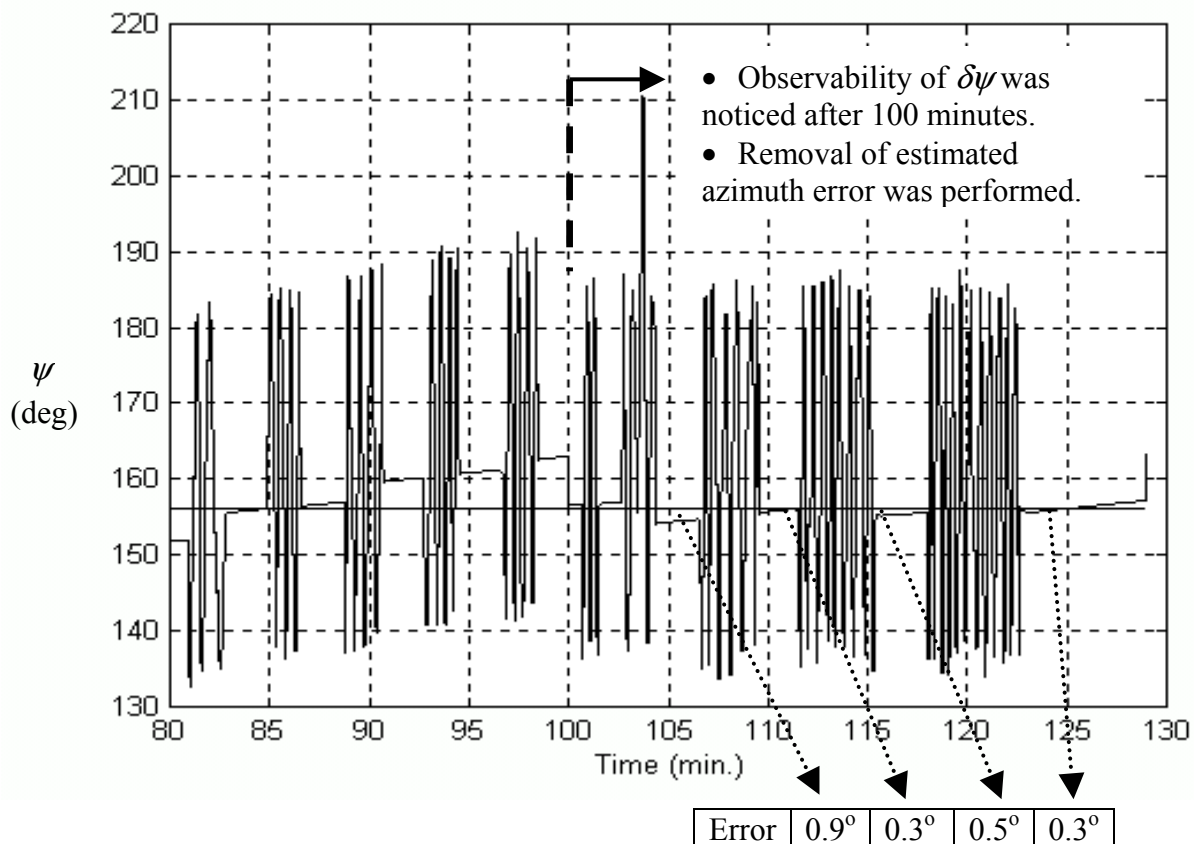


Fig.5.20. The azimuth angle after achieving the convergence of the mean square estimation error and performing error correction.

The unlimited growth of the position errors along the North and the East directions, which respectively correspond to the latitude and the longitude errors  $\delta\phi$  and  $\delta\lambda$ , is shown on Fig.5.21. Errors of less than  $40m$  and  $50m$  were observed over more than two hours along the North ( $\delta P_N$ ) and East ( $\delta P_E$ ) directions, respectively. On the other hand, since an altitude update was performed,  $\delta h$  was limited within the range of  $\pm 0.5m$  and did not drift with time (see Fig.5.21). It can be observed that the altitude error (i.e. position error along the vertical direction) was more noisy than the errors in the other two position components (i.e. the position errors along the horizontal plane). This might be due to the vibration of the surrounding environment, which usually acts along the vertical direction. This effect is expected at the actual drilling site due to the presence of longitudinal vibration along the tool spin axis of the drill pipe. However, since the

Kalman filter is stable by nature, the presence of any external disturbances should not affect the behavior of the observable error states.

The rate of growth of the error components  $\delta P_N$  and  $\delta P_E$  depends on the performance of the accelerometers utilized in this application. These errors were essentially due to the accelerometers bias errors, which drifted over time as shown in Fig.5.22. The three plots shown on Fig.5.22 depict how the accelerometers biases drifted over three hours of stationary experiment. Although part of the bias error was removed by the Kalman filter utilizing the continuous velocity update, the residual errors affected the position components. Another problem, which usually appears when utilizing low cost inertial sensors, is the change of the value of the bias offset of both the FOG and the accelerometers from run to run. This type of error existed in the inertial sensors utilized in this experiment, and it affected the errors associated with all surveying parameters. A navigational grade inertial sensor is therefore recommended to avoid the build-up of those errors that are not observable by the Kalman filter.

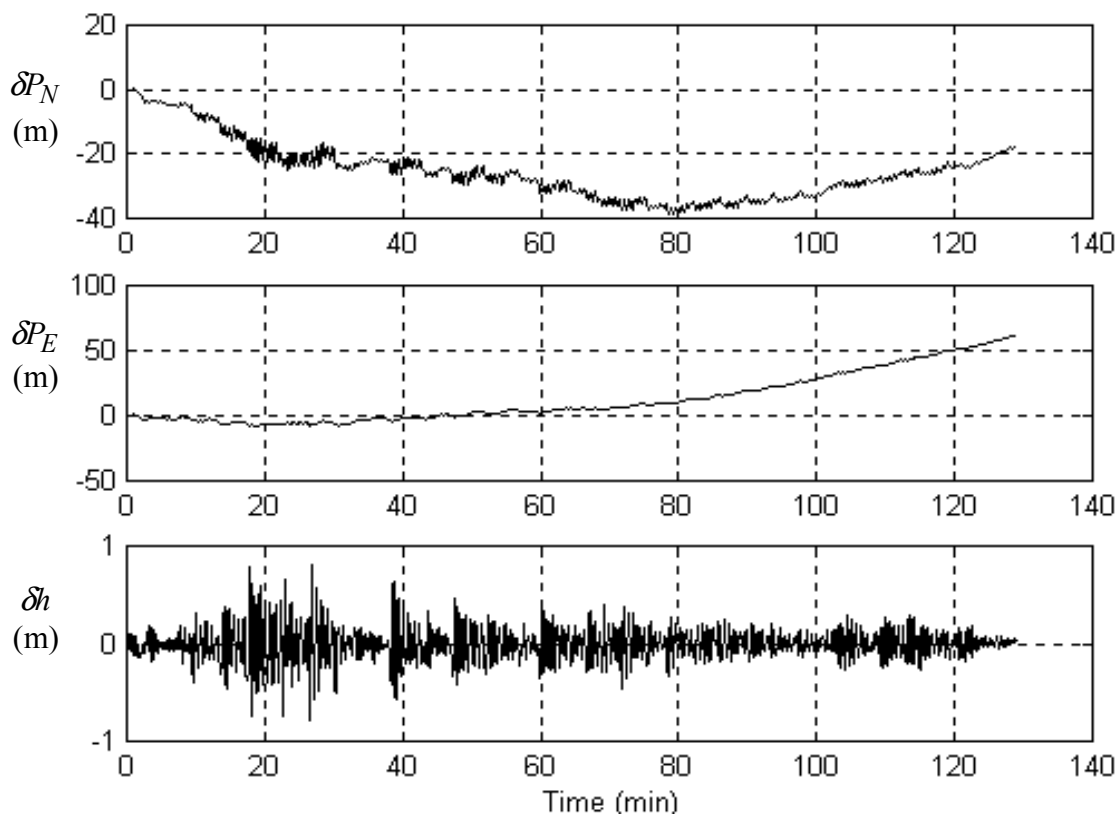


Fig.5.21. Position errors along the North, the East and the vertical directions in meters.

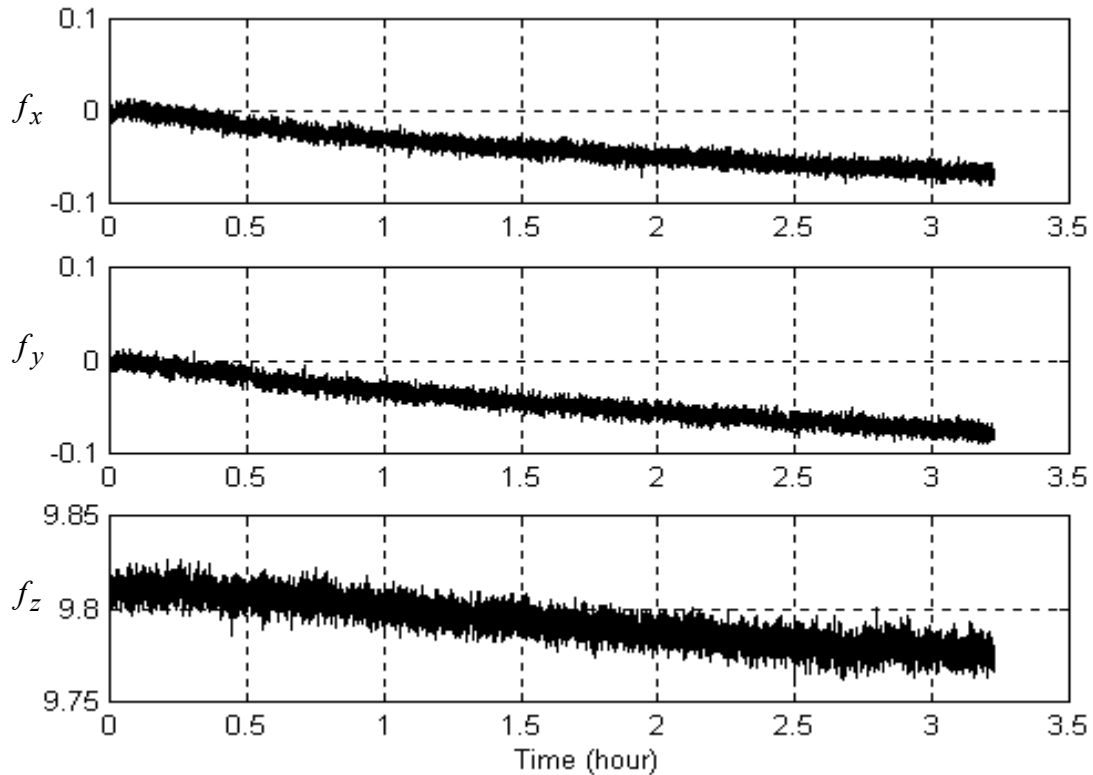


Fig.5.22. Accelerometer measurements (in  $\text{m}/\text{sec}^2$ ) during a stationary experiment.

### 5.3.7.3. ZUPT techniques for limiting velocity errors.

In this experiment, the ZUPT procedure was performed at 37 stations with one to two minutes time interval between neighboring ZUPTs. It was determined that if the time intervals between ZUPTs were more than two minutes, we would have significant deterioration of the system accuracy, given the inertial sensors utilized in this experiment. Longer time intervals can however be applied in a real MWD surveying process with the utilization of navigational grade inertial sensors, which exhibit low drift characteristics.

Since the update phase of Kalman filtering was applied only at ZUPT stations, the MSEE of each of the velocity error states increased between ZUPT stations before returning to its minimum value at the beginning of each ZUPT (see Fig.5.23). Since no ZUPT was performed during the first 4 minutes of the experiment, a considerable growth of the MSEE of each of the velocity error states was observed at the beginning of the

experiment. This was simply because the FOG-based MWD surveying system worked as a stand-alone INS without update. Upon applying ZUPT, the MSEEs of all velocity error states were reduced. If the MSEE of  $\delta V_e$  between  $t=10$  min and  $t=30$  min is analyzed (see Fig.5.23), it can be concluded that it had a relatively high MSEE when the time interval between ZUPTs was extended to 1.8 minutes (at  $t=22$  min) instead of the regular 1-minute interval. This significantly increased the velocity errors and consequently affected the BHA position accuracy.

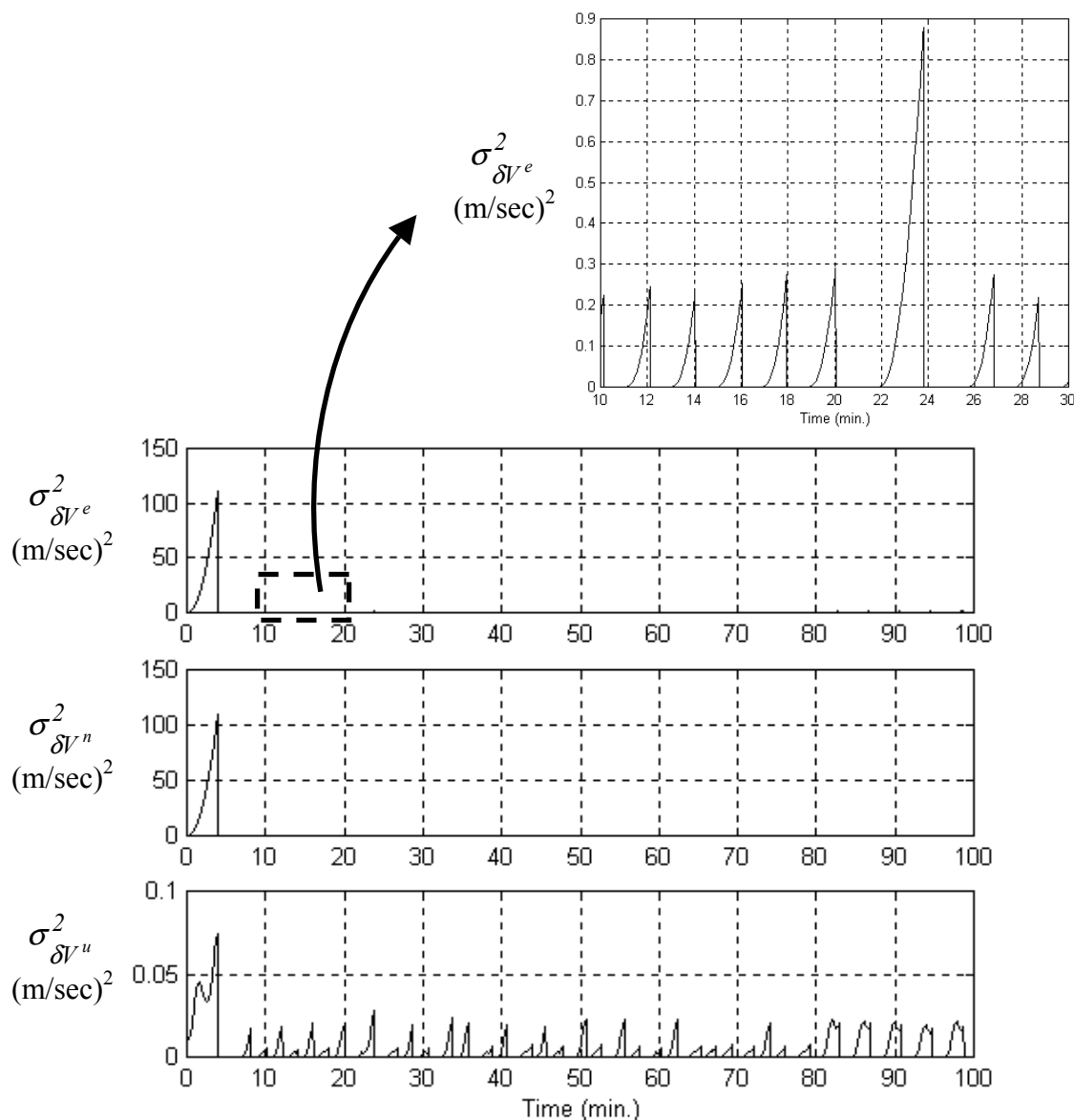


Fig.5.23. The mean square estimation error of the velocity error states in (m/sec)<sup>2</sup> between and during ZUPT procedures.

Since the errors in the position components along the North and East directions were not observable by the Kalman filter,  $\delta P_N$  and  $\delta P_E$  suffered significantly from an unlimited long-term increase. These error components were affected by the velocity errors  $\delta V^n$  and  $\delta V^e$ , respectively. Fig.5.24 shows the velocity errors  $\delta V^e$  and  $\delta V^n$  between  $t = 15$  min and  $t = 35$  min (ZUPT station no.7 to ZUPT station no.14). At each ZUPT station, the velocity error was reset to zero after a certain transitional period of the Kalman filter during which the velocity error oscillated. On the other hand, the position errors along the East and North directions ( $\delta P_E$  and  $\delta P_N$ ) remained constant during measurement at the ZUPT stations and exhibited significant growth during the time intervals between ZUPTs (see Fig.5.25). Between ZUPT stations no.9 and no.10,  $\delta P_E$  and  $\delta P_N$  increased by more than 200 meters. This was due to the relatively long time interval between ZUPTs (1.8 minutes). These two error components continued to increase and showed errors of 500 m and 800 m (respectively for  $\delta P_E$  and  $\delta P_N$ ) after 100 minutes of the same experiment.

#### 5.3.7.4. Impact of the backward velocity error correction.

In order to improve the accuracy of the BHA position components along the East and North directions, the suggested one-step backward velocity error correction was employed [Noureldin et al.<sup>b</sup>, 2001]. This procedure limited the growth of velocity errors between ZUPT intervals and consequently improved the accuracy of both the velocity and the position components. Fig.5.26 shows that  $\delta V^e$  and  $\delta V^n$  were reduced by a ratio of about 1/3 and 1/5, respectively, if compared to their values shown on Fig.5.24 before performing the backward error correction. This significantly improved the accuracy of the position components (see Fig.5.27). At ZUPT station no.10,  $\delta P_E$  was reduced from 400 m to 75 m and  $\delta P_N$  was reduced to about 13 m from 700 m. After the 100-minute experiment, the technique of one-step backward error correction limited the position errors along the horizontal plane to less than 95m.

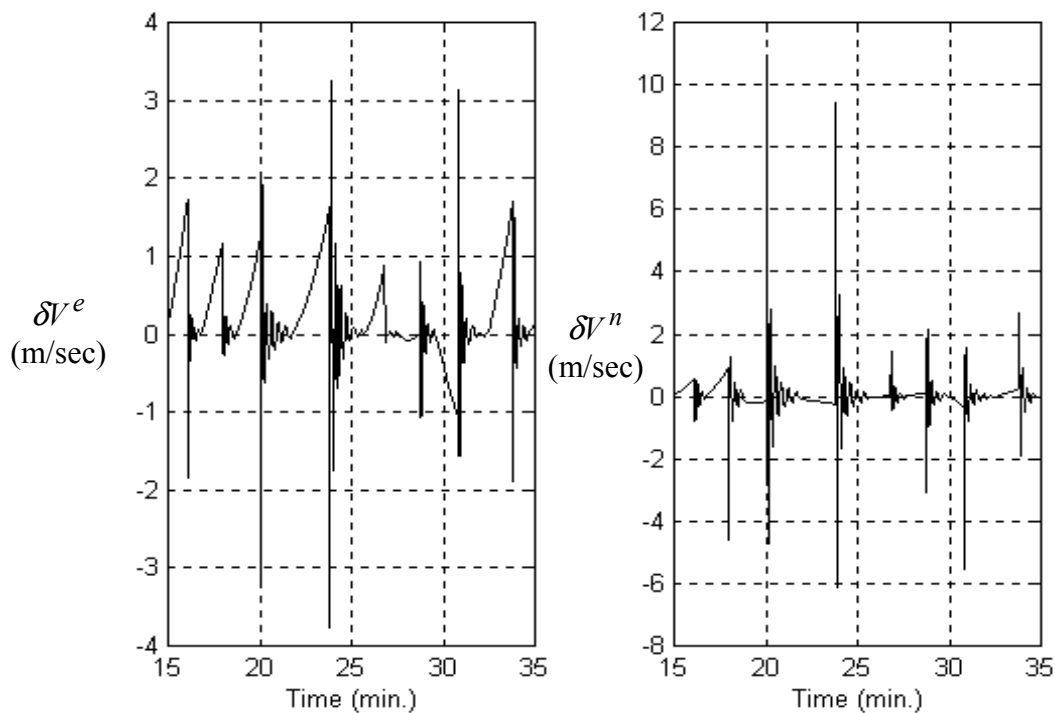


Fig.5.24. The velocity errors (in m/sec) along the East and the North directions ( $\delta V^e$  and  $\delta V^n$ ) between  $t = 15$  min and  $t = 35$  min .

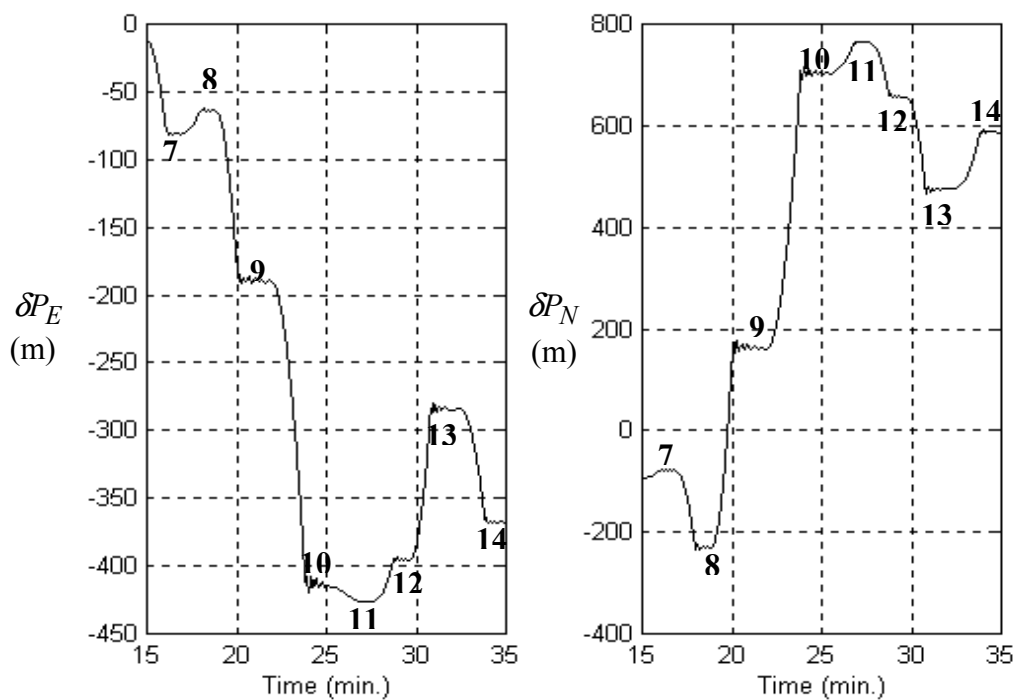


Fig.5.25. The position errors (in meters) along the East and the North directions ( $\delta P_E$  and  $\delta P_N$ ) between  $t = 15$  min and  $t = 35$  min with the number of each ZUPT station indicated.

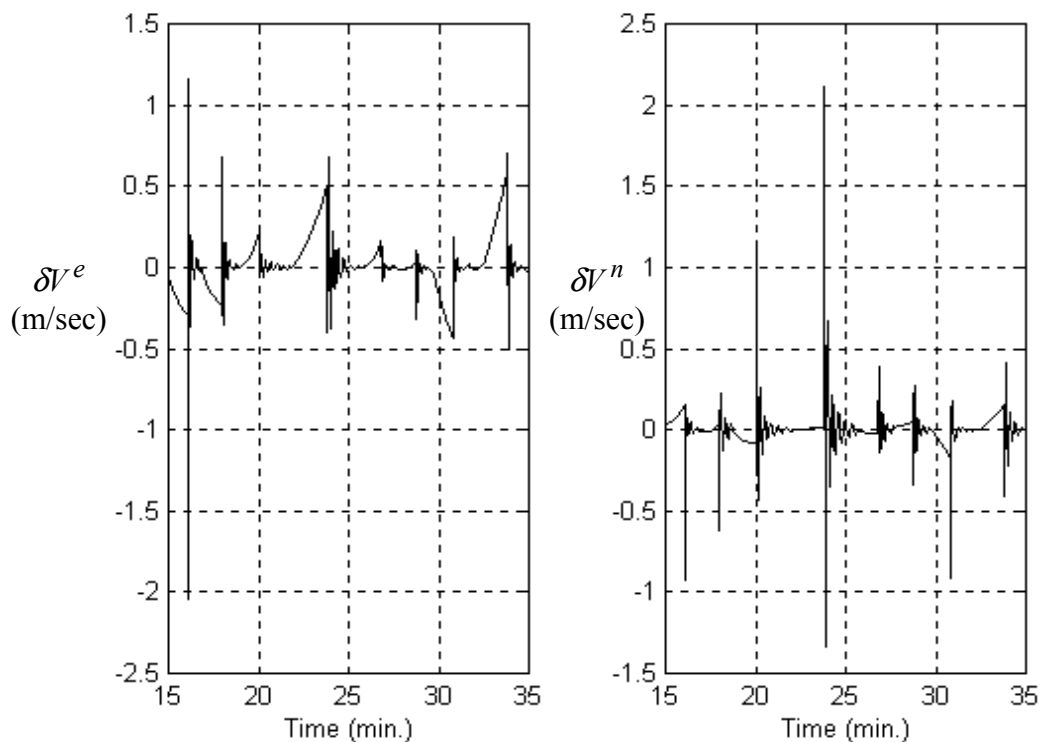


Fig.5.26. The velocity errors (in m/sec) along the East and the North directions ( $\delta V^e$  and  $\delta V^n$ ) between  $t = 15$  min and  $t = 35$  min after performing one-step backward error correction.

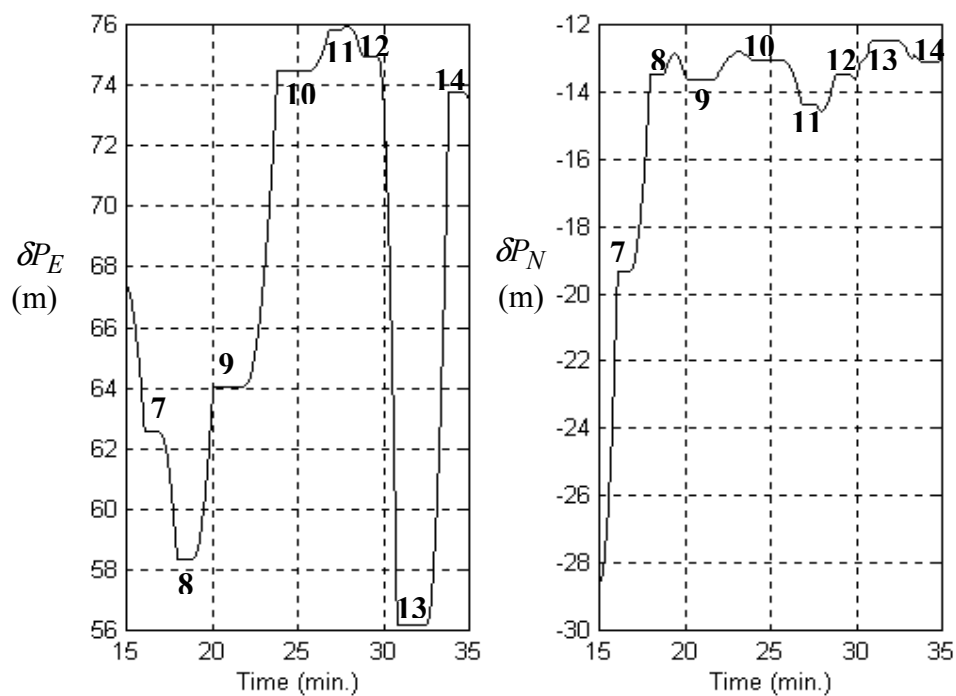


Fig.5.27. The position errors (in meters) along the East and the North directions ( $\delta P_E$  and  $\delta P_N$ ) between  $t = 15$  min and  $t = 35$  min after performing one-step backward error correction.

### 5.3.7.5. Analysis of the errors associated with the transitional inclination angle.

Fig.5.28 shows the inclination errors with respect to different bias errors from  $0.001g$  for navigational grade accelerometers to  $0.01g$  for tactical grade accelerometers while changing the inclination angle between  $0^\circ$  to  $45^\circ$  simulating different transitional limits. The analysis of this three-dimensional graph for small bias errors (i.e.  $\delta f_y = 0.001g$ ) corresponding to navigational grade accelerometers reveals that the inclination error increased slightly by  $0.021^\circ$  with respect to the increase in the inclination angle from  $20^\circ$  to  $45^\circ$ . However, the inclination error experienced an increase of about  $0.2^\circ$  while utilizing tactical grade accelerometers (i.e. values of  $\delta f_y$  around  $0.01g$ ).

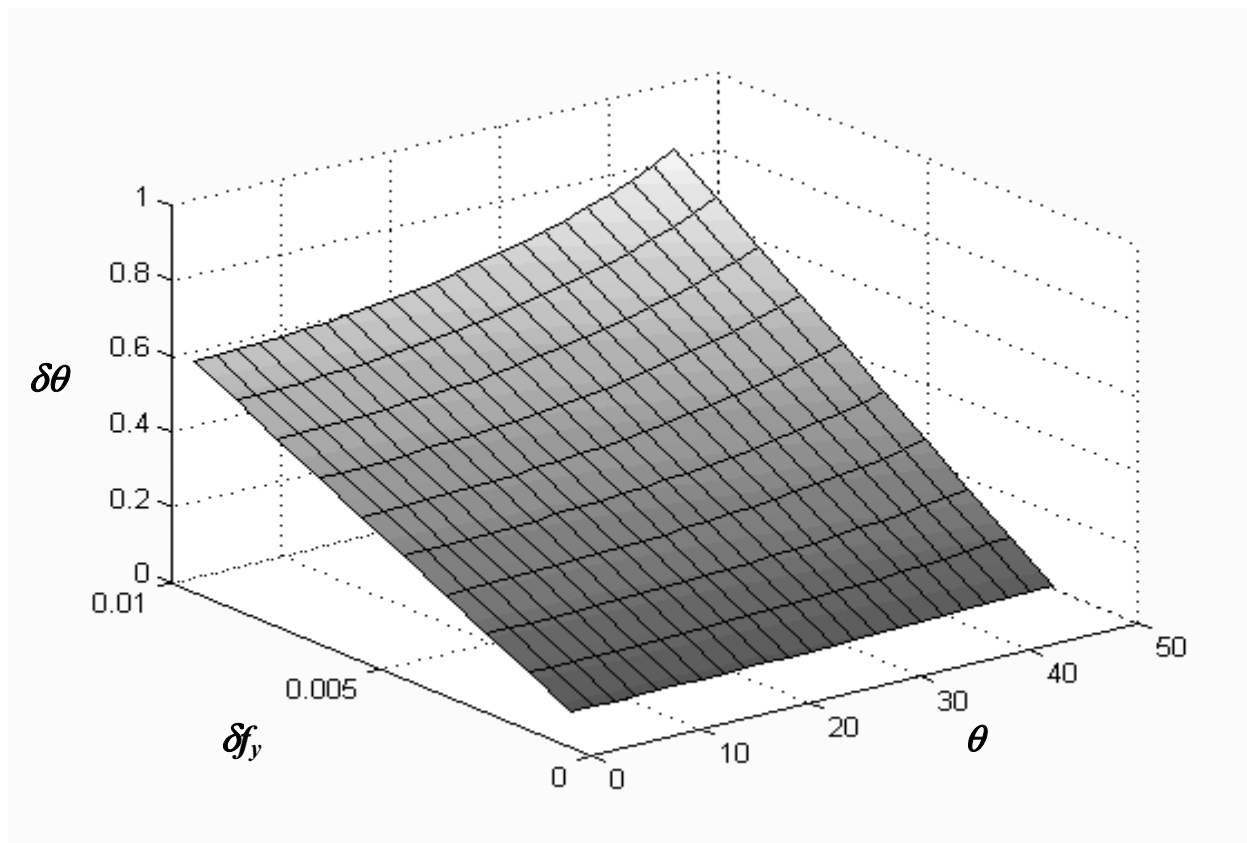


Fig.5.28. Analysis of the inclination error associated with different transitional inclination angles considering different accelerometer errors.

The uncertainties at the accelerometer output became more significant at high inclination. This can be seen on Fig.5.29 for the errors associated with the synthetic rotation component  $\delta\omega_{xs}$ . If Eq.5.44 is examined, one can determine that the reciprocal of the time correlation parameter  $\alpha_y$  (which is usually less than one) attenuates the first term of  $\delta\omega_{xs}$  more than the second term, which is related to the uncertainties at the accelerometer output. The standard deviation of  $\delta\omega_{xs}$  increased to about  $0.015^\circ/\text{sec}$  at high inclination instead of less than  $0.005^\circ/\text{sec}$  for the near vertical section (i.e. less than  $20^\circ$  inclination). The inaccuracy of the synthetic rotation rate component  $\omega_{xs}$  and the inclination angle  $\theta$  at high inclinations may jeopardize the overall MWD surveying accuracy. Therefore, it is recommended to stop the continuous surveying process at small transitional inclination angle when utilizing tactical grade inertial sensors.

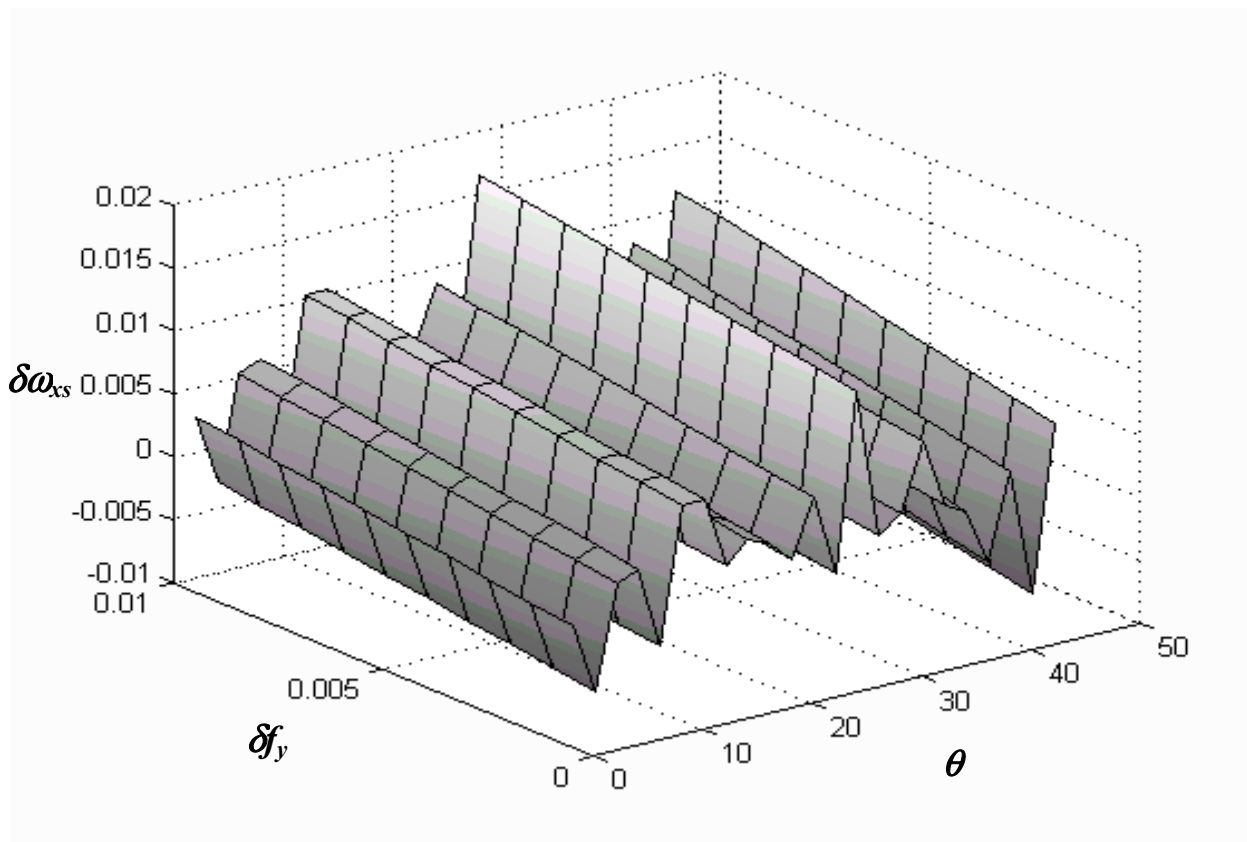


Fig.5.29. Errors of the synthetic rotation rate component with respect to different transitional inclination angles at different accelerometer errors.

### 5.3.8. Applications and limitations of the Single-FOG continuous surveying method in MWD.

The previous sections present a quantitative long-term analysis of various FOG-based continuous surveying errors. Due to the velocity and altitude updates provided to the Kalman filter, the velocity and the altitude errors became strongly observable error states and their MSEEs exhibited very fast convergence to the steady-state minimal value. Therefore, in the long-term, the velocity and the altitude errors were optimally estimated and kept bound.

The strong observability of the velocity and the altitude error states may benefit the other surveying errors and make them observable by the Kalman filter providing some coupling exists between these error states with the velocity or the altitude errors. Fortunately, the inclination and the roll errors ( $\delta\theta$  and  $\delta\phi$ ) are strongly coupled with the velocity errors  $\delta V^n$  and  $\delta V^e$ , respectively [see Appendix C]. The interrelationships between  $\delta V^e$  and  $\delta\phi$  on one hand, and  $\delta V^n$  and  $\delta\theta$  on the other have been observed in all INS-based surveying systems and are known as Schuler loops [Hulsing, 1989; Salychev, 1999]. As a result, the inclination and the roll errors were strongly observable by the Kalman filter and their MSEEs had fast convergence to their minimal values, providing optimal estimates of these two error states. The optimal estimates of  $\delta\theta$  and  $\delta\phi$  were utilized by the continuous aided inertial navigation technique to provide long-term accurate computation of both the inclination and the roll angles. Unfortunately, the azimuth error  $\delta\psi$  is weakly coupled with the velocity errors, thus its MSEE had very slow convergence. Consequently, no optimal estimates of  $\delta\psi$  were provided until the MSEE achieved its steady state minimal value, and the azimuth accuracy became limited by the long-term FOG drift characteristics.

The position errors  $\delta P_E$  and  $\delta P_N$  were determined by integrating  $\delta V^e$  and  $\delta V^n$  (see Fig.5.10). It can be noted, that no coupling exists between these two sets of errors. Therefore, the mathematical integration of the velocity errors, even when bound in time, causes unlimited long-term increase in the position errors, which become limited by the bias errors of the surveying sensors.

Obviously, optimal estimation of the velocity errors is essential to cancel the inclination and the roll errors, to minimize the long-term azimuth error and to partially limit the long-term growth of the position errors. Therefore, either continuous velocity update or regular ZUPT at some predetermined stations was performed to limit the velocity errors. In addition, the one-step backward error correction of the velocity errors was introduced during ZUPT procedures, which dramatically improved both the velocity and the position accuracy.

The choice of the transitional inclination angle and its effect on the surveying accuracy has been studied quantitatively by considering different accelerometer performances. The choice of an exact value of the transitional angle is subject to the desired accuracy and the importance of continuous surveying for the drilling process. When drilling in sections of a multi-well structure, continuous surveying is very critical to avoid collision with nearby wells. In such situations, a larger value of the transitional inclination angle might be considered as long as the surveying accuracy is not dramatically affected. Therefore, the utilization of navigational grade inertial sensors is recommended to reduce the effect of the larger transitional inclination angle on the surveying accuracy.

Unfortunately, continuous surveying performed for the near-vertical section of the well cannot be applied for the entire drilling process due to the error growth in the computation of the inclination angle as the BHA deviates from the vertical direction [Noureldin et al.<sup>b,d</sup>, 2001]. Based on the performance of the surveying sensors utilized, this error becomes significant after an inclination angle of  $20^\circ$ , known as the transitional inclination angle. In fact, at this inclination angle, the *b*-frame axes do not represent the actual motion of the BHA any longer. The *Y*-axis and the *Z*-axis do not point any longer along the forward direction and the vertical direction, respectively. Thus, new axes definition of the *b*-frame is required. Moreover, in highly inclined and horizontal well sections, the rotation along the tool spin axis (monitored by the gyro) is not related to changes in the azimuth angle any more. Consequently, the gyro cannot resolve the azimuth changes. Therefore, when the drilling process reaches the transitional inclination angle, station-based surveying should be performed, and the measurements from the gyro

and the accelerometers should be assessed at some surveying stations while the BHA is completely stationary. In addition, the Y-axis becomes colinear with the tool spin axis while the Z-axis is pointing upward. Fig.5.30 shows a schematic diagram of the *b*-frame axes orientation for the different sections of the horizontal well and their change at the transitional inclination angle.

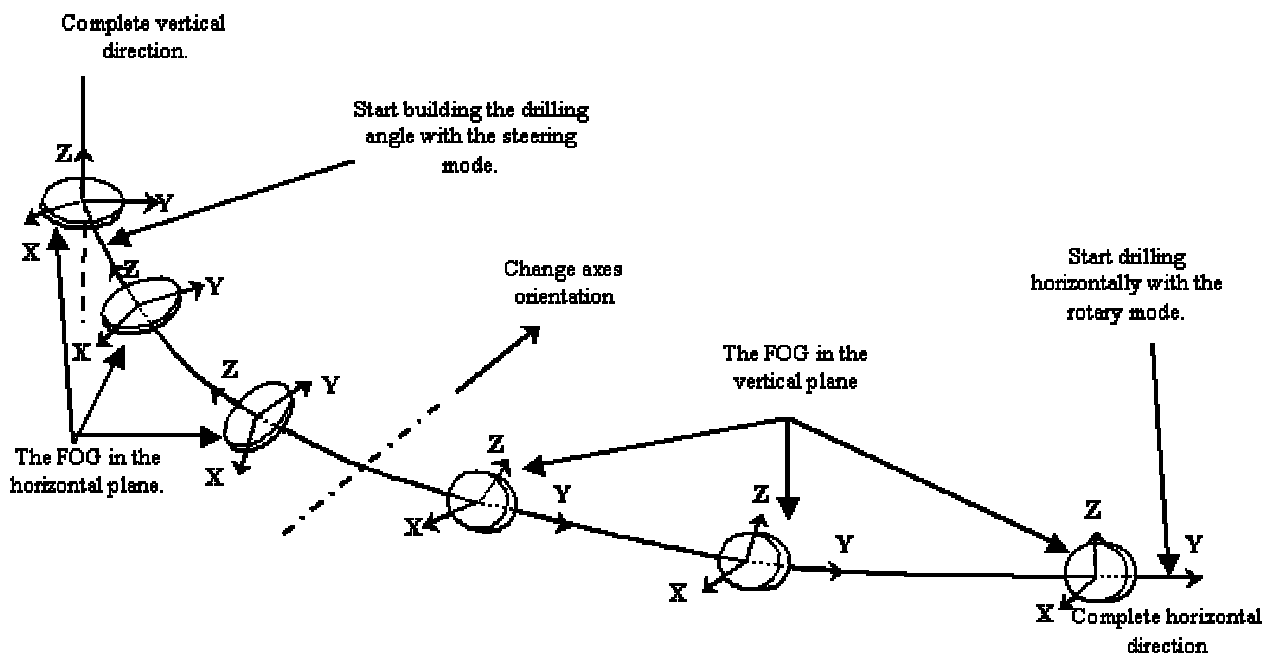
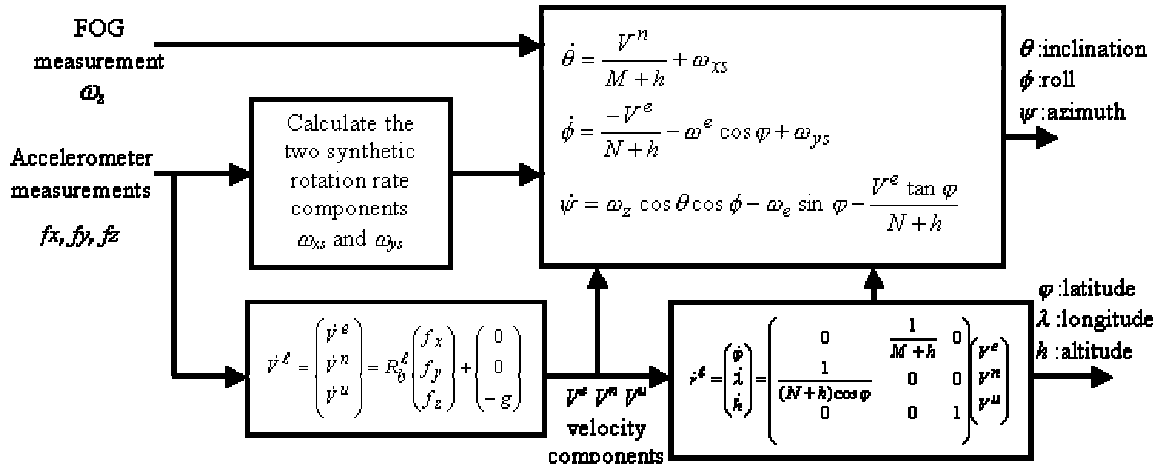


Fig.5.30. A schematic diagram showing the orientation of the FOG and the accelerometers during the horizontal drilling processes.

#### 5.4. Station-based surveying of highly inclined and horizontal well sections.

The aim of this section is to: (1) introduce the gyroscopic station-based surveying method for highly inclined and horizontal well sections; (2) analyze the surveying errors associated with this method at different orientations; and (3) apply some real-time digital signal processing techniques (discussed in Chapter 4) to limit these surveying errors.



$N$ : The prime vertical radius of curvature of the Earth's surface (East-West)  
 $M$ : The meridian radius of curvature (North-South).

Fig.5.9. Block diagram of the Single-FOG technique for MWD continuous surveying process.

### 5.3.3. Error state model of the MWD surveying parameters.

The error state vector for the proposed Single-FOG MWD surveying system includes coordinate errors ( $\delta\varphi, \delta\lambda, \delta h$ ), velocity errors ( $\delta V^e, \delta V^n, \delta V^u$ ), inclination error ( $\delta\theta$ ), roll error ( $\delta\phi$ ) and azimuth error ( $\delta\psi$ ). Since the errors in dynamic systems are variable in time, they are described by differential equations [Titterton and Weston, 1997]. Linearization of a non-linear dynamic system is the most common approach to derive a set of linear differential equations that define the error states of a dynamic system [Britting, 1971; Schwarz and Wei, 1990; Titterton and Weston, 1997]. For example, the error in the BHA coordinate vector  $\delta r^\ell$  is the difference between the true components  $r^\ell$  and the computed ones  $\bar{r}^\ell$ . Using a Taylor series expansion to a first order approximation, the time derivative of the BHA coordinate errors can be obtained as [Schwarz and Wei, 1990]:

$$\delta \dot{r}^\ell = \dot{\bar{r}}^\ell - \dot{r}^\ell = \frac{\partial(\dot{r}^\ell)}{\partial r^\ell} \delta r^\ell \quad (5.30)$$

Thus, the time rate of change of the BHA position errors can be obtained from Eq.5.6:

$$\delta \dot{r}^\ell = \begin{pmatrix} \delta \dot{\varphi} \\ \delta \dot{\lambda} \\ \delta \dot{h} \end{pmatrix} = \begin{pmatrix} 0 & \frac{1}{M+h} & 0 \\ \frac{1}{(N+h)\cos\varphi} & 0 & 0 \\ 0 & 0 & 1 \end{pmatrix} \begin{pmatrix} \delta V^e \\ \delta V^n \\ \delta V^u \end{pmatrix} \quad (5.31)$$

Similarly, the time rate of change of the BHA velocity errors can be written as follows:

$$\delta \dot{V}^\ell = \delta R_b^\ell f^b + R_b^\ell \delta f^b + \delta g^\ell \quad (5.32)$$

where  $\delta f^b$  are the accelerometers measurement errors and  $\delta g^\ell$  is the gravity computational error. It has been shown that  $\delta g^\ell$  is mainly caused by altitude errors ( $\delta h$ ) and is expressed as [Schwarz and Wei, 1999]:

$$\delta g^\ell = \frac{2g}{R} \delta h = \begin{pmatrix} 0 & 0 & 0 \\ 0 & 0 & 0 \\ 0 & 0 & 2g/R_o \end{pmatrix} \delta r^\ell \quad (5.33)$$

where  $R_o$  is the mean radius of the Earth. In addition, the first term of the right hand side of Eq.5.32 ( $\delta R_b^\ell f^b$ ) is given as  $(-F^\ell \varepsilon^\ell)$  [Schwarz and Wei, 1999], where  $\varepsilon^\ell = (\delta\theta \quad \delta\varphi \quad \delta\psi)^T$  is the vector of the attitude angle errors and  $F^\ell$  is the skew-symmetric matrix corresponding to  $f^\ell = R_b^\ell f^b = (f^e \quad f^n \quad f^u)^T$  and is given as:

$$F^\ell = \begin{pmatrix} 0 & -f_u & f_n \\ f_u & 0 & -f_e \\ -f_n & f_e & 0 \end{pmatrix} \quad (5.34)$$

The BHA velocity error can then be written as

$$\delta \dot{V}^\ell = \begin{pmatrix} 0 & f_u & -f_n \\ -f_u & 0 & f_e \\ f_n & -f_e & 0 \end{pmatrix} \varepsilon^\ell - \begin{pmatrix} 0 & 0 & 0 \\ 0 & 0 & 0 \\ 0 & 0 & 2g/R_o \end{pmatrix} \delta r^\ell + R_b^\ell \delta f^b \quad (5.35)$$

The error in each of the three attitude angles is treated individually using the same approach discussed above. The inclination, the roll and the azimuth errors can be respectively described with the following 1<sup>st</sup> order differential equations [Noureddin et

al.<sup>a</sup>, 2001]:

$$\delta\dot{\theta} = \frac{\delta V^n}{M+h} + \delta\omega_{xs} \quad (5.36)$$

$$\delta\dot{\phi} = -\frac{\delta V^e}{N+h} + \delta\omega_{ys} \quad (5.37)$$

$$\delta\dot{\psi} = -\frac{\delta V^e \tan \varphi}{N+h} + (\cos \theta \cos \phi) \delta\omega_z \quad (5.38)$$

where  $\delta\omega_{xs}$  and  $\delta\omega_{ys}$  are respectively the errors in the synthetic rotation rate components  $\omega_{xs}$  and  $\omega_{ys}$ , while  $\delta\omega_z$  is the error in the FOG measurement. Mathematical analysis of the interrelationships between the different surveying errors discussed above is given in Appendix C.

The accelerometers and FOG biases and constant drifts are determined by field calibration and the only remaining errors are considered random. These residual random errors are modelled as stochastic processes. The accelerometer and the FOG random errors are usually correlated in time and modelled as first order Gauss Markov processes as follows [Gelb, 1974; Brown and Hwang, 1992]:

$$\dot{\mathcal{J}}^b = \begin{pmatrix} \dot{\mathcal{J}}_x \\ \dot{\mathcal{J}}_y \\ \dot{\mathcal{J}}_z \end{pmatrix} = \begin{pmatrix} -\alpha_x & 0 & 0 \\ 0 & -\alpha_y & 0 \\ 0 & 0 & -\alpha_z \end{pmatrix} \begin{pmatrix} \mathcal{J}_x \\ \mathcal{J}_y \\ \mathcal{J}_z \end{pmatrix} + \begin{pmatrix} \sqrt{2\alpha_x\sigma_x^2} \\ \sqrt{2\alpha_y\sigma_y^2} \\ \sqrt{2\alpha_z\sigma_z^2} \end{pmatrix} w(t) \quad (5.39)$$

where  $\alpha_x, \alpha_y$  and  $\alpha_z$  are the reciprocals of the time correlation parameters of these random processes respectively associated with the acceleration measurements  $f_x, f_y$  and  $f_z$ ;  $\sigma_x, \sigma_y$  and  $\sigma_z$  are the standard deviations of these random processes; and  $w(t)$  is a unity-variance white Gaussian noise. Similarly, the randomness at the FOG measurements is described as [Brown and Hwang, 1992]:

$$\delta\dot{\omega}_z = -\beta \delta\omega_z + \sqrt{2\beta\sigma_g^2} w(t) \quad (5.40)$$

where  $\beta$  is the reciprocal of the time correlation parameter of the random process associated with the FOG measurement,  $\sigma_g$  is the standard deviation of this random process and  $w(t)$  is unity variance white Gaussian noise.

The errors of the two synthetic rotation rate components can be determined from their definitions given in Eq.5.24 and Eq.5.25 as:

$$\delta\omega_{xs}(t_k) = \frac{\delta\theta(t_k) - \delta\theta(t_{k-1})}{t_k - t_{k-1}} \quad (5.41)$$

where  $\delta\theta(t_k)$  is the inclination angle error at time  $t_k$  and  $\delta\theta(t_{k-1})$  is the inclination angle error at time  $t_{k-1}$ ,

$$\delta\omega_{ys}(t_k) = \frac{\delta\phi(t_k) - \delta\phi(t_{k-1})}{t_k - t_{k-1}} \quad (5.42)$$

where  $\delta\phi(t_k)$  is the roll angle error at time  $t_k$  and  $\delta\phi(t_{k-1})$  is the roll angle error at time  $t_{k-1}$ .

The error in the inclination angle  $\delta\theta$  is obtained from Eq.5.20 and can be written as follows:

$$\delta\theta = \frac{-\delta f_y}{g \cos \theta} \quad (5.43)$$

If we substitute  $\delta\theta(t_k)$  and  $\delta\theta(t_{k-1})$  in Eq.5.41 using Eq.5.43, the error in the synthetic rotation rate  $\delta\omega_{xs}$  can be written as:

$$\delta\omega_{xs} = \frac{\alpha_y}{g \cos \theta} \delta f_y - \frac{\sqrt{2\alpha_y \sigma_y^2}}{g \cos \theta} w(t) \quad (5.44)$$

Consequently, the first order differential equation describing the inclination error (Eq.5.43) is given as:

$$\delta\dot{\theta} = \frac{\delta V^n}{M+h} + \frac{\alpha_y}{g \cos \theta} \delta f_y - \frac{\sqrt{2\alpha_y \sigma_y^2}}{g \cos \theta} w(t) \quad (5.45)$$

The error in the roll angle  $\delta\phi$  is obtained from Eq.5.23 and can be presented as:

$$\delta\phi = \frac{-f_z \delta f_x + f_x \delta f_z}{f_x^2 + f_z^2} \quad (5.46)$$

If we substitute from Eq.5.46 by  $\delta\phi(t_k)$  and  $\delta\phi(t_{k-1})$  in Eq.5.42 with the assumption that the accelerometer measurements do not change between any two consecutive time instants  $t_{k-1}$  and  $t_k$ , the error in the synthetic rotation rate  $\delta\omega_{ys}$  can be written as:

$$\delta\omega_{ys} = \frac{\alpha_x f_z}{f_x^2 + f_z^2} \delta f_x - \frac{\alpha_z f_x}{f_x^2 + f_z^2} \delta f_z + \frac{f_x \sqrt{2\alpha_z \sigma_z^2} - f_z \sqrt{2\alpha_x \sigma_x^2}}{f_x^2 + f_z^2} w(t) \quad (5.47)$$

Consequently, the first order differential equation describing the roll error (Eq.23) can be given as:

$$\delta\dot{\phi} = -\frac{\delta V^e}{N+h} + \frac{\alpha_x f_z}{f_x^2 + f_z^2} \delta f_x - \frac{\alpha_z f_x}{f_x^2 + f_z^2} \delta f_z + \frac{f_x \sqrt{2\alpha_z \sigma_z^2} - f_z \sqrt{2\alpha_x \sigma_x^2}}{f_x^2 + f_z^2} w(t) \quad (5.48)$$

In practical systems employing INS technology, the long-term accuracy deteriorates due to inertial sensor errors and computational errors. The inertial sensor errors are residual random errors in the output of both the FOG and the accelerometers that remain after the removal of the corresponding constant biases by field calibration. Since the remaining FOG error  $\delta\omega_s$ , and accelerometer errors  $\delta f^b = (\delta f_x \quad \delta f_y \quad \delta f_z)^T$  are random, they are described by stochastic processes.

The computational errors of the FOG-based MWD surveying system are the errors associated with the calculation of the surveying parameters and therefore, they are known also as surveying errors [Wolf and de Wardt, 1981; Thorogood, 1989]. These errors include coordinate errors ( $\delta r^\ell : \delta\phi, \delta\lambda, \delta h$ ), velocity errors ( $\delta V^\ell : \delta V^e, \delta V^n, \delta V^u$ ), and attitude errors ( $\varepsilon^\ell : \delta\theta, \delta\phi, \delta\psi$ ). The latitude and the longitude angle errors  $\delta\phi$  and  $\delta\lambda$  can be presented as distance errors  $\delta P_N = (M+h) \times \delta\phi$  and  $\delta P_E = (N+h) \cos\phi \times \delta\lambda$  along the North and East directions. In order to perform dynamic error analysis of the described FOG-based MWD surveying system (see Fig.5.9), differentiation of the

relevant system equations was performed [Noureldin et al.<sup>a</sup>, 2001]. A block diagram describing the dynamic behavior of these error states is shown on Fig.5.10.

The inertial sensor errors and the computational (surveying) errors can be combined together to form the error state vector  $\chi$ .

$$\chi = \left( \delta\varphi \quad \delta\lambda \quad \delta h \quad \delta V^e \quad \delta V^n \quad \delta V^u \quad \delta\theta \quad \delta\phi \quad \delta\psi \quad \delta\omega_z \quad \delta f_x \quad \delta f_y \quad \delta f_z \right)^T \quad (5.49)$$

These errors are passed from one estimate to another with the overall uncertainty in the precision of the estimated quantity drifting with time [Schwarz and Wei, 1990; Titterton and Weston, 1997]. Therefore, error models are required for analysis and estimation of different error sources associated with the proposed MWD surveying system.

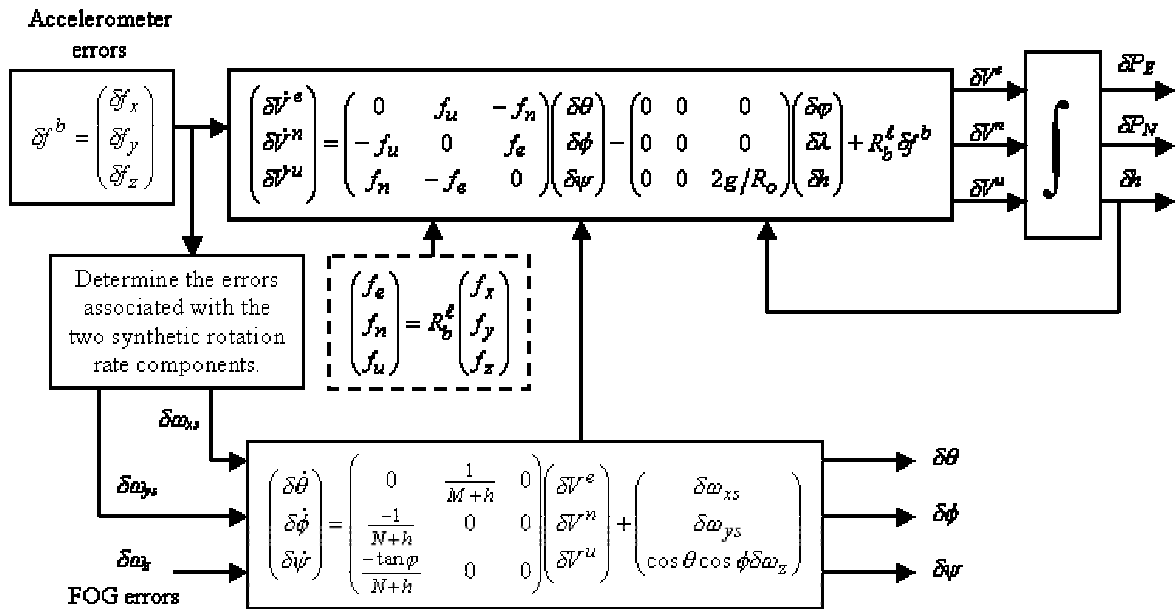


Fig.5.10. Block diagram of FOG-based MWD surveying errors.

### 5.3.4. Quantitative long-term analysis of surveying errors.

The random processes associated with the components of the error state vector  $\chi$  were represented by a group of first-order state equations (see Fig.5.10), which can be augmented together and described by the following discrete linear state equation:

$$\chi_k = F_{k,k-1} \chi_{k-1} + G_{k-1} W_{k-1} \quad (5.50)$$

where  $\chi_k$  is the error state vector  $\chi$  at time  $t_k$ ,  $F_{k,k-1}$  is a dynamic matrix relating  $\chi_{k-1}$  to  $\chi_k$ ,  $W_{k-1}$  is a random forcing function which can be regarded as unity-variance white Gaussian noise with  $G_{k-1}$  being its coefficient vector [Brown and Hwang, 1997]. In order to provide optimal estimation of the above error states  $\chi_k$ , observations for the above discrete system (Eq.5.50) can be provided in the following form:

$$y_k = H_k \chi_k + v_k \quad (5.51)$$

where  $y_k$  is the observations vector at time  $t_k$ ,  $H_k$  is the design matrix giving the ideal noiseless relationship between the observations vector and the state vector, and  $v_k$  is the vector of observations random noise, which is assumed to be white sequence not correlated with  $W_k$  (i.e.  $E(W_k v_k^T) = 0$ ). The observations vector should be formed from measurements of superior accuracy other than those provided by the FOG and the accelerometers.

The Kalman filter was employed as an optimal estimation tool for the error states  $\chi$ . Kalman filtering methods provide a sequential recursive algorithm for an optimal least-mean variance estimation of the error states [Gelb, 1974; Brown and Hwang, 1997]. The Kalman filtering method and its derivation are well described by Brown and Hwang (1997). Appendix D shows the procedure of the Kalman filtering algorithm and presents the related design considerations.

In addition to its benefits as an optimal estimator, the Kalman filter provides real-time statistical data related to the estimation accuracy of the error states, which is very useful for quantitative error analysis. The filter generates its own error analysis with the computation of the error covariance matrix  $P_k$ , which gives an indication of the estimation accuracy [Gelb, 1974]:

$$P_k = E\left([\chi_k - \hat{\chi}_k][\chi_k - \hat{\chi}_k]^T\right) \quad (5.52)$$

where  $\hat{\chi}_k$  is the estimated error state vector provided at time  $t_k$  for the error states  $\chi_k$ . The elements of the major diagonal of the error covariance matrix  $P_k$  represent the mean square estimation error (MSEE) of each of the error states defined in Eq.5.50 [Brown and Hwang, 1997]. During real-time operations, the diagonal elements of  $P_k$  should be tested to check the convergence towards minimal MSEE. Based on the

observations provided to the system, three categories of error states can be identified:

The first category includes the observable error states, which are optimally estimated by the Kalman filter providing short-term convergence to the minimum MSEE.

The second category includes the weakly-observable error states which might be optimally estimated by the Kalman filter in the very long-term only. The MSEE of this category of error states exhibits a very slow convergence to the absolute minimum value.

The third category is related to unobservable error states, which suffer from the divergence of their corresponding MSEE. The MSEE divergence is due to the fact that the Kalman filter fails to provide an optimal estimate of these error states [Brown and Hwang, 1997].

If a non-optimal estimation exists for one or more of the error states, this will be evidenced by an unlimited increase of the corresponding elements along the major diagonal of the error covariance matrix  $P_k$ . As a result, the estimation error of these error states becomes unstable, and one would expect long-term deterioration of the accuracy of the corresponding surveying parameter. If this problem exists for some of the surveying parameters, this means that the observations  $y_k$  do not provide enough information to estimate all error states. Only those error states that are observable by the Kalman filter exhibit stable long-term behavior, with estimation accuracies of the different error states depending on the steady state values of the corresponding MSEE.

The real-time implementation of the Kalman filter for estimating the MWD surveying error states is incorporated with the error system model (Eqs.5.50 and 5.51 ) as shown in Fig.5.11 [Gelb, 1974]. The estimation process starts by providing an *a priori* estimate  $\hat{\chi}_k(-)$  of the error state vector  $\chi_k$  based on the estimate calculated for the previous time instant  $\hat{\chi}_{k-1}(+)$  (Fig.5.11). The error estimate  $\hat{\chi}_k(+)$  at the present time instant  $t_k$  is obtained by updating the *a priori* estimate  $\hat{\chi}_k(-)$  as follows [Gelb, 1974]:

$$\hat{\chi}_k(+) = \hat{\chi}_k(-) + K_k(y_k - H_k \hat{\chi}_k(-)) \quad (5.53)$$

where  $K_k$  is the Kalman gain matrix [Gelb, 1974]. The error covariance matrix  $P_k(+)$  associated with the estimate  $\hat{\chi}_k(+)$  is determined at each time instant  $t_k$  as:

$$P_k(+) = [I - K_k H_k] P_k(-) \quad (5.54)$$

where  $P_k(-)$  is the error covariance matrix associated with  $\hat{\chi}_k(-)$ , which depends on the error covariance matrix  $P_{k-1}(+)$  determined at  $t_{k-1}$ . If the elements of the major diagonal of  $P_k(+)$  are continuously tested during the drilling process, the long-term analysis of surveying errors can be quantified in terms of the convergence of the corresponding MSE. Since  $H_k$  is usually composed of constant elements, it can be observed that the divergence of the diagonal elements of  $P_k(+)$  is due to unstable, relatively high, values of the Kalman gain  $K_k$ . Furthermore, if Eq.5.53 is examined, it can be concluded that the difference between the actual measurements  $y_k$  and the predicted measurements  $H_k \hat{\chi}_k(-)$  is used by the Kalman filtering algorithm as a basis for significant corrections of the error estimates. Hence, this gain can improve the estimate. In general, it has been shown that the Kalman gain is directly proportional to the estimate error covariance and inversely proportional to the variance of the measurement noise [Brown and Hwang, 1997]. Therefore, if there are no measurements (observations) available for some error states (corresponding to extremely high measurement noise), one can expect relatively high values of the corresponding Kalman gain. These high gain values cause long-term instability of the error estimates, thus deteriorating the accuracy of the corresponding surveying parameters.

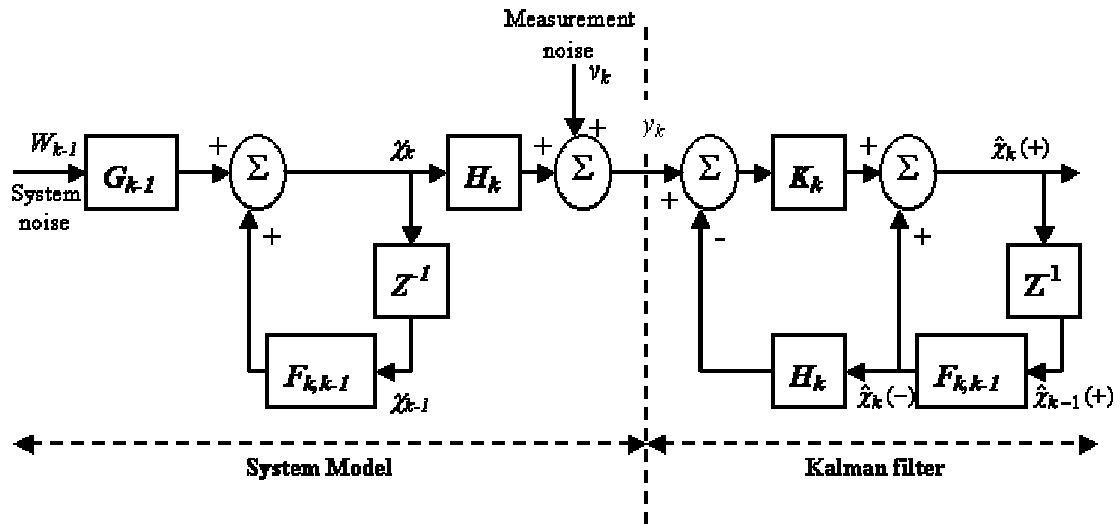


Fig.5.11. Integration between the system model and the discrete Kalman filter [after Gelb, 1974].

Long-term testing of the MSEE of all surveying errors and the analysis of the surveying accuracy of the FOG-based MWD surveying system are performed in a comprehensive (more than 2 hours) experiment using the experimental setup described in Appendix B. This setup is capable of providing continuous rotational and linear motion along three mutually orthogonal axes in the near vertical direction (with inclination angle less than  $20^\circ$ ) similar to the motion experienced by the BHA downhole (see Fig.5.12). The measurements of both the FOG (RA 2100, KVH, Orland Park, IL,  $7.2^\circ/\text{hr}$  drift rate) and the accelerometers (Tri-Axial-2412-005, Silicon Designs, Issaquah, WA) were digitized using a 12 bit A/D card (DAQCard-1200, National Instruments, Austin, TX) with 128 Hz sampling frequency connected to a laptop computer (Compac-433 MHz AMD Processor, Houston, TX) for further analysis. In order to reduce the uncertainty at the outputs of both the FOG and the accelerometers, the measurements were averaged in 1-second time intervals. This averaging process helped in removing some of the high frequency noise components, thus reducing the measurement uncertainties and avoiding the long-term propagation of inertial sensor errors and their effect on surveying errors.

During the same experiment, the surveying process was stopped regularly for short intervals at  $0^\circ$  inclination and at known azimuth angle ( $156.2^\circ$ ) in order to analyze both the inclination and the azimuth with respect to external references. The inclination reference of  $0^\circ$  was determined using an accurate angular scale provided along the  $x$ -axis (inclination axis). This scale was prepared using a rotary table with an accurate indexing head, which gave an accumulative error of less than 1% (see Appendix B). A similar scale was provided to determine the angular changes along the  $z$ -axis (azimuth axis). The azimuth reference of  $156.2^\circ$  was determined using an accurate electronic compass (C100, KVH, Orland Park, IL).

### **5.3.5. Real-time techniques for limiting long-term surveying errors.**

If the FOG-based MWD surveying system operated as stand alone INS utilizing only the FOG and the accelerometer measurements, unlimited growth of surveying errors would be observed. The limitation of the long-term surveying errors depends entirely on how many observations are supplied to the Kalman filter and how accurate these

observations are. Since these observations help the Kalman filter determining the optimal estimation of the surveying errors, they are called aiding sources [Stephenson and Wilson, 1992].

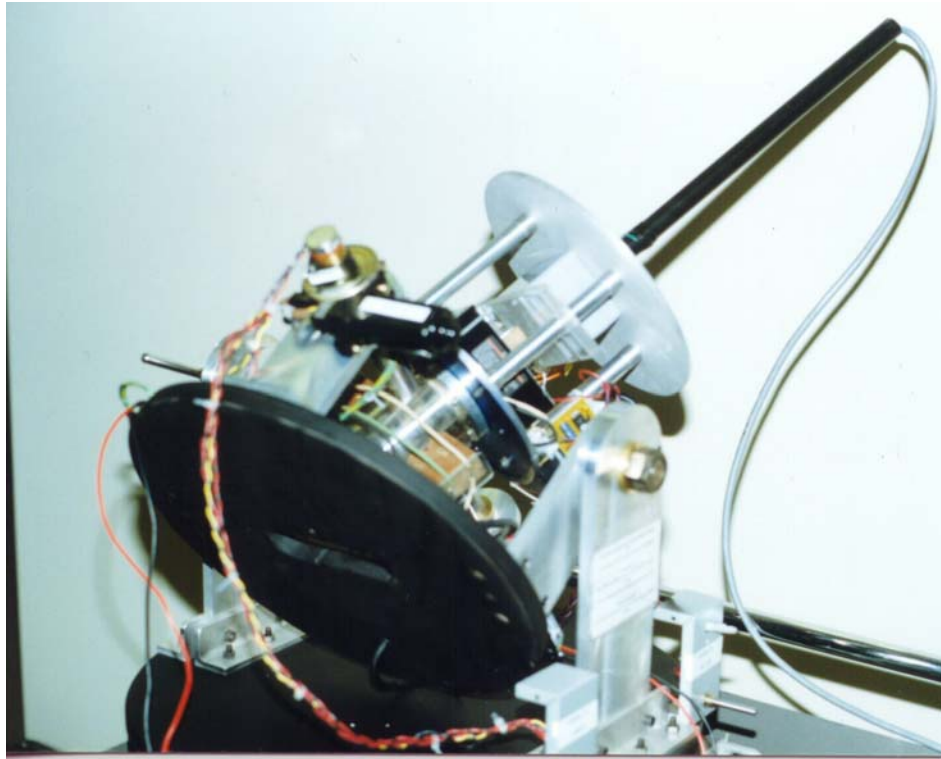


Fig.5.12. The setup while rotating about the three mutually orthogonal axes.

#### **5.3.5.1. Continuous aided inertial navigation technique.**

Two types of continuous aiding sources can be utilized for the MWD surveying system. The first type is the altitude aiding which is based on the continuous measurement of the length of the drill pipe. The second type is the velocity aiding which is based on the continuous measurement of the BHA penetration rate along the downhole formation. The measurements of these two aiding sources are provided in real-time by the MWD equipment and can be integrated with the FOG-based surveying system. The incorporation of the aiding sources with the FOG and the accelerometer measurements provides what is known as aided inertial navigation [Stephenson and Wilson, 1992]. Fig.5.13 shows a block diagram of the technique of aided inertial navigation employing

Kalman filtering. The inertial outputs of the FOG-based system are compared to the outputs of the aiding sources. The errors in between are subjected to Kalman filtering to enhance the performance of the FOG-based system by removing the effect of residual random errors during the continuous surveying process. The errors estimated by the Kalman filter are removed from the outputs of the FOG-based system to provide corrected inertial output in a closed loop fashion.

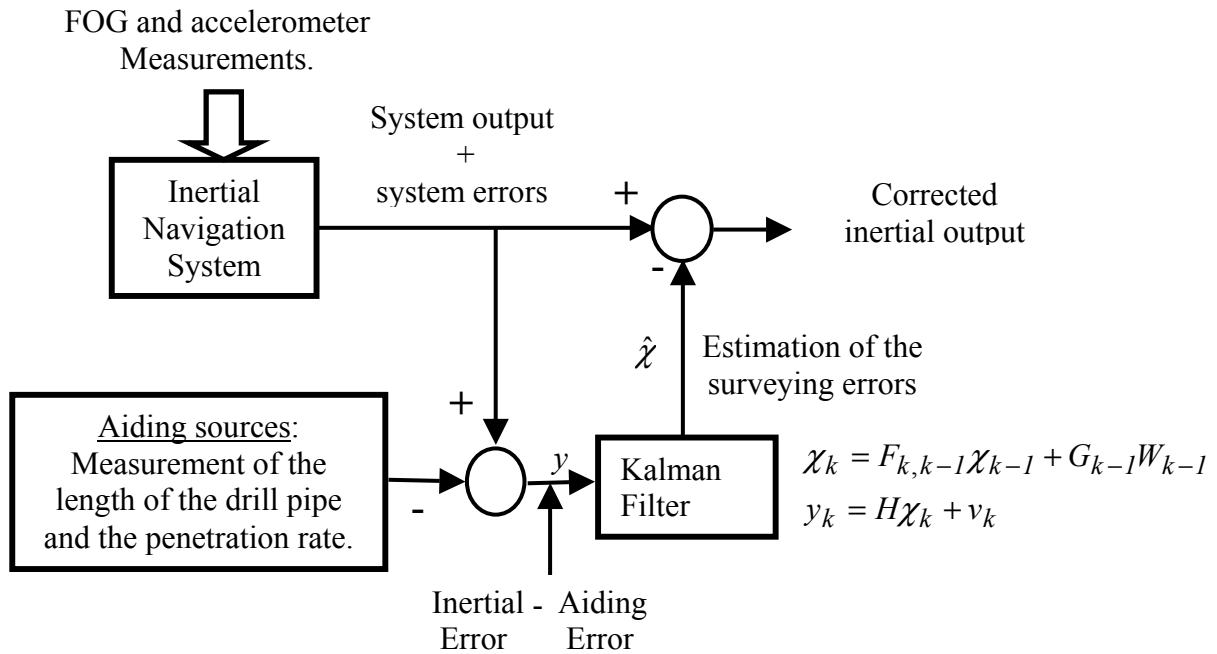


Fig.5.13. Block-diagram describing the technique of aided inertial navigation.

The observation equation (Eq.5.51) is determined by comparing the outputs of the aiding sources to the outputs of the FOG-based system. The true vertical depth determined using the length of the drill pipe ( $h^*$ ) is compared to the corresponding value obtained by the computational MWD surveying procedure ( $h$ ). Similarly, the velocity components determined using the measurements of the BHA penetration rate ( $V^{e*}, V^{n*}, V^{u*}$ ) are compared to the corresponding values obtained by the computational MWD surveying procedure ( $V^e, V^n, V^u$ ). The observation vector  $y_k$  and the design matrix  $H_k$  shown in Eq.3 can be separately written as follows:

$$y_k = \left( h - h^* \quad V^e - V^{e*} \quad V^n - V^{n*} \quad V^u - V^{u*} \right)^T \quad (5.55)$$

$$H_k = \begin{pmatrix} 0 & 0 & 1 & 0 & 0 & 0 & 0 & 0 & 0 & 0 & 0 & 0 & 0 & 0 & 0 \\ 0 & 0 & 0 & 1 & 0 & 0 & 0 & 0 & 0 & 0 & 0 & 0 & 0 & 0 & 0 \\ 0 & 0 & 0 & 0 & 1 & 0 & 0 & 0 & 0 & 0 & 0 & 0 & 0 & 0 & 0 \\ 0 & 0 & 0 & 0 & 0 & 1 & 0 & 0 & 0 & 0 & 0 & 0 & 0 & 0 & 0 \end{pmatrix} \quad (5.56)$$

The FOG-based MWD surveying procedure includes two steps; (1) computing the surveying parameters by solving their first order differential equations numerically in real-time using Euler method (see Fig.2); (2) employing Kalman filtering to optimally estimate the surveying errors and remove them from the parameters computed in the first step.

The real-time statistical data generated by the Kalman filter provides information about the MSEEs of the various MWD surveying errors. This information determines which error states are optimally estimated. It should be highlighted that only those parameters that have optimally-estimated surveying errors (i.e. their MSEEs converging with time) were considered for the closed loop criterion of the aided inertial navigation. If the other non-optimal estimates were to be included, the whole estimation process could be jeopardized resulting in divergence of some of the observable error states. In addition, special attention should be dedicated to those error states that have their MSEE experiencing slow convergence to the steady-state minimum value, and a decision should be made regarding when they should be included in the closed loop criterion of aided inertial navigation.

The techniques discussed in this section have been tested by moving the experimental setup on a flat surface at an altitude of *1104.1m* with constant small velocity (*1 cm/sec.*). In addition, simultaneous changes in the azimuth angle between *135°* and *190°* have been performed while varying the inclination in the range of  $\pm 20^\circ$ .

The surveying method discussed above is based on continuously receiving the updates of both the velocity and the altitude components to avoid the build up of surveying errors. Unfortunately, continuous velocity updates might be unavailable frequently during the drilling process due to some disturbance and vibration effects [Husling, 1989; Orban and Richardson, 1995]. This jeopardizes the accuracy of the

MWD surveying process due to possible unlimited increase of velocity errors and their direct contributions to both the attitude and position errors. Therefore, the zero velocity update (ZUPT) [Salychev, 1999] technique was utilized to limit the velocity errors and to improve the accuracy of the position and the attitude components.

#### **5.3.5.2. Zero velocity update (ZUPT).**

The ZUPT procedure is applied for MWD surveying process in which the continuous velocity updates are not available for part of or for the whole drilling operation. If the proposed FOG-based MWD surveying system was left working as a stand alone INS with no updates, one would expect significant long-term error growth even when utilizing high accuracy navigational grade inertial sensors [Merhav, 1993]. Therefore, interruption of the drilling process regularly at certain ZUPT stations is needed. At each ZUPT station, since the drilling assembly is completely stationary, the output velocity of the MWD inertial surveying system is basically composed of INS velocity errors due to the imperfections associated with inertial sensors (accelerometer bias errors).

In order to restore the INS velocity errors behavior between ZUPT stations, an optimal estimation procedure based on Kalman filtering method was employed. The accuracy of the ZUPT-based MWD inertial surveying system depends on the time interval between neighboring ZUPT stations. Since at each ZUPT station, the length of the drill pipe is known, the altitude update was applied in addition to the velocity update. Therefore, the linear state equations developed for the Kalman filtering in the previous section were completely applicable in this case. The only difference was that the update steps of Kalman filter (Eqs.5.53 and 5.54) were applied only during the ZUPT interval. Between ZUPT stations, the velocity errors grow linearly with time due to the accelerometer bias errors. Because of the velocity updates at each ZUPT station, Kalman filtering limits the growth of velocity errors. The position errors along the East and the North directions are obtained by integrating the corresponding velocity errors. Since no position updates are provided at a given ZUPT station, the position errors cannot be restored and it remains constant at the ZUPT station but grows with time between

neighboring ZUPTs. Therefore, we would expect significant long-term error growth in the position components.

### 5.3.5.3. Backward velocity error correction

In this study a method is proposed to partially limit the growth of position errors in the horizontal plane ( $\delta P_E$  and  $\delta P_N$ ) between ZUPT stations. It has been determined that if the velocity error  $\delta V_k$  estimated during the  $k^{th}$  ZUPT station were averaged with the velocity error  $\delta V_{k-1}$  estimated during the  $(k-1)^{th}$  ZUPT station and removed from the velocity component computed between these two neighboring ZUPTs, the velocity and position errors were significantly reduced. Since the proposed method was performed only one step backward, the real-time operation would practically not be affected. Thus, at each ZUPT station, records of the inertial sensor measurements collected after the end of the previous ZUPT were kept, therefore, in terms of storage, no considerable memory space was needed [Noureldin et al.<sup>b</sup>, 2001]. In addition, with the present hardware capabilities, this computational process can be executed at the end of each ZUPT station without delaying the real-time operation.

The ZUPT technique with and without backward velocity error correction has been tested using the same experimental setup. The ZUPT procedure was performed at 37 ZUPT stations over the two hour experiment, while changing the time duration between consecutive ZUPTs and varying the time interval of each individual ZUPT from one to two minutes to study their effect on the surveying errors.

### 5.3.6. Choice of transitional inclination angle.

The continuous surveying method described above cannot be performed during the entire drilling process since there is an error growth in the computation of the inclination angle as the BHA deviates from the vertical direction [Noureldin et al.<sup>b</sup>, 2000]. Moreover, the FOG can no longer resolve the changes on the azimuth by monitoring the rotation along the tool spin axis. To clarify this point, let us consider the case when the BHA approaches the horizontal direction. In this situation the rotation along the tool spin axis does not provide deviation of the BHA along the horizontal plane,

which means that the azimuth does not change. After a certain inclination angle (between  $20^\circ$  and  $30^\circ$ ), continuous surveying can no longer be performed, thus when the drilling process reaches this transitional inclination angle, station-based surveying should be utilized. However, the interrelationship between the desired surveying accuracy and the value of the transitional inclination angle has not been described, and therefore the exact moment of changing the surveying technique from continuous to station-based has not been quantified as a function of the inclination accuracy.

As mentioned earlier, the accelerometer measurements are combined to determine the inclination ( $\theta$ ) [Noureldin et al.<sup>a,b</sup>, 2001]. Based on the assumption of a slow penetration rate downhole, it can be assumed that the gravity field of the Earth is the major effect acting on the three-axis accelerometer measurements. Thus the inclination angle can be determined as described in Eq.5.22 and is employed to determine the synthetic rotation rate component  $\omega_{xs}$  given in Eq.5.24.

The inclination error is due to the imperfections associated with the accelerometer measurements, which include the bias error of the accelerometer and the measurement uncertainties. If we assume that  $\delta f_y$  is the accelerometer error, the inclination error  $\delta\theta$

can be written as  $\delta\theta = \frac{-\delta f_y}{g \cos \theta}$  (Eq.5.43) and the errors associated with the synthetic

rotation rate component are related to the accelerometer errors and can be expressed as

$$\delta\omega_{xs} = \frac{\alpha_y}{g \cos \theta} \delta f_y - \frac{\sqrt{2\alpha_y \sigma_y^2}}{g \cos \theta} w(t) \quad (\text{Eq.5.44}).$$

Although the Earth gravity  $g$ , with its relatively large value, attenuates the accelerometer error  $\delta f_y$ , the  $1/\cos \theta$  term modulates the  $\delta f_y/g$  error component and increases both  $\delta\theta$  and  $\delta\omega_{xs}$  at high inclinations. Although the inclination angle is the only parameter that is directly affected, its relationship to other surveying parameters might jeopardize the overall surveying accuracy at high inclinations. Therefore, the decision to change the surveying process from continuous to station-based modes should be taken in terms of the performance of the accelerometers utilized and the desired accuracy.

### 5.4.1. Development of surveying equations.

Since the BHA is completely stationary at the surveying station, the accelerometers monitor the components of the Earth gravity field along their sensitive axes, while the gyro monitors the component of the Earth rotation rate along the tool spin axis. The sensitive axes of both the gyro and the accelerometers are known as the BHA  $b$ -frame axes, which are defined by  $X^b$ ,  $Y^b$  and  $Z^b$  along three mutually orthogonal directions as shown on Fig.5.31. The  $Y^b$  axis points towards the forward direction (i.e. along the tool spin axis),  $Z^b$  axis points upward and the  $X^b$  axis completes a right-handed orthogonal frame.

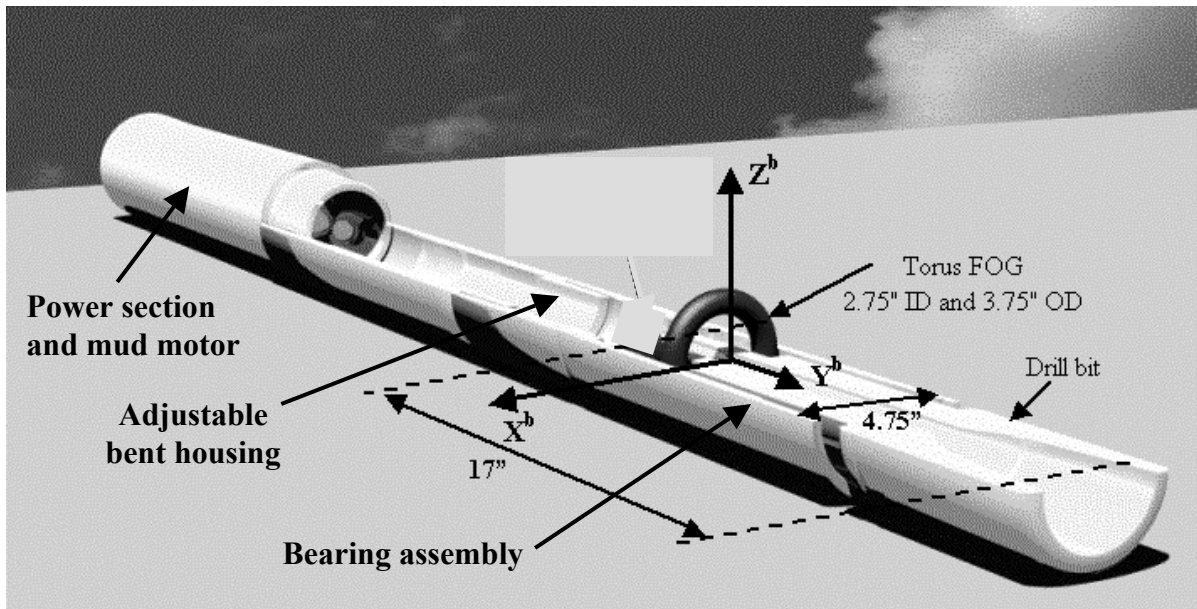


Fig.5.31. A model of the bearing assembly with the surveying sensors installed few inches behind the drill bit.

As shown on Fig.5.32, the effect of Earth gravity along the three components of the  $b$ -frame, i.e. along  $X^b$ ,  $Y^b$  and  $Z^b$ , are monitored by the accelerometers. The accelerometer measurements  $f_x$ ,  $f_y$  and  $f_z$  along these axes are related to the Earth gravity  $g$  as follows:

$$f_x = g \cos \theta \sin \phi \quad (5.57)$$

$$f_y = g \sin \theta \quad (5.58)$$

$$f_z = -g \cos \theta \cos \phi \quad (5.59)$$

where  $\theta$  is the angle between the forward axis  $Y^b$  and the horizontal plane (the pitch angle) and  $\phi$  is the angle between the transversal axis  $X^b$  and the horizontal plane (the tool face angle). From Eqs.(5.56-5.58) the pitch and the roll angles can be expressed as:

$$\theta = \arcsin\left(\frac{f_y}{g}\right) \tag{5.60}$$

$$\phi = \arctan\left(-\frac{f_x}{f_z}\right) \tag{5.61}$$

The inclination angle  $I$  (the deviation from the vertical direction) is related to  $\theta$  with:

$$I = \frac{\pi}{2} - \theta \tag{5.62}$$

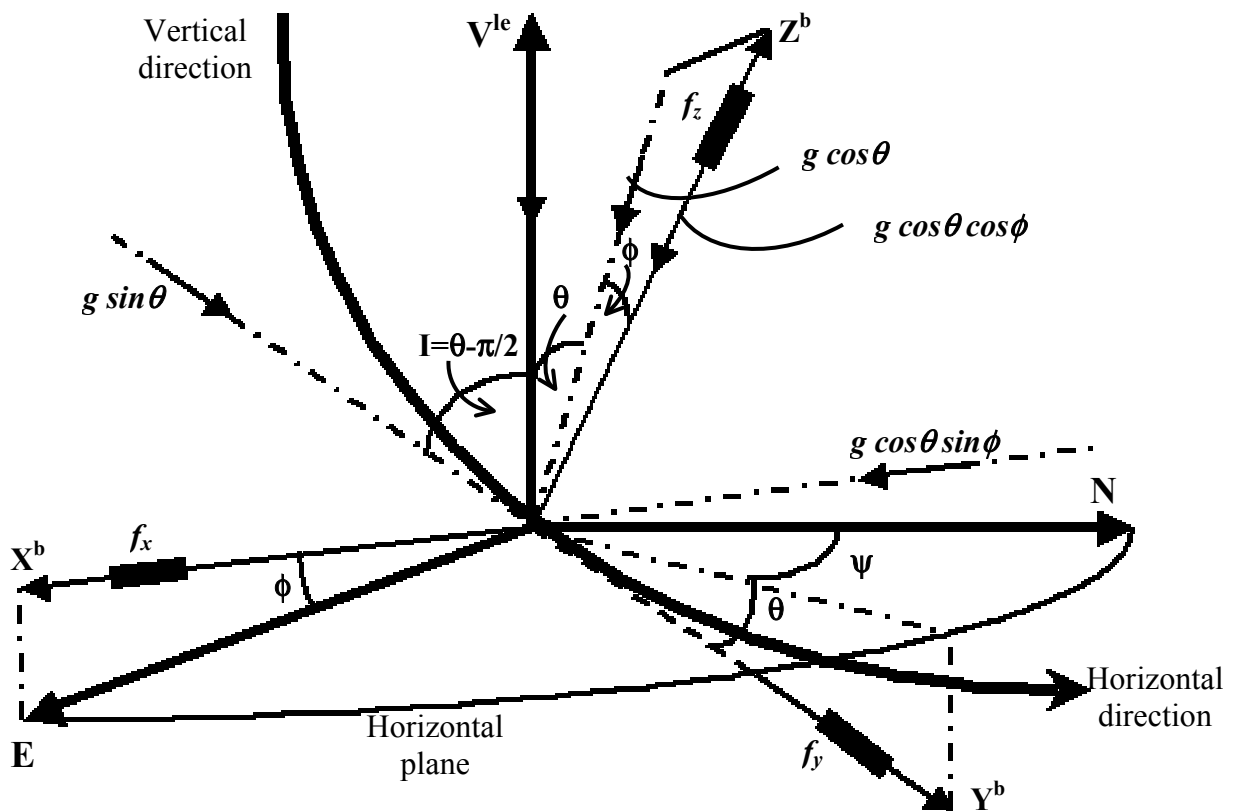


Fig.5.32. Earth gravity components along the BHA b-frame axes.

On the other hand, the Earth rotation rate along its spin axis ( $\omega^e = 15.04^\circ/hr$ ) has two components along the North direction ( $\omega^e \cos \varphi$ ) and the vertical direction ( $\omega^e \sin \varphi$ ) (Fig.5.33). The FOG measurement along its sensitive axis ( $\omega^y$ ) is related to these rotation rate components with:

$$\omega^y = (\omega^e \cos \varphi) \cos \psi \cos \theta - (\omega^e \sin \varphi) \sin \theta \tag{5.63}$$

The azimuth can be determined using the following equation:

$$\cos \psi = \left( \frac{\frac{\omega^y}{\omega^e \cos \varphi} + \tan \varphi \sin \theta}{\cos \theta} \right) \tag{5.64}$$

where  $\varphi$  is the latitude angle of the drilling site.

Since the station-based surveying method is performed for highly inclined and horizontal sections of the drilling well (i.e.  $I > 20^\circ$  and  $\theta < 70^\circ$ ), the presence of  $\cos \theta$  in the denominator of the right hand side of Eq.5.64 will not cause any singularities.

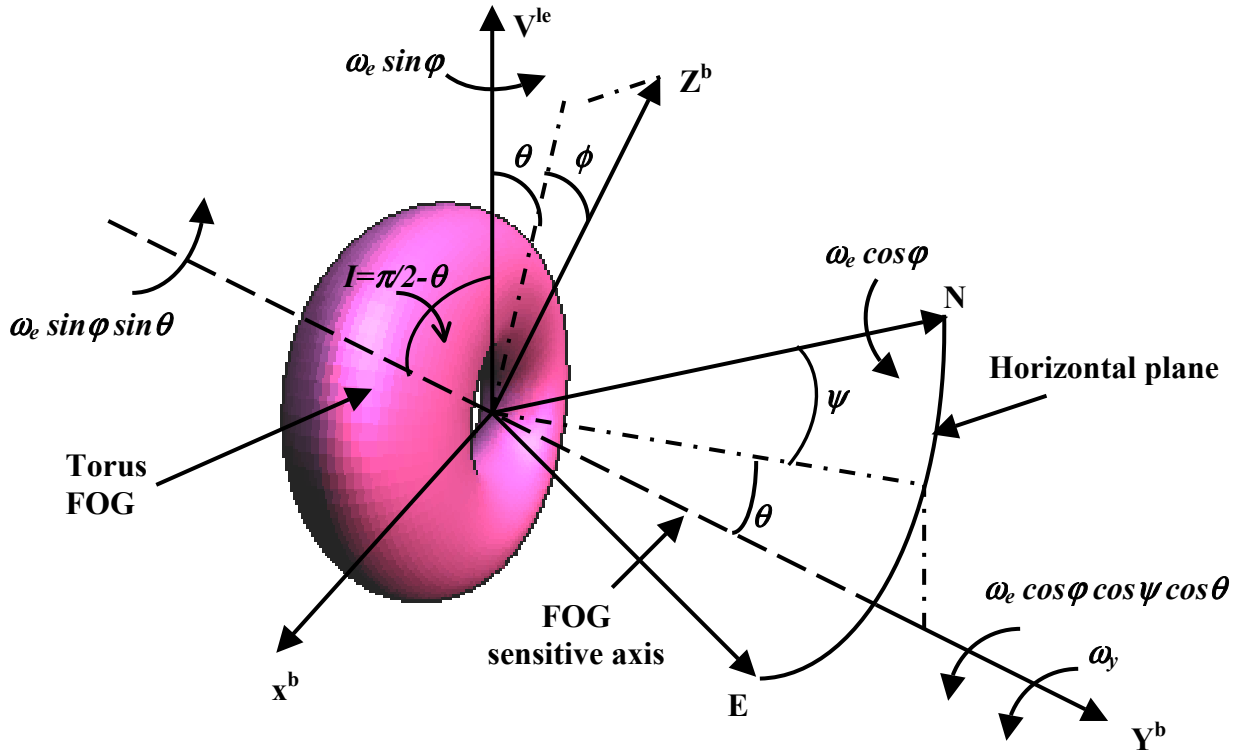


Fig.5.33. Earth rotation rate components along the BHA moving along the  $Y^b$  axis.

### 5.4.2. Surveying errors.

The surveying errors include the inclination and the azimuth errors, which are affected by the measurement errors of the accelerometers and the gyro. The inclination error is related to the imperfections associated with the accelerometer measurements, which include the bias error of the accelerometer mounted along the forward direction (i.e. along  $Y^b$ ) and its measurement uncertainty. If we assume that  $\delta f_y$  is the error associated with the acceleration measurement  $f_y$ , the inclination error  $\delta\theta$  can be obtained as a function of  $\delta f_y$  by differentiating Eq.5.60:

$$\delta\theta = \frac{\delta f_y}{g \cos \theta} \quad (5.65)$$

It can be noticed from Eq.5.65 that although the Earth gravity, with its relatively large value, attenuates the accelerometer error  $\delta f_y$ , the  $1/\cos\theta$  term modulates the  $\delta f_y/g$  error component, thus increasing the inclination error  $\delta\theta$ . However, the effect of the  $1/\cos\theta$  term decreases as the BHA approaches the horizontal direction (i.e.  $I \rightarrow \pi/2$  and  $\theta \rightarrow 0$ ) giving better inclination accuracy.

Similarly, the azimuth error  $\delta\psi$  is affected by the gyro bias error and measurement uncertainty ( $\delta\omega_y$ ) and can be determined by differentiating Eq.5.64:

$$\delta\psi = \frac{\left( \frac{\delta\omega^y}{\omega^e \cos \varphi} \right)}{\cos \theta \sin \psi} \quad (5.66)$$

Since the inclination error is relatively small due to the effect of gravity (see Eq.5.65), particularly when utilizing high accuracy navigational grade accelerometer, the effect of  $\delta\theta$  while calculating the azimuth error  $\delta\psi$  is neglected. It can be noticed from Eq.5.66 that the azimuth error may experience significant growth as the BHA approaches the North direction (i.e.  $\psi \rightarrow 0$ ), which may lead to North direction ambiguity. In addition, the relatively high uncertainty of the FOG output measurements may lead to computational instabilities of the azimuth angle while using Eq.5.64. Therefore, it is imperative to limit the measurement uncertainty before calculating the azimuth and to utilize some real-time digital signal processing techniques to compensate for the effect of

the gyro bias drift. However, before discussing these techniques, the different sources of surveying errors during the drilling process will be introduced.

### **5.4.3. Sources of surveying errors.**

The surveying errors are the inclination and the azimuth errors, both of which depend on the sensor errors as shown in the previous section. These errors can be classified into intrinsic sensor errors and vibration-induced sensor errors.

#### **5.4.3.1. Intrinsic sensor errors.**

The intrinsic sensor errors include the bias calibration error and the measurement uncertainties [Lefevre, 1993; Merhav, 1993]. Calibration of the surveying sensors while they are installed inside the bearing assembly is necessary to determine the bias offset of each sensor taking into account the run-to-run bias errors and the misalignment between the sensors sensitive axes and the BHA tool axes. The values of the bias offsets are removed from the corresponding surveying sensor measurements before processing their outputs in order to determine the surveying parameters. Unfortunately, the bias offsets (especially for gyros) can undergo considerable long-term change due to the internal design of the surveying sensors [Lefevre, 1993; Perlmutter, 1994]. For example as the bias offset may be influenced by the temperature of some of the circuit components of the surveying sensor, then this results in a deterministic relationship between the bias offset and the temperature [Perlmutter, 1994].<sup>21</sup> Although deterministic, it is unknown and changes from one experiment to another, thus jeopardizing the overall long-term surveying accuracy. This effect appears more in gyros while the accelerometers have the advantage of a more stable long-term bias offset [Merhav, 1993]. Therefore, the utilization of navigational grade inertial sensors is necessary for the successful realization of the proposed station-based surveying method.

On the other hand, the measurement uncertainties affect the computation process of the surveying parameters at each surveying station and high measurement uncertainties may lead to azimuth computational instabilities. Thus, it is essential to reduce the measurement uncertainties before the computation of the surveying parameters in order

to limit the computational uncertainty of the inclination and the azimuth angles and to prevent any computational instability of the azimuth.

#### **5.4.3.2. Vibration-induced sensor errors.**

In addition to the intrinsic sensor errors, the surveying accuracy is affected by the vibration induced sensor errors, which are random in nature and increase the measurement uncertainties. It has been reported that axial vibrations (i.e. along the tool spin axis) have the most serious effect on the surveying sensors [Berger and Sele, 2000]. Axial vibrations occur due to the bit bouncing on the bottom within the downhole formation [Brooks and Wilson, 1996]. Although this effect tends to be dampened in a horizontal hole, there are still some vibrations along the drill pipe, which affect the surveying sensors mounted with their sensitive axes parallel to the tool spin axis [Brooks and Wilson, 1996; Berger and Sele, 2000]. Fortunately, the sensitive axes of the surveying sensors used for monitoring the inclination and the azimuth ( $f_y$  and  $\omega_y$ ) for the vertical section of the well are normal to the tool spin axis, and are therefore affected only by the transversal vibrations through the drill pipe, which have less impact than the axial vibrations [Vandiver et al., 1989]. However, the surveying sensors will pick up more vibration-induced uncertainties in the highly-inclined well section since  $f_y$  and  $\omega_y$  measurements are provided by sensors mounted along the tool spin axis.

#### **5.4.4. Real-time techniques for limiting surveying errors.**

In Chapter 4, digital signal processing techniques were reported to limit the FOG output uncertainties using a transversal tap delay line filter with adaptive parameters adjusted using the least mean square (LMS) criterion [Noureldin et al.<sup>c,f</sup>, 2001]. The same approach can be used for the accelerometers since their noise behavior is similar to that of the FOG. Reduction of measurement uncertainties before calculating the inclination and the azimuth prevents the possibility for any computational instability of the azimuth and limits the uncertainties in both the inclination and the azimuth angles [Noureldin et al.<sup>c,f</sup>, 2001]. In addition, this filtering approach can help reducing the effect of

longitudinal (axial) vibrations on the accelerometer mounted along the tool spin axis, which is responsible for monitoring the inclination angle.

#### **5.4.5. Experimental procedure and signal conditioning.**

The technique proposed in this section was tested using LTN90-100 inertial measurement unit (Litton, Woodland Hills, CA), which incorporates three-axis accelerometers and three-axis optical gyroscopes mounted in three mutually orthogonal directions. LTN90-100 is categorized as navigational grade unit with  $0.01^\circ/hr$  gyro drift and  $0.002^\circ/\sqrt{hr}$  gyro random walk. As mentioned earlier in Chapter 4, the optical gyroscopes utilized in this unit are of ring laser type and they have the same performance characteristics as FOGs. These gyros differ from the FOGs in the way the laser beam is propagating inside, while the drift and noise behaviors are exactly the same [Burns, 1994]. Although the size of ring laser gyros cannot be accommodated downhole for MWD processes, they are suitable for laboratory experiments to study the feasibility of station-based surveying processes utilizing a single gyro and three-axis accelerometers. In addition, the LTN90-100 is integrated with KINGSPAD<sup>TM</sup> software (University of Calgary, Department of Geomatics Engineering), which is a kinematic geodetic system for position and attitude determination, and is used to provide reference values of the inclination and the azimuth angles to check the accuracy of the proposed system.

The LTN90-100 was mounted inside a custom-designed setup capable of providing changes in the orientation of the surveying sensors in three mutually orthogonal directions. The accelerometers and the gyro measurements ( $f_x, f_y, f_z$  and  $\omega_y$ ) were delivered at  $64Hz$  data sampling rate. These measurements were averaged in 1-second time interval in order to remove some of the high frequency noise components and reduce measurement uncertainties. The measurements of the other two gyros ( $\omega_x, \omega_z$ ) were only processed by KINGSPAD<sup>TM</sup> to provide reference data. Each of the averaged data sequences was processed individually by a transversal tap delay line filter of 100 tap weights. As discussed in Chapter 4, the optimal values of these tap weights were determined using the LMS adaptive criterion during the calibration process, while the whole setup was in the vertical direction [Noureldin et al.<sup>c</sup>, 2001]. Since the averaging

process at 1-second intervals reduced the data rate from 64Hz to 1Hz, and due to the 100 delay elements of the filter, the output of the filtering stage was delivered after 100 seconds. The computation of the inclination and the azimuth angles was then performed using Eqs.5.60 and 5.62 for the inclination, and Eq.5.64 for the azimuth.

#### **5.4.6. Results.**

##### **5.4.6.1. Computation of the inclination and the azimuth angles.**

The averaging and the filtering procedures were performed before the computation of the inclination and the azimuth angles to limit the measurement uncertainties. The averaging at 1-second interval reduced the output uncertainty of the accelerometer measurements  $f_y$  from  $0.0306 \text{ m/sec}^2$  to  $6.57 \times 10^{-4} \text{ m/sec}^2$ . Further reduction of this measurement uncertainty to  $0.22 \times 10^{-4}$  was obtained using the transversal filter of 100 tap weights. Fig.5.34 shows the acceleration measurement  $f_y$  over 200 seconds before and after the filtering stage. The inclination was then computed with an error of less than  $0.0002^\circ$  and uncertainty of about  $1.5 \times 10^{-4}$  degrees for the near horizontal section of the well (i.e.  $I \rightarrow \pi/2$ ) as shown on Fig.5.35.

It can be observed that the computed value of the inclination angle drifts slightly with time due to the drift of the accelerometer bias. Both the inclination error and its computational uncertainty increased at smaller inclinations where the computation of the inclination angle became more sensitive to the accelerometer error and its measurement uncertainties. An error of  $0.092^\circ$  with computational uncertainty of  $2.2 \times 10^{-4}$  degrees has been determined at inclination of  $44.517^\circ$ . The inclination angle was determined with high accuracy due to the relatively large value of the Earth gravity  $g$ , which attenuates the accelerometer errors.

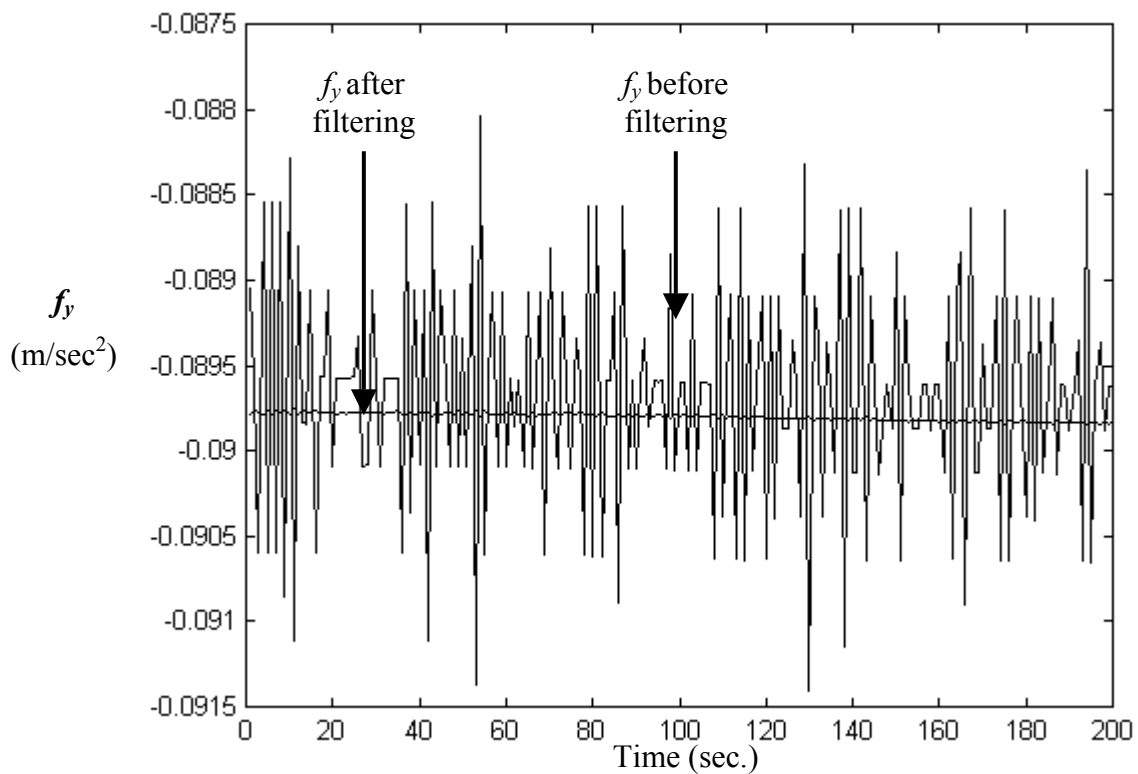


Fig.5.34. Accelerometer measurements  $f_y$  before and after the filtering procedure.

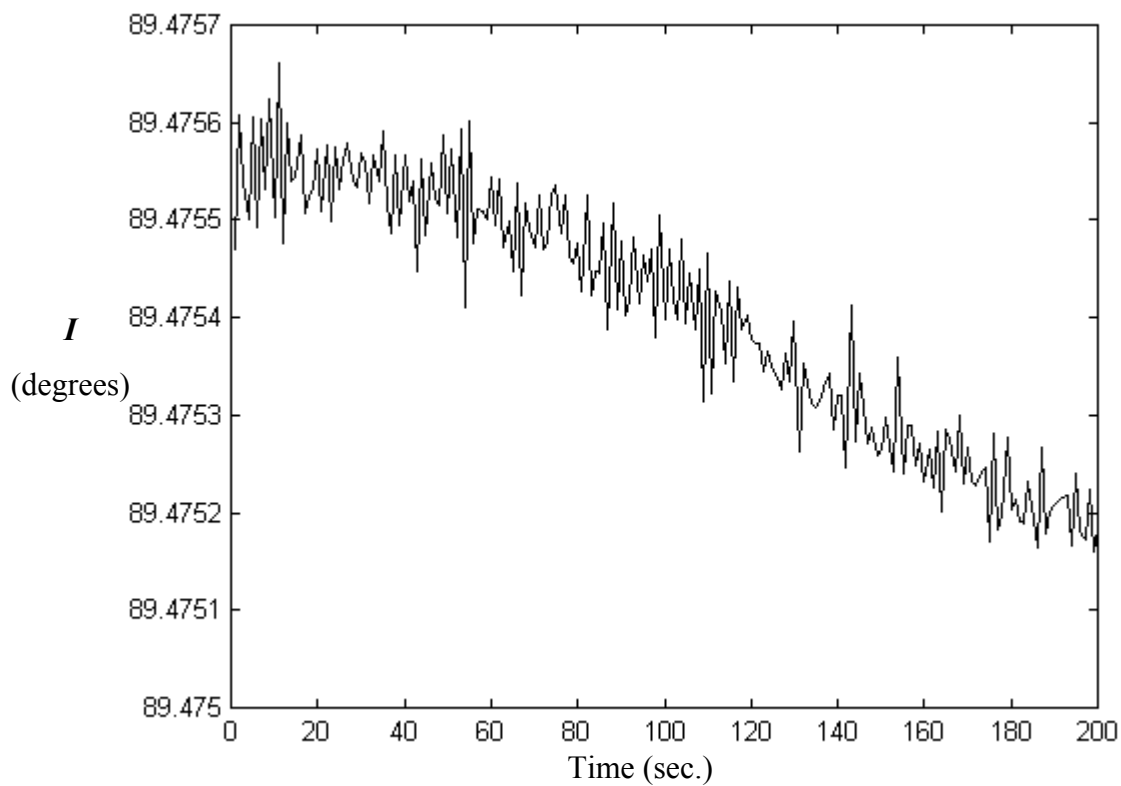


Fig.5.35. Inclination angle at sections near the horizontal direction.

Similarly, the uncertainties of the rotation rate measurements  $\omega_y$  were reduced from  $0.0478^\circ/\text{sec}$  to  $0.0012^\circ/\text{sec}$  after averaging, and to  $1.1575 \times 10^{-5} \text{ }^\circ/\text{sec}$  ( $0.04167^\circ/\text{hr}$ ) after filtering (see Fig.5.36).

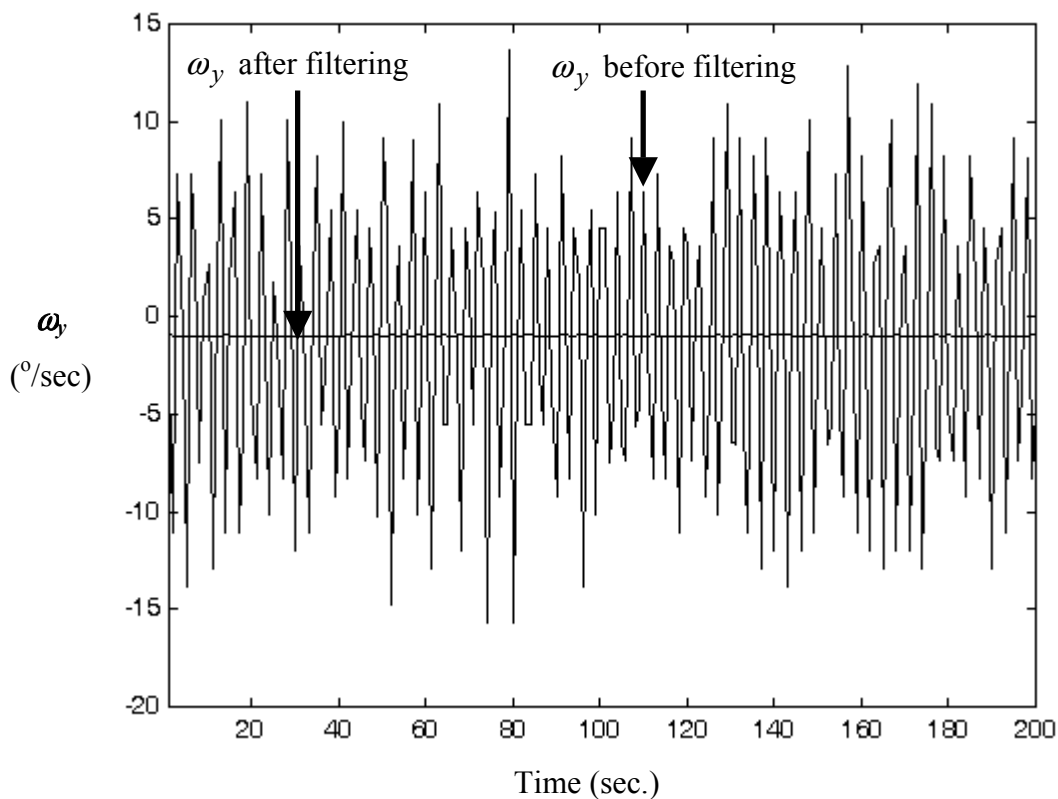


Fig.5.36. Rotation rate measurement  $\omega_y$  before and after filtering.

The computation of the azimuth angle was provided with an error of  $0.02322^\circ$  and uncertainty of  $0.08^\circ$  for the near horizontal section while drilling close to the East direction (i.e.  $\psi \rightarrow \pi/2$ ) as shown on Fig.5.37. The drift of the gyro bias error accounts for the drift of the computed azimuth angle, which can be observed on Fig.5.36. While the setup pointing close to the East direction at the horizontal plane, a change of the roll angle (tool face angle) in steps of  $15^\circ$  was performed and station-based surveying was introduced at each roll angle. The estimated azimuth errors and the corresponding computational uncertainties are shown on Fig.5.38 for the different roll angles.

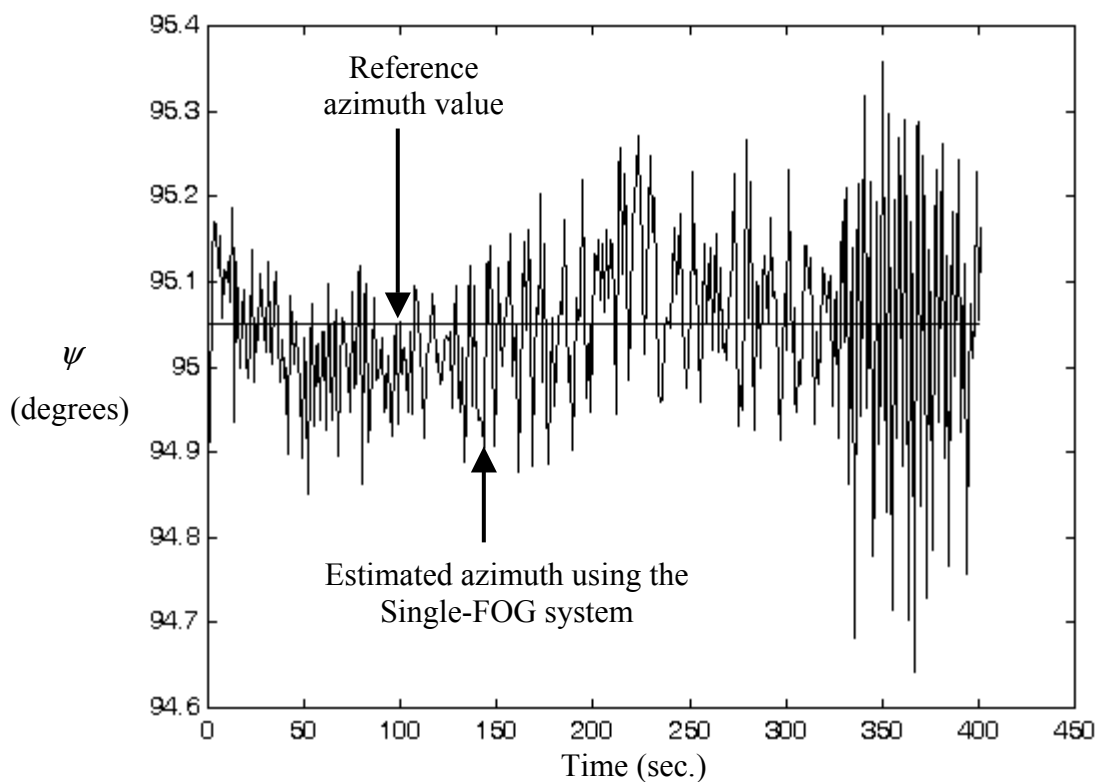


Fig.5.37. Azimuth angle at surveying station near to the horizontal plane and close to the East direction.

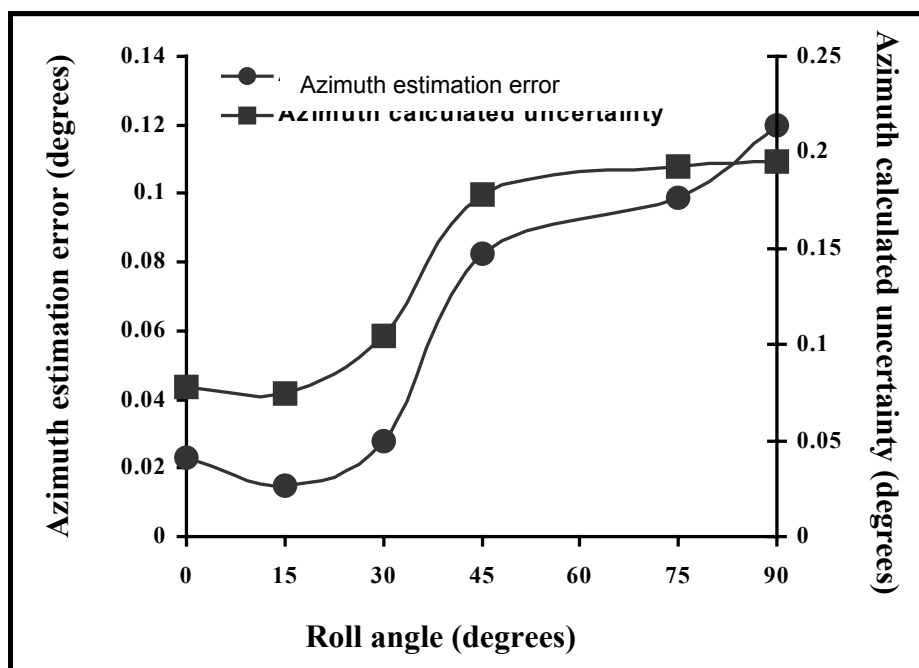


Fig.5.38. Estimated azimuth error and the corresponding uncertainty for different roll angles while the setup near to the horizontal plane and close to the East direction.

In general, the azimuth error and its drift increased at smaller inclination angles and as the BHA started to penetrate closer to the North direction. Unlike the Earth gravity, the Earth rotation rate is of relatively small value and cannot limit the gyro bias error and the measurement uncertainties. In addition, the gyro drift may jeopardize the long-term azimuth accuracy especially at some orientations where small variations in the gyro measurements lead to considerable change in the azimuth angle.

#### 5.4.6.2. Study of the inclination and the azimuth errors.

The inclination and the azimuth errors were due to the imperfections associated with the measurements of the surveying sensors, which contributed differently to the surveying accuracy based on the BHA orientation.

The inclination error  $\delta I$  depends on the BHA deviation from the vertical direction (i.e. the inclination angle). Fig.5.39 shows the inclination error with respect to the BHA inclination at three different azimuth directions. It is noticeable that the inclination error in each of the three cases becomes smaller as the BHA gets closer to the horizontal direction, thus providing better inclination accuracy. In addition, the values of the inclination error when the BHA was close to the East or to the North directions or at the midway between them, were almost the same (i.e. independent of the BHA azimuth) (see Fig.5.39). The small differences between the graphs (less than  $0.25^\circ$ ) were due to the accelerometer bias error  $\mathcal{F}_y$  and its drift over time. In general,  $\mathcal{F}_y$  is pretty small when compared to the Earth gravity and exhibits low drift characteristics, thus providing stable and accurate results for the inclination angle.

On the other hand, the azimuth error depends on both the inclination and the azimuth of the BHA. In addition, the gyro bias error and its drift characteristics highly affect the azimuth accuracy. The dependence of the azimuth error on the inclination angle was tested at an azimuth of about  $95^\circ$  while changing the inclination angle between  $30^\circ$  and  $90^\circ$  and the results are shown on Table 5.1. It can be noticed that the azimuth accuracy improves when the BHA gets closer to the horizontal direction. The worst azimuth accuracy took place when heading close to the North direction and the azimuth error increased for small inclination angles (Fig.5.40).

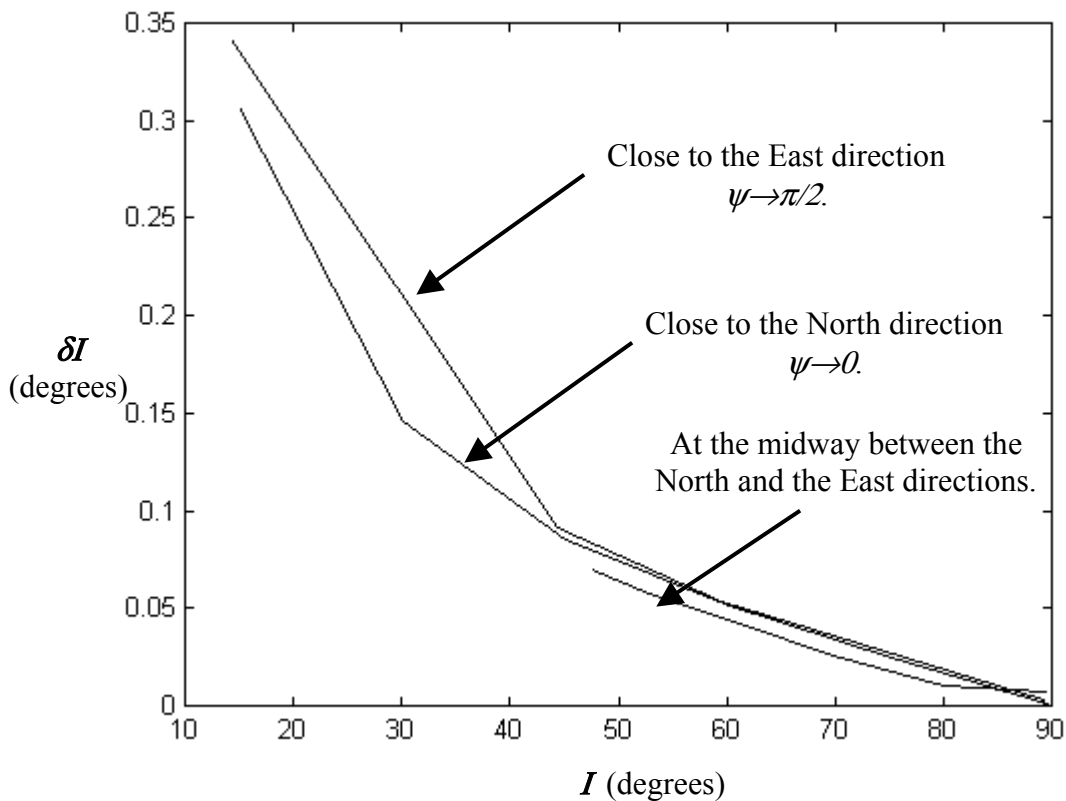


Fig.5.39. Inclination error with respect to the inclination angle at different azimuth directions.

**Table 5.1. The azimuth error at different inclination angles for a given known azimuth.**

Azimuth (deg.)	Inclination (deg.)	Azimuth Error (deg.)
<b>95°</b>		
	30.51	0.19
	45.48	0.06
	89.48	0.02

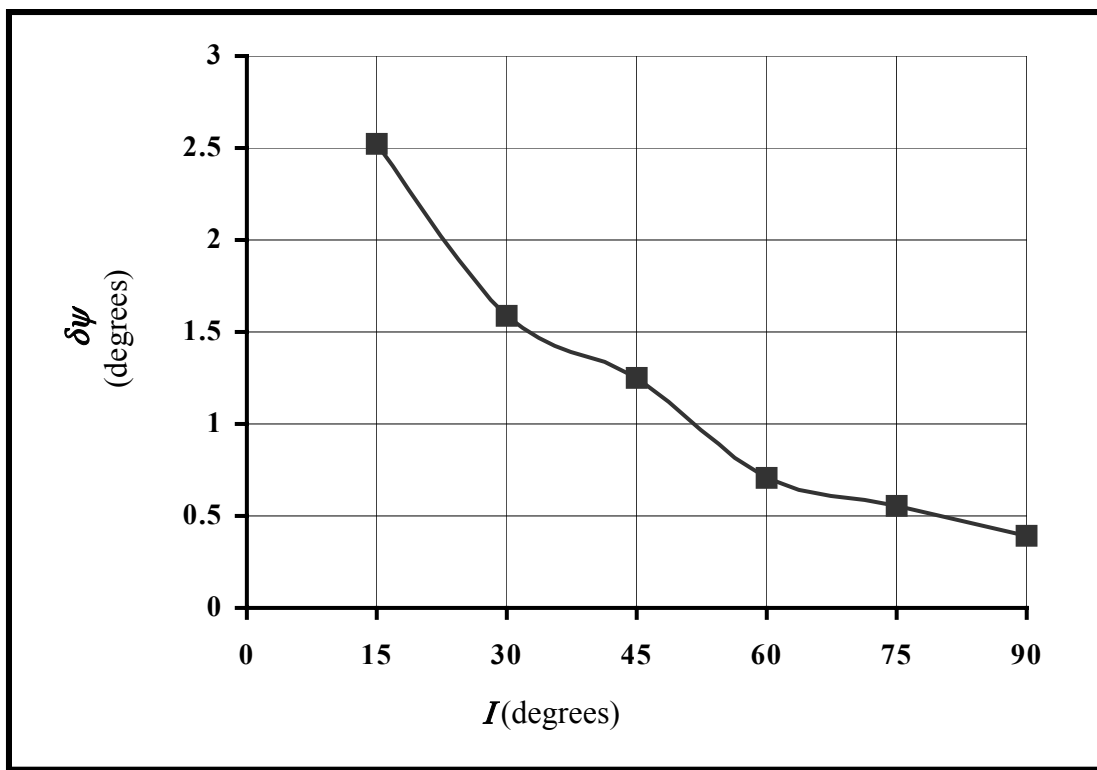


Fig.5.40. Azimuth errors with respect to different inclination angles at orientations close to the North direction (worst azimuth accuracy).

The change of the azimuth error with respect to the BHA azimuth was examined at two different inclination angles. Fig.5.41 shows the azimuth error versus the azimuth angle at  $60^\circ$  and  $90^\circ$  inclinations. It can be noticed that better azimuth accuracy can be obtained while drilling close to the East direction (i.e.  $\psi \rightarrow 90$ ), with additional improvement observed for the near horizontal sections of the well (i.e.  $I \rightarrow 90$  or  $\theta \rightarrow 0$ ). However, one may notice that the azimuth errors at  $60^\circ$  inclination are less than those at  $90^\circ$  inclination for some values of azimuth shown on Fig.5.41. This was due to the gyro bias error that exhibited different drift characteristics for different sets of experiments. Unlike the inclination angle, the azimuth accuracy is highly affected by the gyro bias error and its drift over time. This necessitates the utilization of navigational grade gyros with their relatively low drift characteristics similar to the one used in this study. However, relatively high azimuth errors (from  $1^\circ$  to  $2^\circ$ ) are still observed for surveying

stations close to the North direction. Two factors are responsible for this problem. The first factor is related to the Earth rotation rate ( $15.04^\circ/hr$ ), which is of relatively small value and may become comparable to the gyro bias error at some BHA orientations. The second factor is the measurement of the Earth rotation rate  $\omega_y$  at each surveying station, which is less sensitive to changes in the azimuth angle close to the North direction. To clarify this issue, let us examine the Earth rotation rate component  $\omega_y$  at  $90^\circ$  inclination for values of azimuth between  $0^\circ$  and  $90^\circ$  as shown on Fig.5.42. It can be noticed that the  $\omega_y$  curve becomes almost linear for values of azimuth close to  $90^\circ$ . A change of one degree in the azimuth angle corresponds to a change in  $\omega_y$  by  $0.1623^\circ/hr$  for surveying stations near the East direction ( $\psi=70^\circ \rightarrow 90^\circ$ ) and by  $0.0159^\circ/hr$  for stations near the North direction ( $\psi=0^\circ \rightarrow 20^\circ$ ). Therefore, the small changes in  $\omega_y$  near the North direction might not be accurately resolved by the gyro due to its bias error, thus increasing the azimuth error. However, the impact of the gyro bias error becomes less significant for surveying stations near the East direction.

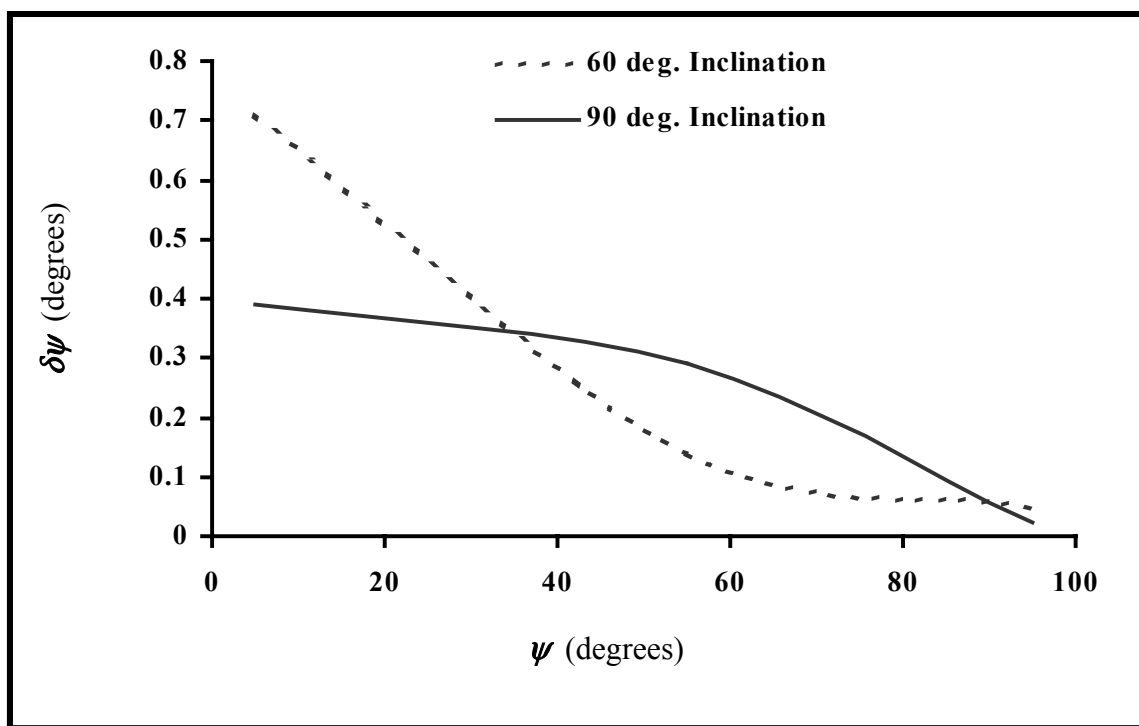


Fig.5.41. The azimuth error with respect to the BHA azimuth at two different inclination angles.

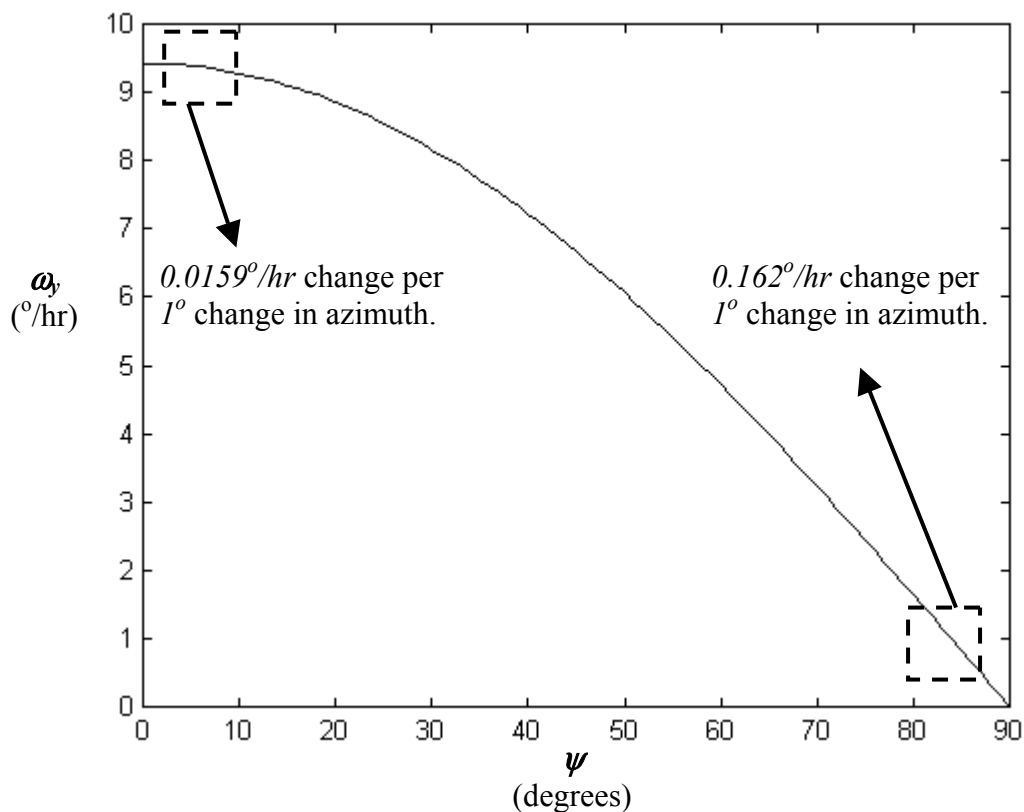


Fig.5.42. Earth rotation rate component along the tool spin axis at  $90^{\circ}$  inclination for different azimuth angles.

#### 5.4.7. Applications and limitations of the single-FOG station-based surveying technique.

The MWD single gyro system, which was originally proposed for surveying near vertical sections of directional wells, can be utilized for highly inclined and horizontal sections of the wells as well. This study suggested surveying these sections of the drilling well at some predetermined stations. At each station, the surveying process involved two steps.

During the first step, the measurements uncertainties of the surveying sensors were reduced by at least 1000 times for both the gyro and the accelerometers. The output

noise associated with the measurements of both the gyro and the accelerometers were reduced using advanced real-time digital signal processing procedures.

The second step involved the computation of the inclination and the azimuth angles based on monitoring the Earth rotation rate and gravity components. The inclination angle was delivered with errors of less than  $0.1^\circ$  for inclination angles larger than  $45^\circ$ . These errors increased to about  $0.3^\circ$  at  $20^\circ$  inclination. The azimuth accuracy at the end of this step was not as good as the inclination accuracy and suffered from an increase of the azimuth error to about  $2.5^\circ$  when approaching the North direction.

Other sources of uncertainty, like the longitudinal vibrations along the drill pipe, may affect the accelerometer aligned along the tool spin axis. Therefore, the design of the transversal filter based on the adaptive LMS criterion should be performed on site after mounting the surveying sensors inside the drill pipe.

## CHAPTER SIX

### DUAL-FOG MWD SURVEYING SYSTEM

A single-axis FOG-based MWD surveying system was proposed and tested in Chapter 5. This system can continuously survey the near-vertical section of the drilling well (until  $20^{\circ}$ - $30^{\circ}$  inclination), which is highly beneficial when drilling from an offshore platform in a section of multi-well structure [Noureldin et al.<sup>a,b</sup>, 2001]. In addition, the single gyro system is capable of surveying highly-inclined and horizontal well sections at various surveying stations when the BHA is completely stationary [Noureldin et al.<sup>d</sup>, 2001].

Although the single-axis gyro system can be employed for continuously surveying the near-vertical section of horizontal wells, it cannot be generalized for surveying highly inclined and horizontal sections. In these sections of the well, the gyro sensitive axis (i.e. the tool spin axis) becomes almost colinear with the horizontal direction. Thus, the changes in the azimuth angle due to rotations along the vertical direction will not be properly monitored by the gyro during continuous surveying. In addition, the station-based surveying utilizing the single gyro system for highly inclined and horizontal sections suffers from relatively large azimuth errors (more than  $1^{\circ}$ ) at some BHA orientations [Noureldin et al.<sup>d</sup>, 2001]. Furthermore, the station-based surveying system cannot be utilized for the near-vertical section (i.e. inclination angles less than  $20^{\circ}$ ) due to the significant growth of the surveying errors [Noureldin et al.<sup>d</sup>, 2001].

This chapter suggests a dual-axis gyroscopic surveying system utilizing two mutually orthogonal FOGs incorporated with three-axis accelerometers, which avoids some of the inadequacies associated with the single gyro system.

The aim of this chapter is to: (1) describe the Dual-FOG MWD surveying setup; (2) present the Dual-FOG continuous surveying technique of the radical section of the well and the station-based surveying methodology at some predetermined surveying stations; (3) discuss sources of surveying errors; and (4) apply the same real-time digital

signal processing techniques utilized in the Single-FOG MWD system to limit these surveying errors, thus evaluating the benefits of the new design.

### **6.1. Dual-FOG MWD surveying setup**

In the proposed design model of a Dual-FOG MWD surveying system, the surveying tools are installed inside the bearing assembly 17'' behind the drill bit (Fig.6.1). These tools are similar to the single gyro system, except for an additional FOG mounted with its sensitive axis normal to the tool spin axis and colinear with the forward direction. This FOG has a diameter of 1.6'' and a thickness of 0.4'' and is denoted as the Normal FOG to distinguish it from the Torus FOG described for the single gyro system [Noureldin et al.<sup>a,b,d</sup>, 2001]. After the establishment of the vertical section of the well, the horizontal drilling process involves three main tasks:

1. Establishing the desired azimuth direction while the drill pipe is still in the vertical direction.
2. Building the radical section of the well using steering mode of operation.
3. Building the horizontal section of the well with using rotary mode of operation.

## **6.2. Continuous surveying of the radical section of horizontal wells**

### **6.2.1. Establishing the desired azimuth direction.**

In order to establish accurately the azimuth direction, the precise value of the initial azimuth should be known. This initial azimuth value is determined when the whole setup is completely stationary. The BHA axes ( $x^b$ ,  $y^b$  and  $z^b$ , Fig.6.2) are chosen so that  $y^b$  points toward the forward direction and along the sensitive axis of the Normal FOG,  $z^b$  points toward the vertical direction and along the sensitive axis of the Torus FOG and,  $x^b$  points toward the transversal direction completing a right-handed orthogonal frame.

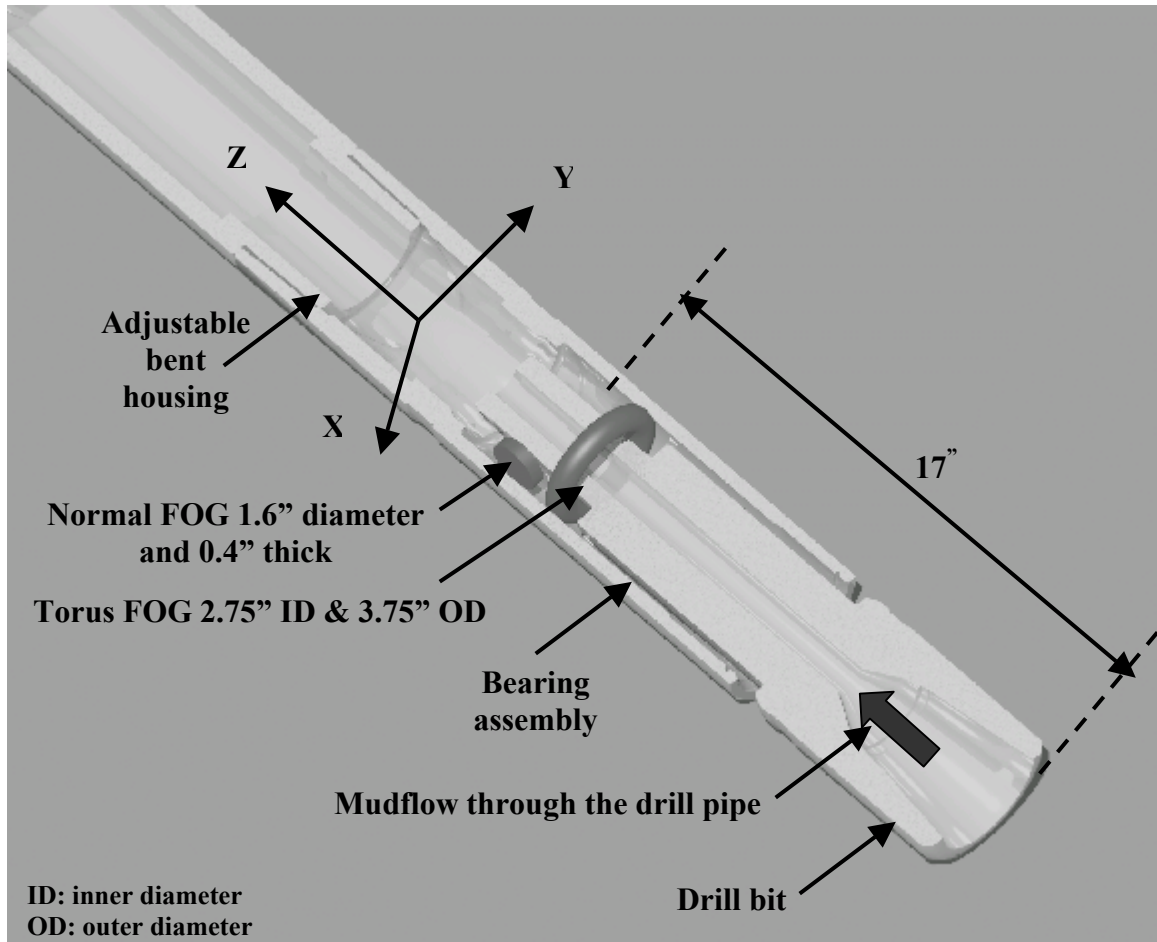


Fig.6.1. Dual-axis FOG-based gyroscopic surveying system mounted inside the bearing assembly.

As indicated in Chapter 5, the initial azimuth can be determined as follows:

$$\cos \psi = \frac{\frac{\omega_y}{\omega^e \cos \varphi} - \sin \theta \tan \varphi}{\cos \theta} \quad (6.1)$$

where  $\omega_y$  is the angular velocity output of the Normal FOG and the pitch (inclination)  $\theta$

is determined from the accelerometer measurements as  $\theta = \arcsin\left(\frac{-f_y}{g}\right)$ .

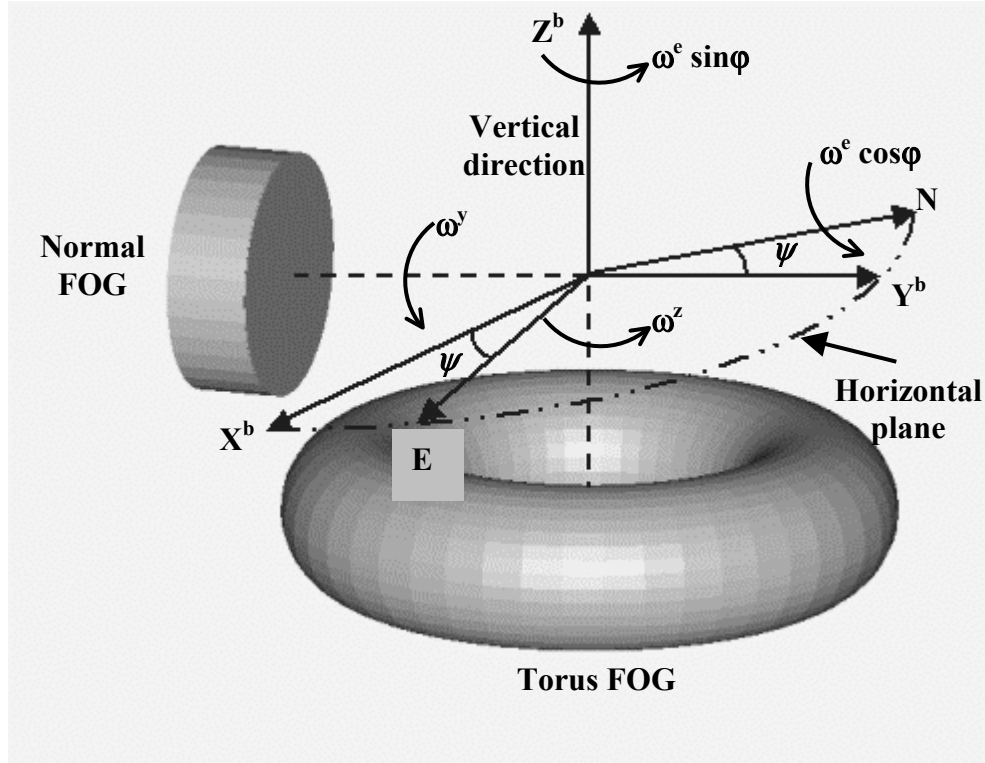


Fig.6.2. Determination of the initial azimuth.

The initial azimuth can be determined using the above equation by substituting  $\omega_y$  after removing the measurement bias and applying an appropriate scaling factor. The residual measurement errors affect the calculation of the azimuth angle and consequently the accuracy of the initial azimuth. The relationship between the initial azimuth error  $\delta\psi$  and the residual measurement errors  $\delta\omega_y$  can be obtained by differentiating Eq.(6.1).

$$\delta\psi = \frac{\left( \frac{\delta\omega_y}{\omega^e \cos \varphi} \right)}{\sin \psi \cos \theta} \quad (6.2)$$

It is clear that the initial azimuth error depends on how close to the North direction the BHA is pointing. As the BHA gets closer to the North direction (i.e.  $\psi \rightarrow 0$ ), the initial azimuth accuracy deteriorates. Therefore, the BHA should be oriented roughly away from the North direction to guarantee an accurate initial azimuth. Such a setting could be performed at the surface and would not affect the drilling operation since the

desired azimuth direction can be established independently by rotating the whole drill pipe around the tool spin axis from the initial azimuth to the desired one.

Once the initial azimuth of the bottom hole assembly is determined, the drill pipe can be rotated to achieve the desired azimuth direction. Although the Normal FOG is responsible for the determination of the initial value of the azimuth, the Torus FOG is responsible for the establishment of the desired azimuth direction.

With the BHA oriented along the vertical direction, the drill pipe is rotated along the tool spin axis until the desired azimuth direction is established. It should be noted that the rotation along the tool spin axis is the only motion, either angular or translational, performed during this operation. Under these circumstances, the Torus FOG monitors the rotation rate along the tool spin axis in addition to the component of Earth rotation along the vertical direction ( $\omega^e \sin \varphi$ ). Therefore, the time rate of change of the azimuth,  $\dot{\psi}$ , can be written as follows:

$$\dot{\psi} = \omega_z \cos \theta \cos \phi - \omega^e \sin \varphi \quad (6.3)$$

where  $\omega_z$  is the measurement delivered by the Torus FOG. Since the drill pipe is completely in the vertical direction while establishing the azimuth direction,  $\theta$  and  $\phi$  are relatively very small values so that  $\cos \theta$  and  $\cos \phi$  can be considered as equal to one. However, It is preferred to include their effect on the above equation with  $\theta$  is determined as  $\arcsin\left(\frac{-f_y}{g}\right)$  and  $\phi$  is calculated as  $\arctan\left(\frac{-f_x}{f_z}\right)$  [Noureldin et al.<sup>g</sup>, 2001].

Eq.6.3 is solved numerically in real-time to provide continuous monitoring of the azimuth angle while rotating the drill pipe. This first-order differential equation can be solved numerically using the Euler method [Yakowitz and Szidarovszky, 1989] after substituting  $\dot{\psi}$  by  $(\psi_{k+1} - \psi_k)/(\Delta t)$ , where  $\psi_{k+1}$  is the azimuth value at time  $t_{k+1}$ ,  $\psi_k$  is the azimuth value at time  $t_k$  and  $\Delta t = t_{k+1} - t_k$ . Then, the azimuth can be continuously monitored using the following equation:

$$\psi_{k+1} = \psi_k + (\omega_z \cos \theta \cos \phi - \omega^e \sin \varphi) \Delta t \quad (6.4)$$

The drill pipe continuously rotates about its tool spin axis, and the azimuth angle is continuously determined from Eq.6.4. Once the desired azimuth direction is established, the rotation of the drill pipe is stopped and building the radical section of the well is initiated. The surveying process during this section of the well is described in the following sub section.

### 6.2.2. Surveying the radical section of the well.

While building the radical section of the well, the BHA starts the drilling process from complete vertical direction and continues toward a complete horizontal direction. At the beginning, while the whole setup is still in the vertical direction, the body frame axes are chosen as shown on Fig.6.3. The X, Y, and Z axes point toward transverse, forward and vertical directions respectively. Therefore, the Z-axis points toward the tool spin axis. With this choice of axes orientation, it is assumed that the BHA motion is along the Y-axis, and sliding along the Z-axis. Hence, both the Torus FOG and the Normal FOG monitor the angular velocities ( $\omega_x$  and  $\omega_y$ ) along two mutually orthogonal directions. The third angular velocity component is a synthetic rotation rate signal generated using the accelerometer measurements in order to deliver  $\omega_{xs}$ .

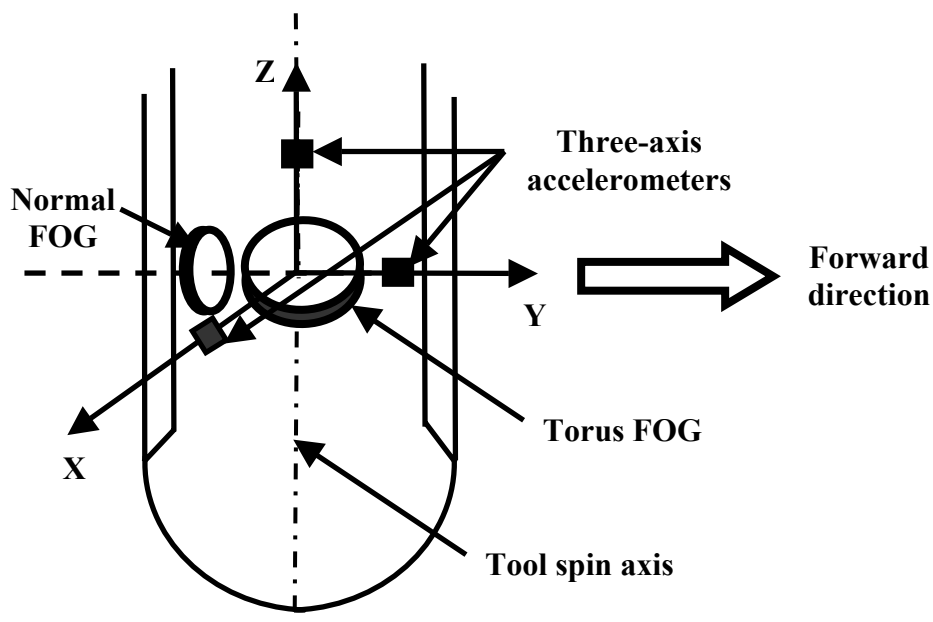


Fig.6.3. The initial arrangement of the FOGs and the accelerometers with the body frame axes inside the bearing assembly.

### 6.2.2.1. Determination of the synthetic rotation rate component.

As illustrated in Chapter 5, the time rate of change of the pitch angle is equivalent to the synthetic rotation rate component along the X-axis. The pitch is determined utilizing the accelerometer measurements and can be written as:

$$\sin \theta = \frac{-f_y}{g} \quad (6.5)$$

The corresponding synthetic rotation rate component  $\omega_{xs}$  is given as:

$$\omega_{xs}(t_k) = \frac{\theta(t_k) - \theta(t_{k-1})}{t_k - t_{k-1}} \quad (6.6)$$

where  $\theta_k$  and  $\theta_{k+1}$  are the values of the pitch angle at time  $t_k$  and  $t_{k+1}$  respectively.

### 6.2.2.2. Determination of the transformation matrix using the quaternion approach

The surveying procedure delivers the BHA navigation data (the position and the orientation) by solving the set of the following first-order differential equations describing the mechanization in the  $\ell$ -frame (see Eq.5.16) [Schwarz and Wei, 1999]:

$$\begin{pmatrix} \dot{r}^\ell \\ \dot{V}^\ell \\ \dot{R}_b^\ell \end{pmatrix} = \begin{pmatrix} D^{-1}V^\ell \\ R_b^\ell f^b - (2\Omega_{ie}^\ell + \Omega_{e\ell}^\ell)V^\ell + g^\ell \\ R_b^\ell (\Omega_{ib}^b - \Omega_{i\ell}^b) \end{pmatrix} \quad (6.7)$$

The first step in solving these equations is the parameterization of the rotation matrix  $R_b^\ell$  [Titterton and Weston, 1997; Salychev, 1998; Schwarz and Wei, 1999]. The most popular method for this purpose is the quaternion approach. According to Euler's Theorem [Salychev, 1998], the rotation of a rigid body (represented by the b-frame) with respect to a reference frame (represented by the  $\ell$ -frame) can be expressed in terms of the rotation angle  $\Theta$  about a fixed axis and the direction cosine of the rotation axis that defines the rotation direction. Thus, quaternion parameters  $Q = (q_1 \ q_2 \ q_3 \ q_4)^T$  are introduced to describe the rotation of the b-frame with respect to the  $\ell$ -frame and they are expressed as follow:

$$Q = \begin{pmatrix} q_1 \\ q_2 \\ q_3 \\ q_4 \end{pmatrix} = \begin{pmatrix} (\Theta_x/\Theta)\sin(\Theta/2) \\ (\Theta_y/\Theta)\sin(\Theta/2) \\ (\Theta_z/\Theta)\sin(\Theta/2) \\ \cos(\Theta/2) \end{pmatrix} \quad (6.8)$$

where  $\Theta = \sqrt{\Theta_x^2 + \Theta_y^2 + \Theta_z^2}$  is the rotation angle and  $\frac{\Theta_x}{\Theta}, \frac{\Theta_y}{\Theta}, \frac{\Theta_z}{\Theta}$  are the three direction cosines of the rotation axis with respect to the  $\ell$ -frame.

The definition of the quaternion parameters described in Eq.6.8 implies that the four quaternion components are not independent since  $q_1^2 + q_2^2 + q_3^2 + q_4^2 = 1$ . This means that only three independent quaternion components are sufficient to describe the rigid body rotation. However, due to computational errors, the above equality may be violated. In order to compensate for this effect, special normalization procedures have been suggested [Salychev, 1998]. Let us consider that an error  $\Delta$  exists after the computation of the quaternion parameters:

$$\Delta = 1 - (q_1^2 + q_2^2 + q_3^2 + q_4^2) \quad (6.9)$$

Consequently, the vector of quaternion parameters  $Q$  should be updated after each computational step as follows:

$$\hat{Q} = \frac{Q}{\sqrt{1-\Delta}} \cong Q \left( 1 + \frac{\Delta}{2} \right) \quad (6.10)$$

The time rate of change of the quaternion is described by the following first-order differential equation:

$$\dot{Q} = \frac{1}{2} \Omega(\omega) Q \quad (6.11)$$

where  $\Omega(\omega)$  is a skew-symmetric matrix given as follows:

$$\Omega(\omega) = \begin{pmatrix} 0 & \omega_z & -\omega_y & \omega_x \\ -\omega_z & 0 & \omega_x & \omega_y \\ \omega_y & -\omega_x & 0 & \omega_z \\ -\omega_x & -\omega_y & -\omega_z & 0 \end{pmatrix} \quad (6.12)$$

where  $\omega_x, \omega_y, \omega_z$  are the angular velocities of body rotation which are determined by Eq.6.6 for  $\omega_x$  and are monitored by the Normal FOG and the Torus FOG for  $\omega_y$  and  $\omega_z$  respectively., after compensating for the Earth rotation and the  $\ell$ -frame change of orientation (i.e.  $\Omega_{i\ell}^b$ ).

To solve the set of first order differential equations given in Eq.6.11, Euler's method can be used to determine the quaternion parameters  $Q_{k+1}$  at time  $t_{k+1}$  based on the values of the quaternion parameters  $Q_k$  at time  $t_k$  as follows:

$$Q_{k+1} = Q_k + \left( \frac{1}{2} \Omega(\omega_k) Q_k \right) \Delta t \quad (6.13)$$

where  $\Delta t = t_{k+1} - t_k$ .

Once the quaternion parameters are determined at a certain time  $t_k$ , the rotation matrix  $R_b^\ell$  can be obtained using the following direct relationship:

$$R_b^\ell = \begin{pmatrix} R_{11} & R_{12} & R_{13} \\ R_{21} & R_{22} & R_{23} \\ R_{31} & R_{32} & R_{33} \end{pmatrix} = \begin{pmatrix} q_1^2 - q_2^2 - q_3^2 + q_4^2 & 2(q_1q_2 - q_3q_4) & 2(q_1q_3 + q_2q_4) \\ 2(q_1q_2 + q_3q_4) & -q_1^2 + q_2^2 - q_3^2 + q_4^2 & 2(q_2q_3 - q_1q_4) \\ 2(q_1q_3 - q_2q_4) & 2(q_2q_3 + q_1q_4) & -q_1^2 - q_2^2 + q_3^2 + q_4^2 \end{pmatrix} \quad (6.14)$$

On the other hand, the quaternion parameters can be obtained from the rotation matrix  $R_b^\ell$  as follows:

$$\begin{pmatrix} q_1 \\ q_2 \\ q_3 \\ q_4 \end{pmatrix} = \begin{pmatrix} 0.25(R_{32} - R_{23})/q_4 \\ 0.25(R_{13} - R_{31})/q_4 \\ 0.25(R_{21} - R_{12})/q_4 \\ 0.5\sqrt{1 + R_{11} + R_{22} + R_{33}} \end{pmatrix} \quad (6.15)$$

The quaternion parameters are introduced for the parameterization of the rotation matrix  $R_b^\ell$  for three reasons [Schwarz and Wei, 1999]. The first reason is that only four differential equations are solved numerically instead of six differential equations if the rotation matrix  $R_b^\ell$  is manipulated directly. The second reason is that the quaternion

solution avoids the singularity problem that might exist with some other solution methods. The third reason is the computational simplicity introduced by the quaternion.

### 6.2.2.3. Computational procedure for the different surveying parameters

The proposed procedure can be described as follows:

1. Receive the measurements from the two FOGs and the three accelerometers and remove the values of the bias offsets. Determine the angular increments corresponding to these angular velocity measurements as follows:

$$\begin{aligned}\Delta\theta_y &= \omega_y \Delta t \\ \Delta\theta_z &= \omega_z \Delta t\end{aligned}\tag{6.16}$$

where  $\Delta\theta_y$  is the measurement of the angular increments provided by the Normal FOG after compensating for the drift rate  $d_y$  and  $\Delta\theta_z$  is the measurement of the angular increments provided by the Torus FOG after compensating for the drift rate  $d_z$ .

Similarly, the velocity increments provided by the accelerometers are given as:

$$\begin{aligned}\Delta v_x &= f_x \Delta t \\ \Delta v_y &= f_y \Delta t \\ \Delta v_z &= f_z \Delta t\end{aligned}\tag{6.17}$$

where  $\Delta v_x$ ,  $\Delta v_y$  and  $\Delta v_z$  are the measured velocity increments along the X, Y and Z-axes, respectively.

2. Determine the inclination (pitch) angle from the accelerometer measurements as given in Eq.6.5. Consequently, the angular increment along the X-direction is given as follows:

$$\Delta\theta_x = \omega_x \Delta t = [\theta(t_{k+1}) - \theta(t_k)]\tag{6.18}$$

3. Determine the effect of the Earth rotation and the  $\ell$ -frame change of orientation in the angular changes monitored along the three axes. The term responsible for the Earth rotation and the  $\ell$ -frame change of orientation is  $\omega_{i\ell}^b$  and is given as follows (see Eq.5.15):

$$\omega_{i\ell}^b = R_\ell^b(t_k) \begin{pmatrix} \frac{-V^n(t_k)}{M+h} \\ \frac{V^e(t_k)}{N+h} + \omega^e \cos \varphi \\ \frac{V^e(t_k) \tan \varphi}{N+h} + \omega^e \sin \varphi \end{pmatrix} \quad (6.19)$$

Then the angular changes corresponding to  $\omega_{i\ell}^b$  can be determined as:

$$\theta_{i\ell}^b = \omega_{i\ell}^b \Delta t \quad (6.20)$$

Consequently, the vector of measured angular increments  $\theta_{ib}^b = (\Delta\theta_x \quad \Delta\theta_y \quad \Delta\theta_z)^T$  is compensated for  $\theta_{i\ell}^b$  to determine the actual BHA angular changes  $\theta_{lb}^b$  as follows:

$$\theta_{lb}^b = \theta_{ib}^b - \theta_{i\ell}^b = (\delta\theta_x \quad \delta\theta_y \quad \delta\theta_z)^T \quad (6.21)$$

4. Update the quaternion. The time rate of change of the quaternion as given in Eq.6.11 corresponds to the time rate of change of the rotation matrix  $R_b^\ell$  as given in Eq.6.7. The quaternion update follows Eq.6.13. The time interval  $\Delta t$  is multiplied by the elements of the skew-symmetric matrix of angular velocities  $\Omega$ , so that  $\omega_x \Delta t = \delta\theta_x$ ,  $\omega_y \Delta t = \delta\theta_y$  and  $\omega_z \Delta t = \delta\theta_z$ . The quaternion update equation is then given as follows:

$$\begin{pmatrix} q_1(t_{k+1}) \\ q_2(t_{k+1}) \\ q_3(t_{k+1}) \\ q_4(t_{k+1}) \end{pmatrix} = \begin{pmatrix} q_1(t_k) \\ q_2(t_k) \\ q_3(t_k) \\ q_4(t_k) \end{pmatrix} + \frac{1}{2} \begin{pmatrix} 0 & \delta\theta_z & -\delta\theta_y & \delta\theta_x \\ -\delta\theta_z & 0 & \delta\theta_x & \delta\theta_y \\ \delta\theta_y & -\delta\theta_x & 0 & \delta\theta_z \\ -\delta\theta_x & -\delta\theta_y & -\delta\theta_z & 0 \end{pmatrix} \begin{pmatrix} q_1(t_k) \\ q_2(t_k) \\ q_3(t_k) \\ q_4(t_k) \end{pmatrix} \quad (6.22)$$

The initial value of the quaternion  $Q(t_0) = (q_1(t_0) \quad q_2(t_0) \quad q_3(t_0) \quad q_4(t_0))^T$  is calculated after determining the initial rotation matrix  $R_b^\ell(t_0)$  (see Eq.6.15) using the initial attitude angles computed during the alignment process.

Consequently, the rotation matrix  $R_b^\ell$  can be determined from its direct relationship to the quaternion  $Q = (q_1 \ q_2 \ q_3 \ q_4)^T$  as given by Eq.6.14. According to the  $R_b^\ell$  definition given in Eq.5.1, the pitch (inclination), the roll and the azimuth are determined as follows:

$$\theta = \arctan\left(\frac{R_{32}}{\sqrt{R_{12}^2 + R_{22}^2}}\right) \quad (6.23)$$

$$\phi = \arctan\left(\frac{R_{31}}{R_{33}}\right) \quad (6.24)$$

$$\psi = \arctan\left(\frac{-R_{12}}{R_{22}}\right) \quad (6.25)$$

5. Determine the BHA velocity changes:

$$\frac{\Delta V^\ell}{\Delta t} = R_b^\ell f^b - (2\Omega_{ie}^\ell + \Omega_{el}^\ell)V^\ell + g^\ell$$

or

$$\Delta V^\ell = R_b^\ell f^b \Delta t - (2\Omega_{ie}^\ell + \Omega_{el}^\ell)V^\ell \Delta t + g^\ell \Delta t \quad (6.26)$$

Since the specific force measurement  $f^b = (f_x \ f_y \ f_z)^T$  is related to the velocity increment measurements  $\Delta v^b = (\Delta v_x \ \Delta v_y \ \Delta v_z)^T$  with  $f^b = \Delta v^b / \Delta t$ , Eq.6.26 can be given as:

$$\Delta V^\ell(t_{k+1}) = R_b^\ell \Delta v^b(t_{k+1}) - (2\Omega_{ie}^\ell + \Omega_{el}^\ell)V^\ell(t_k) \Delta t + g^\ell \Delta t \quad (6.27)$$

where  $\Omega_{ie}^\ell$  and  $\Omega_{el}^\ell$  are given in Eqs.5.10 and 5.11 respectively, while  $g^\ell$  is the gravity field vector.

The first term on the right-hand side of Eq.6.27 is the measured velocity increments transformed to the  $\ell$ -frame. The second term is the Coriolis correction that compensates for the Earth rotation and the  $\ell$ -frame change of orientation. The third term is the gravity correction. The velocity components at the current time epoch  $t_{k+1}$  are computed using the modified Euler formula as follows:

$$V^\ell(t_{k+1}) = V^\ell(t_k) + \frac{1}{2}(\Delta V^\ell(t_k) + \Delta V^\ell(t_{k+1})) \quad (6.28)$$

where  $V^\ell = (V^e \quad V^n \quad V^u)$  are the velocity components as described in the  $\ell$ -frame.

6. Determine the altitude of the bottom hole assembly,  $h$ , (i.e. the true vertical depth TVD) using the vertical component of the velocity vector,  $V^u$ . Since  $\dot{h} = V^u$ , the TVD can be computed at time instant  $t_{k+1}$  using the modified Euler formula:

$$h(t_{k+1}) = h(t_k) + \frac{1}{2}(V^u(t_{k+1}) + V^u(t_k))\Delta t \quad (6.29)$$

Once the TVD is determined, the latitude  $\varphi$ , and the longitude  $\lambda$ , can be computed.  $\varphi$  and  $\lambda$  can be computed at time instant  $(t_{k+1})$  using the modified Euler formula as follows:

$$\varphi(t_{k+1}) = \varphi(t_k) + \frac{1}{2} \frac{(V^n(t_{k+1}) + V^n(t_k))}{M + h} \Delta t \quad (6.30)$$

$$\lambda(t_{k+1}) = \lambda(t_k) + \frac{1}{2} \frac{(V^e(t_{k+1}) + V^e(t_k))}{(N + h)\cos\varphi} \Delta t \quad (6.31)$$

It should be noted that the computation of the longitude,  $\lambda$ , will suffer from singularities if this procedure is performed closer to the poles where the latitude  $\varphi$  becomes equal to  $\pi/2$ .

The six steps described above are repeated for each new set of measurements received from the two FOGs and the three accelerometers. A block diagram describing the functionality of this procedure is shown on Fig.6.4. The above steps of the computational procedure were implemented using MATLAB computer-aided design software (Mathworks, Natick, MA) on an IBM-PC PIII system.

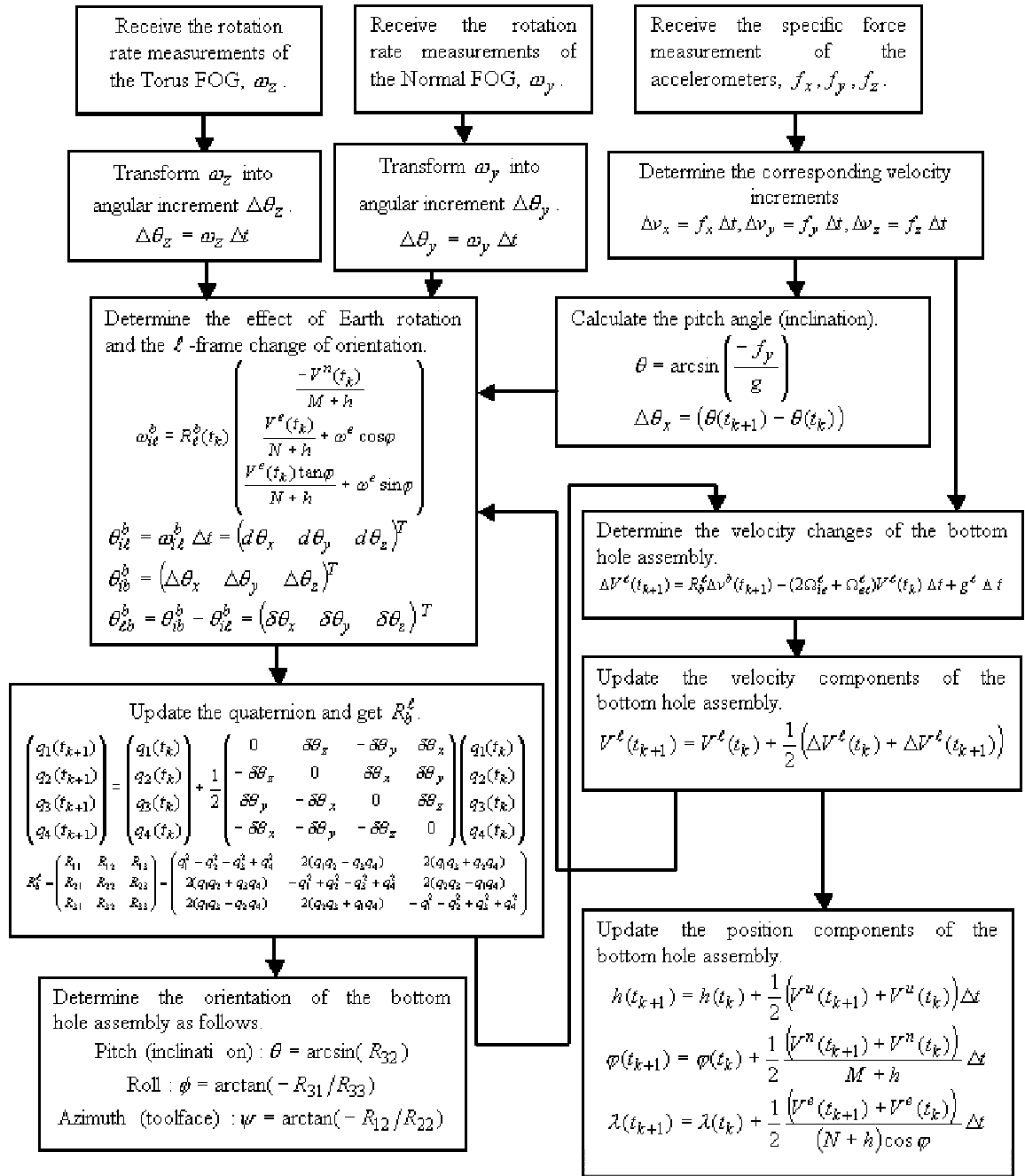


Fig.6.4. A block diagram describing the functionality of the surveying procedure for the radical section of the well.

### 6.2.3. Modeling surveying errors by linear state equations.

Errors in dynamic systems are variable in time and therefore described by differential equations. Linearization of the non-linear dynamic system is the most common approach for deriving a set of linear differential equations, which define the error states of the dynamic system [Stephenson and Wilson, 1992; Schwarz and Wei, 1999]. The error states expressed in the  $\ell$ -frame for the mechanization equations given in the previous section are defined as follows:

$$e^\ell = (\delta\varphi, \delta\lambda, \delta h, \delta V_e, \delta V_n, \delta V_u, \delta\theta, \delta\phi, \delta\psi, \delta\omega_y, \delta\omega_z, \delta f_x, \delta f_y, \delta f_z) \quad (6.32)$$

where:

$\delta\varphi, \delta\lambda, \delta h$	are the coordinate errors;
$\delta V^e, \delta V^n, \delta V^u$	are the velocity errors;
$\delta\theta, \delta\phi, \delta\psi$	are the attitude errors;
$\delta\omega_y, \delta\omega_z$	are the errors in the angular velocity measurements;
$\delta f_x, \delta f_y, \delta f_z$	are the errors in the specific force measurements.

#### 6.2.3.1. Attitude errors

Attitude errors ( $\delta\theta$ ,  $\delta\phi$  and  $\delta\psi$ ) depend on two main sources. The first source is the errors in the measurement of angular velocities provided by the FOGs. The second source is the errors generated due to the Earth rotation and the change of orientation of the  $\ell$ -frame. The expression describing the time rate of change of the attitude errors  $\varepsilon^\ell = (\delta\theta \ \delta\phi \ \delta\psi)^T$  is given as follows [Schwarz and Wei, 1999]:

$$\dot{\varepsilon}^\ell = -\Omega_{i\ell}^\ell \varepsilon^\ell - \delta\omega_{i\ell}^\ell + R_b^\ell d \quad (6.33)$$

where  $\delta\omega_{i\ell}^\ell = \delta\omega_{ie}^\ell + \delta\omega_{e\ell}^\ell$  is the angular velocity error vector corresponding to  $\omega_{i\ell}^\ell$  and  $d = (\delta\omega_x \ \delta\omega_y \ \delta\omega_z)^T$  is the vector of angular velocities measurement errors (FOG drift rates). Both  $\delta\omega_y$  and  $\delta\omega_z$  are described as first order Gauss-Markov processes (see Chapter 5) while  $\delta\omega_x$  is given in terms of the accelerometer errors (see Eq.5.44).

The second term in the right hand side of Eq.6.33,  $\delta\omega_{i\ell}^\ell$ , depends implicitly on the velocity errors  $\delta V^\ell = (\delta V^e \ \delta V^n \ \delta V^u)^T$  and the coordinate errors  $\delta r^\ell = (\delta\varphi \ \delta\lambda \ \delta h)^T$ . This angular velocity error consists of two terms,  $\delta\omega_{ie}^\ell$  and  $\delta\omega_{e\ell}^\ell$ , which are given as:

$$\delta\omega_{ie}^{\ell} = \begin{pmatrix} 0 & 0 & 0 \\ -\omega^e \sin \varphi & 0 & 0 \\ \omega^e \cos \varphi & 0 & 0 \end{pmatrix} \begin{pmatrix} \delta\varphi \\ \delta\lambda \\ \delta h \end{pmatrix} \quad (6.34)$$

$$\delta\omega_{el}^{\ell} = \begin{pmatrix} 0 & 0 & \frac{V^n}{(M+h)^2} \\ 0 & 0 & \frac{-V^e}{(N+h)^2} \\ \frac{V^e}{(N+h)\cos^2 \varphi} & 0 & \frac{-V^e \tan \varphi}{(N+h)^2} \end{pmatrix} \begin{pmatrix} \delta\varphi \\ \delta\lambda \\ \delta h \end{pmatrix} + \begin{pmatrix} 0 & \frac{-1}{M+h} & 0 \\ \frac{1}{N+h} & 0 & 0 \\ \frac{\tan \varphi}{N+h} & 0 & 0 \end{pmatrix} \begin{pmatrix} \delta V^e \\ \delta V^n \\ \delta V^u \end{pmatrix} \quad (6.35)$$

With the substitution of the expressions of  $\delta\omega_{ie}^{\ell}$  (Eq.6.34) and  $\delta\omega_{el}^{\ell}$  (Eq.6.35), the attitude errors (Eq.6.33) can be rewritten as:

$$\begin{pmatrix} \delta\dot{\theta} \\ \delta\dot{\varphi} \\ \delta\dot{\psi} \end{pmatrix} = \begin{pmatrix} 0 & \omega^e \sin \varphi + \frac{V^e \tan \varphi}{N+h} & -\omega^e \cos \varphi - \frac{V^e}{N+h} \\ -\omega^e \sin \varphi - \frac{V^e \tan \varphi}{N+h} & 0 & -\frac{V^n}{M+h} \\ \omega^e \cos \varphi + \frac{V^e}{N+h} & \frac{V^n}{M+h} & 0 \end{pmatrix} \begin{pmatrix} \delta\theta \\ \delta\varphi \\ \delta\psi \end{pmatrix} + \begin{pmatrix} 0 & 0 & \frac{-V^n}{(M+h)^2} \\ \omega^e \sin \varphi & 0 & \frac{V^e}{(N+h)^2} \\ -\omega^e \cos \varphi - \frac{V^e}{(N+h)\cos^2 \varphi} & 0 & \frac{V^e \tan \varphi}{(N+h)^2} \end{pmatrix} \begin{pmatrix} \delta\varphi \\ \delta\lambda \\ \delta h \end{pmatrix} + \begin{pmatrix} 0 & \frac{1}{M+h} & 0 \\ \frac{-1}{N+h} & 0 & 0 \\ \frac{-\tan \varphi}{N+h} & 0 & 0 \end{pmatrix} \begin{pmatrix} \delta V^e \\ \delta V^n \\ \delta V^u \end{pmatrix} + R_b^{\ell} d \quad (6.36)$$

### 6.2.3.2. Coordinate errors

Since the coordinates of the bottom hole assembly depend only on the velocity components  $V^e, V^n$  and  $V^u$ , the coordinate errors  $\delta\varphi, \delta\lambda$  and  $\delta h$  are given directly in terms of velocity errors  $\delta V^e, \delta V^n$  and  $\delta V^u$ . The expression for the coordinate errors is

obtained by differentiating those equations describing the relationship between the time rate of change of the coordinate components and the velocity components.

$$\delta \dot{\mathbf{r}}^\ell = \begin{pmatrix} \delta \dot{\varphi} \\ \delta \dot{\lambda} \\ \delta \dot{h} \end{pmatrix} = \begin{pmatrix} 0 & \frac{1}{M+h} & 0 \\ \frac{1}{(N+h)\cos\varphi} & 0 & 0 \\ 0 & 0 & 1 \end{pmatrix} \begin{pmatrix} \delta V^e \\ \delta V^n \\ \delta V^u \end{pmatrix} + \begin{pmatrix} 0 & 0 & \frac{-V^n}{(M+h)^2} \\ \frac{V^e \tan\varphi}{(N+h)\cos\varphi} & 0 & \frac{-V^e}{(N+h)^2 \cos\varphi} \\ 0 & 0 & 0 \end{pmatrix} \begin{pmatrix} \delta\varphi \\ \delta\lambda \\ \delta h \end{pmatrix} \quad (6.37)$$

### 6.2.3.3. Velocity errors

The complete implementation of the  $\ell$ -frame mechanization equations requires the computation of the three velocity components  $V^e, V^n$  and  $V^u$ . The corresponding error equations are similar to those given in Chapter 5, but after taking the Coriolis effect into consideration.

$$\begin{pmatrix} \delta \dot{V}^e \\ \delta \dot{V}^n \\ \delta \dot{V}^u \end{pmatrix} = \begin{pmatrix} 0 & f_u & -f_n \\ -f_u & 0 & f_e \\ f_n & -f_e & 0 \end{pmatrix} \begin{pmatrix} \delta\theta \\ \delta\varphi \\ \delta\psi \end{pmatrix} + R_b^\ell \begin{pmatrix} \delta f_x \\ \delta f_y \\ \delta f_z \end{pmatrix} + \begin{pmatrix} (2\omega^e \sin\varphi)V^u + (2\omega^e \cos\varphi)V^n + \frac{V^n V^e}{(N+h)\cos^2\varphi} & 0 & 0 \\ (-2\omega^e \cos\varphi)V^e - \frac{(V^e)^2}{(N+h)\cos^2\varphi} & 0 & 0 \\ (-2\omega^e \sin\varphi)V^e & 0 & \frac{2\gamma}{R} \end{pmatrix} \begin{pmatrix} \delta\varphi \\ \delta\lambda \\ \delta h \end{pmatrix} + \begin{pmatrix} \frac{-V_u}{N+h} + \frac{V_n}{N+h} \tan\varphi & 2\omega^e \sin\varphi + \frac{V^e \tan\varphi}{(N+h)} & -2\omega^e \cos\varphi - \frac{V^e}{N+h} \\ -2\omega^e \sin\varphi - \frac{2V^e \tan\varphi}{N+h} & -\frac{V^u}{M+h} & \frac{-V^n}{M+h} \\ 2\omega^e \cos\varphi + \frac{2V^e}{N+h} & \frac{2V^n}{M+h} & 0 \end{pmatrix} \begin{pmatrix} \delta V^e \\ \delta V^n \\ \delta V^u \end{pmatrix} \quad (6.38)$$

where  $f_e, f_n$  and  $f_u$  are three components of the specific force vector

$f^\ell = (f_e \ f_n \ f_u)^T = R_b^\ell f^b = R_b^\ell (f_x \ f_y \ f_z)^T$ , where  $f_x, f_y$  and  $f_z$  are the specific force measurement outputs of the accelerometers and  $R$  is the mean radius of the Earth.

#### **6.2.4. Limiting surveying errors using continuous aided inertial navigation and ZUPT techniques.**

Since the Dual-FOG MWD surveying system cannot work as stand-alone INS due to the growth of the different surveying errors with time, the previously described INS-aiding techniques are utilized. These aiding techniques include either continuous aided inertial navigation utilizing the measurements of the drill pipe length and the penetration rate or the zero velocity update techniques. These techniques have been employed and tested successfully for the Single-FOG MWD surveying system.

#### **6.2.5. Experimental procedure and signal conditioning.**

The proposed dual-axis gyroscopic surveying system integrates the measurements from two mutually orthogonal FOGs and three accelerometers, and provides the BHA orientation. The experimental work for this study was performed at the Inertial Laboratory of the University of Calgary using a custom-designed setup capable of providing changes in the orientation of the surveying sensors in three mutually orthogonal directions, thus simulating different BHA orientations. An inertial measurement unit (LTN90-100, Litton, Woodland Hills, CA) incorporating three-axis accelerometers and three-axis optical gyroscopes was mounted inside the experimental setup. LTN90-100 is a navigational grade unit with  $0.01^\circ/hr$  gyro drift and  $0.002^\circ / \sqrt{hr}$  gyro angle random walk. As mentioned earlier in Chapter 5, the optical gyroscopes utilized in this unit are of ring laser type and they differ from FOGs in the way the laser beam is propagating inside, while the drift and noise behaviors are exactly the same. The LTN90-100 is suitable for laboratory experiments to study the feasibility of the Dual-FOG MWD surveying system and compare it to the full IMU solution. In addition, the LTN90-100 is integrated with KINGSPAD<sup>TM</sup> software (University of Calgary, Department of Geomatics Engineering), which is a kinematic geodetic system for

position and attitude determination, and is used to provide reference values of the navigation parameters in order to check the accuracy of the proposed system.

Accelerometer and gyro measurements ( $f_x, f_y, f_z$  and  $\omega_y, \omega_z$ ) were delivered at a sampling rate of  $64\text{Hz}$ . Averaging at  $1$ -second time intervals was performed for all the measurements in order to reduce the output uncertainties. The measurements of the third gyro ( $\omega_x$ ) were only processed by KINGSPAD<sup>TM</sup> software to provide reference data. Comparison between the dual-gyro solution and the full IMU solution would determine how the synthetic rotation rate component  $\omega_{xs}$  agrees with the actual one  $\omega_x$  provided by the LTN90-100. In addition, this comparison is essential for determining the accuracy of the proposed Dual-FOG MWD surveying system when navigational grade inertial sensors are utilized.

## 6.2.6. Results

### 6.2.6.1. Comparison between dual-gyro and full IMU solution.

The navigation parameters calculated using the dual gyro system were compared to the output of KINGSPAD<sup>TM</sup> while changing the inclination angle in the range of  $\pm 75^\circ$ , the roll angle in the range of  $\pm 30^\circ$  and the azimuth angle between  $80^\circ$  and  $120^\circ$ . The calculated synthetic rotation rate component  $\omega_{xs}$  was compared to the rotation rate measurement of the third gyro  $\omega_x$ . Fig.6.5 shows that  $\omega_x$  and  $\omega_{xs}$  were quite similar over the entire experiment. In order to show the slight differences between the two rotation rate components, Fig.6.6 presents  $\omega_x$  and  $\omega_{xs}$  over about  $1$ -minute time range. It can be suggested that although the synthetic component had a small delay from the measured one,  $\omega_{xs}$  was still able to follow the changes of  $\omega_x$ . The synthetic rotation rate component  $\omega_{xs}$  was processed with the other two mutually orthogonal rotation rate measurements  $\omega_y$  and  $\omega_z$  to determine the three attitude angles (inclination, roll and azimuth). A comparison between the output of the dual gyro system computation and the full IMU computation (provided by KINGSPAD<sup>TM</sup>) is shown on Fig.6.7. The output of any of the two solutions almost coincided with the other for each of the three attitude angles. Errors of less than  $0.03^\circ$  for the inclination,  $0.05^\circ$  for the roll and  $1^\circ$  for the azimuth were observed over the entire experiment.

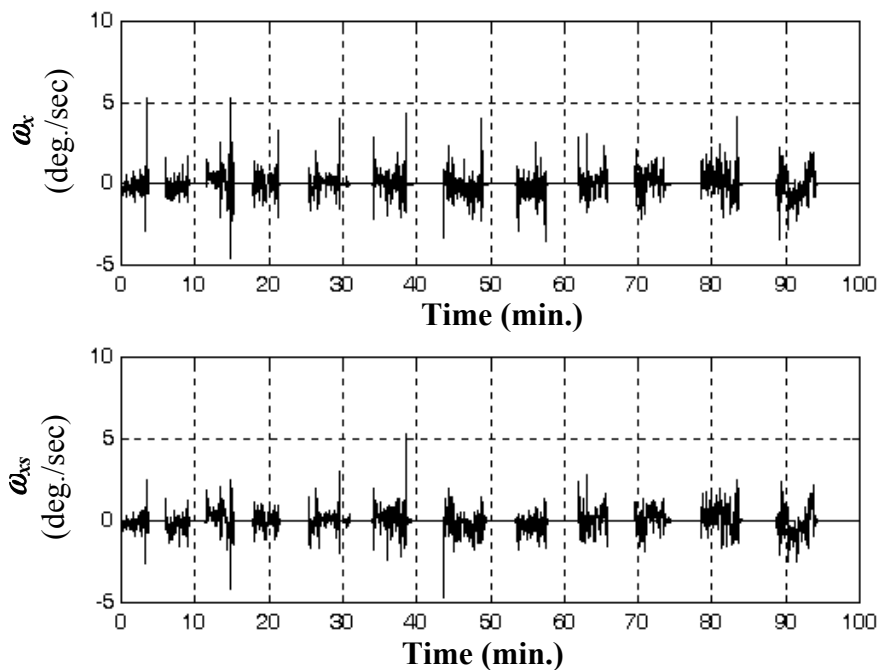


Fig.6.5. Comparison between the actual rotation rate measurement  $\omega_x$  and the corresponding synthetic rotation rate component  $\omega_{xs}$ .

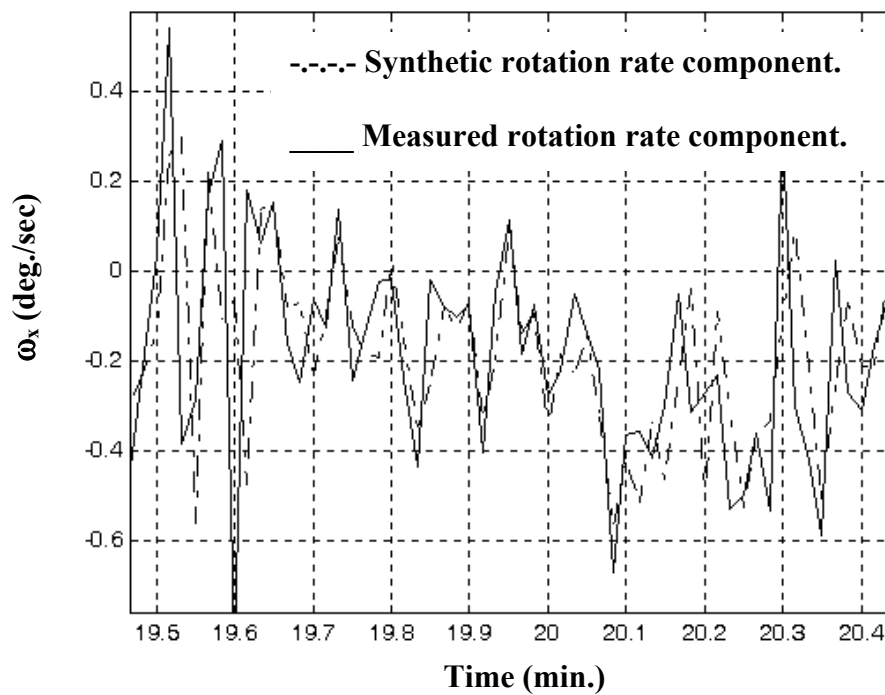


Fig.6.6. Differences between the synthetic and the measured rotation rate components along the X-axis.

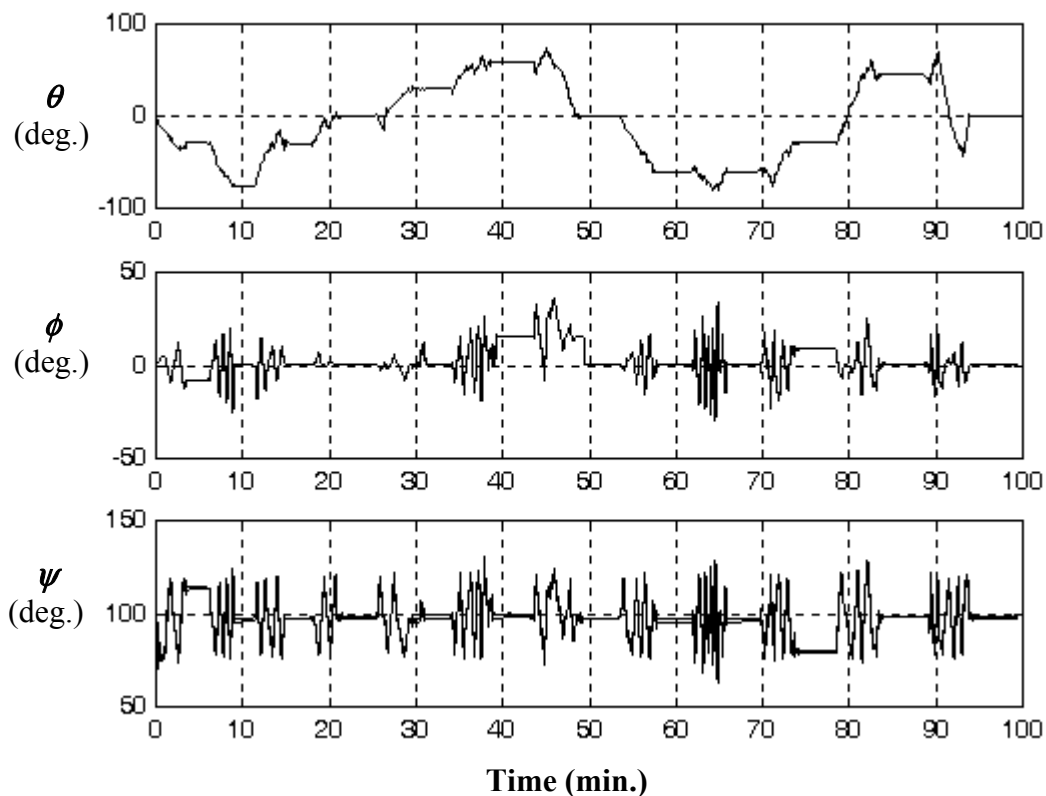


Fig.6.7. Computation of the attitude components with the dual gyro system and the full IMU system.

Fig.6.8 shows the calculated azimuth angle using both the dual gyro system and the full IMU system for part of the same experimental results shown on Fig.6.7. The largest difference between the two solutions was observed at one of the stationary intervals while the whole setup was not rotating (see Fig.6.8). This error occurred when the setup was at about  $75^\circ$  inclination (between  $t=39 \text{ min}$  and  $t=44 \text{ min}$ ), which corresponds to a highly inclined section of a horizontal well. Although the accuracy of the inclination angle was not affected at such high inclination, it is obvious that relatively large azimuth errors would be expected. However, this azimuth error was still less than the maximum error expected from any current MWD surveying system.

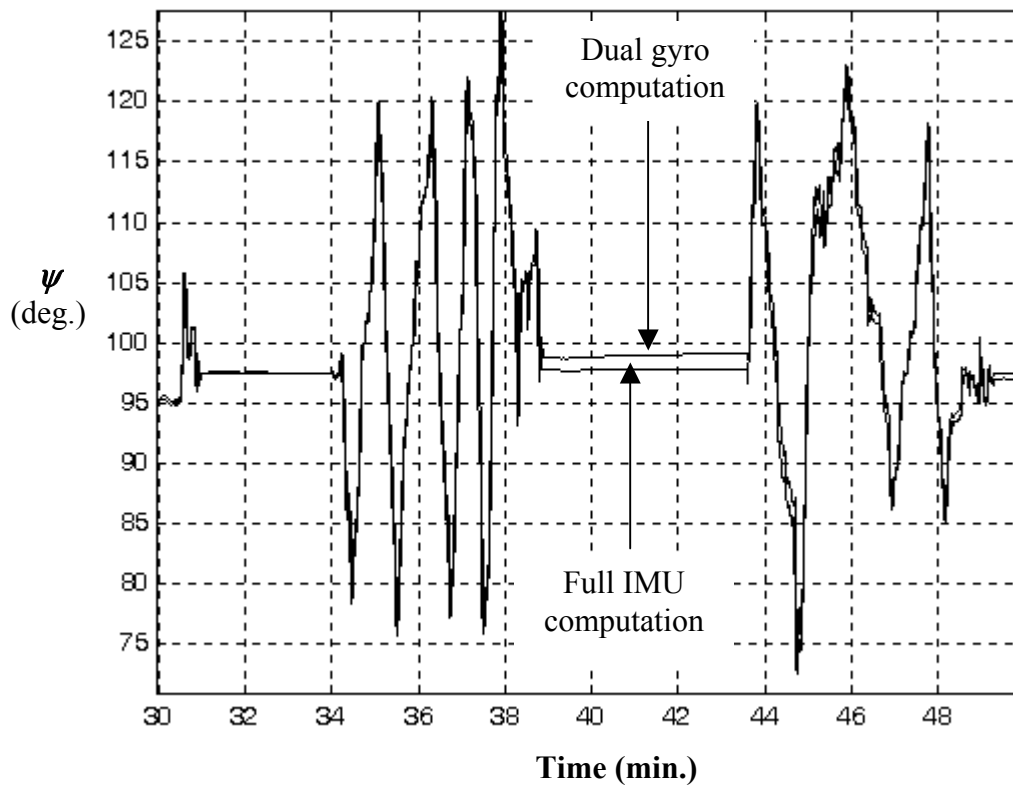


Fig.6.8. Computation of the azimuth angle between  $t=30 \text{ min}$  and  $t=50 \text{ min}$  with the dual-gyro configuration of the full IMU system.

### 6.2.6.2. Continuous aided inertial navigation.

Velocity error states were strongly observable by Kalman filter due to the continuous velocity update provided by the measurement of BHA penetration rate. Consequently, the MSEE of these velocity error states converged within short duration of time into their minimum values as shown on Fig.6.9. The minimum MSEE has been determined as  $3.7 \times 10^{-8} \text{ (m/sec)}^2$  for  $\delta V^e$ ,  $0.8 \times 10^{-8} \text{ (m/sec)}^2$  for  $\delta V^n$  and  $0.4 \times 10^{-8} \text{ (m/sec)}^2$  for  $\delta V^u$ . Since the pitch and the roll error states are strongly coupled with  $\delta V^n$  and  $\delta V^e$ , respectively, their MSEE converged rapidly to the corresponding minimum values ( $4.94 \times 10^{-7} \text{ (deg.)}^2$  for  $\delta \theta$  and  $2.7 \times 10^{-5} \text{ (deg.)}^2$  for  $\delta \phi$ ) as shown on Fig.6.10. On the other hand, the MSEE of the azimuth error state took longer to converge and achieved relatively higher minimum MSEE ( $0.0325 \text{ (deg.)}^2$ ). This resulted in a relatively high azimuth error when compared to either the inclination or the roll errors.

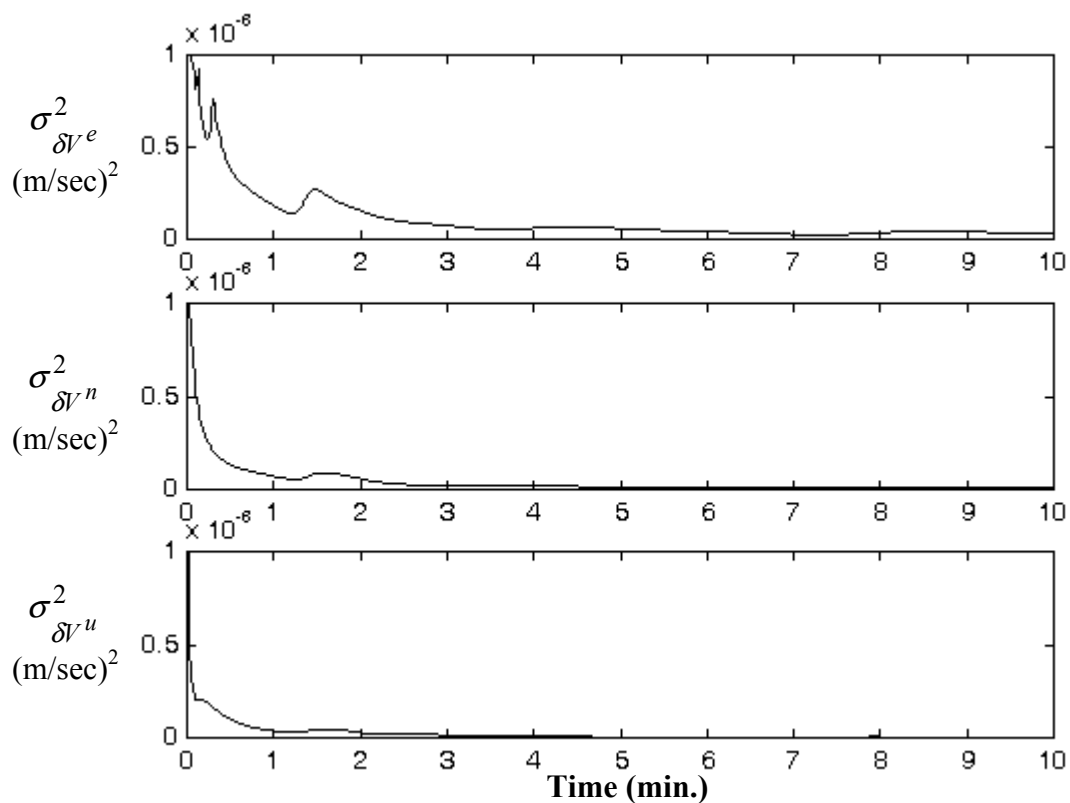


Fig.6.9. Mean square estimation error of the velocity error states in (m/sec)<sup>2</sup>.

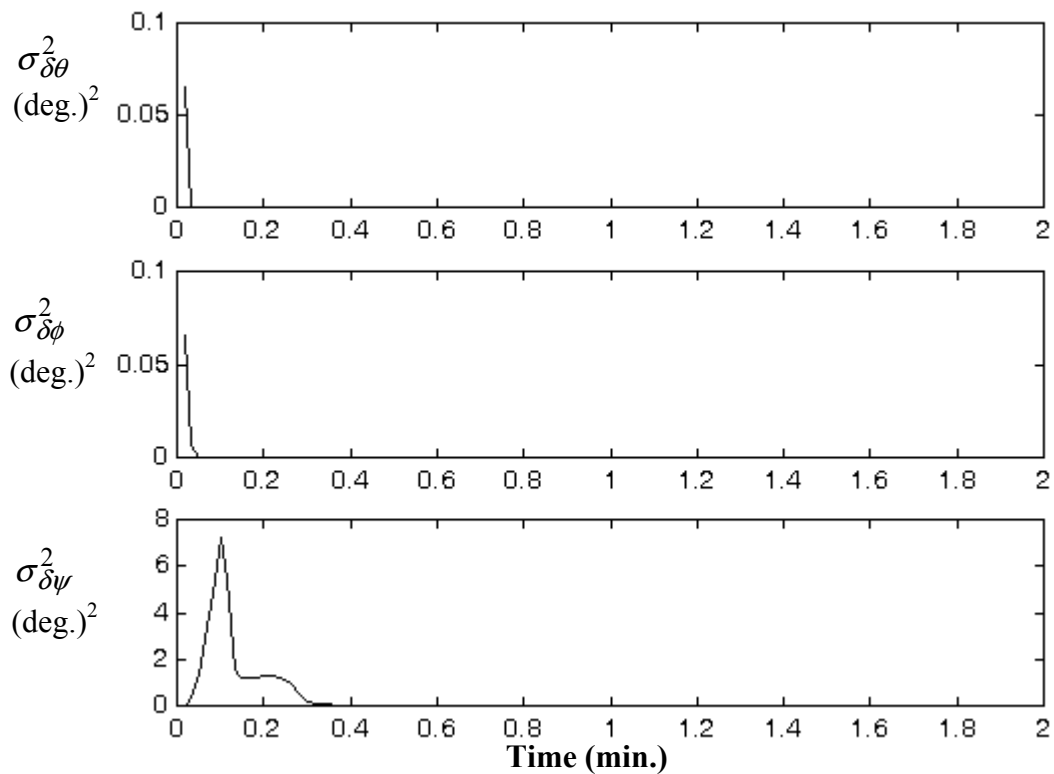


Fig.6.10. Mean square estimation error of the attitude error states in (deg.)<sup>2</sup>.

The accuracy of the position components along the horizontal directions (i.e. East and North directions) is directly affected by the velocity errors along the horizontal plane. Since these velocity-error states were optimally estimated by Kalman filtering and kept as minimal as possible, the growth of the horizontal position error components became limited over time. During an experiment of 100 minutes, the position errors along both the East and the North directions were kept below 5 meters. It should also be noted that the position errors along the horizontal directions are indirectly affected by the azimuth error (see Appendix C). Large azimuth errors may jeopardize the position accuracy in the horizontal directions especially at relatively high penetration rates.

### **6.2.6.3. Impact of the ZUPT procedure.**

The ZUPT procedure with the one-step backward velocity error correction was applied to the measurements obtained from the LTN90-100. Since it is desirable to employ navigational grade inertial sensors with a performance similar to the LTN90-100, this experiment was performed while taking into consideration the drilling process constraints. These constraints permit interrupting the drilling process each 4 to 5 minutes (time between neighbouring ZUPTs) for only one to two minutes (ZUPT interval). It should be noted that this procedure could not be utilized for the tactical grade sensors utilized in Chapter 5, because the position errors of this system would increase significantly for the relatively long time intervals between neighboring ZUPTs.

This experiment involved 11 ZUPT stations over 90 minutes. The velocity and the position errors along the North direction are shown on Fig.6.11. The velocity error growth between neighboring ZUPTs reached values between 1 and 3 *m/sec*. These relatively high velocity errors jeopardized the position accuracy, giving a position error  $\delta P_N$  of about 300 *m* after 90 *min* [See Fig.6.11]. In order to limit the long-term growth of position errors, the backward velocity error correction criterion was employed and the results are shown in Fig.6.12. This criterion limited the growth of velocity errors between neighboring ZUPTs to about 1/3 of their original values. Consequently, position accuracy was significantly improved giving errors of less than 40 *m* between ZUPTs.

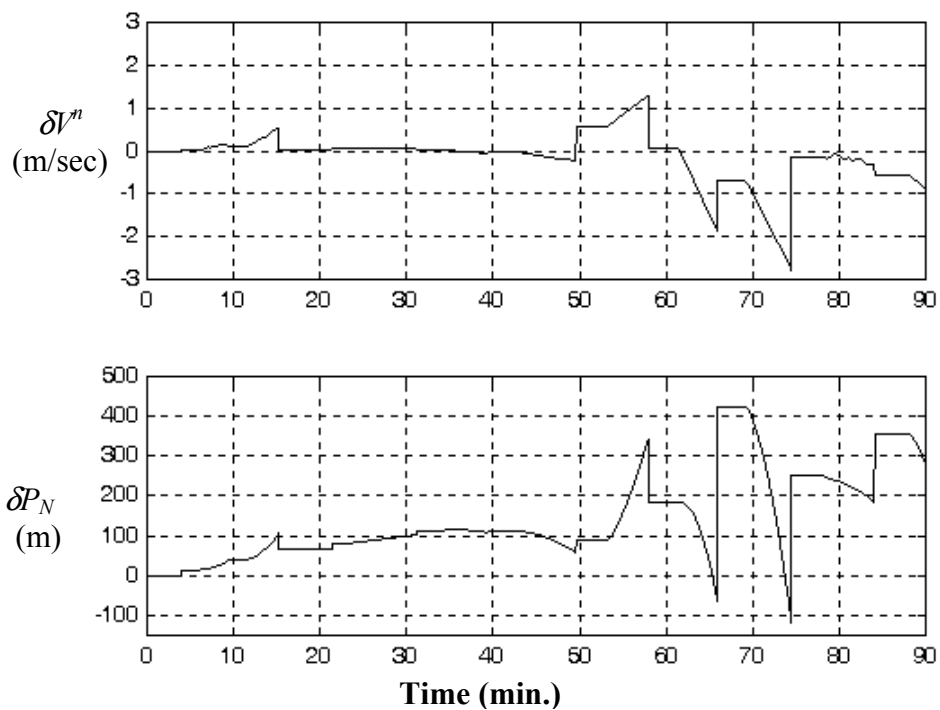


Fig.6.11.Velocity and position errors along the North direction before applying the backward velocity error correction criterion.

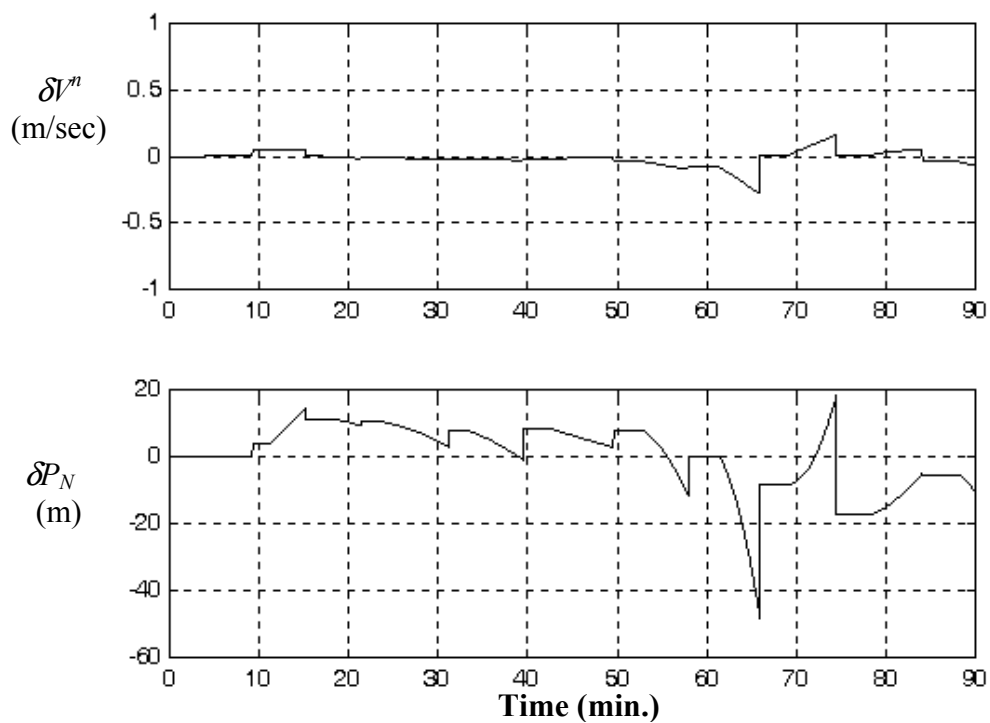


Fig.6.12.Velocity and position errors along the North direction after applying backward velocity error correction criterion.

### 6.3. Station-based surveying technique.

This section presents the station-based surveying methodology for the Dual-FOG MWD surveying system. The aim of this section is to: (1) describe the dual-axis gyroscopic surveying methodology at some predetermined surveying stations; (2) show the performance improvement of station-based surveying systems when utilizing dual gyros and changing the body axes orientation; and (3) apply the same real-time digital signal processing techniques utilized in the single gyro system to limit the surveying errors, thus evaluating the benefits of the new design.

#### 6.3.1. Motivation for station-based surveying.

In general, the station-based surveying method is essential for horizontal/directional drilling processes when the rotary mode of drilling is utilized. During this drilling operation, the whole drill pipe rotates about its spin axis. The rotary mode of drilling is always used to drill the horizontal section of the well. In addition, due to some special conditions related to the downhole formation and the drilling plan, the rotary mode can be utilized for the radical section of the well instead of the steering mode of drilling. In these cases, the continuous surveying methods cannot be applied. Thus, the MWD procedure interrupts the drilling process at some surveying stations for the station-based surveying method to determine the BHA inclination and azimuth.

#### 6.3.2. Performance improvement by utilizing dual FOGs and changing body axes orientation.

The two FOGs monitor two orthogonal components of the Earth rotation rate along their sensitive axes. At each surveying station, the azimuth ( $\psi$ ) is monitored by relating the gyroscopic measurements to the Earth rotation rate components along the North ( $\omega^e \cos\varphi$ ) and the vertical ( $\omega^e \sin\varphi$ ) directions, where  $\varphi$  is the latitude of the drilling site and  $\omega^e$  is the Earth rotation rate around its spin axis ( $15.04^\circ/hr$ ). Similarly, the accelerometer mounted along the tool spin axis monitors the component of Earth gravity along its sensitive axis to determine the inclination ( $I$ ), while the other two accelerometers are responsible of determining the roll angle ( $\phi$ ).

### 6.3.2.1. Station-based surveying of the near-vertical section.

The BHA axes settings established while determining the initial azimuth are kept the same when surveying the near-vertical section of the well. As shown on Fig.6.13, the accelerometers and the gyros monitor different components of the Earth gravity and the Earth rotation rate. The inclination, the roll and the azimuth angles can be expressed in terms of the accelerometer and gyroscopic measurements as follows [Noureldin et al., 2001]:

$$I = \theta = \arcsin\left(\frac{-f_y}{g}\right) \quad (6.39)$$

$$\phi = \arctan\left(\frac{-f_x}{f_z}\right) \quad (6.40)$$

$$\psi = \arccos\left(\frac{\frac{\omega^y}{\omega^e \cos \phi} - \tan \phi \sin \theta}{\cos \theta}\right) \quad (6.41)$$

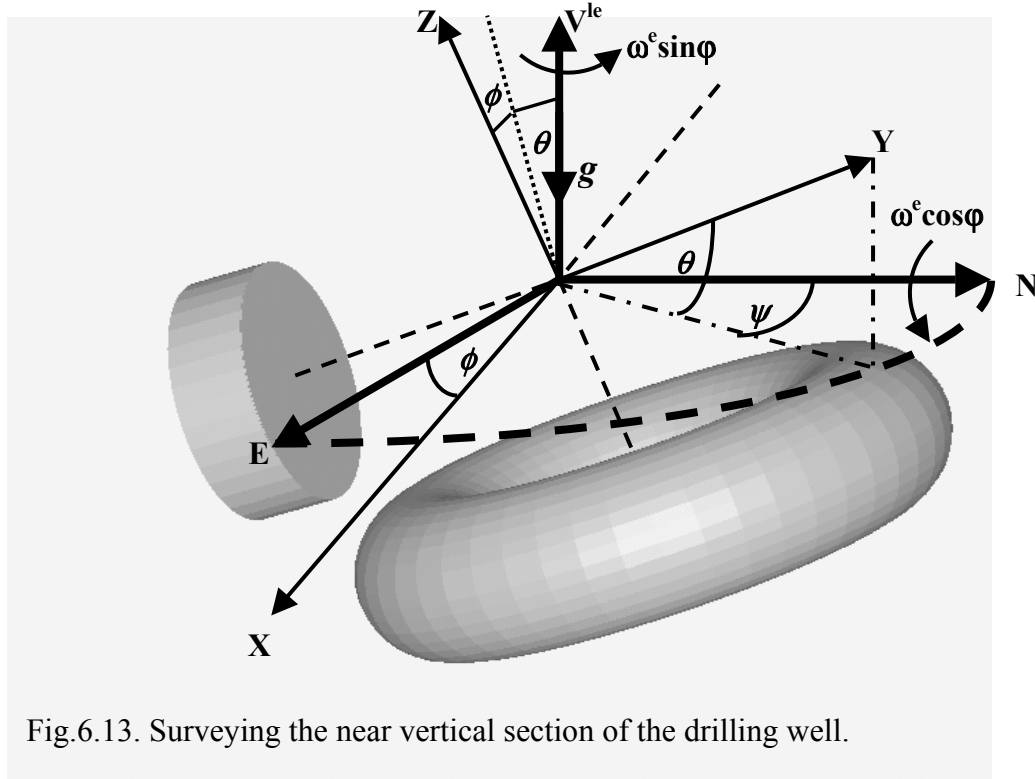


Fig.6.13. Surveying the near vertical section of the drilling well.

The inclination error  $\delta I$  can be evaluated by differentiating Eq.6.39 and it is related to the accelerometer measurement error  $\delta f_y$ .

$$\delta I = \delta \theta = \frac{\left( -\frac{\delta f_y}{g} \right)}{\cos \theta} \quad (6.42)$$

Navigational grade surveying sensors utilize accelerometers with measurement errors of less than  $0.0005g$ , which is a very small value when compared to the Earth gravity  $g$ . Thus, we would expect relatively small inclination errors. In addition, accelerometer biases do not exhibit high drifts over time, thus keeping high inclination accuracy for the entire process. If, for simplicity, we neglect the small inclination error, the azimuth error is related to the Normal FOG measurement error as follows:

$$\delta \psi = \frac{\left( \frac{\delta \omega^y}{\omega^e \cos \varphi} \right)}{\sin \psi \cos \theta} \quad (6.43)$$

Unfortunately, unlike the Earth gravity, the Earth rotation rate ( $\omega^e$ ) is of a relatively small value when compared to the level of gyroscopic errors and their drift over time. Thus, we would expect low azimuth accuracy at certain orientations and some digital signal processing techniques should be utilized to limit the azimuth errors.

The surveying method discussed in this section can be applied for the near-vertical section of the drilling well. At certain inclination angle, switching to the surveying method for highly inclined and horizontal sections should take place. The choice of this transitional inclination angle is related to the growth of errors of the surveying parameters and the desired accuracy. If the expressions of both the inclination and the azimuth errors, Eqs.(6.42) and (6.43), are examined, one can notice the presence of the  $\cos \theta$  term in the denominators. This implies an increase in both the inclination and the azimuth errors as the BHA deviates from the vertical direction (i.e. at higher inclination angles). Such error growth also exists while surveying the highly inclined and the horizontal section of the drilling well as the BHA is getting away from the horizontal section (i.e. at smaller inclination angles). Therefore, we decided to choose this

transitional inclination angle to be exactly at the midway between the vertical and the horizontal directions (i.e. at  $45^\circ$  inclination).

### 6.3.2.2. Station-based surveying of highly inclined and horizontal well sections.

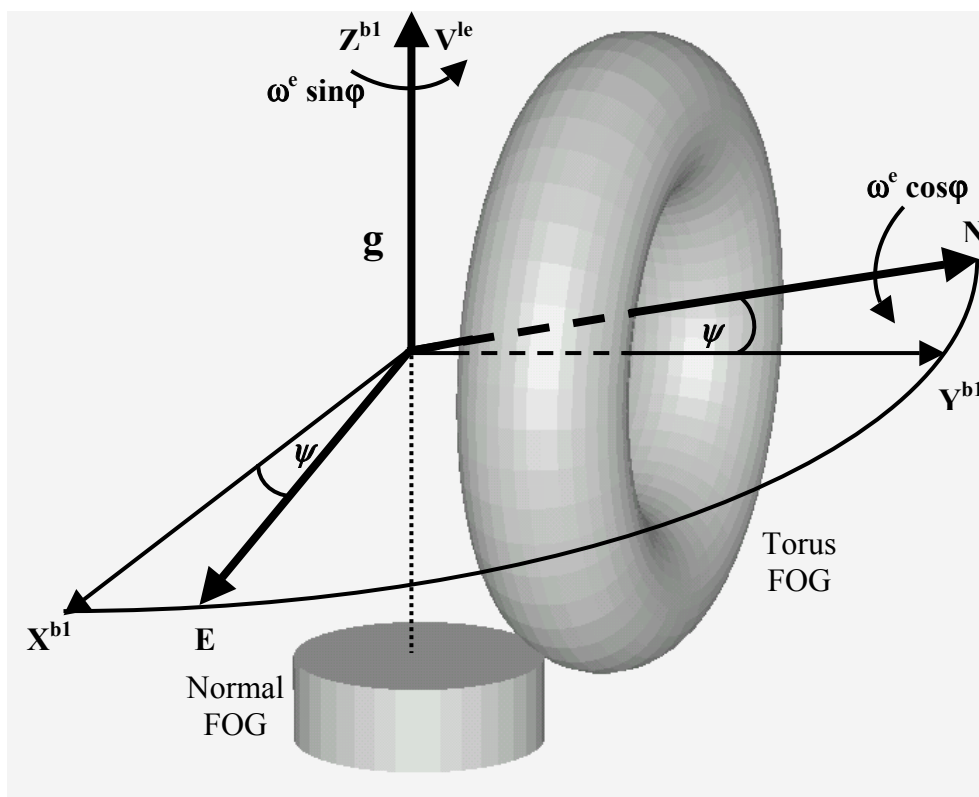
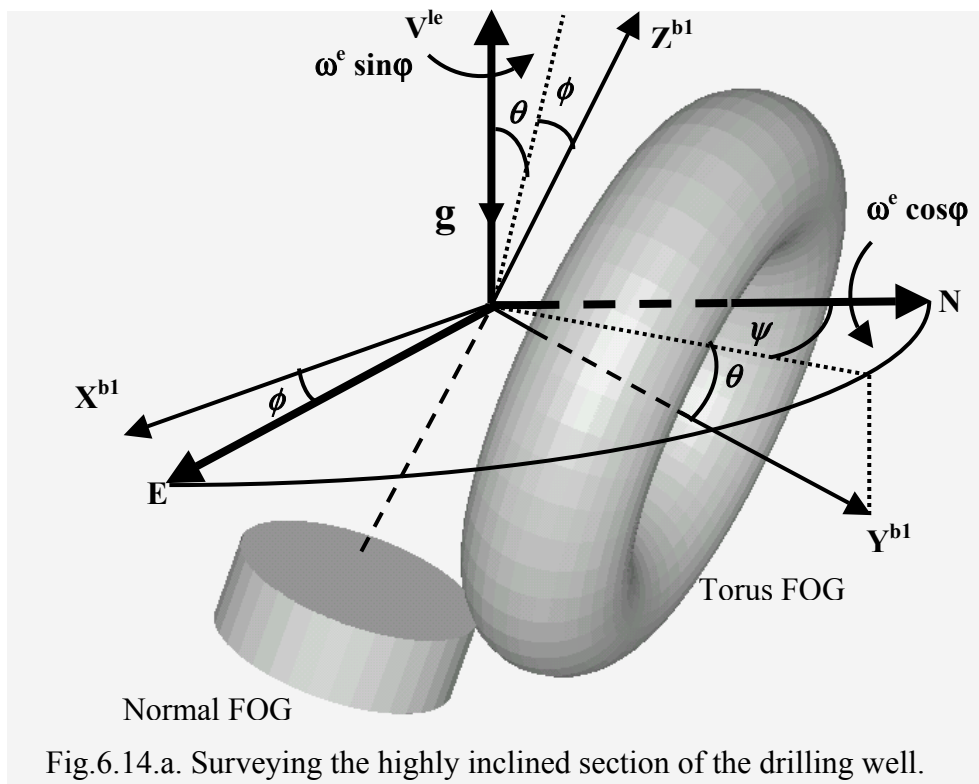
New axes orientation is employed for these sections of the well to keep the definitions of the  $y^{bl}$  axis toward the forward direction, of the  $z^{bl}$  axis along the vertical direction, and of the  $x^{bl}$  axis along the transversal direction as shown on Fig.6.14.a and Fig.6.14.b. It can be noticed that the  $y^{bl}$  and the  $z^{bl}$  axes of this orientation replace the  $z^b$  and the  $y^b$  axes of the near vertical orientation. This means that the Torus FOG measurement can be denoted as  $\omega^y$  and the Normal FOG measurements can be denoted as  $\omega^z$ . Another important difference between the two situations is the relationship between the pitch and the inclination angles. Unlike the near vertical case, the inclination angle  $I$  for highly inclined and horizontal well sections is equal to  $\pi/2 - \theta$ . This is due to the definition of  $\theta$  as the deviation from the horizontal plane, which in this case is at  $\pi/2$  from the vertical direction.

Using the same analysis technique utilized in the previous section, we can determine the inclination and the azimuth angles by applying the following equations (which are similar to the single gyro case discussed in Chapter 5):

$$I = \frac{\pi}{2} - \theta; \quad \text{and} \quad \theta = \arcsin\left(\frac{f_y}{g}\right) \quad (6.44)$$

$$\psi = \arccos\left(\frac{\frac{\omega^y}{\omega^e \cos \varphi} + \tan \varphi \sin \theta}{\cos \theta}\right) \quad (6.45)$$

It is apparent that the expressions for both the inclination and the azimuth for this section of the well are quite similar to those for the near-vertical section. The signs of some of the terms are different because of the different axes orientation. However, the expressions for both the inclination and the azimuth errors are exactly the same.



Eqs.6.44 and 6.45 can be used for the horizontal section of the well and without the need for any simplification, by assuming  $\theta = 0$ . This takes into account the small deviation of the BHA from the horizontal direction that might exist while penetrating this section of the well with a rotary mode of drilling.

### **6.3.3. Real-time techniques for limiting surveying errors.**

Improving the surveying accuracy necessitates reducing the measurement uncertainties due to intrinsic sensor errors and vibration effects as well as compensating for the effect of bias drift of the surveying sensors (especially of the gyro). The block diagram of Fig.6.15 describes the overall surveying process, including the digital signal processing techniques utilized to limit the surveying errors. The reduction of the measurement uncertainties was performed in two stages prior to the computation of the inclination and the azimuth angles. During the first stage, the sensor measurements were averaged over *1-second* time interval to limit the output uncertainties to a level that helps the functionality of the next stage [Noureldin et al.<sup>f</sup>, 2001]. The averaged data sequences were processed individually at the second stage with a transversal tap delay line filter, which incorporated a group of tap delay elements and their corresponding tap weights (see Fig.6.15). The optimal design of this filter utilizing the least mean square (LMS) criterion was previously described in Chapter 4 [Noureldin et al.<sup>c</sup>, 2001]. The values of the tap weights obtained during the design procedure were kept constant during the entire surveying process.

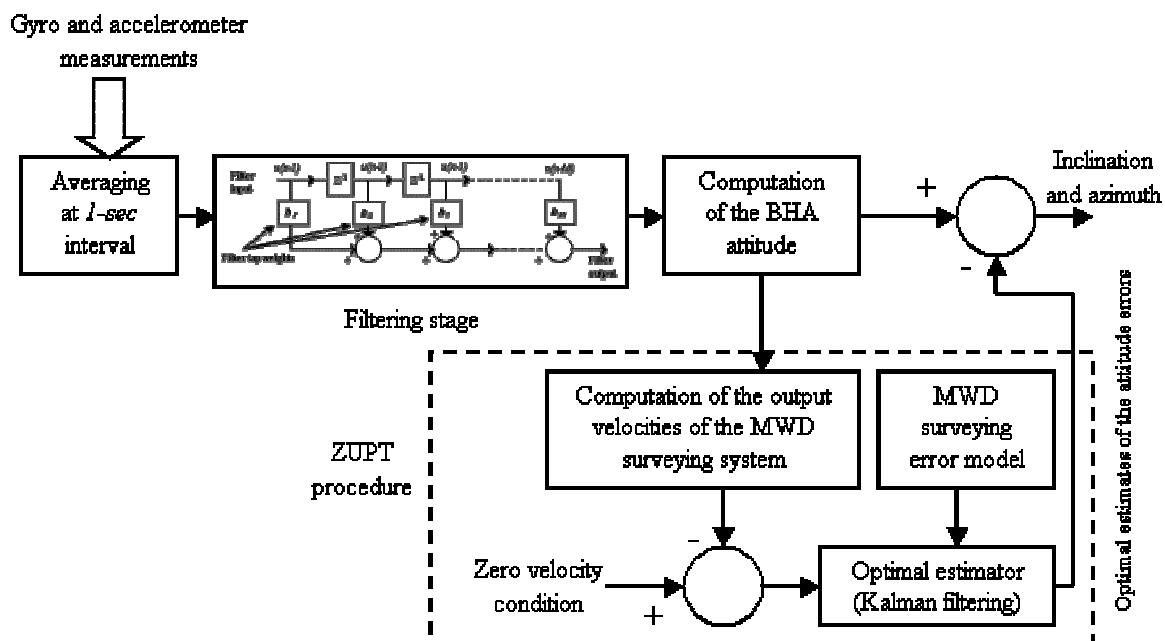


Fig.6.15. Block diagram showing the surveying methodology with all digital signal processing techniques.

The drift of the bias offsets of the surveying sensors lead to computational errors, which are particularly significant for the azimuth angle. Reduction of the surveying errors due to this effect is performed after the computation of the surveying parameters, utilizing the previously described zero velocity update (ZUPT) procedure at each surveying station [Wong and Schwarz, 1988]. Kalman filtering method was employed to optimally estimate the surveying errors during the ZUPT procedure. The error model of the Dual-FOG MWD surveying system was developed based on a set of first order differential equations [see section 6.2.3]. This error model is supplied to the Kalman filtering algorithm together with the difference between the output velocity of the surveying system and the zero velocity condition (see Fig.6.15).

#### **6.3.4. Comparative performance study between the single and the dual gyro systems.**

Although utilizing the same algorithm, the station-based surveying process for the single gyro system is applicable only for the highly inclined and horizontal well sections but over a wider range than that of the dual gyro system. While for the dual gyro case this process is applied starting from  $45^\circ$ , the single gyro system performs station based surveying starting at  $20^\circ$  inclination. This causes an increase in the inclination error at small inclination angles, which might affect the azimuth accuracy at certain orientation [Noureldin et al.<sup>d</sup>, 2001]. The dual FOG system overcomes this increase of the inclination error by adding one more gyro in the orthogonal direction and changing the BHA axes orientation at  $45^\circ$  inclination. The comparison between the two systems is therefore studied in terms of the inclination accuracy over the entire range of inclination angles of the radical section of the well.

#### **6.3.5. Experimental procedure.**

The experimental setup introduced earlier in this chapter for testing the continuous surveying process of the Dual-FOG system was utilized for the station-based surveying system. Accelerometer and gyro measurements ( $f_x, f_y, f_z$  and  $\omega_x, \omega_y, \omega_z$ ) were delivered at a sampling rate of  $64\text{Hz}$ . Averaging at 1-second time intervals was performed for all the measurements in order to reduce the output uncertainties. The measurements of the third gyro ( $\omega_x$ ) were only processed by KINGSPAD<sup>TM</sup> software to provide the reference data. Each of the averaged data sequences was processed individually by a transversal tap delay line filter of 100 tap weights. Since the averaging process at 1-second interval reduced the data rate from  $64\text{Hz}$  to  $1\text{Hz}$ , and due to the 100 delay elements of the filter, the output of the filtering stage was delivered after 100 seconds. The computation of the inclination and the azimuth angles was then performed. In order to improve the azimuth accuracy and to compensate for the effect of gyro bias error, the ZUPT procedure was performed for 200 seconds to allow for the convergence of the mean square estimation error (MSEE) of the error states of the surveying parameters provided by Kalman filter.

### 6.3.6. Results.

#### 6.3.6.1. Computation of the inclination and the azimuth angles.

The experimental setup was used to test the station-based surveying procedure at three different situations; near the East direction, near the North direction and at the mid way between the North and the East directions. For each of these directions, the setup was mounted at an inclination of  $75^\circ$ . The comparison between the computed azimuth angle and the reference value, provided by KINGSPAD<sup>TM</sup> after including the measurement of the third gyro, is shown on Fig.6.16. Errors of less than  $0.2^\circ$  occurred for the setup close to the East direction. These errors increased to about  $1.7^\circ$  at around  $50^\circ$  azimuth and to about  $2.5^\circ$  when heading close to the North direction. The utilization of the ZUPT procedure was necessary to limit the values of these errors especially for orientations close to the North direction.

For the near vertical section of the well, the surveying parameters were determined while changing the orientation of the experimental setup up to  $45^\circ$  inclination. The inclination angle was computed accurately and errors of less than  $0.08^\circ$  were observed (see Fig.6.17). The impact of the internal sensor errors and the other environmental effects were kept minimal due to the large values of the Earth gravity components. The increase of the inclination error as the BHA was deviating from the vertical direction reached its maximum at  $45^\circ$  inclination where the change of axes orientation took place.

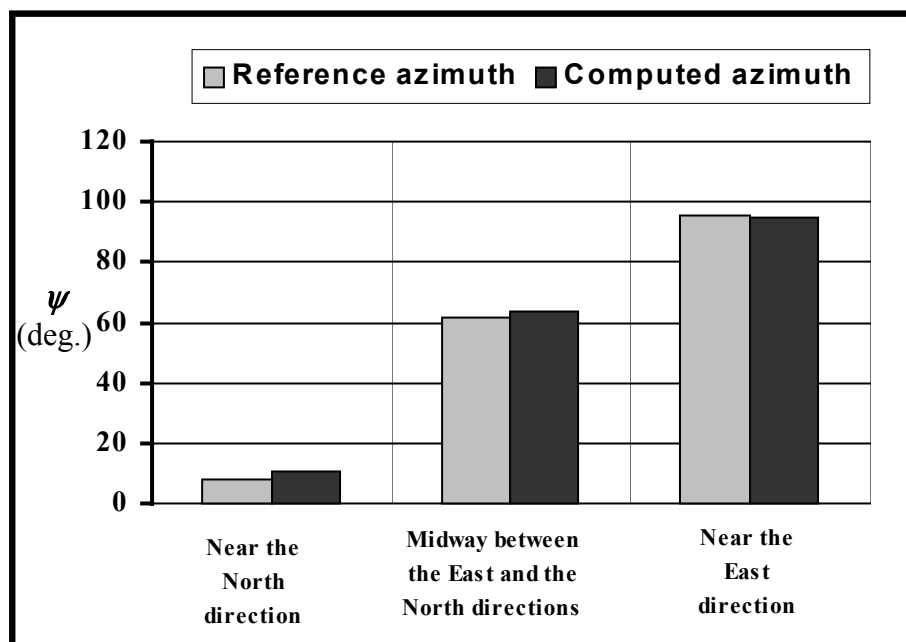


Fig.6.16. Comparison between the reference azimuth and the computed azimuth for inclination angle of  $75^\circ$ .

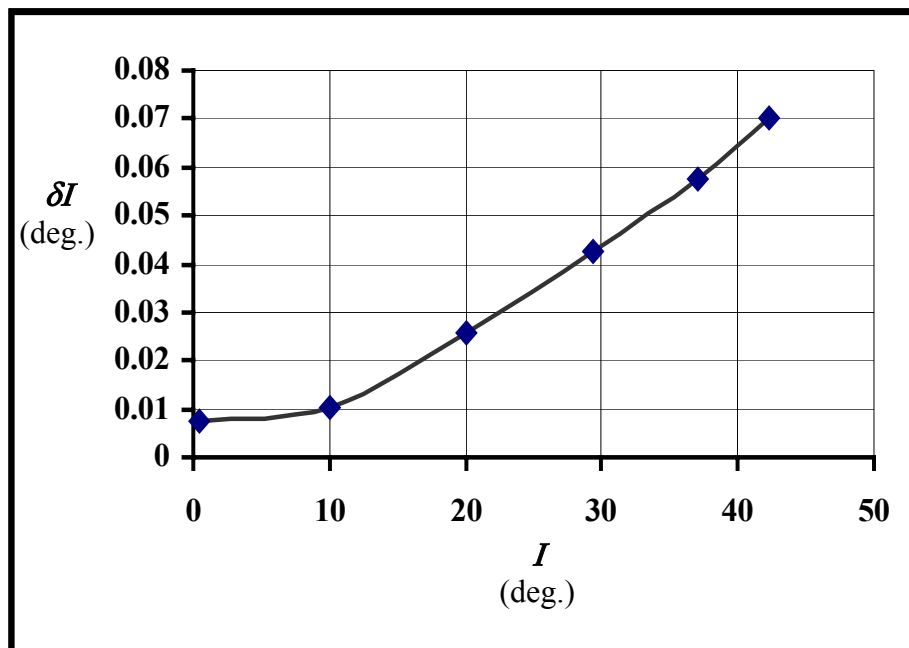


Fig.6.17. The inclination error versus the inclination angle for the near vertical section of the well up to  $45^\circ$  inclination.

The experimental setup was employed to simulate several orientation changes between  $45^\circ$  inclination and the horizontal direction for the highly inclined section of the well. The change of axes orientation at  $45^\circ$  inclination caused the inclination error to decrease as the BHA was approaching the horizontal direction (see Fig.6.18). Thus, the worst inclination accuracy was measured at around  $45^\circ$  inclination. Along the horizontal direction slight deviations of the inclination angle from  $90^\circ$  affected the inclination accuracy and there was a small increase in the inclination error as the setup slightly deviated from the horizontal direction (Fig.6.19).

Moreover, it was noticed that the inclination error is essentially independent of the azimuth direction. Fig.6.20 shows the inclination errors in the highly inclined section of the well at three different azimuth directions. Slight differences of less than  $0.02^\circ$  can be observed between the three graphs and these were due to the change of the accelerometer bias errors.

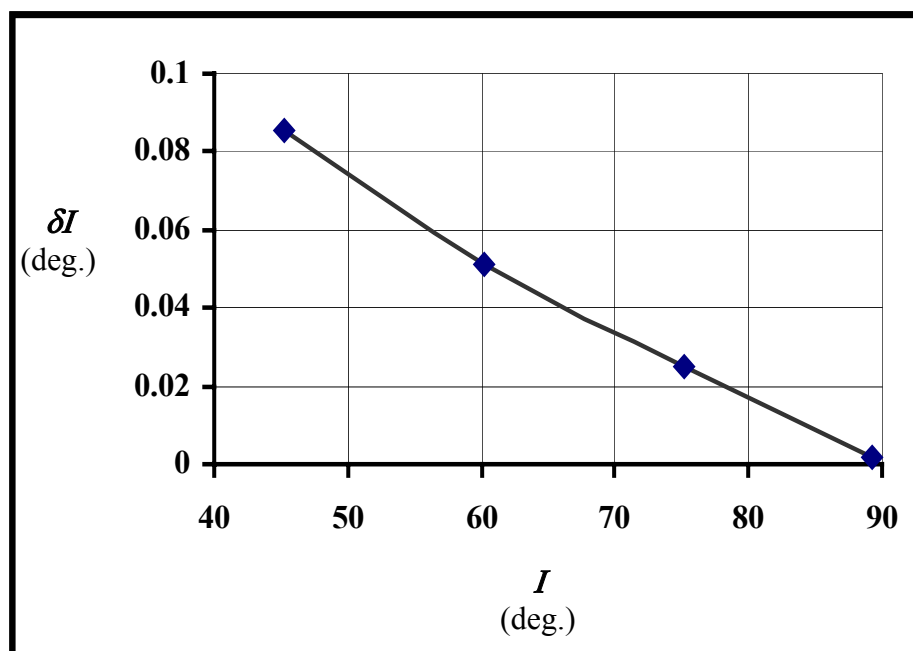


Fig.6.18. The inclination error versus the inclination angle for the highly inclined section of the well above  $45^\circ$  inclination.

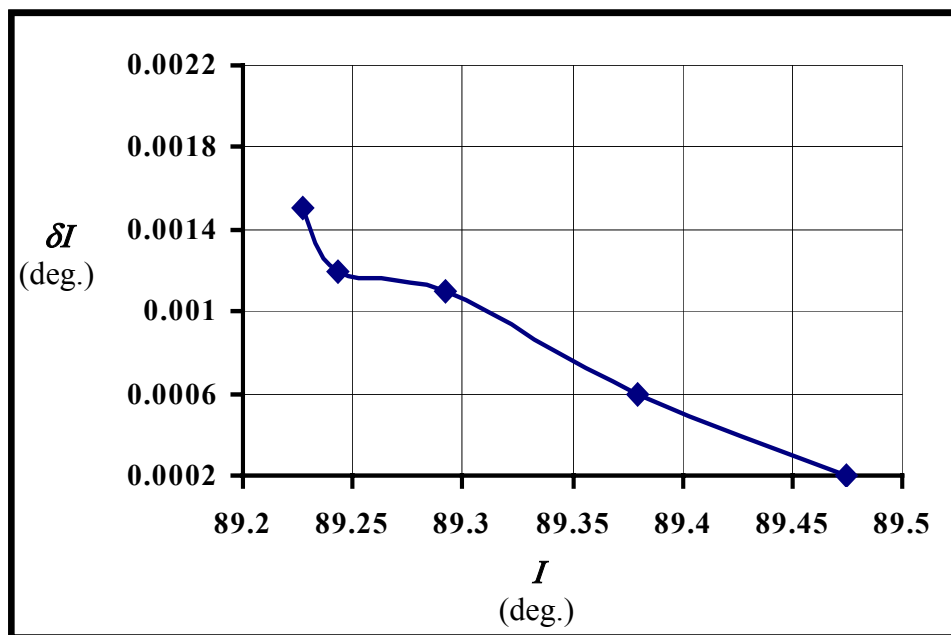


Fig.6.19. The inclination error versus the inclination angle in the horizontal section of the well.

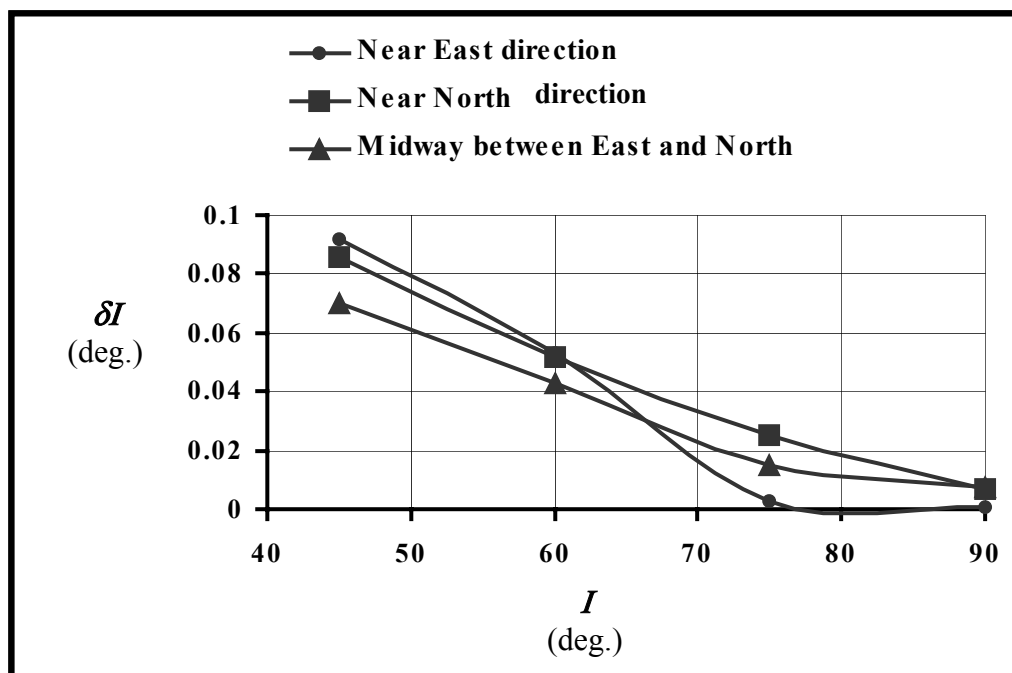


Fig.6.20. The inclination error versus the inclination angle in the highly inclined section of the well for different azimuth directions.

On the other hand, the azimuth accuracy depends on both the BHA deviation from the vertical direction (i.e. on the inclination) and on its azimuth direction. The dependence on the inclination angle was tested at  $95^\circ$  azimuth for both the near-vertical and the highly inclined sections of the well. As shown on Fig.6.21, the highest azimuth accuracy was obtained when the setup was close to either the horizontal direction (i.e.  $I \rightarrow 90^\circ$ ) or the vertical direction (i.e.  $I \rightarrow 0^\circ$ ). The azimuth error increased in between and reached its maximum around  $45^\circ$  inclination, where the change of BHA axes orientation took place. It can also be observed that the azimuth error was not symmetric around  $45^\circ$  inclination due to the drift of the gyros bias errors with time. However, it can be noticed that the change of axes orientation and the utilization of dual gyros with their sensitive axes normal to each other avoided the growth of the azimuth errors at high inclinations which usually happens when a single gyro is utilized [See Chapter 5].

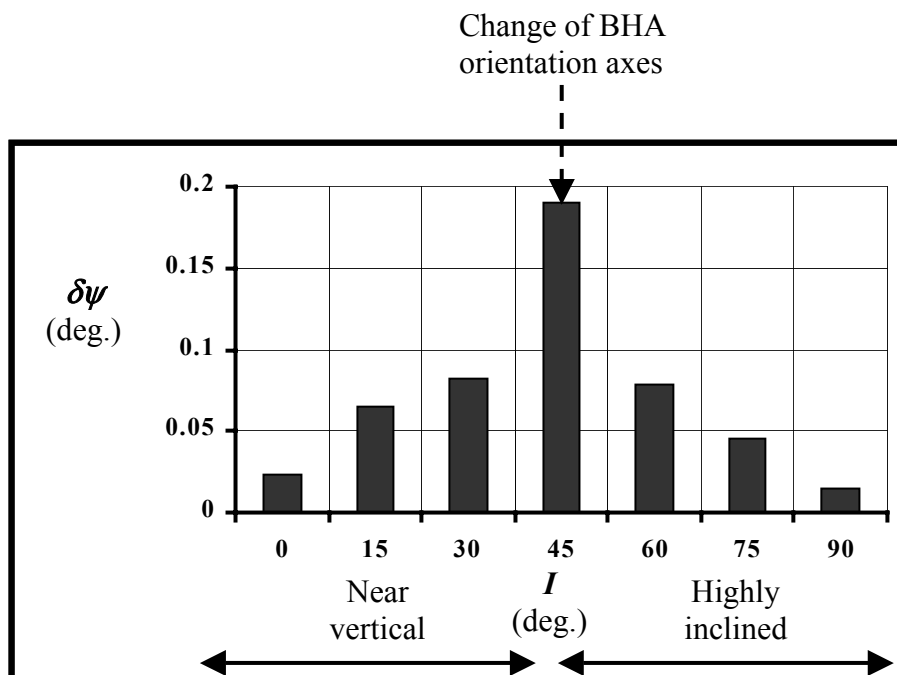


Fig.6.21. The azimuth error versus the inclination angle for orientations close to the East direction.

Furthermore, the surveying method suffers from an apparent growth of the azimuth error as the BHA is heading towards the North direction. The azimuth accuracy dependence on the BHA azimuth direction was explored at different inclination angles while pointing the setup close to the East direction, close to the North direction and at the midway between the East and the North directions (see Fig.6.22). It can be concluded from this figure that the highest azimuth error was obtained when pointing close to the North direction at  $45^\circ$  inclination. At each inclination angle, the worst azimuth accuracy corresponds to the situation close to the North direction (see Fig.6.22). In such a situation, any small change in the gyro measurement  $\omega_y$  corresponds to a considerable change in the azimuth angle. A change of one degree in the azimuth angle corresponds to a change in  $\omega_y$  by  $0.1623^\circ/hr$  for stations near the East direction ( $\psi=70^\circ \rightarrow 90^\circ$ ) and by  $0.0159^\circ/hr$  for surveying stations near the North direction ( $\psi=0^\circ \rightarrow 20^\circ$ ).

In general, the azimuth error was relatively much higher than the inclination error and a ZUPT procedure is therefore suggested to limit the azimuth error and to improve the overall surveying accuracy.

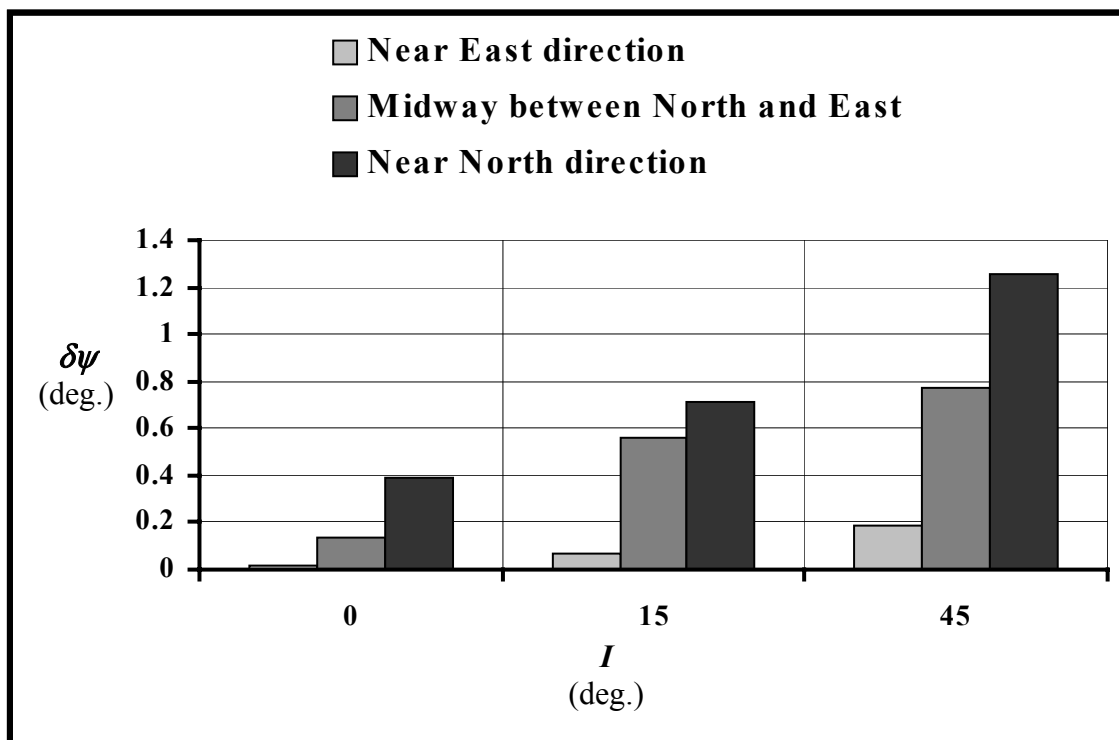


Fig.6.22. The azimuth errors at three different inclination angles for orientations close to the East direction, the North direction and the midway between the East and the North.

It should be highlighted that the measurement uncertainties affected the computation of both the inclination and the azimuth angles. Fig.6.23 compares the inclination angle before and after processing the accelerometer measurements with the transversal tap delay line filter. The inclination uncertainty was reduced from  $0.004^\circ$  to  $0.00013^\circ$  by filtering the accelerometer measurements. Although the inclination accuracy could be computed without filtering despite the relatively higher measurement uncertainties, the azimuth could not be determined directly due to the high uncertainty level at the gyro output. Fig.6.24 depicts the  $\cos(\psi)$  term of Eq.(6.41) before and after filtering. It is clear that before filtering,  $\cos(\psi)$  varied between the full span of  $\pm 1$  which corresponded to values of azimuth between  $0^\circ$  and  $180^\circ$ . This caused computational instabilities of the azimuth angle. Therefore, it was imperative to implement the filtering process before the determination of the azimuth angle. This filtering approach performed efficiently in limiting the gyro measurement uncertainties but left the effect of the gyro bias error to be compensated by the ZUPT procedure.

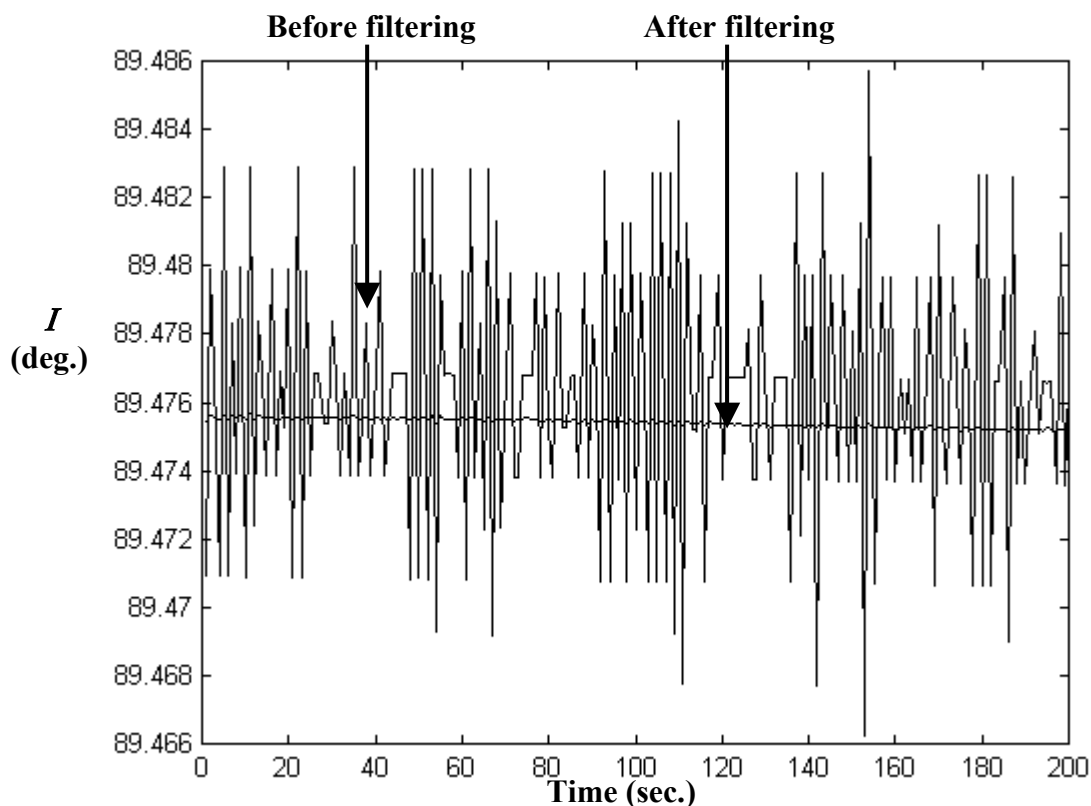


Fig.6.23. The inclination angle before and after filtering with a transversal tap delay line filter of 100 tap weights.

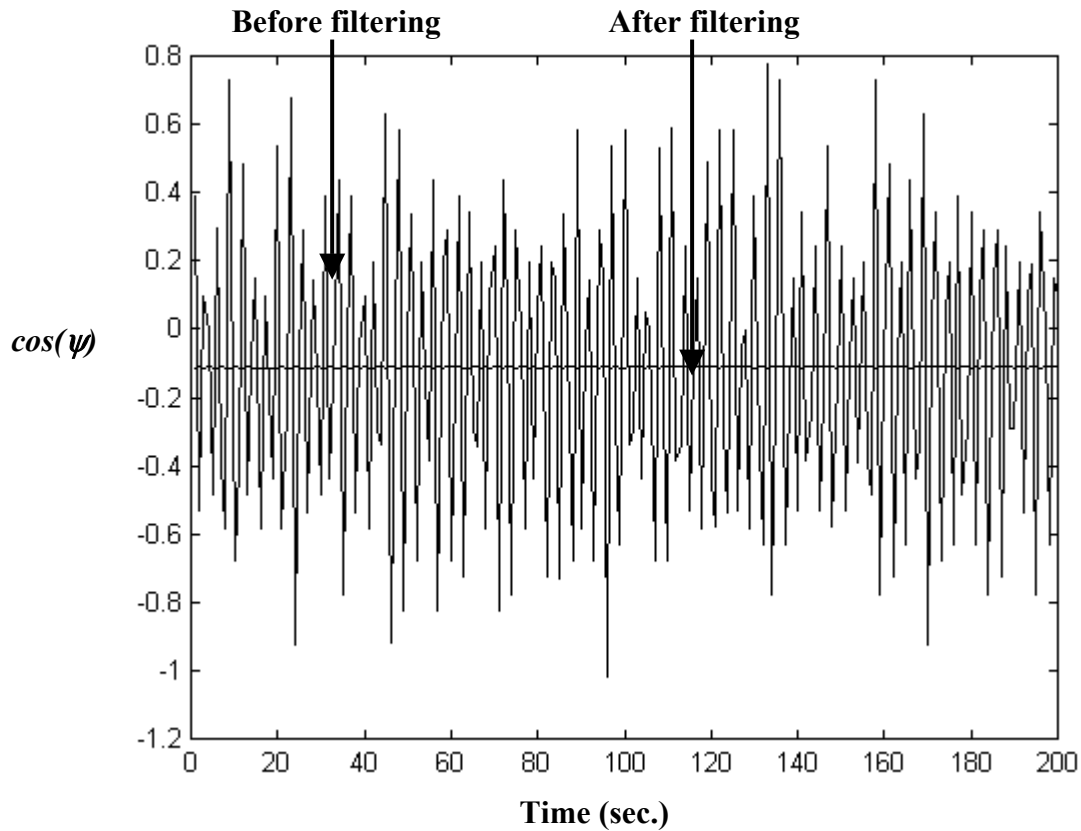


Fig.6.24. The value of  $\cos(\psi)$  before and after filtering with a transversal tap delay line filter of 100 tap weights.

### 6.3.6.2. Improvement of azimuth accuracy by the ZUPT procedure.

During the ZUPT procedure, the Kalman filtering algorithm provided an optimal estimate of both the inclination and the azimuth angles. Consequently, the mean square estimation error of the inclination ( $\sigma_{\delta\theta}^2$ ) and the azimuth ( $\sigma_{\delta\psi}^2$ ) converged to their minimum values of  $5 \times 10^{-7} (\text{°/hr})^2$  and  $5.5 (\text{°/hr})^2$  respectively (Fig.6.25). Apparently, the MSE of the azimuth was much higher than that of the inclination, since the azimuth was provided with lower accuracy at the beginning of the ZUPT. Therefore, longer ZUPT intervals might be highly beneficial in reducing the estimation error of the azimuth error state, as long as they are not delaying the drilling process.

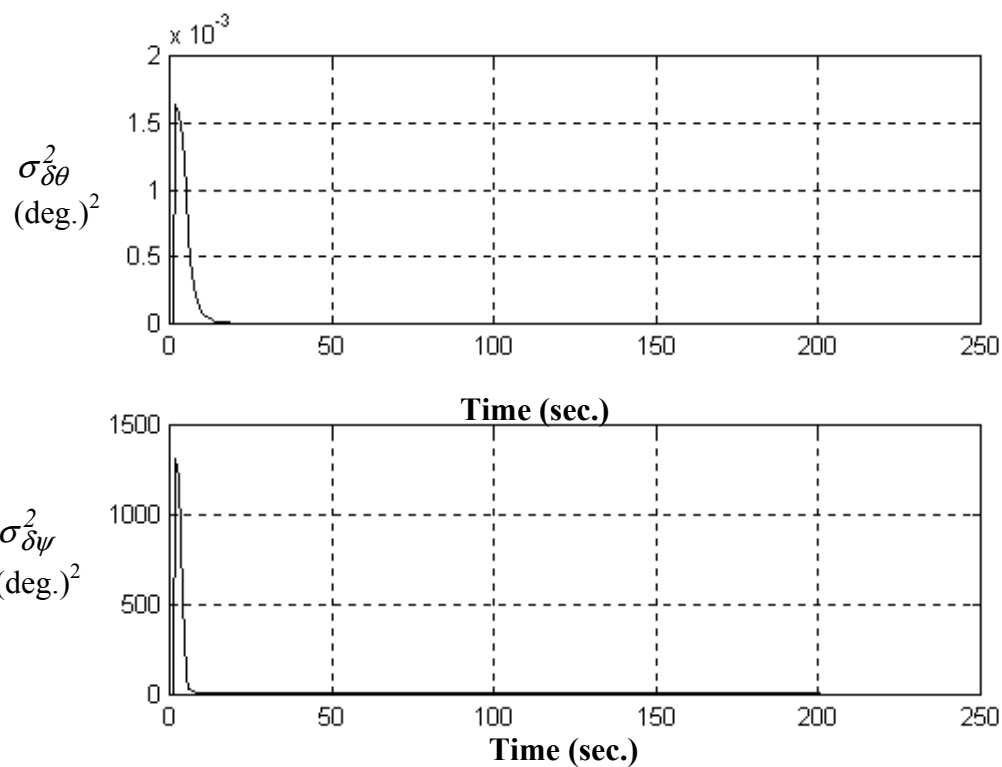


Fig.6.25. Mean square estimation error of the inclination and the azimuth error states.

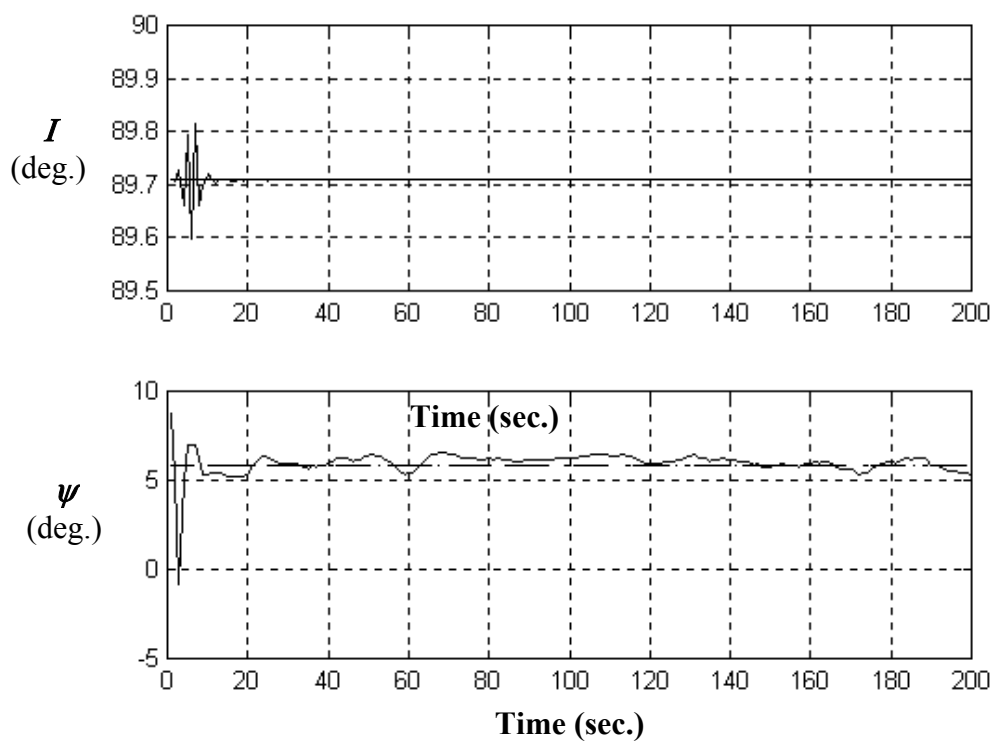


Fig.6.26. Variation of the inclination and the azimuth angles during the ZUPT procedure.

We have tested the influence of the ZUPT procedure at one surveying station located at  $5.85^\circ$  azimuth. As mentioned earlier, stations close to the North direction suffer from the highest azimuth errors. At the beginning of the ZUPT, the inclination and the azimuth were provided with errors of about  $0.01^\circ$  and  $2.85^\circ$ , respectively. After a small transient period, equal to the convergence of the corresponding MSEEs, the inclination and the azimuth angles started to approach the reference values. In fact, it can be observed in Fig.6.26 that the inclination angle coincides completely with the reference value provided by KINGSPAD<sup>TM</sup>. On the other hand, the azimuth oscillated around the corresponding reference value with errors less than  $0.5^\circ$ .

### 6.3.6.3. Comparison between the single and the dual gyro systems.

The utilization of the dual gyro system overcame the increase of the inclination error at small inclination angles typical for the single gyro system [Noureldin et al.<sup>d</sup>, 2001]. Fig.6.27 shows the inclination error  $\delta I$  over the entire range of the inclination angles of the radical section of the well. Apparently, the increase of  $\delta I$  for the single gyro system at small inclinations to more than  $0.3^\circ$  has been avoided in the dual gyro case. It can be observed that the dual gyro system kept the inclination error lower than  $0.1^\circ$ , and its maximum was at  $45^\circ$  inclination. In addition, the dual gyro system avoided the deterioration of the azimuth accuracy at small inclinations.

It has been determined that the single gyro system failed to monitor the azimuth angle at  $14^\circ$  inclination and  $94.68^\circ$  azimuth due to the amplification of the gyro bias error

$$\delta\omega^y \text{ at small inclination angles } \left( \delta(\cos\psi) = \frac{I}{\sin I} \left( \frac{\delta\omega^y}{\omega^e \cos\varphi} \right) \right) \text{ [Noureldin et al.}^d, 2001]$$

by the  $\frac{I}{\sin I}$  term. When the dual gyro system was utilized and the change of axes orientation was implemented, we were able to monitor the azimuth angle at this orientation with error of less than  $0.03^\circ$ .

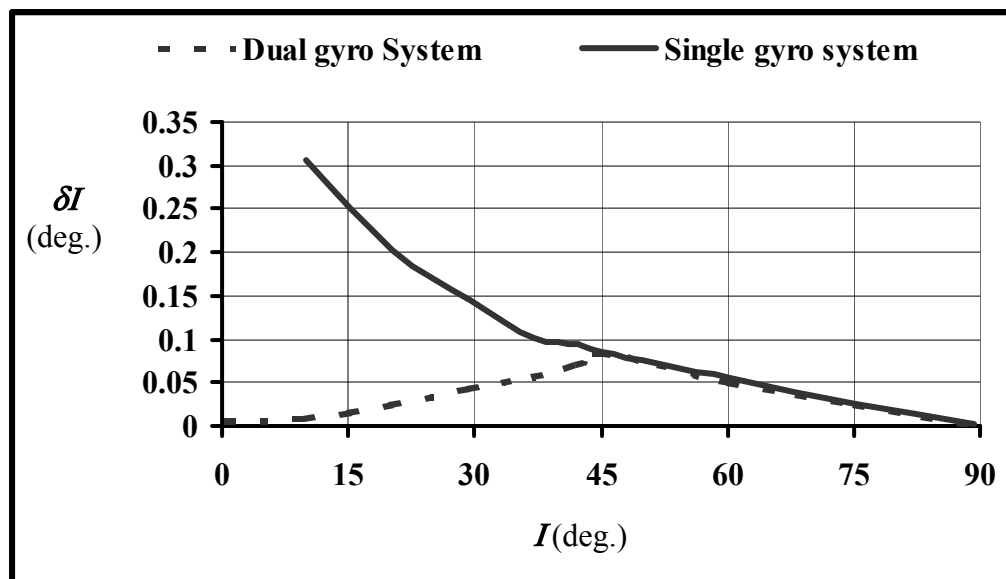


Fig.6.27. Comparison of the inclination accuracy between the single and the dual gyro systems.

#### 6.4. Conclusion.

The Dual-FOG MWD surveying system introduces full navigation solution downhole for the different sections of the horizontal well and for the different drilling modes. Moreover, the Dual-FOG system avoids the limitations of the Single-FOG system. First, it can provide continuous surveying of the whole radical section of horizontal wells. Second, it overcomes the accuracy problems existing with the station-based surveying processes utilizing the single-FOG system. The significant growth of the surveying errors at some inclination angles were avoided by the change of axes orientation at  $45^\circ$  inclination and the utilization of another orthogonal gyro in the monitoring process.

## CHAPTER SEVEN

### CONCLUSION AND RECOMMENDATIONS FOR FUTURE RESEARCH

#### 7.1. Summary.

This thesis aimed at introducing a new technique for MWD surveying of directional/horizontal wells in the oil industry. The objective was to design, develop and test a new MWD surveying system that replaces the present magnetic surveying technology, avoids its shortcomings and provides reliable azimuth monitoring methodology that satisfies today's directional drilling requirements.

This research started with a quantitative study of the feasibility of utilizing FOGs for MWD processes in the oil industry, which showed the low susceptibility of the FOG to various types of downhole vibration and shock forces.

One, and subsequently two FOGs were incorporated with three-axis accelerometers to provide a full surveying solution downhole. The integration between the FOGs and the accelerometers was carried out using inertial navigation techniques.

This research proposed two MWD surveying techniques. The first technique is based on a single FOG system, which incorporates one FOG with its sensitive axis along the tool spin axis and three mutually orthogonal accelerometers. This technique provided continuous surveying for the near-vertical section of directional/horizontal wells followed by station-based surveying for the highly-inclined and the horizontal well sections. The second technique improved the functionality of the first by utilizing a dual-FOG system, which used an additional FOG with its sensitive axis normal to the tool spin axis. This technique provided continuous surveying for the whole radial section of the well followed by station-based surveying for the horizontal section.

The FOG performance was enhanced by utilizing some adaptive filtering techniques to reduce its output uncertainty so that the Earth rotation rate component could be monitored accurately during station-based surveying processes. In addition, applied optimal estimation techniques based on Kalman filtering methods were employed to improve the surveying accuracy.

## 7.2. Conclusions.

The following conclusions can be drawn from the results of both the computer modeling and the experimental work performed in the course of this study:

□ **Quantitative feasibility study for the applicability of FOGs in MWD processes:**

FOGs are reliable replacements of magnetometers in MWD borehole surveying processes. In addition, the utilization of FOG technology instead of magnetometers eliminates the need for the costly nonmagnetic drill collars. Due to its small size and high reliability, the FOG can be installed inside the bearing assembly 17" behind the drill bit. Thus, reliable surveying data can be obtained so that the drill bit can penetrate the downhole formation without deviating from its desired path. The computer model introduced in Chapter 3 showed that the FOG could perform adequately if utilized downhole, even in the presence of severe shock and vibration forces.

□ **De-noising the FOG output signal:**

The FOG output uncertainty was significantly reduced by utilizing one of the two adaptive filtering methods introduced in Chapter 4. The forward linear prediction technique was found to be suitable for low cost and tactical grade FOGs with their relatively high output uncertainty. The FLP filter was capable of reducing the output uncertainty from  $46.6^\circ/hr$  to  $0.694^\circ/hr$  and  $0.152^\circ/hr$  when utilizing 300 and 600 tap weights, respectively. The FLP method has the advantage of repeating the design of the filter at each surveying station, thus taking into consideration the dynamics that might exist at the given station.

The FLP technique cannot be applied for navigational grade FOGs due to the presence of colored (correlated) noise at their outputs. Thus, an alternative technique based on the utilization of known Earth rotation rate component as a reference signal during the learning process was suggested. This method is different from the FLP, because the filter is designed once at the beginning of the drilling process. Therefore, at each surveying station, the time used by the FLP process to obtain the optimal tap

weights is eliminated. Although this method does not adapt the filter tap weights to the different dynamics existing at different surveying stations, it has the advantage of being suitable for all type of FOGs. This method was capable of monitoring the Earth rotation rate with errors of less than  $1^\circ$  for tactical grade FOGs and less than  $0.5^\circ$  for navigational grade FOGs.

□ **Single-FOG MWD surveying system.**

The Single-FOG system provided continuous surveying for the near vertical section of the well up to  $20^\circ$  inclination. Aided inertial navigation techniques utilizing either continuous velocity and altitude updates or ZUPTs were considered to enhance the long-term performance of the Single-FOG system. The experimental results when applying the continuous aiding technique with tactical grade inertial sensors showed inclination error of less than  $0.4^\circ$ , azimuth error of about  $0.9^\circ$ , maximum altitude error of about  $50\text{ cm}$  and horizontal position errors of less than  $50\text{ m}$  over 2 hours experiment. The regular ZUPT procedure was improved by a backward velocity error correction method to keep the position errors less than  $95\text{ m}$  while utilizing two-minute time interval between neighboring ZUPTs.

Due to the velocity and altitude updates provided to the Kalman filter, the velocity and the altitude errors became strongly observable error states and their MSEs exhibited very fast convergence to the steady-state minimal value. Therefore, the velocity and the altitude errors were optimally estimated and kept bound in the long term. Moreover, the strong coupling between the velocity errors and the pitch and the roll errors was very beneficial for improving their estimation accuracy.

At a certain transitional inclination angle, a virtual change of axes orientation was performed to avoid the increase of the inclination error. Station-based surveying at some predetermined surveying points was also considered. At each surveying station, the inclination was monitored with errors of less than  $0.35^\circ$  when utilizing navigation- grade inertial sensors. This inclination error was reduced considerably at high inclination angles and became less than  $0.05^\circ$  at inclination angles of more than  $60^\circ$ . In addition, the inclination error did not show any dependence on the azimuth direction. On the other

hand, the azimuth error depended on both the azimuth direction and the inclination angle. The worst azimuth accuracy (errors between  $1^\circ$  and  $2^\circ$ ) was obtained when the platform was oriented close to the North direction (azimuth angle of less than  $5^\circ$ ) at small inclination angles (inclinations of less than  $45^\circ$ ).

□ **Dual-FOG MWD surveying system.**

The Dual-FOG system avoided some limitations of the Single-FOG system by adding one more FOG with its sensitive axis normal to the tool spin axis and colinear to the forward direction. Thus, the radical section of the well could be surveyed continuously without interrupting the drilling process. The experimental results obtained using navigational grade inertial sensors showed that azimuth errors as low as  $0.5^\circ$  could be achieved using the Dual-FOG system. Inclination errors of less than  $0.03^\circ$  and position errors of less than 5 meters were obtained over *100 min* experiment while utilizing continuous velocity updates. ZUPTs with backward velocity error correction criterion kept position errors to less than *40 m*.

In general, station-based surveying is useful when utilizing the rotary mode of drilling and for the horizontal section of the well. The accuracy of the station based surveying technique was significantly improved by introducing the Normal FOG in the Dual-FOG system. This was achieved by introducing change of axes orientation at  $45^\circ$  inclination. The highest azimuth error was less than  $1.2^\circ$  at  $45^\circ$  inclination and close to the North direction. In addition, the worst inclination accuracy ( $0.1^\circ$  error) was obtained at  $45^\circ$  inclination. The azimuth accuracy was then improved by utilizing Kalman filtering, which reduced the largest azimuth error to  $0.5^\circ$ .

### **7.3. Thesis contributions.**

In this thesis, new surveying methodologies based on inertial navigation techniques utilizing fiber optic rotation sensors were introduced as a replacement of the widely used magnetic surveying systems. The inertial navigation technology incorporates three-axes gyroscopes and three-axes accelerometers to provide a full navigation solution of a moving platform. It was desirable to install the inertial sensors as close as possible to

the drill bit and to employ sensors that could be mounted in the limited space available downhole. This thesis introduced two different surveying scenarios that utilized either one or two high accuracy FOGs. In order to position a FOG with its sensitive axis along the tool spin axis inside the bearing assembly, a Torus FOG was suggested to allow the flow of mud through the drill pipe. The Single-FOG and the Dual-FOG systems provided full and reliable MWD surveying solution during directional/horizontal drilling processes.

This research presented a comprehensive method for FOG modeling. The model can test the FOG performance and its stability and sensitivity to both internal design parameters and external environmental factors (e.g. vibration and shock forces).

The performance of the FOG was enhanced by utilizing some adaptive filtering techniques. These techniques used the LMS adaptive algorithm for designing a tap delay line filter, but suggested the utilization of a changeable step size parameter during the adaptation process to ensure fast convergence of the algorithm while providing minimal error of the monitored Earth rotation rate. These techniques were very beneficial in significantly reducing the FOG measurement uncertainty while monitoring the Earth rotation rate. Thus, a single FOG installed along the forward direction of an INS could precisely monitor the component of the Earth rotation rate along its sensitive axis. Consequently, the deviation from the North direction (i.e. the azimuth angle) could be determined accurately.

The FOG-based MWD surveying system proposed in this research cannot work as a stand alone INS because of the long-term growth of surveying errors. This thesis employed the technology of aided inertial navigation and suggested the utilization of the velocity and altitude updates as external aiding sources. The velocity updates can be obtained using ZUPTs or continuous measurement of the drill bit penetration rate along the downhole formation, which is provided at the surface of any drilling site. The altitude update is obtained using the measurement of the length of the drill pipe, which is also provided at the surface.

The ZUPT procedure utilized by both the Single-FOG and the Dual-FOG surveying systems was enhanced using the backward velocity error correction criterion.

This criterion partially limited the velocity errors and the growth of the position errors between ZUPT stations. In addition, it can be implemented in real-time without affecting the drilling process.

#### **7.4. Recommendations for future research.**

The MWD surveying techniques developed in this thesis are a first step towards the actual implementation of the whole technology downhole. Fortunately, the results in this thesis started to attract several major oil companies to support further investigations related to this research area, in addition to the downhole implementation of the FOG-based surveying system. Therefore, the following recommendations are made for future studies on the applicability of the FOG-based MWD surveying system:

##### **□ Optimal band-limiting and de-noising of surveying sensor signals.**

After installing the necessary set of surveying sensors downhole, the issue of providing accurate measurements by these sensors becomes pivotal for the successful implementation of this technology. Therefore, it might be beneficial to investigate the design of time invariant filters to effectively band-limit the surveying sensor signals before the computation of the surveying parameters. This process might eliminate a considerable portion of the sensor noise. Since slow BHA motion and rotations are usually performed downhole, the sampling rate of the inertial sensors usually exceeds the frequency contents of the BHA motion by at least 10 times. Thus, the BHA motion is represented in the lower part of the signal spectra and the band-limiting process acts like a low pass filtering. FIR filters will, therefore, be utilized to process the surveying sensor measurements. The optimal design of such FIR filter including the choice of an appropriate minimization criterion and the choice of filter parameters should be investigated in future research.

The band-limiting technique could be extended further towards those frequency ranges in which sensor noise is mixed with the signal of interest. Filtering over a frequency band of mixed signal and noise requires the knowledge of how the noise and the signal are distributed in order to avoid signal distortion. De-noising using wavelet

techniques might therefore be beneficial [Skaloud, 1999]. This approach could also help in detecting the drift performance of the surveying sensors during station-based surveying processes.

□ **Utilization of adaptive Kalman filtering techniques.**

In order to avoid the shortcomings of the conventional estimation algorithm provided by Kalman filtering techniques, the corresponding adaptive criterion and its suitability for the FOG-based MWD surveying methods might be investigated. The adaptive Kalman filter approach has been successfully applied for kinematic positioning [Mohammed, 1999]. Such approach takes into account the dynamic change of the estimation environment and the ambiguity in choosing the initial conditions. Measurement sequence from an independent source is utilized to optimally estimate the system noise and/or the measurement noise, which, in the conventional case, are kept at their initial values. Consequently, the filter becomes self-learning, so that it could adapt itself to the present surveying situation, including drilling dynamics, increase of uncertainties of some of the surveying parameters due to some specific drilling conditions, or unpredictable change of one or more of these parameters [Mohammed, 1999].

## REFERENCES

Advanced Motion Control: "PWM servo amplifiers;" Technical Manual, California, USA, 1996.

Aein J.M.: "An optical signal processing model for the Interferometric Fiber Optic Gyroscope;" RAND, Santa Monica, C.A. (USA), 1995.

Algrain M.C. and Ehlers D.E.: "Novel Kalman filtering method for the suppression of gyroscope noise effects in pointing and tracking systems;" Journal of Optical Engineering, **V34** (10), pp: 3016-3030, 1995.

Analog Devices: "AD620-instrumentational amplifier;" Amplifiers Reference Manual, Norwood, MA, 1994.

Anderton, W.E.: "Electronics in oil;" Wireless World, **V81**(1469), pp:4-9, 1975.

Anon, A.: "Horizontal and multilateral wells: Increasing production and reducing overall drilling and completion costs;" Journal of Petroleum Technology, **V51**(7), 1999.

Anon, A.: "New facts about horizontal well technology;" Gas Industries, October 1990.

Arditty H.J. and Lefevre H.C.: "Sagnac effect in fiber gyroscopes;" Optics Letters, **V6** (8), pp: 401-403, 1981.

Bell R.A., Hinkel R.M., Bunyak M.J., Payne J.D. and Hood J.L.: "Application of innovative extended reach and horizontal drilling technology in oilfield development" In: Proceedings of the SPE/IADC Drilling Conference, Dallas, TX, pp: 277-298, Feb 15-18, 1994.

Bennet S.M., Dyott R., Allen D., Brunner J., Kidwell R. and Miller R.: "Fiber optic rate gyros as replacement for mechanical gyros;" AIAA, **V44(01)**, 1998.

Bennett S.M., Emge S. and Dyott R.B.: "Fiber optic gyroscopes for vehicular use;" IEEE Conference on Intelligent Transportation Systems, Boston, Nov. 9-12, 1997.

Berger P.E. and Sele R.: "Improving wellbore position accuracy of horizontal wells by using a continuous inclination measurements from a near bit inclination MWD sensor;" Journal of Canadian Petroleum Technology, **V39** (10), Oct. 2000.

Bielas M.S. and Taylor W.L.: "Progress in interferometric fiber optic gyroscopes for space inertial reference units;" SPIE, **V2070**, 1993.

Bowser M., Hammond J., Perlmutter M. and Christopher R.: "Broad fiber optic gyroscopes for a broad range of applications" In: Proceedings of the IEEE Position, Location and Navigation Symposium, Atlanta, GA, pp: 553-558, Apr. 22-26, 1996.

Brandon T.L., Mintchev, M.P and Tabler, H.: "Adaptive compensation of the mud pump noise in a measurement-while-drilling system;" Journal of the Society of Petroleum Engineers (SPE), **V4(2)**, July 1999.

Brindley C.P.: "Continuous orientation measurement systems minimize drilling risk during coring operation;" In: Proceedings of the SPE/IADC Drilling Conference, Dallas, Tx, Feb. 28 – Mar. 2, pp.341-346, 1988.

Britting K.R.: "Inertial navigation system analysis;" John Wiley and Sons, New York, 1971.

Brooks A.G. and Wilson H.: “An improved method for computing wellbore position uncertainty and its application to collision and target intersection probability analysis;” In: Proceedings of the SPE European Petroleum Conference; Milan, Oct. 22 – 24, 1996.

Brown R.G. and Hwang P.Y.C.: “Introduction to random signals;” John Wiley and Sons, New York, 1992.

Burns W.K. (Editor): “Optical fiber rotation sensing;” Academic Press, Inc, San Diego, CA, 1994.

Cheatham C.A., Shih S., Churchwell D.L., Woody J.M. and Rodney P.F.: “Effect of magnetic interference on directional surveys on horizontal well;” In: Proceedings of the IADC/SPE Drilling Conference, New Orleans, LA, pp: 101-110, Feb. 18-21, 1992.

Chin G.H., Cordova A., Goldner E.L.: “Extended environmental performance of attitude and heading reference grade fiber optic rotation sensors;” SPIE **V1367**, 1990.

Clary M.M. and Stafford T.W.: “MWD performance and economic benefits in the Zu horizontal drilling program;” In: Proceedings of SPE/IADC 1987 Drilling Conference, New Orleans, LA, pp: 749-754, Mar. 15 - 18, 1987.

Computalog Drilling Services: “Magnetic multi-shot survey instrument;” [www.computalog.com](http://www.computalog.com), 2002.

Conti P.F.: “Controlled horizontal drilling;” In: Proceedings of SPE/IADC 1989 Drilling Conference, New Orleans, LA, pp: 749-754, Feb. 28 – Mar. 3, 1989.

Cook R.L., Nicholson J.W. and Sheppard M.C.: "First real time measurement of downhole vibration, forces and pressures used to monitor directional drilling operations;" In: Proceedings of SPE/IADC 1989 Drilling Conference, New Orleans, LA, February 28 - March 3, pp.283-290, 1989.

Dareing D., Balkenbush B.: "Controlling drill string vibration;" Western Oil Reporter, v 41(8), pp.61-64, 1984.

Disperio R.: "Method of correcting for axial error components in magnetometer readings during wellbore survey operation;" US patent # 5452518, 1995.

Dooley S. and Nandi A.: "Subsample time delay estimation with variable step size control;" Signal Processing, **V80**, pp.: 343-347, Feb. 2000.

van Dongen J., Maekiaho L.: "Method for determining the azimuth of a borehole;" US patent # 4682421, 1987.

Doo S. and Kang M.: "Generalized adaptive spatio-temporal auto-regressive model for video sequence rotation" In: Proceedings of the IEEE Intl. Conference on Image Processing, Los Alamitos, CA, pp.: 185 – 188, Oct. 24 – 28, 1999.

Dubrulle O. and Nelson P.H.: "Evaluation of directional survey errors at Prudhoe Bay;" SPE Drilling Engineering, **V2** (3), pp.257-267, September 1987.

Engebretson H.: "Error reduction in compensation of drill string interference for magnetic survey tools;" US patent # 5155916, 1992

Fibersense Technology corporation: "Fibersense FOG 200/45 family;" Fibersense, Canton, MA, 2001.

Fibersense Technology corporation: "Fibersense FOG 750/65 family;" Fibersense, Canton, MA, 2001.

Fisher E.K. and French M.R.: "Drilling the first horizontal well in the gulf of Mexico: A case history of East Cameron Block 278 well B-12;" In: Proceedings of SPE Annual Technical Conference and Exhibition, Dallas, TX, October 6 – 9, pp.111-120, 1991.

Franklin G.F., Powell J.D. and Workman M.L.: "Digital control of dynamic systems;" Addison-Wesley, Menlo Park, C.A. (USA), 1990.

Gabris P.M. and Hansen R.R.: "A field comparison of the directional survey of MWD in comparison with six other survey tools;" In: Proceedings of SPE/IADC 1988 Drilling Conference, Dallas, TX, February 28 - March 2, pp.325-332, 1988.

Gardner W.R. and Merchant G.A.: "Nonlinear equalizer for measurement-while-drilling telemetry system;" US patent # 5490121, 1996.

Gavasheli L.Sh.: "Longitudinal and transverse vibrations at the frame and the machine section of a rotary drilling rig;" Soviet mining science, v 5, pp.443-450.

Gelb A.: "Applied optimal estimation;" MIT Press, Cambridge, England, 1974.

Gesbert D. and Duhamel, "Unbiased blind adaptive channel identification and equalization" *IEEE Transactions on Signal Processing*, **V48**(1), pp.: 148-158, Jan 2000.

Girard A. and Mintchev M.P.: "Testing non-linear adaptive compensators in non-ideal noise environments;" In: Proceedings of the 4<sup>th</sup> IEEE International Workshop on Intelligent Signal Processing and Communication Systems (ISPACS), Melbourne, Australia, Nov. 4–6, 1998.

Gibbons F.L., Hense U.: "A three-axis laser gyro system for borehole wireline surveying;" In: Proceedings of 62<sup>nd</sup> SPE annual technical conference and exhibition, Dallas, TX, September 27-30, pp.277-282, 1987.

Graham; S.A.: "Completing horizontal drain holes from a vertical well;" US patent # 5301760, 1994

Grindord S. and Wolf C.: "Calculation of NMDC length required for various latitudes developed from field measurements of drill string magnetization;" In: Proceedings of SPE/IADC 1983 Drilling Conference, New Orleans, LA, pp: 217-224, Feb. 20-23, 1983.

Haykin S.: "Adaptive filter theory – 3<sup>rd</sup> edition;" Prentice Hall, Upper Saddle River, N.J., 1996.

Hartmann R.: "Method of qualifying a borehole survey;" US patent # 5787997, 1998.

Helm W.: "Method and apparatus for measurement of azimuth of a borehole while drilling;" US patent # 5012412, 1991.

Holmes A.: "A method to analyze directional surveying accuracy;" In: Proceedings of 62<sup>nd</sup> SPE annual technical conference and exhibition, Dallas, TX, September 27-30, pp.283-290, 1987.

Holmes A.B., Vanaman F.B., Drzewiecki T.M.: "Vortex chamber mud pulser;" US patent # 5455804, 1995.

Hotate K. and Hayashi G.: "Resonator fiber optic gyro using digital serrodyne modulation – Method to reduce the noise induced by the back scattering and closed loop operation using digital signal processing" In: Proceedings of the 13<sup>th</sup> SPIE conference, Kyongju, South Korea, **V3746**, pp: 104 – 107, Apr. 12 – 16, 1999.

Hsu P., Tsai T. and Lee F.: "Application of a variable step size algorithm to QCEE adaptive IIR filters;" *IEEE Transactions on Signal Processing*, **V48** (1), pp.: 250-254, Jan. 2000.

Huang S., Sarma N., Killian K. and Goodwin J., "Optical signal noise reduction for fiber optic gyroscopes" *US patent # 5898496*, April 1999.

Hughes P.: "Spacecraft attitude dynamics;" John Wiley and Sons, New York, N.Y., 1986.

Hulsing R.: "Borehole survey system utilizing strapdown inertial navigation;" *US patent # 4812977*, 1989.

Irvine R.: "Operational amplifiers characteristics and applications – 3<sup>rd</sup> edition;" Prentice Hall, Englewood Cliffs, NJ, 1994.

Jones W.B.: "Introduction to optical fiber communication systems;" Holt, Rinehart and Winston Inc., New York, 1987.

Joshi S.D. and Ding W.: "The cost benefits of horizontal drilling;" In: *Proceedings of the 1991 American Gas Association*, Arlington, VA, pp: 679-684, Apr. 29 - May 1, 1991.

Kelsey J.B.: "A wellbore inertial navigation system;" In: *Proceedings of SPE/IADC 1983 Drilling Conference*, New Orleans, LA, February 20-23, pp.291-304, 1983.

Killian K.: "Pointing grade fiber optic gyroscope" *IEEE Aerospace and Electronic System Magazine*, **v9** (7), pp: 6-10, 1994.

Kim B.Y.: "Optical fiber rotation sensing;" Academic Press, Inc, New York, N.Y., 1994.

KVH Industries Inc: “KVH E-core 2000 FOG;” KVH, Rhode Island, N.Y., 1998.

deLange J.I., Nijen Twihaar G.D. and Pelgrom J.J.: “Accurate surveying: An operator’s point of view;” In: Proceedings of the IADC/SPE Drilling Conference, Dallas, TX, Feb.28 – Mar 2, pp:325-332, 1988.

Lefevre H.: “ The Fiber optic gyroscope;” Artech-House, MA, 1993.

Lin J., Kuo K. and Yeh C.: “Phase domain model of a second order fiber optic gyroscope dynamic system;” In: Proceedings of the IEEE Instrumentation and Measurement Technology Conference; Taiwan, May 10-12, 1994.

Mantha V., Duncan R., Wu Y., Zhao J., Ganapathiraju A. and Picone J., “Implementation and analysis of speech recognition front-ends” In: Proceedings of the IEEE Southeast Conference, Lexington, KY, pp.: 32-35, Mar. 25 – 28, 1999.

Macpherson J.D., Mason J.S. and Kingman J.E.: “Surface measurement and analysis of drill string vibrations while drilling;” In: Proceedings of SPE/IADC 1983 Drilling Conference, New Orleans, LA, February 20-23, pp.953-963, 1983.

Martell H., Wong R., Knickmeyer E., and Schwarz K.P: “Report on alignment, body axes transformation and navigation equations for a strapdown inertial system;” Department of Geomatics Engineering at the University of Calgary, 1988.

Merhav, S.: “Aerospace sensor systems and applications;” Springer-Verlag, New York, N.Y., 1993.

Morgan D.J. and Scott A.: “High accuracy directional surveying of wells employing inertial techniques;” In: Proceedings of the 12<sup>th</sup> annual offshore technology conference, Houston, TX, April 30 – May 3, pp.33-40, 1979

Muritala L., Onwuazo C., Adewumi F. and Aibangbe O.: "Improved horizontal well placement and performance using at bit inclination measurement tool" In: Proceedings of the SPE/CIM International Conference on Horizontal Well Technology, Calgary, Alberta, Canada, Nov. 6-8, 2000.

Mohamed A.H.: "Optimizing the estimation procedure in INS/GPS integration for kinematic applications;" *Ph.D. thesis*, Department of Geomatics Engineering, University of Calgary, *UCGE report # 20127*, April 1999.

Nichelson J.: "Method for determining borehole direction;" US patent # 5435069, 1995.

Njaerheim A., Breivik A.K., Rovde R., Kvale E., Kvamme S.A. and Bjoerneli H.M.: "New well design in the Statfjord field utilizing a multi-lateral well in low productive zones in the Brent reservoir;" In: Proceedings of the 1998 IADC/SPE Drilling Conference, Dallas, TX, pp: 547-558, Mar 3-6, 1998.

Noureldin A.<sup>f</sup>, Tabler H., Irvine-Halliday D. and Mintchev M.P.; "A new technique for reducing the angle random walk at the output of fiber optic gyroscopes during alignment processes of inertial navigation systems", *Journal of Optical Engineering*, **V40**(10), pp: 2097-2106, Oct. 2001.

Noureldin A.<sup>e</sup>, Irvine-Halliday D., Herb T. and Mintchev M.P. (2001) Improving wellbore surveying accuracy of horizontal wells by utilizing dual-axis optical gyro system. *Journal of the Society of Petroleum Engineers (Drilling & Completion)*, Oct. 2001.

Noureldin A.<sup>d</sup>, Irvine-Halliday D. and Mintchev M.P.; "Measurement-While-Drilling Surveying of Highly-Inclined and Horizontal Well Sections Utilizing Single-Axis Gyro Sensing System," Submitted to the *IEEE Transactions on Geoscience and Remote Sensing*, July 2001.

Noureldin A.<sup>c</sup>, Tabler H., Irvine-Halliday D. and Mintchev M.P.; "Reduction of the FOG noise level during station-based surveying processes of highly-inclined and horizontal wells in the oil industry," In: Proceedings of the International Symposium on Kinematic Systems in Geodesy, Geomatics and Navigation, Banff, AB, June 5-8, pp.: 213-219, 2001.

Noureldin A.<sup>b</sup>, Irvine-Halliday D. and Mintchev M.P.; "Accuracy limitations of FOG-based continuous measurement-while-drilling surveying instruments for horizontal wells", Submitted to the IEEE Transactions on Instrumentation and Measurement, May 2001.

Noureldin A.<sup>a</sup>, Tabler H., Irvine-Halliday D. and Mintchev M.; "Measurement-while-drilling surveying of near-vertical wells and in sections of multi-well structure using FOG-based INS;" In: Proceedings of the National Technical Meeting of the Institute of Navigation, Long Beach, CA, Jan 22-26, pp.: 193-204, 2001.

Noureldin A.<sup>c</sup>, Tabler H., Irvine-Halliday D. and Mintchev M.P.; "Quantitative study of the applicability of fiber optic gyroscopes for measurement-while-drilling borehole surveying", Journal of the Society of Petroleum Engineers (JSPE), V 5(4), pp: 363-370, Dec. 2000.

Noureldin A.<sup>b</sup>, Tabler H., Irvine-Halliday D., Mintchev M.: "Testing the applicability of fiber optic gyroscope for azimuth monitoring in measurement-while-drilling processes for the oil Industry," In: Proceedings of the IEEE Position, Location and Navigation Symposium, San Diego, CA, Mar. 12-16, pp: 291-298, 2000.

Noureldin A.<sup>a</sup>, Tabler H., Irvine-Halliday D. and Mintchev M.; " A New borehole surveying technique for horizontal drilling process using one fiber optic gyroscope and three accelerometers," In: Proceedings of the SPE/IADC, New Orleans, LA, Feb. 23-25, 2000.

Noureldin A., Mintchev M., Irvine-Halliday D., Tabler H.; "Computer modelling of microelectronic closed loop fiber optic gyroscope"; In Proceedings of IEEE Canadian Conference on Electrical and Computer Engineering; May 9-12, Edmonton, AB, pp: 633-638, 1999.

Noy K.A. and Leonard J.G.: "A new rate gyroscopic wellbore survey system achieves the accuracy and operational flexibility needed for today's complex drilling challenges;" In: Proceedings of SPE/IADC Drilling Conference, Amsterdam, Netherlands, pp: 773-783, Mar. 4-6, 1997.

Nuttall J.D.: "Optical gyroscopes;" IEE Journal, Electronics and Power, **V33**(11), 1987.

Orban J. and Richardson N.W.: "Method for directionally drilling a borehole;" US patent# 5467832, 1995.

Parkinson W.D.: "Introduction to Geomagnetism;" Scottish Academic Press, Edinburgh, 1983.

Pazaitis D. and Constantinides A.: "Novel Kurtosis driven variable step-size adaptive algorithm;" IEEE Transactions on Signal Processing, **v47** (3), pp: 864-872, Mar. 1999.

Perlmutter M.S., Reynolds C.I and Yahalom R.; "Initial production results of a new family of fiber optic gyroscope;" In: Proceedings of the Gyro Technology Symposium; Stuttgart, Germany, Sept. 16-17; 1997.

Perlmutter M.S.: "A tactical fiber optic gyro with all digital signal processing;" In: Proceedings of the IEEE Position Location and Navigation Symposium, Las Vegas, NV, pp: 170-175, Apr. 11-15, 1994.

Phoenix Technology Services: "Phoenix Geolink MWD System;" [www.phoenixcan.com/geolink.htm](http://www.phoenixcan.com/geolink.htm), 2002.

Rehm W.A., Trunk T.D., Baseflug T.D., Cromwell S.L., Hickman G.A., Nickel R.D. and Lyon M.S.: "Horizontal drilling method and apparatus;" US patent # 5042597, 1991.

Rehm W.A., Garcia A. and Cia S.A.: "Horizontal drilling in mature oil fields;" In: Proceedings of SPE/IADC 1989 Drilling Conference, New Orleans, LA, pp: 755-764, Feb. 29 – Mar. 3, 1989.

Rong Z., Zhang Y. and Lian B.: "Novel neural networks for eliminating errors existing in FOG;" In: Proceedings of the SPIE – Integrated Optics Devices, San Jose, CA, **V3936**, pp: 301-308, Jan 24 - 25, 2000.

Russel A.W. and Roesler R.F.: "Reduction of nonmagnetic drill collar length through magnetic azimuth correction technique;" In: Proceedings of SPE/IADC Drilling Conference, New Orleans, LA, Mar. 6-8, 1985.

Russel, M. K. and Russel A. W.: "Surveying of boreholes;" US patent # 4163324, 1979.

Salychev O.: "Inertial systems in navigation and geophysics;" Bauman MSTU Press, Moscow, 1998.

Schwarz K.P and Wei M.: "INS/GPS integration for geodetic applications;" Lecture notes for ENGO 623, Department of Geomatics Engineering at the University of Calgary, 1999.

Schwarz K.P. and Wei M.: "A framework for modelling kinematic measurements in gravity field applications;" *Bulleting Geodesique*, v **64** (4), 331-346, October 1990.

Senior J.: "Fiber optic data transmission;" Prentice Hall, 1993.

Sesay A.B.: “Adaptive signal processing;” Lecture notes for ENEL 671, Department of Electrical and Computer Engineering at the University of Calgary, Calgary, Alberta, Canada, 1999.

Shiells G., Kerridge D.: “Borehole surveying;” US patent # 6021577, 2000.

Silicon Designs, Inc.: “Tri-axial analog accelerometer – 2412;” Silicon Designs, Issaquah, WA, 1999.

Skaugen E.: “The effect of quasi-random drill bit vibrations upon drill string dynamic behavior;” In: Proceedings of the SPE 62<sup>nd</sup> Annual Technical Conference and Exhibition, Dallas, TX, 105-116, 1987.

Skillingstad T.: “At-bit inclination measurements improves directional drilling efficiency and control;” In: Proceedings of SPE/IADC 2000 Drilling Conference, New Orleans, LA, Feb. 23 – 25, 2000.

Skaloud J.: “Optimizing geo-referencing of airborne survey systems by INS/DGPS.” Department of Geomatics Engineering, University of Calgary, *UCGE report # 20127*, March 1999.

Stephenson M.A. and Wilson H.: “Improving quality control of directional survey data with continuous inertial navigation;” *SPE Drilling Engineering*, **V7(2)**, 100-105, June 1992.

Solo V. and Xuan K.: “Adaptive signal processing algorithms;” Prentice Hall, N.J., 1995.

Tanaka R., Kurokawa A., Sato Y., Magome T., Hayakawa Y., Nakatani I., and Kawaguchi J.: “Signal processing for FOG;” *Journal of the SPIE on Fiber optic and laser sensors*, vol. 2292: 192-202; 1994.

Thomson W. T.: "Vibration theory and applications;" Prentice-Hall Inc, Englewood Cliffs, N.J., 1965.

Thorogood J.L.: "Instrument performance models and their application to directional surveying operations;" SPE Drilling Engineering, **V5** (4), pp: 294-298, Dec. 1990.

Thorogood J.L. and Knott, D.R.: "Surveying techniques with a solid state magnetic multi-shot device;" SPE Drilling Engineering, **V5**(3), pp:209-214, Sept. 1990.

Thorogood J.L. and Knott, D.R.: "Surveying techniques with a solid state magnetic multi-shot device;" In: Proceedings of SPE/IADC Drilling Conf., New Orleans, LA, pp: 841-856, Feb.28–Mar.3, 1989.

Thorogood J.L.: "Directional survey operations management;" Journal of Petroleum Technology, pp: 1250-1252, 1989

Thorogood J.L.: "How to specify and implement well surveys;" World Oil, July 1986.

Thorp M., "An analysis of discrepancies between gyro surveys;" In: Proceedings of the SPE/IADC Drilling Conference, New Orleans, LA, March 15 –18, pp: 103-110, 1987.

Titterton D.H. and Weston, J.L.: "Strapdown inertial navigation technology;" Peter Peregrinus Ltd., London, UK, 1997.

Trofimenkoff F.N., Segal M., Klassen A., Haslett J.W.: "Characterization of EM downhole to surface communication links;" IEEE Transactions on Geoscience and Remote Sensing, **V38**(6), pp: 2539-2548, Nov.2000.

Trowsdale L.: "Borehole survey method and apparatus for drilling substantially horizontal boreholes;" US patent # 4361192, 1982.

Tubel P., Bergeron C., Bell S.: "Mud pulse telemetry system for downhole measurement-while-drilling;" In: Proceedings of the IEEE Instrumentation and Measurement Technology Conference (IMTC'92), New York, NY, pp: 219-223, 1992.

Uttecht, G.W. and de Wadrt, J.P.: "Application of small diameter inertial grade gyroscopes significantly reduces borehole position uncertainty;" In: Proceedings of SPE/IADC 1983 Drilling Conference, New Orleans, LA, February 20-23, 31-40, 1983.

Vandiver J.K., Nicholson J.W. and Shyu R.J.: "Case studies of the bending vibration and whirling motion of drill collars;" In: Proceedings of SPE/IADC 1989 Drilling Conference, New Orleans, LA, pp: 291-304, Feb. 28 – Mar. 3, 1989.

Walker B.H.: "Some technical and economic aspects of stabilizer placement;" Journal of Petroleum Technology, pp.: 10-18, June 1973.

Walstrom J.E., Brown A.A. and Harvey R.P.: "An analysis of uncertainty in directional surveying;" Journal of Petroleum Technology, pp.515-523, April 1969.

Wang L.P., Wang L.J., He Y.H. and Yang Z.J.: "Prediction and computer simulation of dynamic thrust and torque in vibration drilling;" In: Proceedings of the Institute of Mechanical Engineers, Vol. 212 (B), pp.489-497.

Widrow B. and Stearns S.: "Adaptive signal processing;" Prentice Hall, N.J., 1985.

Widrow B., Glover J.R., McCool J.M., Kaunitz J., Williams C.S., Hearn R.H., Zeidler J.R., Dong Jr., Goodin R.C.: "Adaptive noise cancellation: principles and application," In: Proceedings IEEE, **V63**, pp.1692-1716, 1975.

Wolf C.J.M. and de Wardt, J.P.: “Borehole position uncertainty – Analysis of measuring methods and derivation of systematic error model;” *Journal of Petroleum Technology*, pp: 2339-2350, Dec. 1981.

Wong R.V. and Schwarz K. P.: “Development and field testing of a RLG strapdown inertial survey system;” In: *Proceedings of the IEEE Position, Location and Navigation Symposium*, New York, NY, pp.: 480-487, Nov.29 – Dec.2, 1988.

Wright J.W.: “Directional drilling azimuth reference systems;” In: *Proceedings of the SPE/IADC Drilling Conference*, Dallas, Tx, Feb. 28 – Mar. 2, pp.309-324, 1988.

Xia, M.Y. and Chen, Z.Y.: “Attenuation predictions at extremely low frequencies for measurement-while-drilling electromagnetic telemetry system;” *IEEE Transactions on Geoscience and Remote Sensing*, **V31**(6), pp: 1222-1228, Nov. 1993.

Yakowitz S. and Szidarovszky F.: “An introduction to numerical computations;” *Macmillan Publication Company*, NY, 1989.

## **APPENDIX A**

### **DETERMINISTIC ANALYSIS OF FOG PERFORMANCE.**

The FOG is a true single-axis rotation sensor providing immunity to cross-axis rotation, shock and vibration with no moving parts and high reliability. The FOG is modeled as a symmetric pair of classical communication channels sharing a common physical channel in opposite direction of propagation [Aein, 1995]. The FOG, as shown in Fig.3.2, consists of the following parts:

1. A rotation sensing coil: The fiber optic coil is chosen as a single mode fiber (and in some advanced systems it may be polarization-maintaining fiber). The length of this coil affects the accuracy desired.
2. A solid state wide band optical source: Superluminescent diodes with their high emitting power and narrow spectral width are usually used in navigational grade high accuracy FOGs. Other types of LEDs or laser sources are utilized for low cost systems.
3. An optical directional coupler and multifunction integrated optics chip (MIOC): (A) divides and carries optical source beam to opposite ends of the fiber coil where they propagate as clockwise CW and counter-clockwise CCW signals. (B) Electro-optically modulates the light. (C) Adds the returning CW and CCW beams from the coil ends and carries the vector-summed beam back to the optical detector. (D) Acts like a polarizer to select and orient the unpolarized light source onto the desired polarization axis.
4. AC bias modulator: it activates the phase shifter inside the MIOC to make a phase modulation of the counter-propagating beams. This increases the sensitivity of the FOG and produces direction sensitive output.
5. Serrodyne Phase Modulator: It filters the Sagnac signal and derives a voltage control phase shifter to cancel out the Sagnac phase shift. Consequently, the monitored rotation rate signal can be taken from the derive input to the voltage controlled optical shifter.

The reduction of the cost of the FOG manufacturing while keeping the same performance characteristics depends on the following factors:

1. Development of MIOC, optical source, and photodetector using solid state devices fabricated with the available components.
2. Low cost high quality polarization maintaining fiber coil.
3. Robotic packaging and assembly of various parts in small volume (2.5" diameter and 0.5" height).
4. Optimization of signal processing electronics to give bias drift less than  $0.1^\circ/hr$ .

The presently available FOG products use optical signals of a wavelength in the range from  $1.3$  to  $1.5\mu m$  that gives the minimum possible attenuation and pulse broadening (dispersion) [Senior, 1993]. A fiber optic coil between  $250m$  and  $1000m$  length is wound with polarization-maintaining fiber, which improves the optical reciprocity of the light path by reducing the level of the unwanted cross-polarized light being cross-correlated on the photodetector [Aein, 1995]. Although increasing the coil length improves the FOG accuracy, longer fiber optic coil lengths impose more attenuation on the optical signal. Thus, the coil length is limited by the power of the optical source and the attenuation characteristics of the fiber optic coil.

### **A.1. FOG Operating Principle.**

Upon rotation, the FOG sensing coil is an accelerating frame of reference. The FOG photodetector mechanizes the output intensity of the interference between the two counter-propagating beams. With no rotation, the peak value of the optical source intensity is sensed. Any mechanical rotation rate along an axis normal to the FOG coil causes an optical path difference and a time delay between the counter-propagating beams, which affects the intensity of the optical beam at the input of the photodetector. However, the following problems arise with the output of the photodetector [Aein, 1995]:

1. Rotation direction cannot be directly sensed as all the intensity functions describing the interference of the two counter propagating beams are even functions of delay.

2. The rotation rate sensor gain is low at low rotation rate because the intensity has zero differential sensitivity at zero rotation input.
3. The need of a DC electronic amplification circuit as the output of photodetector is a DC output.

The above three problems have been solved by introducing a phase modulation at multi-KHz frequency *AC* bias modulator for the counter-propagating beams before the photodetector. This can be achieved by the utilization of the optical phase modulator on one of the sensing coil terminals (see Fig.3.2). The derive voltage to the phase modulator periodically varies the optical path time delay through the modulator. This produces optical phase modulation time shift of the counter-propagating beams with respect to each other by the beam propagation time through the coil. The CCW beam is affected by the phase modulator before going through the fiber coil while the CW beams is affected by it after going through the fiber coil. This *AC* bias signal realizes the following:

1. The utilization of less expensive *AC* photodetector output amplifiers centered on the imposed phase modulation carrier frequency.
2. A direction sensitive detector output signal.
3. More sensitivity to low rotation rates.

The output becomes a sinusoidal signal function of the Sagnac phase shift. The mathematical analysis of this phase modulation will be discussed later in this appendix.

The last problem facing the development of FOGs is their dynamic range. Since the sinusoid is linear only for small values of its argument, the useful measurement dynamic range is further restricted by the fact that the FOG sensor gain (scale factor) becomes nonlinear at high rotation rates.

The measurement feedback with the serrodyne modulator is used to increase the dynamic range without the loss of accuracy. As the Sagnac phase shift sensed by the photodetector, feedback electronics at the photodetector output filters the Sagnac signal and derive a voltage controlled optical phase shifter to cancel out the developing Sagnac effect optical signal. The rotation rate signal can be taken from the drive input to the voltage controlled optical shifter. The optical shifter drives voltage that is directly

proportional to the rotation rate. The mathematical analysis of this phase modulation will be discussed later in this appendix.

### A.2. Deterministic Analysis.

Let us assume that  $\Omega$  is the rotation rate of a certain platform and  $\hat{\Omega}$  is the FOG estimate of  $\Omega$  at its output so that  $\hat{\Omega}$  is unbiased, linear and direction sensitive. The following analysis does not take into consideration the scattering, attenuation and dispersion problems through the fiber. Let us consider that the source will launch the following signal to the system

$$V = A_0 \cos(\omega_0 t + \phi_n(t)) \quad (\text{A.1})$$

Where  $A_0$  is the source maximum amplitude,  $\omega_0$  is the mean center frequency of the source ( $\omega_0 = 2\pi / \lambda_0$ ) and  $\phi_n(t)$  is the broadband source noise. The two counter-propagating beams remain in the same polarization state by the polarization-maintaining fiber.

The phase modulator in the MIOC changes the refractive index in the optical wave guide in proportion to the applied voltage by employing the electro-optic effects. The resulting time delay variation in the beam passing through the phase modulator is proportional to the externally applied voltage. The CCW will be affected by the phase modulation  $\phi_m$  before entering the fiber loop while the CW will be affected by the phase modulation  $\phi_m$  after leaving the loop (i.e. after time  $\delta_0 = \frac{L}{V} = \frac{Ln}{C_o}$  through the fiber coil of length  $L$  and refractive index  $n$ ; where  $C_o$  is the free space light velocity). The CW and CCW beams can be expressed as follows:

$$\begin{aligned} CW &= \frac{A_0}{2} \cos(\omega_0 t + \phi_n(t) + \phi_m(t - \delta_0)) \\ CCW &= \frac{A_0}{2} \cos(\omega_0 t + \phi_n(t) + \phi_m(t)) \end{aligned} \quad (\text{A.2})$$

The output of the photodetector is given as the average of the intensity of the composite beam impinging the photodetector.

$$V_o(t) = \frac{1}{2} \overline{|CW + CCW|^2} \quad (\text{A.3})$$

which can be written as

$$V_o(t) = \frac{1}{2} \overline{|CW|^2} + \frac{1}{2} \overline{|CCW|^2} + \frac{1}{2} \overline{|CW * CCW|^2} \quad (\text{A.4})$$

Squaring both CW and CCW expressed at Eq.A.2 and get their average and substitute in (A.4), one can get:

$$V_o(t) = \left( \frac{A_o^2}{4} \right) + \frac{1}{2} \overline{|CW * CCW|^2} \quad (\text{A.5})$$

The first term in Eq.A.5 is a non-information-bearing DC term, which can be removed by the synchronous detector and the loop filter (see Fig.3.2). However, the second term presents the correlation between CW and CCW and can be processed to give:

$$V_o(t) = \left( \frac{A_o^2}{8} \right) \cos(\phi_m(t - \delta_0) - \phi_m(t)) \quad (\text{A.6})$$

It should be noted that the output voltage of the photodetector given in Eq.A.6 corresponds to the case of no rotation applied to the FOG platform. One may note also that the source noise  $\phi_n(t)$  is eliminated and is not participating in the output voltage.

Let us consider that the platform carrying the FOG rotates by angular velocity  $\Omega$ , the fiber coil rotates with the same angular velocity and the fiber coil ends will move a distance  $\Delta = \frac{d}{2} \Omega \delta_0$  [Lefevre, 1993], where  $d$  is the diameter of the fiber optic coil. In addition, the time delay arising from this motion between the two counter-propagating beam is given as  $2\Delta/V = 2\Delta n/C_o$ . This time delay produces a Sagnac phase shift given as the value of the time delay multiplied by  $\omega_0$  (the mean center frequency of the source). Then, the Sagnac phase shift can be written as:

$$\phi_s = \omega_0 \left( \frac{2\Delta n}{C_o} \right) = \omega_0 \left( \frac{d \Omega n \delta_0}{C_o} \right) \quad (\text{A.7})$$

Substituting  $\omega_0$  by  $2\pi C_o / \lambda$  and  $\delta_0$  by  $Ln/C_o$ , one can get:

$$\phi_s = \left( \frac{2\pi Ld}{\lambda C_o} \right) \Omega \quad (\text{A.8})$$

It is obvious that the Sagnac phase shift is proportional to the input rotation rate. The produced Sagnac phase shift changes both the *CW* and *CCW* expressions given in (A.2) to be as follows:

$$\begin{aligned} CW &= \frac{A_0}{2} \cos \left( \omega_0 t + \phi_n(t) + \phi_m(t - \delta_0) - \frac{\phi_s}{2} \right) \\ CCW &= \frac{A_0}{2} \cos \left( \omega_0 t + \phi_n(t) + \phi_m(t_0) + \frac{\phi_s}{2} \right) \end{aligned} \quad (\text{A.9})$$

Consequently, the output voltage can be determined as:

$$V_o(t) = \left( \frac{A_o^2}{8} \right) \cos(\phi_m(t) - \phi_m(t - \delta_0) + \phi_s) \quad (\text{A.10})$$

If the above analysis were made without considering the effect of the *AC*-bias modulator, the output voltage would become a *DC* signal given as  $V_o(t) = \left( \frac{A_o^2}{8} \right) \cos(\phi_s)$  which is an even function of the Sagnac phase shift and consequently the rotation rate. Consequently, the rotation direction cannot be determined.

If we consider the phase modulation signal given as follows [Aein, 1995]:

$$\phi_m(t) = -\frac{A}{2} \sin \omega_m t \quad (\text{A.11})$$

where  $\omega_m = 2\pi f_m$  and  $f_m$  is the modulation frequency in the range of 100 KHz. If  $\phi_m$  is substituted in the expression of the output voltage given in Eq.A.10, the synchronous photodetector output  $\tilde{V}$  can be determined as follows:

$$\tilde{V} = \left( \frac{A_o^2}{8} \right) J_1(A) \sin \phi_s \quad (\text{A.12})$$

where  $J_1(A)$  is the Bessel function of first order. In fact,  $\omega_m$  is chosen such that  $\omega_m \delta_0 = (2k+1)\pi$ , where  $k$  is a positive integer. The output voltage is maximized by using  $A = 1.8$  which gives  $J_1(1.8) = 0.5815$ .

Apparently, the sinusoidal *AC*-bias modulator produces a *DC*-free direction sensitive output. In addition, for small rotation rates and consequently small values of Sagnac phase shift,  $\sin \phi_s$  can be approximated as  $\phi_s$  and the output voltage in this case becomes directly proportional to the Sagnac phase shift and consequently to the rotation rate and can be given as

$$\tilde{V} = \left( \frac{A_o^2}{8} \right) (0.5815) \left( 2\pi * \frac{Ld}{\lambda C} \right) * \Omega \quad (\text{A.13})$$

Unfortunately, this simple open loop structure fails, if the produced Sagnac phase shift  $\phi_s$  gets larger at large input rotation rate. Moreover, the open loop system suffers from the non-linearity of the sinusoidal function at high rotation rates. This problem is solved by operating the FOG in a closed loop configuration utilizing the optical phase locked loop (PLL).

### A.3. Feedback FOG with Serrodyne Modulator.

For a closed loop FOG, an additional phase modulation on the MIOC is introduced to null out the Sagnac phase shift  $\phi_s$  developed by the rotation rate  $\Omega$ . The nulling signal is obtained by estimating  $\phi_s$  and then using this estimate to cancel it. Thus, the resulting estimate of the rotation range  $\hat{\Omega}$  will be proportional to  $\Omega$  over a wide range.

Let us define the error phase  $\phi_\epsilon$  as the difference between the Sagnac phase shift  $\phi_s$  and the voltage controlled external phase shift obtained from the estimation of  $\phi_s$  and introduced by the closed loop of the FOG. Consequently, the phase shift between the two counter-propagating beams becomes  $\phi_\epsilon$  which replaces  $\phi_s$  in Eq.A.12. Because this closed loop is in lock,  $\phi_\epsilon$  is very small so that  $\sin \phi_\epsilon \cong \phi_\epsilon$  even for large rotation rates. The objective of the PLL is to keep  $\phi_\epsilon$  very small and drive it to zero when  $\Omega$  is constant.

The implementation of the PLL requires a voltage control oscillator (*VCO*) with its output is an optical wave whose frequency is adjusted by a *DC* control voltage. The

frequency shift is equivalent to adding an unbounded phase ramp to the phase of the *VCO* output optical wave with the slope of this ramp is equal to the frequency shift. The slope of the phase ramp is controlled using the *DC* input voltage. However, it is impossible to physically implement this *VCO* function with the electro-optic effect in the *MIOC*. Since the electro-optic effect on the *MIOC* can achieve only a bounded time delay, the phase ramp must be periodically reset to produce a serrated (serrodyne) waveform as shown in Fig.A.1. The serrodyne phase modulation that mechanizes the *VCO* function on the *MIOC* is shown in Fig.A.2.

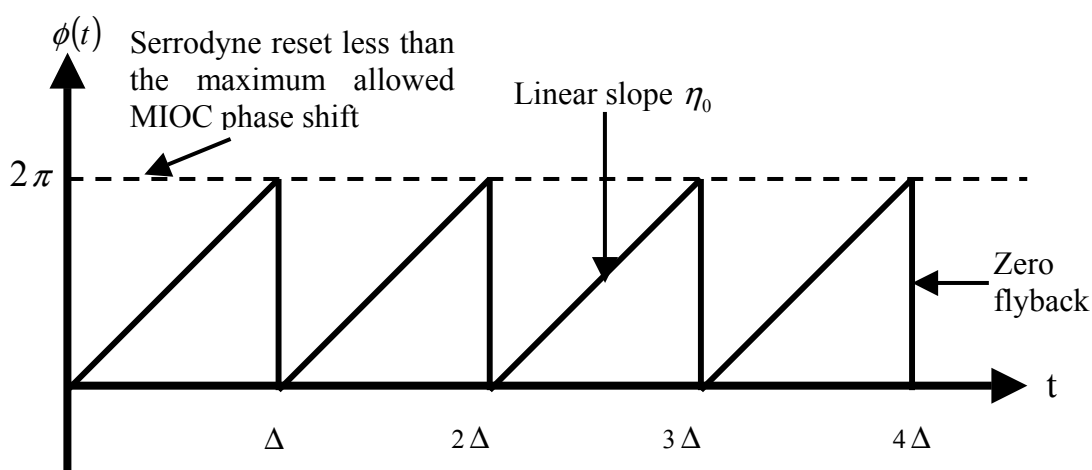


Fig.A.1. Ideal Serrodyne Modulator.

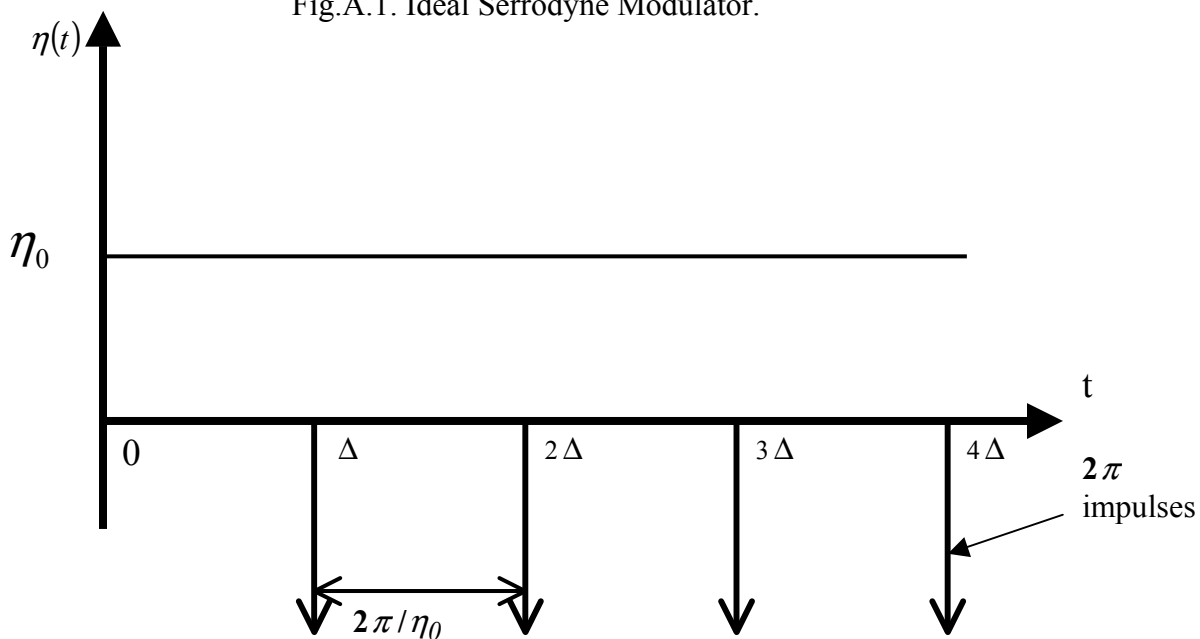


Fig.A.2. Frequency function  $\eta(t)$ .

The output phase of any phase modulator can be mathematically represented by the indefinite integral of a time-varying frequency,  $\eta(t)$ .

$$\phi(t) = -\int \eta(t) dt \quad (\text{A.14})$$

where  $\eta(t)$  is the optical frequency modulation waveform outputting from the serrodyne modulator and is given by the derivative of the serrodyne phase waveform ( $\eta(t) = \frac{d}{dt}\phi(t)$ ). As shown in Fig.A.2,  $\eta(t)$  is the superposition of a DC value  $\eta_0$  and an impulse train caused by the flyback resets in  $\phi(t)$ .

The serrodyne modulator is added to the Ac bias modulation to produce a total phase modulation,  $\phi_m(t)$  which is given by:

$$\phi(t) = -\left( \int \eta(t) dt + \frac{A}{2} \sin \omega_m t \right) \quad (\text{A.15})$$

$\phi_m(t)$  shown in Eq.A.11 is modified with the new expression of Eq.A.15 and then substituted in Eq.A.10 to get the new expression of the output voltage as follows:

$$V_o(t) = \left( \frac{A_o^2}{8} \right) \cos \left( \phi_s - \int_{t-\delta_0}^t \eta(t) dt - A \sin \omega_m t \right) \quad (\text{A.16})$$

This output voltage passes through the synchronous detector and is filtered about  $\omega_m$  to give the output  $\tilde{V}$  :

$$\tilde{V} = \left( \frac{A_o^2}{8} \right) J_1(A) \sin \left( \phi_s - \int_{t-\delta_0}^t \eta(t) dt \right) \quad (\text{A.17})$$

which can be rewritten in terms of the error phase  $\phi_\varepsilon$  as follows:

$$\tilde{V} = \left( \frac{A_o^2}{8} \right) J_1(A) \sin(\phi_\varepsilon) \quad (\text{A.18})$$

where  $\phi_{\mathcal{E}} = \phi_s - \int_{t-\delta_0}^t \eta(t) dt$

Let us assume that the *VCO* output frequency is held constant such that  $\eta(t) = \eta_0$ ,

then we can consider that  $\int_{t-\delta_0}^t \eta(t) dt = \eta_0 \delta_0$  and hence the error phase  $\phi_{\mathcal{E}} = \phi_s - \eta_0 \delta_0$ .

Consequently, when the measured Sagnac phase shift is obtained and the system sets  $\eta_0 = \phi_s / \delta_0$ , the error phase  $\phi_{\mathcal{E}}$  goes to zero. This is exactly the condition for a PLL to stabilize. However, as mentioned earlier, the implementation of an ideal VCO is not possible as the MIOC has a peak phase shift. The peak ramp phase value,  $\eta_0 \Delta$ , is hold constant and equal to  $2\pi$ . Upon rotation,  $\eta_0$  changes with respect to the variation of the Sagnac phase shift  $\phi_s$  to cancel it by varying the period of the ramp function  $\Delta$ . The angular frequency function  $\eta(t)$ , for this serrodyne phase waveform, is given by:

$$\eta(t) = \eta_0 - \sum_{\ell=-\infty}^{\infty} 2\pi\delta(t - \ell\Delta) \quad (\text{A.19})$$

where  $\Delta = 2\pi / \eta_0$ . In fact,  $\eta(t)$  becomes the desired function that is dependant on the rotation rate. It consists of constant frequency value  $\eta_0$  and unwanted impulse train and its integral is given as:

$$\int_{t-\delta_0}^t \eta(t) dt = \eta_0 \delta_0 - 2\pi \sum_{\ell=-\infty}^{+\infty} \text{rect}(t - \ell\Delta) \quad (\text{A.20})$$

where  $\text{rect}(t - \ell\Delta) = \begin{cases} 1 & \ell\Delta < t < \ell\Delta + \delta_0 \\ 0 & \text{elsewhere} \end{cases}$

The necessary part of the serrodyne modulation in Eq.A.20 is only the first term  $\eta_0 \delta_0$ . The problem with using the serrodyne modulation is the impulse train of period  $\Delta$  with the area under each pulse equal to  $2\pi$ . These impulses result from the flyback needed to keep the value of the maximum phase equal to  $2\pi$  and they cannot be neglected. With taking into consideration the effect of these impulse train, the error phase  $\phi_{\mathcal{E}}$  can be written as

$$\phi_{\varepsilon} = \phi_s - \eta_0 \delta_0 + 2\pi \sum_{\ell=-\infty}^{+\infty} \text{rect}(t - \ell\Delta) \quad (\text{A.21})$$

These unwanted pulse trains switch between 0 and  $2\pi$  corresponding to  $\sum_{\ell=-\infty}^{+\infty} \text{rect}(t - \ell\Delta)$  switching between 0 and 1. If the optical parameters are carefully controlled to keep the peak serrodyne phase always at  $2\pi$ , we can write that  $\phi_{\varepsilon} = \phi_s - \eta_0 \delta_0$ . This is achieved by keeping  $\eta_0 \Delta = 2\pi$ .

The closed loop operation derives  $\eta_0 \delta_0 = \phi_s$ . Since  $\eta_0 \Delta = 2\pi$ , the flyback frequency  $\Delta^{-1}$  becomes equal to  $\frac{\phi_s}{2\pi \delta_0}$ . If we substitute by the expression of  $\phi_s$  from Eq.A.8, the relationship between the flyback frequency of the serrodyne modulator and the applied rotation rate can be obtained as follows:

$$\Delta^{-1} = \left( \frac{Ld}{\lambda C \delta_0} \right) \Omega \quad (\text{A.22})$$

By taking into consideration that  $\delta_0 = Ln/C$ , equation (A.22) can be rewritten as:

$$\Delta^{-1} = \left( \frac{d}{\lambda n} \right) \Omega \quad (\text{A.23})$$

For the presently available FOG products, the applied rotation rate is evaluated by directly measuring the flyback frequency  $\Delta^{-1}$  using simple digital counting circuits and employs the scale factor  $\lambda n/d$ . The success of the serrodyne phase modulation depends on stable and accurate values of the scale factor  $\lambda n/d$ , precise adjustment and tuning of the trigger threshold  $\eta_0 \Delta = 2\pi$  and an ideal instantaneous serrodyne flyback time. The above analysis shows that the feedback operation of the closed loop FOG can give accurate measurements of rotation rate with high sensitivity, accuracy and dynamic range. The noise associated with the propagation will affect the FOG performance. Among these noise sources, one can mention the attenuation and dispersion of the optical signal along the fiber, the source noise, and the shot noise and thermal noise of photodetector. These noise effects can be minimized utilizing some digital signal processing techniques.

## **APPENDIX B**

### **DESIGN AND IMPLEMENTATION OF THE EXPERIMENTAL SETUP**

The purpose of this appendix is to describe the design and the implementation of a special experimental setup, which simulates the three-dimensional rotational and translational motion of the bottom hole assembly (BHA). In fact, testing the surveying methods developed in this thesis directly downhole could be counterproductive since controlled experiments would be very difficult if not impossible. Therefore, a comprehensive BHA motion simulator was necessary to test these new surveying methods.

#### **B.1. Design of the experimental setup.**

The experimental setup was designed to satisfy specific requirements related to the directional drilling process. It is capable of providing simultaneous rotation about three mutually orthogonal axes as well as translational motion. Since the penetration rate of the drill bit through the downhole formation is very small (about *1 cm/sec.*), the inclination angle (the pitch) changes very slowly during the directional drilling process. Before the beginning of the directional drilling process, a desired azimuth direction is established, and therefore, only small changes in the azimuth angle are expected due to the downhole formation. The tool face angle (the roll) is controlled by the drilling engineer and small angular changes are expected as well.

The layout of the experimental setup is shown on Fig.B.1. An angular scale is provided along each of the three axes allowing the user to follow the angular changes along any axis. The whole setup (Fig.B.1) consists of three circular discs. The first disc simulates the changes in the inclination angle and carries the whole setup. The second disc carries the inertial sensors (the FOG and the accelerometers). The third disc carries the batteries that supply the FOG and the accelerometers. In addition it prepares the FOG and the accelerometer signals for telemetry to the processing unit.

Rotation about each individual axis should be controlled in order to deliver small angular changes similar to the downhole situation during the horizontal drilling process. This can be implemented by DC motors controlled by a DC servo amplifier in a closed loop control system as shown on Fig.B.2. The fundamental idea of rotational motion control is to have an accurate control over a remote, distant, or isolated mechanical system [PWM servo amplifiers, Advanced Motion Control, CA, 1996]. The three key elements are: (1) the basic controller which links time, motion and position for the purpose of performing a series of tasks; (2) the servo amplifier which converts the low level analog or digital command signal from the controller into either voltage or current to drive the motor; (3) the servo motor which converts the electrical energy into mechanical energy. The link between the controller and the energy conversion system is the servo amplifier.

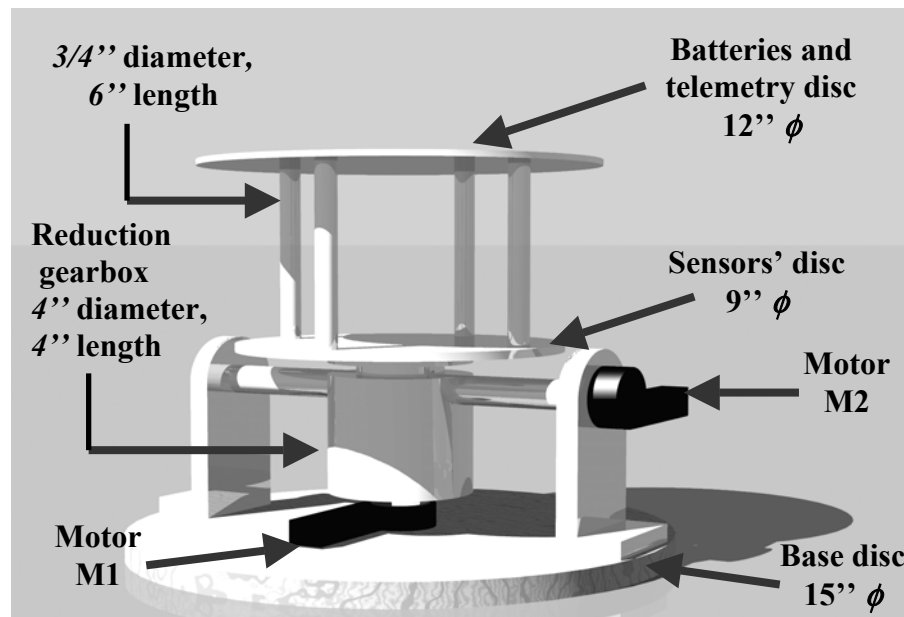


Fig.B.1. Layout of the experimental setup.

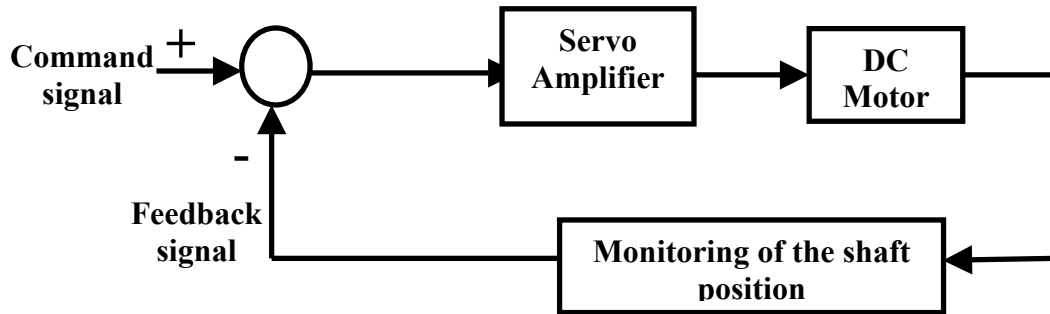


Fig.B.2. Closed loop analog position control of DC motor.

As shown on Fig.B.1, the motor M1 is coupled to the sensor disc to provide rotation about the horizontal plane simulating the change in the azimuth angle. The motor M2 is attached to another shaft perpendicular to the vertical one and crosses cylindrical box (Fig.B.1) to simulate changes in the roll. This cylindrical box should be designed to minimize the vibration and to allow the AC power to be delivered to the sensor and the batteries discs.

The inertial sensors required for this experiment include single FOG and three accelerometers. The FOG should be mounted originally in the horizontal plane of the sensors' disc. Three mutually orthogonal accelerometers are then mounted with one of them having its sensitive axis aligned along the FOG sensitive axis. In addition, the setup should incorporate an electronic compass to determine the initial azimuth and to provide a reference to the values determined for the azimuth during the station-based surveying processes by the FOG and the accelerometers. The outputs of the FOG and the accelerometers are then delivered to an analog-to-digital converter (A/D). The measurements is digitized in real-time by a suitable A/D card and then processed by a computer unit. In addition a suitable software program is necessary for real-time manipulation of the measurements.

## **B.2. Implementation of the experimental setup.**

The experimental setup was prepared according to the design discussed in the previous section. The reference for the rotation along the three mutually orthogonal axes was provided by an angular scale prepared using a rotary table with an accurate indexing

head, which gave an accumulative error of less than 1%. The rotational motion about each individual axis was provided by a 12 Volts brush type DC motor with a 5/8'' diameter shaft. The three discs shown on Fig.B.1 were prepared with dimensions and materials suitable for the measurement and control devices used in this experiment. The first disc is a base wooden disc, which is of 15'' diameter. The sensors disc is 9'' diameter steel disc mounted above a cylindrical steel box (4'' in diameter and 4'' in length) and the box has internal structural supports that contain a reduction gearbox. The motor (M1) is mounted onto the bottom of the box to provide rotation of the sensors' disc around the vertical axis (Fig.B.1) to simulate the change in the azimuth. The motor is linked to the reduction gearbox by a vibration-absorbing coupler attached to the drive shaft. The output shaft of the gearbox has two specially designed copper brush rings attached with wires running through the center of the shaft to the second and the third discs. The 120VAC power is delivered through copper commutator rings and carbon brushes, which are attached to the output shaft of the reduction gearbox as described above. The second motor (M2) is attached to another shaft perpendicular to the vertical one and crosses the cylindrical box as shown on Fig.B.1 to simulate the changes in the roll. The third disc hosts the batteries and data telemetry devices. This disc is mounted using four steel legs that are attached to the sensors' disc as shown on Fig.B.1. Each leg is cylindrical in shape with a length of 6'' and a diameter of 0.75''. The third disc carries two 12VDC, 1.1 Ah batteries and a single 7.2 VDC, 1.5 Ah battery. The 12 VDC batteries provide the supply for the FOG and the electronic compass. The 7.2 VDC battery provides the supply for the three-axis accelerometer package. Since the power needed by the accelerometers package is 5VDC, a simple regulating circuit utilizing the 7805 voltage regulator is used to reduce the 7.2 Volts into 5 Volts. The outputs from the FOG, the compass and the accelerometers are collected at the terminal block TB-1. These outputs are transmitted from the platform through a shielded cable to the terminal block TB-2 that connects the measurements to the analog-to-digital (A/D) converters attached to the laptop. A photograph of this setup is shown on Fig.B.3.

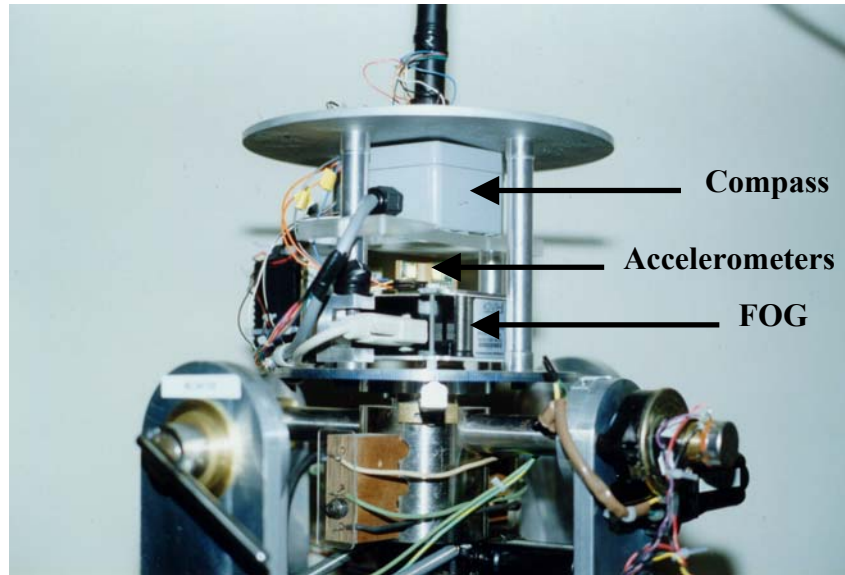


Fig.B.3. The experimental setup with showing the inertial measurement devices (the FOG and the three accelerometers).

The FOG used in this study is E-Core-2000 (KVH, Orland Park, IL) low-cost gyroscope with a tactical grade performance ( $7.2^\circ/hr$  drift rate and  $5^\circ/hr/\sqrt{Hz}$  angle random walk (ARW)). The three-axis-accelerometers is Tri-Axial 2412-005 (SILICON DESIGNS, Issaquah, WA) with  $\pm 5g$  input range and 1% of the full range bias calibration error, 2% cross axis sensitivity,  $50$  (ppm of span) $^\circ C$  bias temperature drift and  $0.002g$  output noise (RMS).

### **B.2.1 Control of rotational motion.**

DC servo amplifiers (25A8, ADVANCED MOTION CONTROL, Camarillo, CA) were used to drive the brush-type DC motors at a high switching frequency. The servo amplifiers required a  $20$  VDC power supply positioned under the whole setup. The servo amplifiers are configured to work at the analog position loop mode to implement the closed loop control system shown on Fig.B.2.

The Command analog signal is obtained from the setup operator by controlling the wiper of a  $10$  K $\Omega$  potentiometer. The feedback analog signal is obtained by establishing a mechanical connection between the motor shaft and the wiper of another

10  $k\Omega$  potentiometer. The wiper is attached to the motor shaft using special glue and left for one complete day to harden before attaching the motor to the whole setup. Both potentiometers receive a  $\pm 5$  VDC supply from the servo amplifier. The commanding signal from the first potentiometer is connected to one of the differential input terminals while the feedback signal from the second potentiometer is connected to the other differential input terminal. These two signals are compared, conditioned and then processed by the control logic circuit inside the servo amplifier to drive the DC motor (Fig.B.4). In addition to the angular position control, the rotation rate can be controlled with an optical encoder attached to the motor shaft. The output of the optical encoder is connected to the tachometer input available at the servo amplifier.

### **B.2.2. Signal conditioning and data acquisition.**

The experimental setup described in the previous section incorporates single FOG and three accelerometers. The output of each of them is an analog signal in the range of  $\pm 2.0$  Volts (corresponding to  $-100$  °/s to  $100$  °/s) for the FOG and  $0.5$  Volts to  $4.5$  Volts (corresponding to  $-5g$  to  $5g$ ) for the accelerometers. In addition the electronic compass (C100, KVH, Orland Park, IL) provides an analog output in the range from  $0.1$  Volts to  $1.9$  Volts (corresponding to  $0$  to  $360$  degrees). The orientation of zero azimuth is adjusted initially before turning on the motors to avoid the possible magnetic interference from the motor coils. In addition, we tried to keep the compass as far away as possible from any steel or iron materials associated with the setup.

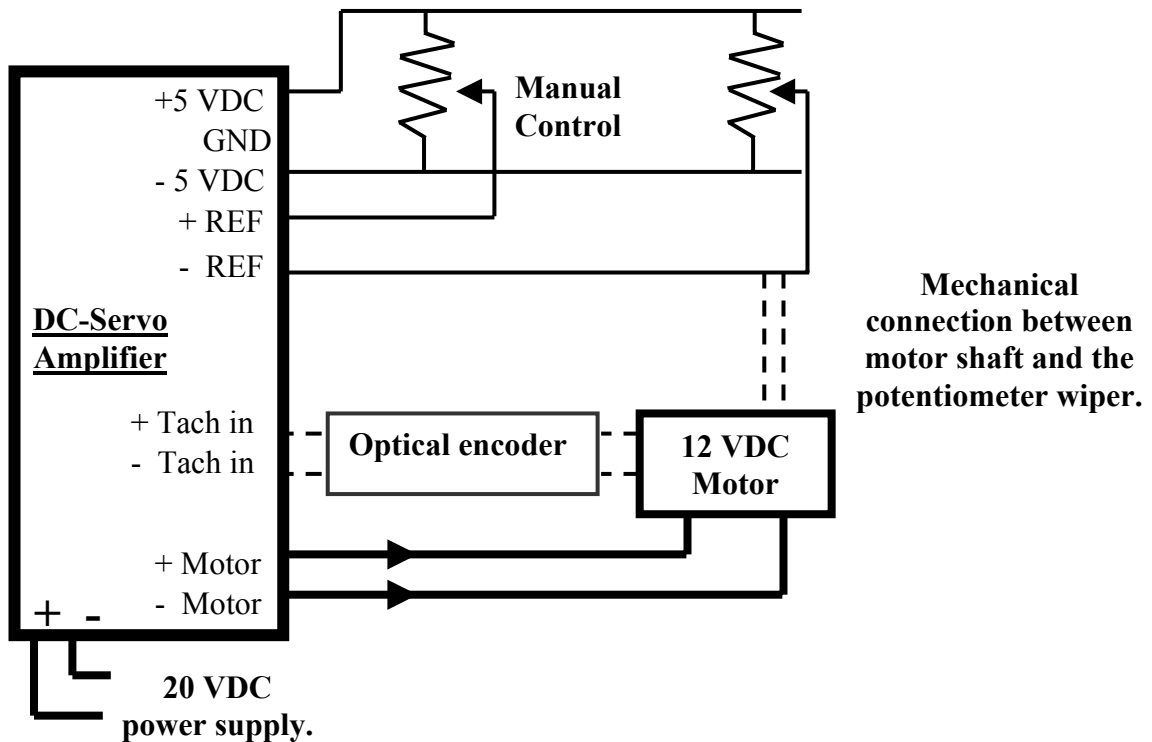


Fig.B.4. Connection diagram for the DC motor positioning and speed control.

It is recommended by the manufactures of the FOG and the accelerometers to use the differential output from the devices rather than the single ended outputs. Each of these devices provides an output signal that carries information about either the rotation rate (for the FOG) or the linear acceleration (for the accelerometers). The single-ended connection can be established by referring the output signal to the common ground provided by the device. In this circumstance the zero rotation rate and zero acceleration will correspond to + 2.5 Volts for either the FOG or the accelerometers. However, this is not as accurate as the differential measurement. Both the FOG and the accelerometers deliver a reference signal at 2.5 Volts, which fluctuates and/or is biased similar to the main output. In this situation the zero rotation rate and the zero acceleration will correspond to zero volts for both the FOG and the accelerometers. In our experiments the differential outputs of the FOG and the accelerometers were delivered to the A/D card via shielded cable from the batteries and telemetry disc to the A/D terminal block located outside the whole setup (Fig.B.5).

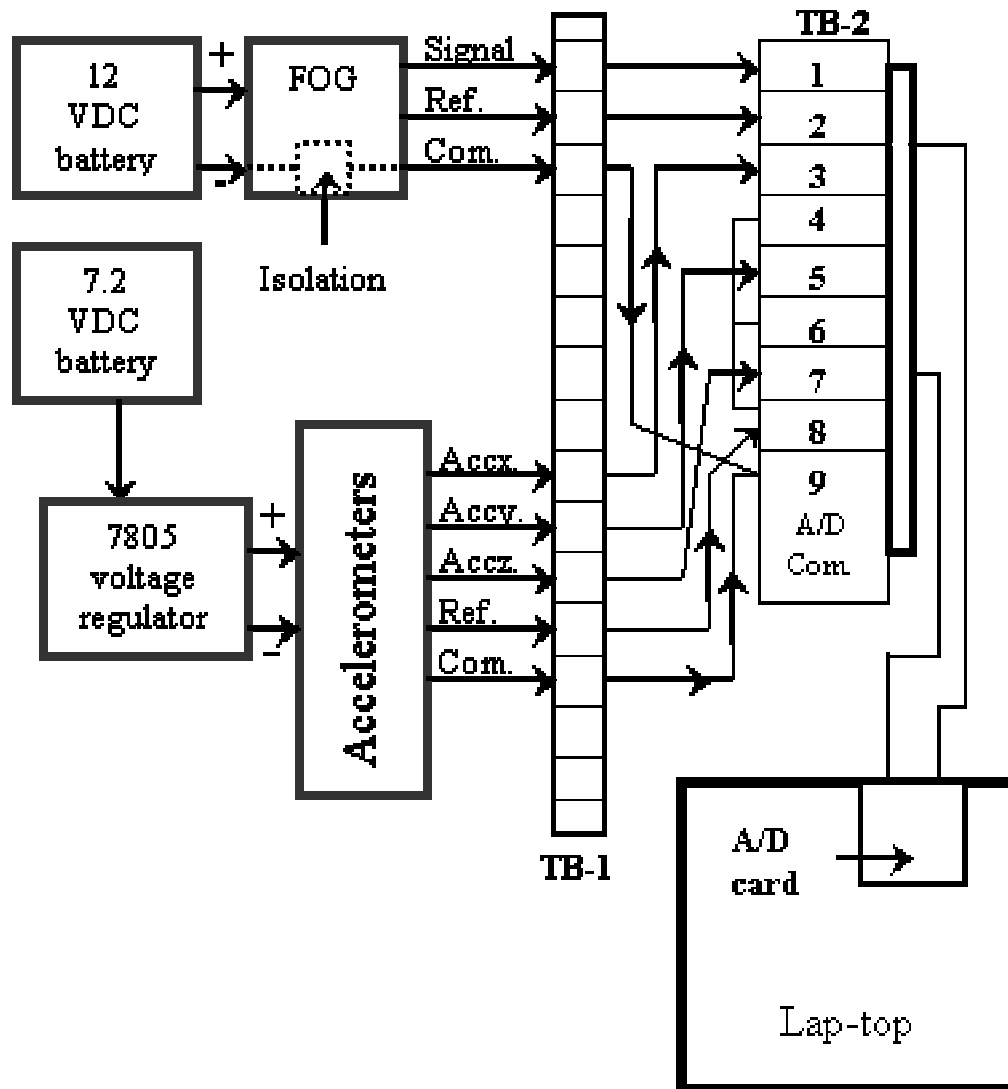


Fig.B.5. The connection diagram for processing the FOG and the accelerometers output signal and interfacing them to the A/D system [Noureldin et al.<sup>b</sup>, 2000].

The A/D card (DAQCard-1200, National Instruments, Austin, TX) is 12-bit analog-to-digital converter that can accommodate up to 8 channels in single ended mode and 4 channels in differential mode. This A/D card was configured to receive differential input signals. Since the A/D card can only accommodate four differential inputs, the output from the electronic compass was measured at the beginning of each experiment by a digital voltmeter to determine the initial azimuth. The connection diagram for the FOG

and the accelerometers is shown on Fig.B.5. It can be noted that although differential input signals are processed, the common of the A/D card still needs to be connected to the common of each of these input signals. If this connection is not provided, the received signals are highly corrupted by the noise of the external environment. The signal common of the FOG is isolated from the power supply common, while the signal common of the accelerometers is connected to the power supply common. The isolation between the FOG signal common and its power supply common reduces the noise at the FOG output signal. Therefore any connection between the FOG signal common and the power supply common produces a drop in the voltage of the FOG output signal. If the FOG signal common is connected with the signal common of the accelerometers at the A/D terminal block and both devices are supplied from the same power source, a drop in the FOG output signal is expected. To avoid this problem two different batteries were used to supply the FOG and the accelerometers thus separating the FOG power supply common from the rest.

The FOG and the accelerometer signals were connected to the A/D terminal block (TB-2, Fig.B.3). The A/D card is installed inside a laptop computer (Compac 433 MHz, AMD processor and 64 MB RAM). A special software program was prepared for this setup using CVI development environment (Ver.5, National Instruments, Austin, TX). This program provides real-time acquisition of the four analog input signals and plots them in real-time on the screen with a graphical user interface that allows the user to monitor the variation of the FOG and accelerometer signals (Fig.B.6). Moreover, this program allows the user to set different ranges for the vertical axis of the four channels for proper monitoring of the measurement process [see Fig.B.7.]. The process of reading data from the four input channels starts first by acquiring the data into a buffer and then transferring these data into an array for each channel. The value inside each array is saved in real-time into a file for further off-line processing. Therefore, after each experiment different files archive the measurements for the FOG and the accelerometers. Furthermore, the program can be configured not only to acquire measurements using the A/D card (real-time analysis) but also to read data from already existing files for further off-line analysis of the raw measurements (see Fig.B.8).

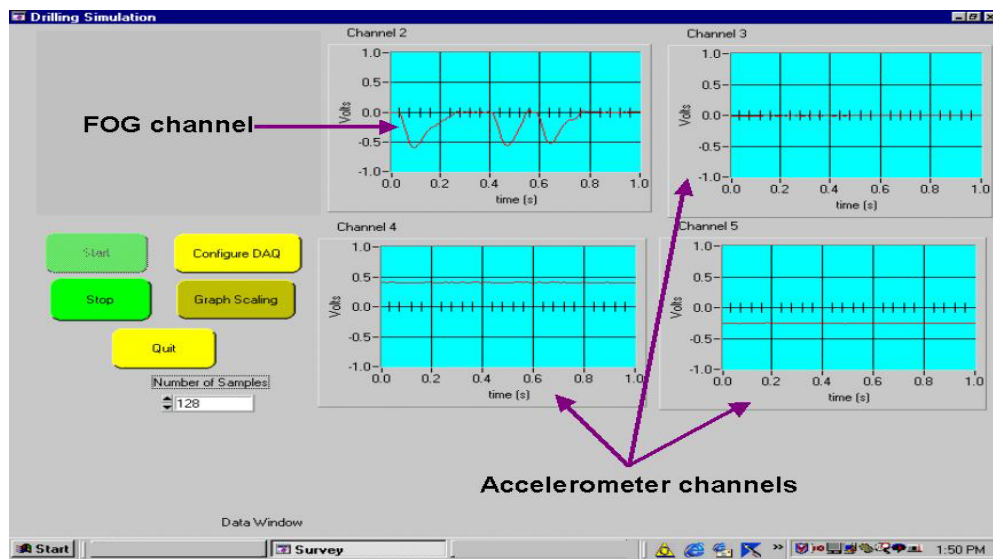


Fig.B.6. Software program for 4-channels data acquisition.

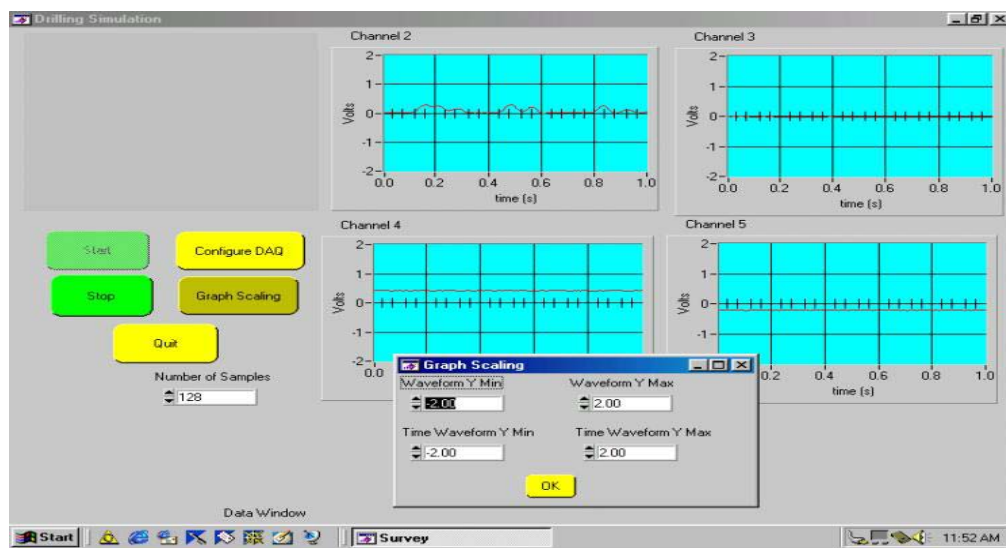


Fig.B.7. Changing the range of the vertical axes of the four channels in real-time during the data acquisition process.

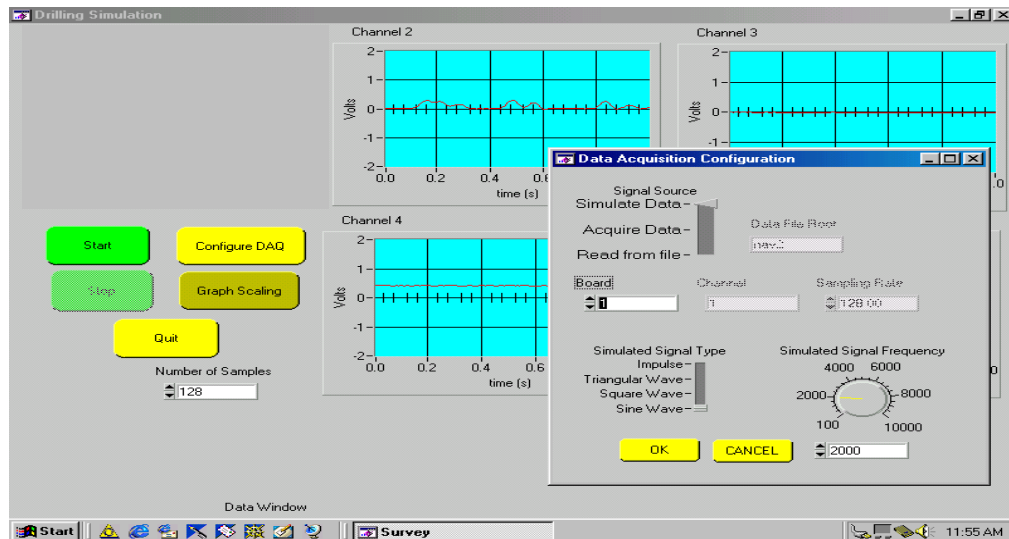


Fig.B.8. Configuration of the software program for different signal sources (acquiring data through the A/D card or reading data from a file).

The 12-bit A/D converter used to digitize the FOG and the accelerometer signals has a dynamic bipolar range of  $\pm 5$  Volts. Therefore, the resolution of this A/D converter is computed as  $R/2^r$  (where  $R$  is the peak to peak voltage range and  $r$  is the number of bits used for digitization) giving a resolution of  $2.44 \text{ mV}$  and digitization error of  $1.22 \text{ mV}$ . During the station-based surveying process while the FOG is monitoring the Earth's rotation rate (maximum of  $15^\circ/\text{hr}$ ) the maximum value of the voltage signal expected from the FOG is  $0.083 \text{ mV}$  above its bias. This value is obtained after applying the FOG scale factor given as  $20 \text{ mV}/(^\circ/\text{sec.})$ . It is clear that the value of  $0.083 \text{ mV}$  is below the resolution of the A/D converter. Therefore, the FOG output signal needs to be amplified during the alignment process to bring the voltage value above the resolution limit of the A/D converter. The amplification of the FOG differential signal is implemented using a low-cost, low-power instrumentation amplifier AD620 [Analog Devices, Amplifiers reference manual, 1994]. This 8-pin IC is equivalent to the three operational amplifiers configuration shown on Fig.B.9 [Irvine, 1994]. The value of the resistance  $R_g$  controls the desired gain value. The total error of AD620 is about one half that of the traditional circuit shown on Fig.9.a with lower noise level (less than  $9 \text{ nV}/\sqrt{\text{Hz.}}$ ). For the AD620,

the gain is defined as  $G = 1 + \frac{49.9 * 1000}{R_g}$ , where  $R_g$  is an external resistor connected to the AD620 IC as shown on Fig.B.10. In this experiment, a standard  $51\Omega$  resistor is used to give 979.43 amplification ratio.

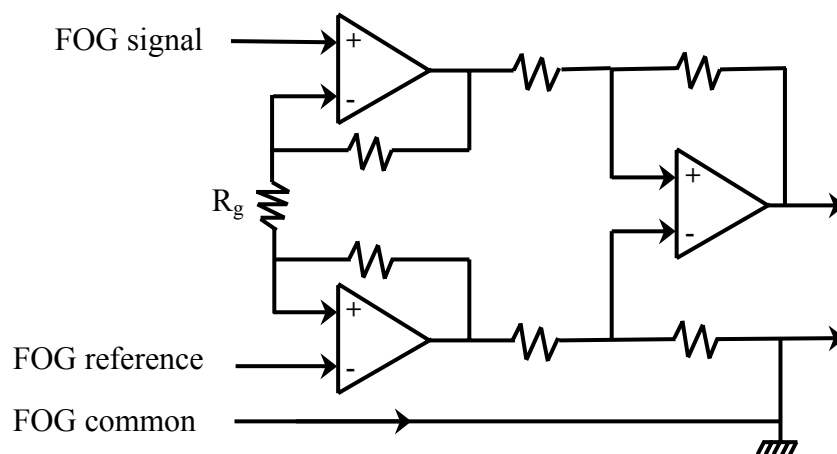


Fig.B.9. The traditional amplification circuit for differential signals.

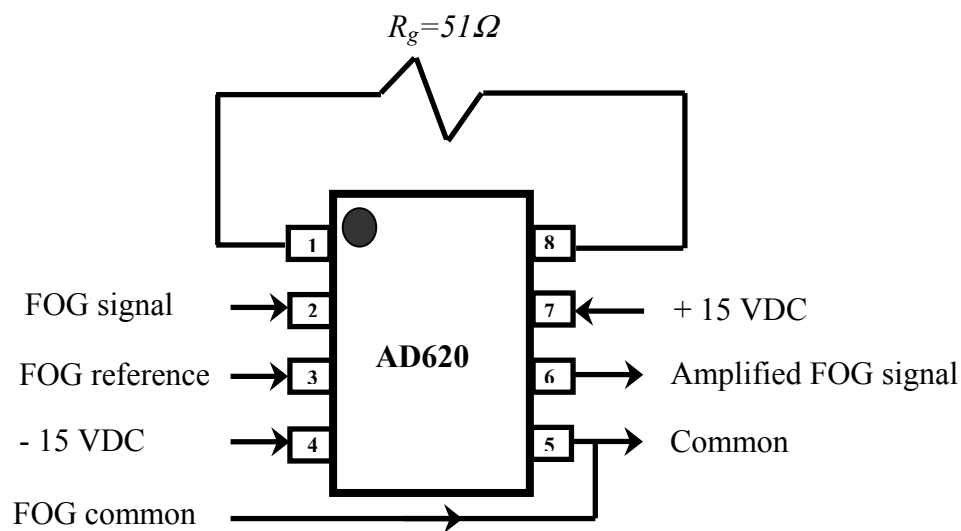


Fig.B.10. Connection diagram for the amplification of the FOG signal during the alignment process using AD620.

### APPENDIX C.

#### STUDYING THE LONG-TERM BEHAVIOR AND THE INTERRELATIONSHIP BETWEEN THE VARIOUS SURVEYING ERRORS.

In general, the velocity errors ( $\delta V^e$ ,  $\delta V^n$  and  $\delta V^u$ ), derived for the simplified Single-FOG MWD near-vertical surveying system or those given for the Dual-FOG system, depend on two major set of surveying errors. The first set includes the attitude errors ( $\delta\theta$ ,  $\delta\phi$  and  $\delta\psi$ ) and the second set represents the accelerometer bias errors.

$$\begin{pmatrix} \delta \dot{V}^e \\ \delta \dot{V}^n \\ \delta \dot{V}^u \end{pmatrix} = \begin{pmatrix} 0 & f_u & -f_n \\ -f_u & 0 & f_e \\ f_n & -f_e & 0 \end{pmatrix} \begin{pmatrix} \delta\theta \\ \delta\phi \\ \delta\psi \end{pmatrix} + \begin{pmatrix} \delta f_e \\ \delta f_n \\ \delta f_u \end{pmatrix} \quad (\text{C.1})$$

where  $f_e$ ,  $f_n$  and  $f_u$  are the specific force measurements after being transformed into the  $\ell$ -frame and  $\delta f_e$ ,  $\delta f_n$  and  $\delta f_u$  are the accelerometer bias errors after being transformed into the  $\ell$ -frame. Similarly, the error terms which have significant effect on the attitude errors include the velocity errors ( $\delta V^e$ ,  $\delta V^n$  and  $\delta V^u$ ) and the gyro drift errors.

$$\begin{pmatrix} \delta \dot{\theta} \\ \delta \dot{\phi} \\ \delta \dot{\psi} \end{pmatrix} = \begin{pmatrix} 0 & \frac{1}{M+h} & 0 \\ \frac{-1}{N+h} & 0 & 0 \\ \frac{-\tan \varphi}{N+h} & 0 & 0 \end{pmatrix} \begin{pmatrix} \delta V^e \\ \delta V^n \\ \delta V^u \end{pmatrix} + \begin{pmatrix} \delta \omega_e \\ \delta \omega_n \\ \delta \omega_u \end{pmatrix} \quad (\text{C.2})$$

where  $\delta \omega_e$ ,  $\delta \omega_n$  and  $\delta \omega_u$  are the gyro drifts after being transformed into the  $\ell$ -frame.

In general,  $f_e$  and  $f_n$  are very small acceleration components (close to zero) if compared to  $f_u$ , which is close to gravity ( $9.808 \text{ m/sec}^2$ ). It can be determined from the velocity error equations that  $\delta V^e$  and  $\delta V^n$  are respectively related to  $\delta\phi$  and  $\delta\theta$  through the acceleration component  $f_u$  while being related to the azimuth error  $\delta\psi$  through the acceleration components  $f_n$  and  $f_e$  respectively. Consequently, a strong

coupling exists between  $\delta V^e$  and  $\delta\phi$  and between  $\delta V^n$  and  $\delta\theta$ , while weak coupling appears between either  $\delta V^e$  or  $\delta V^n$  and  $\delta\psi$ .

If two INS surveying errors states are strongly coupled to each other, any dynamical changes in one of them over time will be shown on the other. Therefore, if one of these error states is accurately estimated with an appropriate optimal estimation tool (like Kalman filtering), the other error state can be estimated accurately too. For example, accurate estimation of the velocity error states by any suitable velocity update measurements does not only improve the accuracy of velocity computation but also the accuracy of the computed inclination and roll angles.

### C.1. The Schuler effect.

The velocity errors  $\delta V^e$  and  $\delta V^n$  are composed of two components. The first component is called Schuler component, which describes the strong coupling with  $\delta\phi$  or  $\delta\theta$ . The second component is a non-stationary component, which depends on the BHA acceleration components along the horizontal plane and relates the velocity errors to the azimuth error. These two components can be rewritten as follows [Salychev, 1998]:

$$\begin{aligned} \delta \dot{V}_{Sch}^e &= f_u \delta\phi + \delta f^e & \& & \delta \dot{V}_{nst}^e &= -f_n \delta\psi \\ \delta \dot{V}_{Sch}^n &= -f_u \delta\theta + \delta f^n & \& & \delta \dot{V}_{nst}^n &= f_e \delta\psi \end{aligned} \quad (C.3)$$

where  $\delta V_{Sch}^e$  and  $\delta V_{nst}^e$  are respectively the Schuler and the non-stationary components of  $\delta V^e$  and  $\delta V_{Sch}^n$  and  $\delta V_{nst}^n$  are respectively the Schuler and the non-stationary components of  $\delta V^n$ .

The strong coupling between  $\delta V^e$  and  $\delta\phi$  on one hand, and  $\delta V^n$  and  $\delta\theta$  on the other are described by the block diagrams shown on Figs.C.1.a and C.1.b. These block diagrams are well known in INS as Schuler loops describing the errors in the velocity and the attitude components in the horizontal plane (i.e. along the East and the North directions) [Salychev, 1998; Mohammed, 1999].

If we differentiate the Schuler component of both  $\delta V^e$  and  $\delta V^n$  and substitute by the corresponding rate of change of  $\delta\theta$  and  $\delta\phi$ , the following linear non-homogeneous 2<sup>nd</sup> order differential equations can be obtained [Salychev, 1998]:

$$\delta \dot{V}_{Sch}^e + \frac{f_u}{N+h} \delta V_{Sch}^e = f_u \delta \omega_n \quad (C.4)$$

$$\delta \dot{V}_{Sch}^n + \frac{f_u}{M+h} \delta V_{Sch}^n = f_u \delta \omega_e \quad (C.5)$$

The solution of these 2<sup>nd</sup> order differential equation yields velocity errors  $\delta V^e$  and  $\delta V^n$  along the horizontal directions oscillating over time with a very small frequency equal to 1/5000 Hz called the Schuler frequency  $f_s \cong \frac{1}{2\pi} \sqrt{\frac{f_u}{N+h}} \cong \frac{1}{2\pi} \sqrt{\frac{f_u}{M+h}}$  [Titterton and Weston, 1997]. This frequency corresponds to time interval of about 84.4 minutes. Consequently, the velocity error becomes bounded over time.

Due to the strong coupling of  $\delta\theta$  and  $\delta\phi$  with the Schuler components of  $\delta V^e$  and  $\delta V^n$ , the inclination and the roll errors become bounded over time and oscillate with approximately the same Schuler frequency.

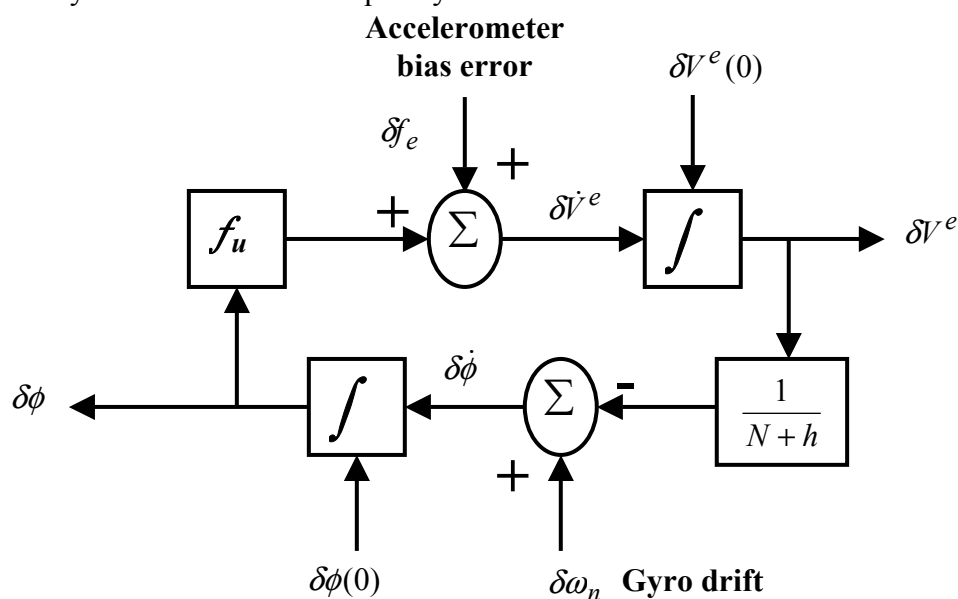


Fig.C.1.a. Block diagram showing the Schuler loop describing the coupling between  $\delta V^e$  and  $\delta\phi$  (i.e. along the East channel).

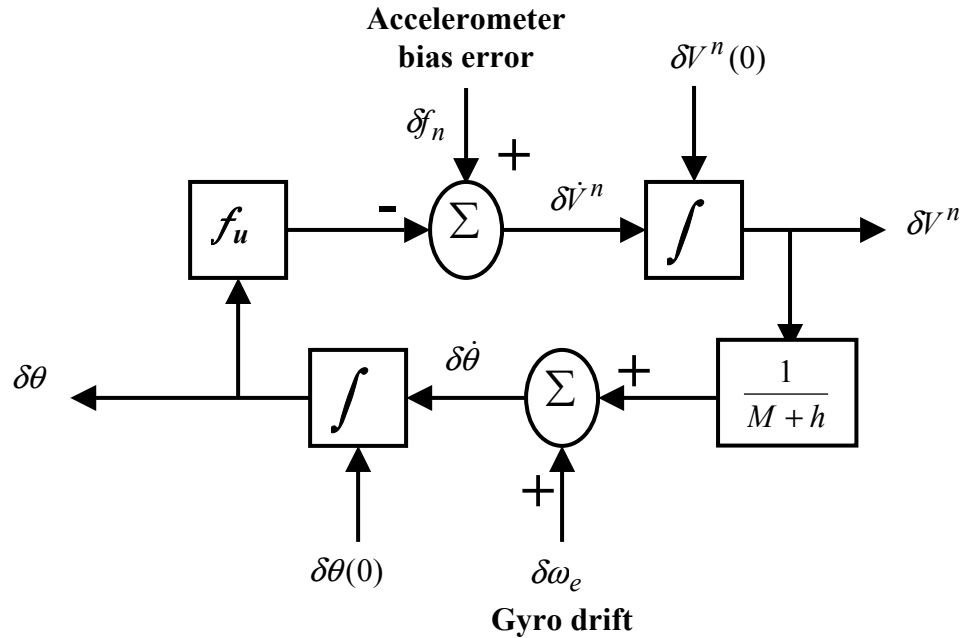


Fig.C.1.b. Block diagram showing the Schuler loop describing the coupling between  $\delta V^n$  and  $\delta\theta$  (i.e. along the North channel).

## C.2. Non-stationary components of surveying errors.

The non-stationary parts of both  $\delta V^e$  and  $\delta V^n$  can jeopardize the long-term accuracy of the position components along the North and East directions. If we process  $\delta \dot{V}_{nst}^e$  and  $\delta \dot{V}_{nst}^n$  (see Eq.C.3) by integrating twice over time, the corresponding position errors  $\delta P_{E_{nst}}$  and  $\delta P_{N_{nst}}$  can be given as follows:

$$\delta P_{E_{nst}}(t_k) = \delta P_{E_{nst}}(t_{k-1}) - \left( V^n \delta \psi \right) \Delta t \quad (\text{C.6})$$

$$\delta P_{N_{nst}}(t_k) = \delta P_{N_{nst}}(t_{k-1}) + \left( V^e \delta \psi \right) \Delta t \quad (\text{C.7})$$

While determining the last two equations, it has been assumed that  $\int f_n dt = V^n$  and  $\int f_e dt = V^e$  for simplicity. It can be observed that  $\delta P_{E_{nst}}$  and  $\delta P_{N_{nst}}$  drifts with time at a rate of  $V^n \delta \psi$  and  $V^e \delta \psi$  respectively. The azimuth error ( $\delta \psi$ ) is therefore playing an important role in determining the long-term accuracy of the position components. Since it is modulated by the velocity components either along the North or

the East direction, the effect of azimuth error becomes particularly significant at high velocities. Fortunately, this is not the case with the present application of MWD surveying because the BHA always has slow penetration rate. However, if no optimal estimation of velocity errors are continuously determined and removed from the velocity components, we can expect significant long-term growth of the velocity errors, which give large inconsistent values of  $V^e$  and  $V^n$ . These large velocities values modulate the azimuth error and jeopardize the BHA position accuracy in the long-term. Therefore, it is essential to establish accurate computation of the velocity components to cancel the inclination and the roll errors and limit the growth rate of the position components.

### C.3. Solution of the surveying errors state equations.

The surveying errors in this section are categorized as errors along the horizontal channels (i.e. along the East and the North directions) and errors along the vertical channel. The errors along the horizontal channels include  $\delta P_{E_{nst}}$  and  $\delta P_{N_{nst}}$  for position errors along the East and the North directions,  $\delta V^e$  and  $\delta V^n$  for the velocity errors and  $\delta\theta$  and  $\delta\phi$  for the attitude errors. The errors along the vertical channel include the altitude error  $\delta h$ , the vertical velocity error  $\delta V^u$  and the azimuth error  $\delta\psi$ .

#### C.3.1. Surveying errors along the horizontal channels.

The behavior of surveying errors along the East channel  $\delta P_{E_{nst}}$ ,  $\delta V^e$  and  $\delta\phi$  are similar to that of the North channel  $\delta P_{N_{nst}}$ ,  $\delta V^n$  and  $\delta\theta$ , respectively. Thus, for simplicity, these error states are denoted as  $\delta P$  for the position error,  $\delta V$  for the velocity error and  $\varepsilon$  for either the inclination or the roll errors.

The different error sources contributing to these surveying errors are shown on Table C.1 for the velocity errors and Table C.2 for the position errors and Table C.3 for the attitude errors [Mohammed, 1999].

**Table C.1. Sources of velocity errors along any of the horizontal channels.**

$\delta V$ (Horizontal channel)	Error sources	
	Initial velocity errors $\delta V_0$ .	$\delta V_0 \cos(2\pi f_s t)$
	Initial misleveling $\varepsilon_0$ (i.e. initial errors in either the inclination or the roll angles).	$\varepsilon_0 R_o (2\pi f_s) \sin(2\pi f_s t)$
	Accelerometer bias errors ( $b$ )	$\frac{b}{2\pi f_s} \sin(2\pi f_s t)$
	Gyro drift ( $d$ )	$d R_o [1 - \cos(2\pi f_s t)]$

**Table C.2. Sources of position errors along any of the horizontal channels.**

$\delta P$ (Horizontal channel)	Error sources	
	Initial position errors $\delta P_0$ .	$\delta P_0$
	Initial velocity errors $\delta V_0$ .	$\frac{\delta V_0}{2\pi f_s} \sin(2\pi f_s t)$
	Initial misleveling $\varepsilon_0$ (i.e. initial errors in either the inclination or the roll angles).	$\varepsilon_0 R_o [1 - \cos(2\pi f_s t)]$
	Accelerometer bias errors ( $b$ )	$\frac{b}{4\pi^2 f_s^2} [1 - \cos(2\pi f_s t)]$
	Gyro drift ( $d$ )	$d R_o \left[ t - \frac{1}{2\pi f_s} \sin(2\pi f_s t) \right]$

**Table C.3. Sources of attitude errors along any of the horizontal channels.**

$\varepsilon$ (Horizontal channel)	Error sources	
	Initial velocity errors $\delta V_0$ .	$\frac{-\delta V_0}{2\pi f_s R_o} \sin(2\pi f_s t)$
	Initial misleveling $\varepsilon_0$ (i.e. initial errors in either the inclination or the roll angles).	$\varepsilon_0 \cos(2\pi f_s t)$
	Accelerometer bias errors ( $b$ )	$\frac{b}{4\pi^2 f_s^2 R_o} [\cos(2\pi f_s t) - 1]$
	Gyro drift ( $d$ )	$\frac{d}{2\pi f_s} \sin(2\pi f_s t)$

### C.3.2. Surveying errors along the vertical channel.

The different error sources contributing to these surveying errors  $\delta V^u$ ,  $\delta h$  and  $\delta \psi$  are shown on Tables C.4, Table C.5 and Table C.6, respectively.

**Table C.4. Sources of velocity errors along the vertical channel.**

$\delta V^u$ (Vertical channel)	Error sources	
	Initial velocity errors $\delta V_{u0}$ .	$\delta V_{u0}$
	Accelerometer bias errors ( $b_u$ ) along the vertical channel	$b_u t$

**Table C.5. Sources of position errors along the vertical channel.**

$\delta h$ (Vertical channel)	Error sources	
	Initial position errors $\delta h_0$ .	$\delta h_0$
	Initial velocity errors $\delta V_{u0}$ .	$\delta V_{u0} t$
	Accelerometer bias errors ( $b_u$ ) along the vertical channel.	$\frac{1}{2} b_u t^2$

**Table C.6. Sources of attitude errors along the vertical channel.**

$\delta \psi$ (Vertical channel)	Error sources	
	Initial velocity errors $\delta V_0$ along the horizontal channel.	$-\frac{\delta V_0}{R_o} \tan \varphi \left( \frac{\sin(2\pi f_s t)}{2\pi f_s} \right)$
	Initial misalignment $\delta \psi_0$ (i.e. initial azimuth errors).	$\delta \psi_0$
	Initial misleveling $\varepsilon_0$ (i.e. initial errors in either the inclination or the roll angles).	$\varepsilon_0 \tan \varphi [-1 + \cos(2\pi f_s t)]$
	Accelerometer bias errors ( $b$ )	$-\frac{b}{R} \tan \varphi \left( \frac{1}{4\pi^2 f_s^2} \right) [1 - \cos(2\pi f_s t)]$
	Horizontal Gyro drift ( $d$ )	$d \tan \varphi \left[ \frac{\sin(2\pi f_s t)}{2\pi f_s} - t \right]$
	Vertical Gyro drift ( $d_u$ )	$d_u t$

#### C.4. Simulation results.

Apparently, the surveying errors along either the horizontal or the vertical channels are related to the corresponding initial error, the misleveling at the roll or the pitch angles, the azimuth misalignment, the accelerometer bias errors and the gyro drifts. The different error terms shown on Tables C.1 to C.6 have been modeled using MATLAB computer-aided design software (Mathworks, Natick, MA). The following parameters were considered as constants and were assigned the shown values:

Latitude ( $\varphi$ )	: $51.07^\circ$
Initial misleveling $\varepsilon_0$	: $0.01^\circ$
Initial azimuth misalignment	: $0.1^\circ$
Gyro drift	: $0.01^\circ/hr$
Accelerometer bias error	: $100 \mu g \cong 9.8080 \times 10^{-4}$
Earth mean radius $R_o$	: $6374.5 km$
Initial velocity error	: $0.1 cm/sec$
Initial altitude error	: $1 m$
Initial horizontal position error	: $0.1 m$
Simulation time	: $2 hr$

The simulation results for the different surveying parameters due to the several factors indicated above can be shown on Figs.C.2 to C.7. It can be determined that each figure shows the individual impact of the different error sources as well as their total effect into the surveying parameter.

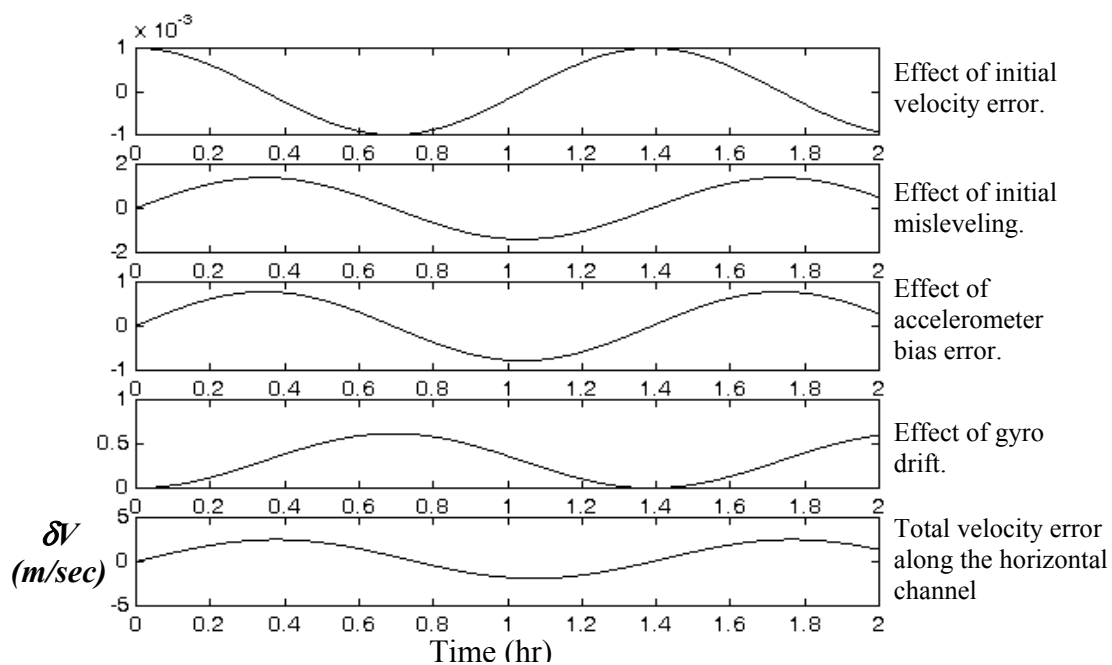


Fig.C.2. The different factors affecting the velocity error along the horizontal channel and their total effect.

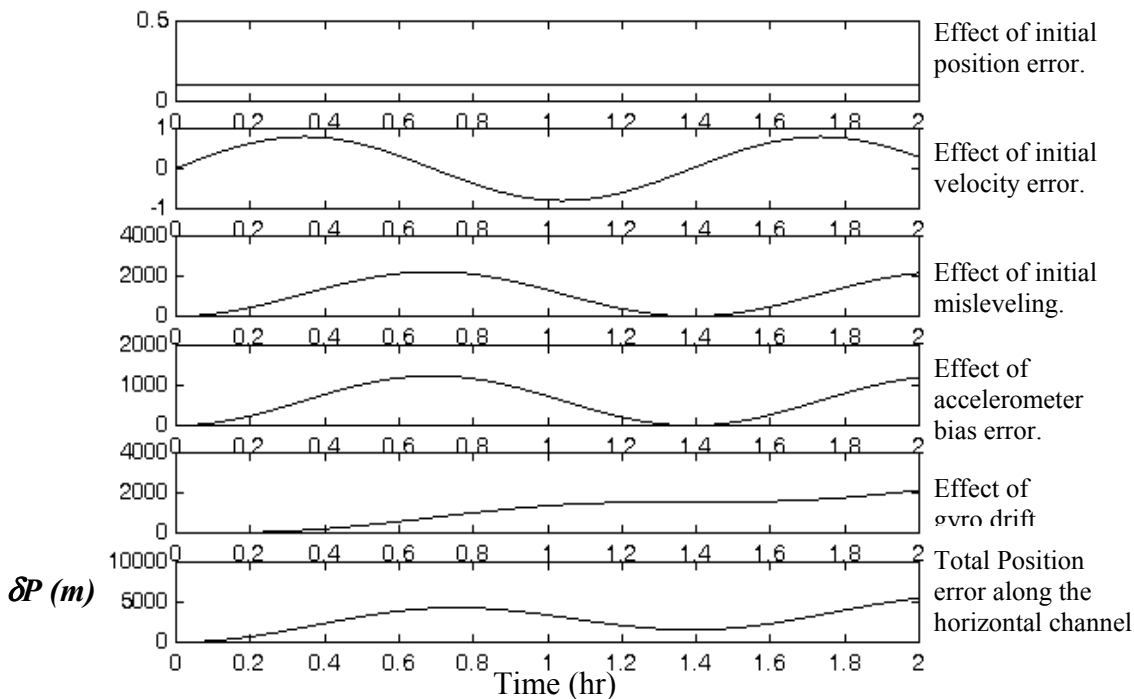


Fig.C.3. The different factors affecting the position error along the horizontal channel and their total effect.

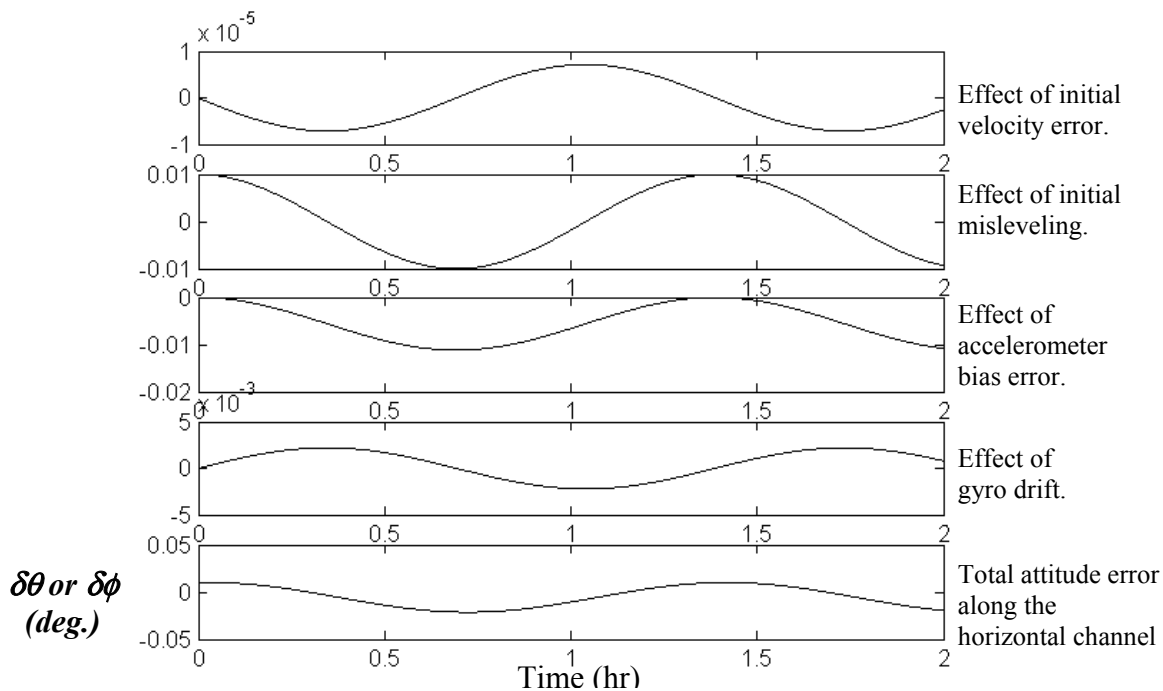


Fig.C.4. The different factors affecting the pitch or the roll error and their total effect.

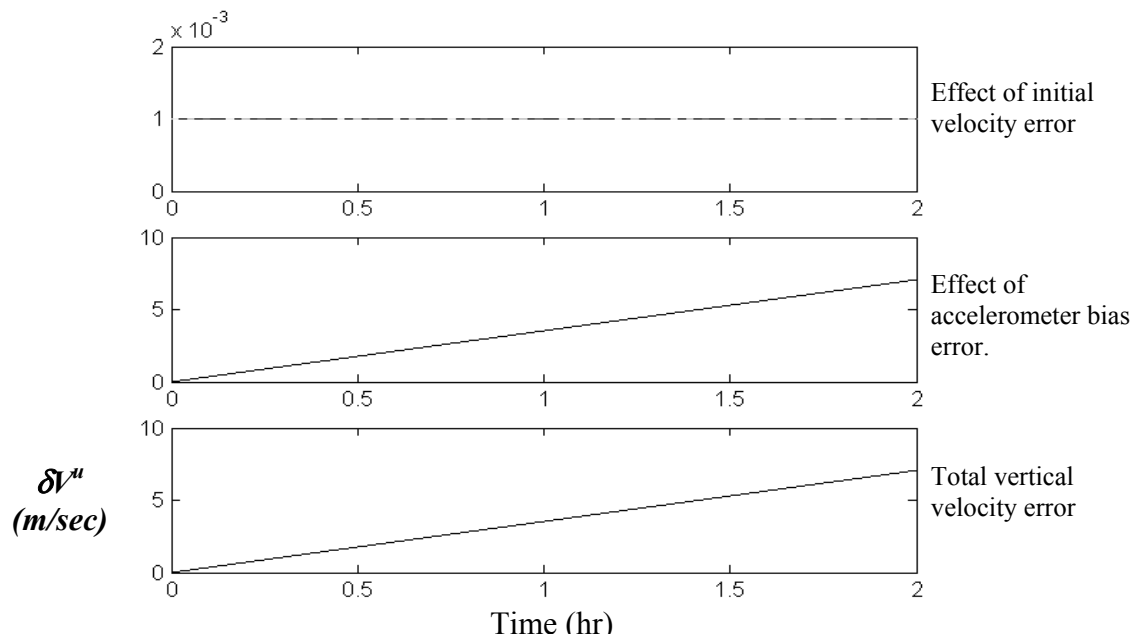


Fig.C.5. The different factors affecting the vertical velocity error and their total effect.

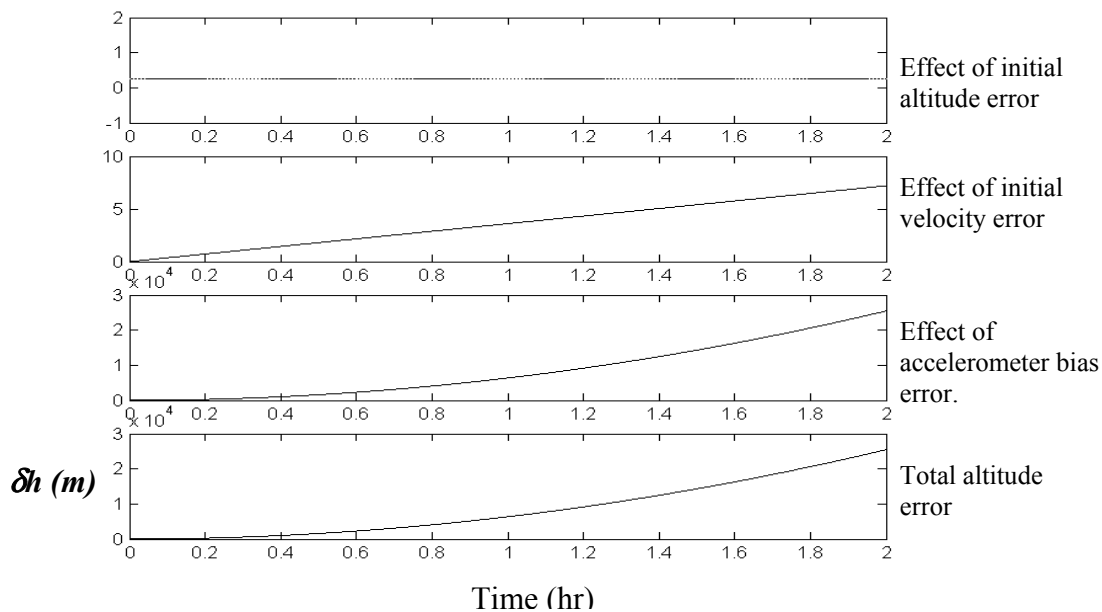


Fig.C.6. The different factors affecting the altitude error and their total effect.

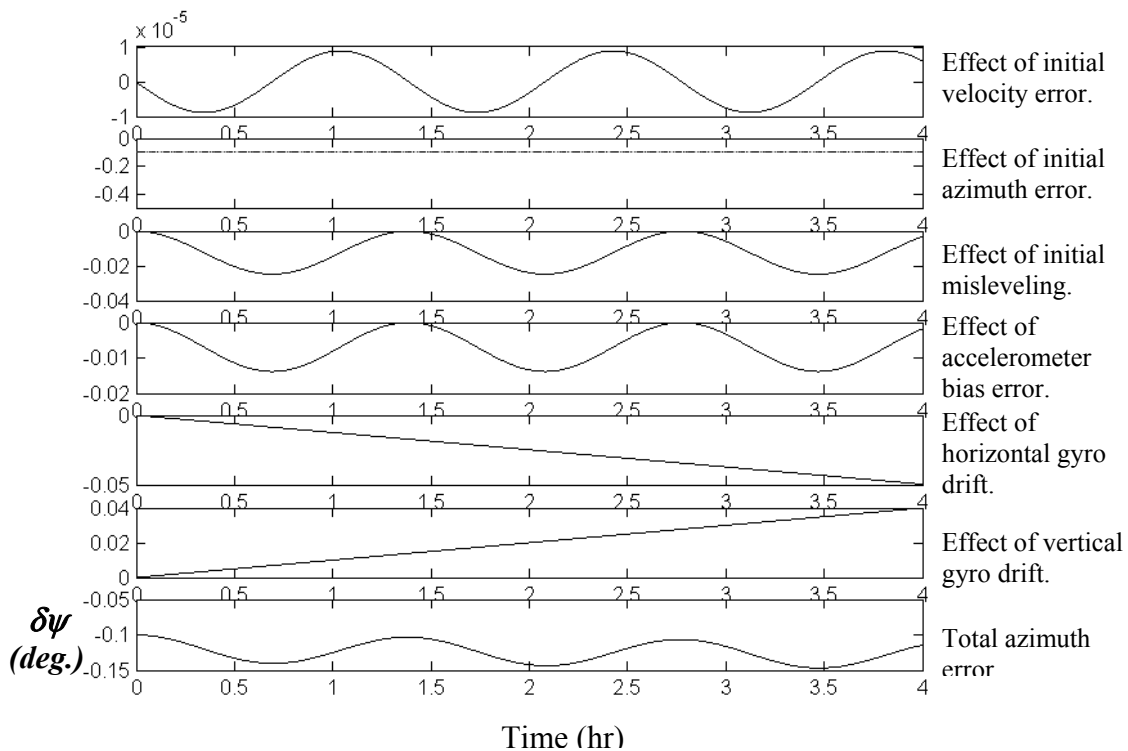


Fig.C.7. The different factors affecting the azimuth error and their total effect.

**APPENDIX D**  
**KALMAN FILTERING ALGORITHM AND THE RELATED DESIGN**  
**CONSIDERATIONS**

Kalman filtering is an optimal estimation tool that provides a sequential recursive algorithm for the optimal least mean variance estimation of the system states [Gelb, 1974]. In addition to its benefits as an optimal estimator, the Kalman filter provides real-time statistical data related to the estimation accuracy of the system states, which is very useful for quantitative error analysis [Brown and Hwang, 1997]. The filter generates its own error analysis with the computation of the error covariance matrix, which gives an indication of the estimation accuracy.

Let us assume that the random process to be estimated can be modeled using the following discrete state space representation:

$$x_k = F_{k,k-1}x_{k-1} + G_{k-1}w_{k-1} \quad (\text{D.1})$$

where  $x_k$  is the process state vector,  $F_{k,k-1}$  is a square matrix relating  $x_k$  to  $x_{k-1}$  and is called the state transition (dynamic) matrix and  $w_{k-1}$  is a random forcing function which is considered as a unity-variance white Gaussian noise with  $G_{k-1}$  being its coefficient vector.

The observation (measurement) of the process is assumed to occur at discrete points in time and follow the linear relationship:

$$y_k = H_k x_k + v_k \quad (\text{D.2})$$

where  $y_k$  is the measurement vector at time  $t_k$ ,  $H_k$  is the design matrix giving the ideal noiseless relationship between the observations vector and the state vector, and  $v_k$  is the vector of observations random noise, which is assumed to be white sequence with known covariance structure and having zero correlation with  $w_k$ .

The covariance matrices for the two noise sequences  $w_k$  and  $v_k$  vectors are given by:

$$E[w_k w_i^T] = \begin{cases} Q_k & i = k \\ 0 & i \neq k \end{cases} \quad (\text{D.3})$$

$$E[v_k v_i^T] = \begin{cases} R_k & i = k \\ 0 & i \neq k \end{cases} \quad (\text{D.4})$$

$$E[w_k v_i^T] = 0 \quad \text{for all } i \text{ and } k. \quad (\text{D.5})$$

It is also assumed that an initial estimate of the state vector  $x_k$  is known at  $k=0$ . This a priori estimate is denoted as  $\hat{x}_0$ . In addition, the error covariance matrix associated with the estimate of  $\hat{x}_0$  is known and given as follows:

$$P_0 = E[e_0 e_0^T] = E[(x_0 - \hat{x}_0)(x_0 - \hat{x}_0)^T] \quad (\text{D.6})$$

The sequential recursive algorithm for the optimal least mean variance estimation of the error states can be described by the block diagram shown on Fig.D.1.

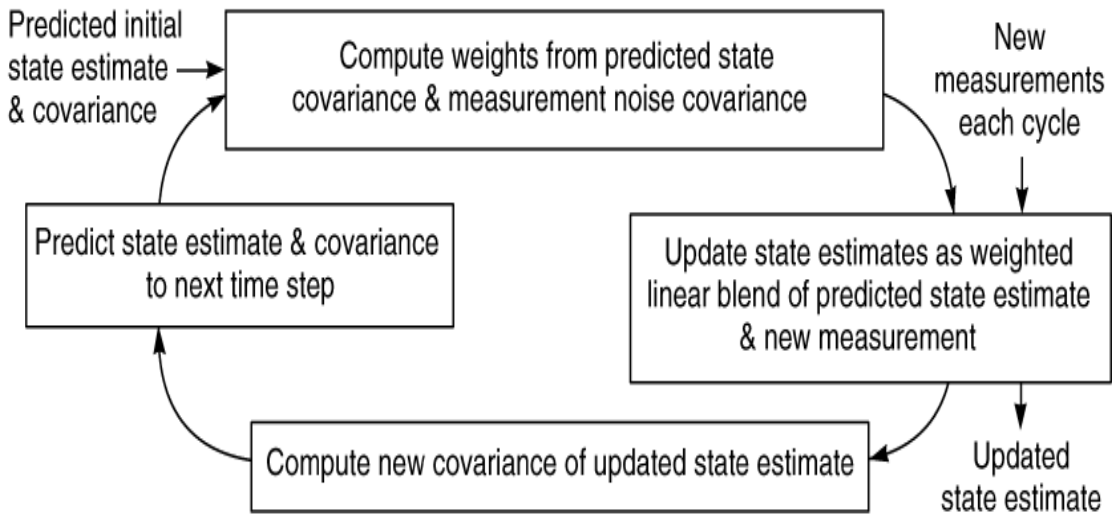


Fig. D.1. Block diagram of Kalman filtering sequential recursive algorithm.

In general, the Kalman filter algorithm involves two steps. The first step is to make a prediction  $\hat{x}_k(-)$  of the error states  $x_k$  based on the estimation of the previous error states  $\hat{x}_{k-1}(+)$ . The second step is to update the predicted estimation using the available measurement  $y_k$  at the current moment. This procedure can be described by the diagram shown on Fig.D.2. With each prediction and update step, the covariance matrices

$P_k(-)$  and  $P_k(+)$  corresponding to the predicted  $\hat{x}_k(-)$  and the updated  $\hat{x}_k(+)$  estimates are calculated as indicated on the Kalman filtering algorithm shown on Fig.D.3. The update estimate  $\hat{x}_k(+)$  is determined based on the computation of the Kalman gains  $K_k$ .

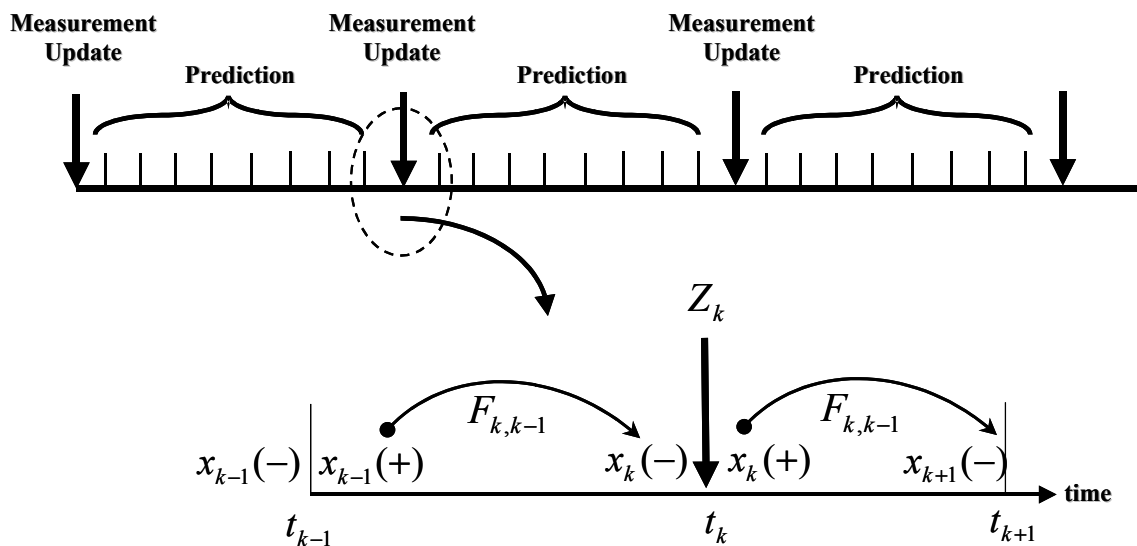


Fig.D.2. Prediction and update procedures of Kalman filtering algorithm.

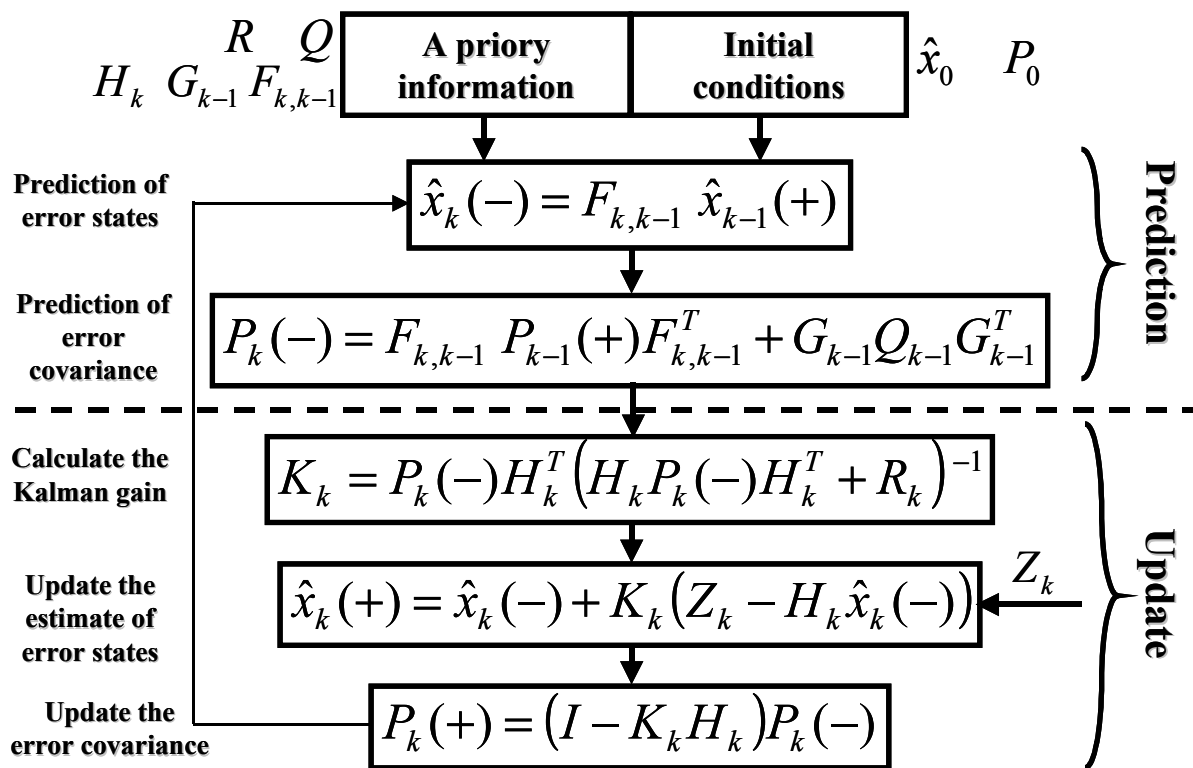


Fig.D.3. Kalman filtering recursive algorithm.